

Experimental and Computational Study of Haemodialysis Vascular Access



David Fulker

University of New South Wales

School of Mechanical and Manufacturing Engineering

A thesis presented for the degree of

Doctor of Philosophy

August 2016

THE UNIVERSITY OF NEW SOUTH WALES
Thesis/Dissertation Sheet

Surname or Family name: Fulker

First name: David

Other name/s: John

Abbreviation for degree as given in the University calendar: PhD

School: Mechanical and Manufacturing Engineering

Faculty: Engineering

Title: Experimental and computational study of haemodialysis vascular access

Abstract 350 words maximum:

The need to maintain long term vascular access patency is critical for patients with kidney failure. Vascular access allows artificial blood filtration through haemodialysis and failure of the access can be life threatening. The mechanisms for failure are not understood and dialysis needles may be a key contributor.

Haemodynamic parameters play an important role in vascular health and have been linked to the development of intimal hyperplasia, a pathological growth of the blood vessel initiated by injury. The primary objective of this thesis is to examine the haemodynamic forces produced by dialysis needles and to determine methods of identifying and minimising the risk of vascular access failure.

Computational fluid dynamic models have been utilised to examine the haemodynamics produced by the needles, in particular the high shear stresses on the vein wall and the oscillatory shear with high particle residency times. Pressures were also examined to determine the potential of microbubble formation due to cavitation. These computational simulations were validated using stereoscopic particle image velocimetry measurements on a flow rig. Clinical data was also used to support the models.

Both needles produced disturbed flows with high residency times which may lead to endothelial dysfunction, whilst the venous needle also produced high shear stresses at the point of jet impingement, which may damage the endothelial layer. Elevated blood flow rates (>600 ml/min) and sharp changes in geometry were catalysts for cavitation at the arterial needle, whilst Doppler ultrasound measurements revealed a high level of pulsatility within the extracorporeal circuit.

Patient data confirmed that stenosis in the venous outflow segment is pertinent in late fistula failure. Shallow needle angles with optimal placement away from the walls of the vein and the use of blood flow rates around 300 ml/min may minimise potential endothelial damage. A plastic cannula for haemodialysis is also a viable alternative to the current metal needles. In regards to microbubble formation, cavitation at the arterial needle was shown to be possible but is unlikely to occur under normal dialysis conditions. However, microbubbles may develop at the roller pump due to the highly pulsatile flow it generates.

Declaration relating to disposition of project thesis/dissertation

I hereby grant to the University of New South Wales or its agents the right to archive and to make available my thesis or dissertation in whole or in part in the University libraries in all forms of media, now or here after known, subject to the provisions of the Copyright Act 1968. I retain all property rights, such as patent rights. I also retain the right to use in future works (such as articles or books) all or part of this thesis or dissertation.

I also authorise University Microfilms to use the 350 word abstract of my thesis in Dissertation Abstracts International (this is applicable to doctoral theses only).

.....
Signature

.....
Witness Signature

..... Date

The University recognises that there may be exceptional circumstances requiring restrictions on copying or conditions on use. Requests for restriction for a period of up to 2 years must be made in writing. Requests for a longer period of restriction may be considered in exceptional circumstances and require the approval of the Dean of Graduate Research.

FOR OFFICE USE ONLY

Date of completion of requirements for Award:

Certificate of Originality

Copyright Statement

I hereby grant the University of New South Wales or its agents the right to archive and to make available my thesis or dissertation in whole or part in the University libraries in all forms of media, now or here after known, subject to the provisions of the Copyright Act 1968. I retain all proprietary rights, such as patent rights. I also retain the right to use in future works (such as articles or books) all or part of this thesis or dissertation.

I also authorise University Microfilms to use the 350 word abstract of my thesis in Dissertation Abstract International (this is applicable to doctoral theses only).

I have either used no substantial portions of copyright material in my thesis or I have obtained permission to use copyright material; where permission has not been granted I have applied/will apply for a partial restriction of the digital copy of my thesis or dissertation.

Signed:

Date: 8/11/2016

Authenticity Statement

I certify that the Library deposit digital copy is a direct equivalent of the final officially approved version of my thesis. No emendation of content has occurred and if there are any minor variations in formatting, they are the result of the conversion to digital format.

Signed:

Date: 8/11/2016

Originality Statement

I hereby declare that this submission is my own work and to the best of my knowledge it contains no materials previously published or written by another person, or substantial proportions of material which have been accepted for the award of any other degree or diploma at UNSW or any other educational institution, except where due acknowledgment is made in the thesis. Any contribution made to the research by others, with whom I have worked at UNSW or elsewhere, is explicitly acknowledged in the thesis. I also declare that the intellectual content of this thesis is the product of my own work, except to the extent that assistance from others in the project's design and conception or in style, presentation and linguistic expression is acknowledged.

Signed:

Date: 8/11/2016

Acknowledgements

Before beginning this PhD it was described to me as a roller coaster ride with great ups and downs. They could not have been more right. This has been the greatest challenge I have faced thus far and it required much intellectual and emotional effort on my behalf. It would not have been possible without the help from many people.

Firstly, I would like to thank my supervisors, Associate Professor Tracie Barber and Professor Anne Simmons for their never wavering support. You were always available to chat and made the experience so much more enjoyable. You supported me in every decision and gave me the freedom to pursue my research interests. These words can never express my gratitude.

A huge appreciation goes to the technical staff in the School of Mechanical Engineering. I would like to thank Joe Tscherry for his knowledge of laser systems and technical support. Ian Cassapi, Andy Higley and Vince Carnevale, three brilliant engineers whose help in designing and building the pumps and bench top flow rigs made my experiments possible and turned a drawing into reality. I'd also like to thank Professor John Reizes for all his suggestions in computational modelling, PIV and endless supply of dad jokes.

A big thank you to the dialysis team at the Prince of Wales Hospital (Debbie Pugh, Jael Wolk, Dr Shannon Thomas and Professor Zoltan Endre) for allowing me to collect clinical data and provide an opportunity that most engineers do not get to experience.

I'd also like to thank my family for encouraging me to never give up. Especially, mum and dad who helped review my work and always inquired about my day. It helped more than you know. Although I would appreciate a bit more meat at dinner.

To my grandparents, Ann and Don Fulker, and the late Keith and Nancy Burnham, you always showed so much interest in my research. I hope to be as successful at engineering as Don and Keith were. I hope you enjoy reading this.

To my fellow PhD comrades Reza, PJ, James, Azi, Julia, Kyle, Eamonn and John for making the CFD/Fluids lab a fun place to work in. We had so many good times from policing the cluster and throwing around the stress ball to adventuring around the Harvard campus. I wish you all the best in your futures and can't wait to read your theses.

To my lab rats/undergraduate monkeys Xiaomeng Xie, Tan Zhi Ming and Ken Lee for helping ease the work load. Most people have a phobia of needles whilst I have a strange interest in them. Thanks for giving me the opportunity to teach you guys about dialysis needles.

And finally to my official review team of Kaitlyn, Glen "Crouchy" Clifton, Geoff and Sammy, who helped me make amazing presentations and edited my final drafts. Geoff and Sammy's competition to find mistakes, whilst not appreciated, really contributed to the final draft. Statistically speaking though there wasn't that many. I also shouldn't have made this deal and will regret it when I read this in 10 years. Here we go... Go Leicester!

Special shout out to Squincy Bones.

List of Publications

Journal Papers

David Fulker, Martin Kang, Anne Simmons, and Tracie Barber. The flow field near a venous needle in hemodialysis: a computational study. *Hemodialysis International*, 17(4): 602-611, 2013

David Fulker, Gholamreza Keshavarzi, Anne Simmons, Debbie Pugh, and Tracie Barber. Pulsatility produced by the hemodialysis roller pump as measured by Doppler ultrasound. *Artificial Organs*, 39(11):945-950, 2015

David Fulker, Anne Simmons Kaveh Kabir, Lauren Kark, and Tracie Barber. The hemodynamic effects of hemodialysis needle rotation and orientation in an idealized computational model. *Artificial Organs*, 40(2):185-189, 2015

David Fulker, Anne Simmons, and Tracie Barber. Computational Model of the Arterial and Venous Needle during Haemodialysis. *Journal of Biomechanical Engineering*, 139(1), 2017

David Fulker, Anne Simmons, and Tracie Barber. Time-resolved stereo particle image velocimetry of the impinging venous needle jet during haemodialysis. *International Journal of Heat and Fluid Flow*, **Under Review**

David Fulker, Zakir Sayed, Anne Simmons, and Tracie Barber. Computational Fluid Dynamic Analysis of the Haemodialysis Plastic Cannula. *Artificial Organs*, **Accepted for publication**

Conference Papers

David Fulker, Tracie Barber, Anne Simmons, and Gholamreza Keshavarzi. Investigation into the existence of cavitation within haemodialysis needles. *Applied Mechanics and Materials*, 553:199-204, 2014

Conference Abstracts

David Fulker, Xiaomeng Xie, Tracie Barber, and Anne Simmons. Analysis of Flow Rate on Haemodialysis Venous Needle Turbulence Using Flow Visualisation Techniques. *Australian Biomedical Engineering Conference (ABEC)*, October 16, Sydney, Australia, 2013

David Fulker, Zhi Ming Tan, Anne Simmons, and Tracie Barber. Particle Image Velocimetry of the Venous Needle Jet in Haemodialysis. *American Society of Artificial Internal Organs Annual Conference*, June 18-21, Washington DC, United States, 2014

David Fulker, Tracie Barber, and Anne Simmons. The effects of needle rotation and orientation on vascular access patency. *Renal Society of Australia Annual Conference*, August 25-27, Leuven, Belgium, 2014

David Fulker, Anne Simmons, and Tracie Barber. Optimal Placement of the Arterial and Venous Needle in a Radio-Cephalic Fistula. *Nordic Society of Nephrology Annual Conference*, August 26-29, Stavanger, Norway, 2015

David Fulker, Zakir Sayed, Anne Simmons, and Tracie Barber.
Haemodynamic Comparison of Metal Needles and Plastic Cannulae in
Haemodialysis. *European Society of Artificial Internal Organs Annual
Conference*, September 2-5, Leuven, Belgium, 2015

Abstract

The need to maintain long term vascular access patency is critical for patients with kidney failure. Vascular access allows artificial blood filtration through haemodialysis and failure of the access can be life threatening. The mechanisms for failure are not understood and dialysis needles may be a key contributor.

Haemodynamic parameters play an important role in vascular health and have been linked to the development of intimal hyperplasia, a pathological growth of the blood vessel initiated by injury. The primary objective of this thesis is to examine the haemodynamic forces produced by dialysis needles and to determine methods of identifying and minimising the risk of vascular access failure.

Computational fluid dynamic models have been utilised to examine the haemodynamics produced by the needles, in particular the high shear stresses on the vein wall and the oscillatory shear with high particle residency times. These computational simulations were validated using stereoscopic particle image velocimetry measurements on a flow rig. The flow field produced by the arterial needle remained localised around the needle tip indicating that the two needles can be placed in close proximity to each other without increasing the risk of access recirculation.

Conversely, the flow field produced by the venous needle was more dynamic due to the presence of the jet. Both needles produced disturbed flows with high residency times which may lead to endothelial dysfunction, whilst the venous needle also produced high shear stresses at the point of jet impingement, which may damage the endothelial layer. Shallow needle angles with optimal placement away from the walls of the vein and the use of blood flow rates around 300 ml/min may minimise potential endothelial damage. Needle rotation, a technique usually performed to alleviate pressure in the arterial line, was shown to have no haemodynamic benefit and can increase the risk of infiltration.

A plastic cannula for haemodialysis offers a viable alternative to the current metal needles. Its symmetric geometry with four staggered side holes also negates the requirement of rotation.

Pressures were also examined to determine the potential of microbubble formation due to cavitation. Elevated blood flow rates (>600 ml/min) and sharp changes in geometry were catalysts for cavitation at the arterial needle. Doppler ultrasound measurements revealed a high level of pulsatility within the extracorporeal circuit. This indicated that cavitation at the arterial needle is unlikely to occur under normal dialysis conditions, but may occur at the roller pump.

Clinical measurements pertaining to each dialysis session were also analysed to determine the incidence of late fistula failure. Patient data confirmed that stenosis in the venous outflow segment is pertinent in late fistula failure. The risk of stenosis was higher in the first six months of fistula use, as the blood vessels adapt to frequent cannulation. This was reflected by the increase in vascular resistance over the life of the access. The patient data supports the computational results, which indicates that stenosis in the outflow vein may be caused by the haemodynamics produced by dialysis needles.

Contents

Abstract	iii
List of Figures	xxx
List of Tables	xxxiii
Nomenclature	xxxvi
1 Introduction	1
1.1 Overview	1
1.2 Haemodialysis	3
1.3 Vascular Access	4
1.4 Vascular Access Related Complications	7
1.4.1 Thrombosis	8
1.4.2 Stenosis	8
1.4.3 Aneurysm	10
1.4.4 Infection	11
1.4.5 Microbubbles	11
1.4.6 Minor Complications	12
1.5 Thesis Outline	13
2 Literature Review	15
2.1 The Role of Haemodynamics in Vascular Access Failure	16

2.1.1	Metrics of Predicting Vascular Complications	16
2.1.2	Shear Stress	17
2.1.3	Residence Time	19
2.1.4	Turbulence	19
2.1.5	Alternative Indices	20
2.2	Current Research into Haemodialysis Haemodynamics	21
2.2.1	Haemodialysis Cannulation	22
2.2.2	Arteriovenous Fistulae and Arteriovenous Grafts	28
2.2.2.1	In-vivo Experiments	28
2.2.2.2	In-vitro Experiments	30
2.2.2.3	Numerical Modelling	33
2.3	Summary of Literature	37
2.4	Thesis Objectives	38
3	Clinical Study: Correlation between haemodynamics and late fistula failure	41
3.1	Introduction	42
3.2	Methods	44
3.2.1	Study Design	44
3.2.2	Data Analysis Methodology	45
3.2.3	Statistical Analysis	47
3.3	Results	48
3.3.1	Complications	48
3.3.2	Standard least-squares regression analysis	49
3.3.3	Effects of Fistula Survival	51
3.3.4	Effects of Vascular Health	54
3.4	Discussion	56
3.5	Limitations	61
3.6	Conclusion	62
4	Experimental Study of Cannulation Technique: Methods	63

4.1	Introduction	63
4.2	Experimental Methods	65
4.2.1	Bench Top Flow Rig	65
4.2.2	Dimensional Scaling	71
4.2.3	Blood Analogue Fluid	72
4.2.4	Stereo-PIV Setup	74
4.3	Experimental Uncertainty	82
4.3.1	Methodology	82
4.3.2	Bias Error	84
4.3.3	Precision Error	85
4.3.4	PIV Error	88
4.3.5	Repeatability	89
5	Experimental Study of Cannulation Technique: Results and Discussion	93
5.1	Summary of Cases	93
5.2	Results	96
5.2.1	Arterial Needle	96
5.2.1.1	Antegrade Orientation	96
5.2.1.2	Retrograde Orientation	103
5.2.2	Venous Needle	109
5.3	Discussion	117
5.3.1	Arterial Needle	118
5.3.2	Venous Needle	119
5.3.3	Limitations	123
5.4	Conclusion	123
6	Numerical Study of Cannulation Technique	125
6.1	Introduction	126
6.2	Numerical Methods	128
6.2.1	Computational Domain	128

6.2.2	Boundary Conditions	131
6.2.3	Metric Analysis	134
6.3	Numerical Uncertainty	135
6.4	Numerical Validation	136
6.5	Results	143
6.5.1	Arterial Needle in Antegrade	143
6.5.2	Arterial Needle in Retrograde	146
6.5.3	Venous Needle	150
6.5.4	Needle Rotation	155
6.6	Discussion	160
6.6.1	Arterial Needle	161
6.6.2	Venous Needle	164
6.6.3	Influence of the needles on vascular health	166
6.6.4	Needle Rotation	167
6.6.5	Limitations	169
6.7	Conclusion	170
7	Analysis of Cavitation in Haemodialysis Needles	172
7.1	Introduction	173
7.2	Methods	175
7.2.1	Computational Model	175
7.2.2	Clinical Analysis	176
7.2.2.1	Haemodialysis Setup	176
7.2.2.2	Ultrasound Setup	178
7.2.2.3	Statistical analysis	179
7.3	Results	180
7.3.1	Arterial Needle Computational Model	180
7.3.2	Venous Needle Computational Model	183
7.3.3	Clinical Measurements	184
7.4	Discussion	188
7.5	Conclusion	193

8 Covidien Cannula: An alternative device for Vascular Access	195
8.1 Introduction	195
8.2 Numerical Methods	197
8.2.1 Validation and Verification	199
8.3 Results	200
8.3.1 Analysis of the Cannula Flow Field	200
8.3.2 Comparison against the standard metal needle	208
8.4 Discussion	214
8.4.1 Flow Dynamics and Clinical Implications	215
8.4.2 Benefit of using a plastic cannula over the standard metal needle	218
8.5 Conclusion	221
9 Conclusions	222
9.1 Key Findings	223
9.2 Future Direction	228
A Experimental Uncertainty Analysis	231
A.1 Vein Diameter	232
A.2 Needle Diameter	233
A.3 Solution Concentration	233
A.4 Temperature	239
A.5 Density	241
A.6 Viscosity	243
A.7 Piston Velocity (Fistula Pump)	248
A.8 Piston Velocity (Needle Pump)	250
B PIV Uncertainty Analysis	253
B.1 Image Distortion:	253
B.2 Particle Image Diameter:	253
B.3 Particle Image Displacement:	255

B.4	Particle Image Density:	256
B.5	Image Quantisation:	258
B.6	Background Noise:	259
B.7	Displacement Gradients:	260
C	Computational Sensitivity Analysis	262
C.1	Analysis of Mesh Size	262
C.2	Analysis of Time Step Size	266
D	Numerical Validation	269

List of Figures

1.1	Haemodialysis Setup	4
1.2	a) Central Venous Catheter b) Arteriovenous Fistula c) Arteriovenous Graft	5
1.3	Cost of ESRD Treatments per patient per year (PPPY)	7
1.4	Common locations of stenosis formation in arteriovenous fistulae	9
2.1	Puncture sites for various methods of cannulation. a) Rope Ladder b) Area c) Button hole	22
2.2	Various needle designs. a) Oval Back Eye b) Ellipse Back Eye c) Two Back Eyes d) Side Eyes	25
2.3	Needle orientation where the arrow indicates the direction of blood flow in the vein. a) Antegrade b) Retrograde	27
2.4	Movement of the stagnation point throughout the cardiac cycle in vascular grafts. The figures are labelled as: heel (H), toe (T), proximal (P), distal (D), laminar flow (LF), stagnation point (SP). a) Early Systole b) Mid-Systole	29
2.5	Effects of refractive index matching on acrylic models. a) No refractive index matching fluid b) Refractive index matching fluid	32
2.6	Isosurfaces of helicity showing the development of transitional flow at the anastomosis. a) Systole b) Diastole	34
2.7	CFD and PIV data on flow through a patient specific AVF	37

3.1	Prevalence of End Stage Renal Disease in the United States .	42
3.2	Incident rates in the United States of primary causes of ESRD	43
3.3	Relationship between average blood flow rate averaged over all sessions per patient and time to failure (useful fistula age). Standard deviation is the average across all measurements for the cohort of patients.	49
3.4	Relationship between average arterial pressure averaged over all sessions per patient and time to failure (useful fistula age). Standard deviation is the average across all measurements for the cohort of patients.	50
3.5	Relationship between average venous pressure averaged over all sessions per patient and time to failure (useful fistula age). Standard deviation is the average across all measurements for the cohort of patients.	51
3.6	Kaplan Meier Survival Analysis for each patient group	55
4.1	Features of the impinging VNJ including: free stream jet (1), recirculation zone (2), wall jet (3) and impingement zone (4). Regions in red show the boundary layer between the various flow zones	64
4.2	Fistula pump used in the experiments. 1) Reservoir 2) Control unit 3) Cylinder and piston 4) Stepper Motor 5) Encoder 6) Four solenoid valves 7) Atrato Ultrasonic flow meter 8) MRC22 PT100 pressure transducer and Monel Thermowell PT100 temperature transducer 9) Bleed system .	66
4.3	Flow meter data (measured at the outlet of the pump) from one cycle of the fistula pump	67
4.4	Pressure data (measured at the outlet of the pump) from one cycle of the fistula pump	67
4.5	Experimental Setup	68
4.6	Schematic of the Experimental Setup	69

4.7	Needle placed within the PMMA block. 1) Vein 2) Needle 3) Locating Pin 4) Nut and Ferrule	70
4.8	Back eye dimensions in the scaled 10G needle	70
4.9	Camera Setup	74
4.10	Schematic for the reconstruction of three components of the velocity vector for stereoscopic PIV measurements	75
4.11	Angle displacement arrangement of the Scheimpflug condition	77
4.12	Laser and camera setup for stereoscopic particle image velocimetry measurements. 1) Phantom M310 high speed camera 2) Nikkor 105 mm lens 3) Mounting on traverse system 4) 058-5 calibration plate 5) Laser head to the Nd:YLF New Wave Pegasus laser 6) Needle 7) PMMA Rig 8) Pump	79
4.13	Schematic displaying the sections captured around the needle. a) Venous needle b) Arterial needle in antegrade c) Arterial needle in retrograde	80
4.14	Uncertainty comprised of precision and bias errors	83
4.15	Convergence of the number of images required to achieve a repeatable time averaged result. Velocity profile measured 5d from the venous needle tip.	90
4.16	Convergence of the number of images required to achieve a repeatable time averaged result. Maximum velocity in the jet as measured 5d from the venous needle tip.	91
4.17	Repeatability of PIV results. Velocity profile measured 5d from the venous needle tip.	92

5.1	Contours of time averaged z-velocity with vectors of normalised velocity for the arterial needle in the antegrade orientation with different needle flow rates. The needle tip is placed in the middle of the vein at an angle of 20°. A steady flow rate of 666 ml/min is passed through the vein. a) 200 ml/min b) 300 ml/min c) 400 ml/min	97
5.2	Velocity profiles from the arterial needle in the antegrade orientation for different needle flow rates. The needle tip is placed in the middle of the vein at an angle of 20°. A steady flow rate of 666 ml/min is passed through the vein. a) Needle tip b) 5d downstream of the needle tip c) 10d downstream of the needle tip d) 15d downstream of the needle tip	98
5.3	Contours of time averaged z-velocity with vectors of normalised velocity for the arterial needle in the antegrade orientation with different needle depths. The needle is placed at an angle of 20° with an equivalent blood flow rate of 300 ml/min. A steady flow rate of 666 ml/min is passed through the vein. a) bottom b) middle c) top	99
5.4	Velocity profiles from the arterial needle in the antegrade orientation for different needle depths. The needle is placed at an angle of 20° with an equivalent blood flow rate of 300 ml/min. A steady flow rate of 666 ml/min is passed through the vein. a) Needle tip b) 5d downstream of the needle tip c) 10d downstream of the needle tip d) 15d downstream of the needle tip	100

5.5	Contours of time averaged z-velocity with vectors of normalised velocity for the arterial needle in the antegrade orientation with different needle angles. The needle tip is placed in the middle of the vein with an equivalent blood flow rate of 300 ml/min. A steady flow rate of 666 ml/min is passed through the vein. The black section represents the region which was masked due to shadows produced by the o-ring and block alignment pins. a) 10° b) 20° c) 30°	101
5.6	Velocity profiles from the arterial needle in the antegrade orientation for different needle angles. The needle tip is placed in the middle of the vein with an equivalent blood flow rate of 300 ml/min. A steady flow rate of 666 ml/min is passed through the vein. a) Needle tip b) 5d downstream of the needle tip c) 10d downstream of the needle tip d) 15d downstream of the needle tip	102
5.7	Contours of time averaged z-velocity with vectors of normalised velocity for the arterial needle in the retrograde orientation with different needle flow rates. The needle tip is placed in the middle of the vein at an angle of 20°. A steady flow rate of 666 ml/min is passed through the vein. a) 200 ml/min b) 300 ml/min c) 400 ml/min	103
5.8	Velocity profiles from the arterial needle in the retrograde orientation for different needle flow rates. The needle tip is placed in the middle of the vein at an angle of 20°. A steady flow rate of 666 ml/min is passed through the vein. a) Needle tip b) 5d upstream of the needle tip c) 10d upstream of the needle tip	105

5.9	Contours of time averaged z-velocity with vectors of normalised velocity for the arterial needle in the retrograde orientation with different needle depths. The needle is placed at an angle of 20° with an equivalent blood flow rate of 300 ml/min. A steady flow rate of 666 ml/min is passed through the vein. a) bottom b) middle c) top	106
5.10	Velocity profiles from the arterial needle in the retrograde orientation for different needle depths. The needle is placed at an angle of 20° with an equivalent blood flow rate of 300 ml/min. A steady flow rate of 666 ml/min is passed through the vein. a) Needle tip b) 5d upstream of the needle tip c) 10d upstream of the needle tip	107
5.11	Contours of time averaged z-velocity with vectors of normalised velocity for the arterial needle in the retrograde orientation with different needle angles. The needle tip is placed in the middle of the vein with an equivalent blood flow rate of 300 ml/min. A steady flow rate of 666 ml/min is passed through the vein. The black section represents the region which was masked due to shadows produced by the o-ring and block alignment pins. a) 10° b) 20° c) 30°	108
5.12	Velocity profiles from the arterial needle in the retrograde orientation for different needle angles. The needle tip is placed in the middle of the vein with an equivalent blood flow rate of 300 ml/min. A steady flow rate of 666 ml/min is passed through the vein. a) Needle tip b) 5d upstream of the needle tip c) 10d upstream of the needle tip	109

5.13	Contours of time averaged z-velocity with vectors of normalised velocity for the venous needle with different needle flow rates. The black section represents the region which was masked due to shadows produced by the o-ring and block alignment pins. The needle tip is placed in the middle of the vein at an angle of 20°. A steady flow rate of 666 ml/min is passed through the vein. a) 200 ml/min b) 300 ml/min c) 400 ml/min	111
5.14	Velocity profiles from the venous needle for different needle flow rates. The needle tip is placed in the middle of the vein at an angle of 20°. A steady flow rate of 666 ml/min is passed through the vein. a) Needle tip b) 20d downstream of the needle tip c) 40d downstream of the needle tip d) 60d downstream of the needle tip	112
5.15	Contours of time averaged z-velocity with vectors of normalised velocity for the venous needle with different needle angles. The needle tip is placed in the middle of the vein with an equivalent blood flow rate of 300 ml/min. A steady flow rate of 666 ml/min is passed through the vein. The black section represents the region which was masked due to shadows produced by the o-ring and block alignment pins. a) 10° b) 20° c) 30°	113
5.16	Velocity profiles from the venous needle for different needle angles. The needle tip is placed in the middle of the vein with an equivalent blood flow rate of 300 ml/min. A steady flow rate of 666 ml/min is passed through the vein. a) Needle tip b) 20d downstream of the needle tip c) 40d downstream of the needle tip d) 60d downstream of the needle tip	114

5.17	Contours of time averaged z-velocity with vectors of normalised velocity for the venous needle with different needle depths. The needle is placed at an angle of 20° with an equivalent blood flow rate of 300 ml/min. A steady flow rate of 666 ml/min is passed through the vein. The black section represents the region which was masked due to shadows produced by the o-ring and block alignment pins. a) bottom b) middle c) top	116
5.18	Velocity profiles from the venous needle for different needle depths. The needle is placed at an angle of 20° with an equivalent blood flow rate of 300 ml/min. A steady flow rate of 666 ml/min is passed through the vein. a) Needle tip b) 20d downstream of the needle tip c) 40d downstream of the needle tip d) 60d downstream of the needle tip	117
5.19	Schematic showing the mechanics of wall jet detachment . . .	121
6.1	Schematic of the inserted and rotated needle position. a) Inserted b) Rotated	128
6.2	Back eye dimensions for a 15G needle	129
6.3	Detail of the hexahedral mesh around the needle tip	129
6.4	Needle waveform imposed on the arterial and venous needle for a blood flow rate of 300 ml/min. The arterial needle inlet was pulsatile due to the motion of the peristaltic pump. The waveform was captured using Duplex ultrasound as explained in Chapter 7. The venous needle flow remained constant due to the dampening effects of the air traps and dialyser.	132
6.5	Transient waveform imposed on the cephalic vein	133
6.6	Summary of the computational setup	134

6.7	Comparison between experimental and computational velocity profiles from the arterial needle in the antegrade orientation at a blood flow rate of 300 ml/min. The needle tip is placed in the middle of the vein at an angle of 20°. a) Needle tip b) 5d downstream of the needle tip c) 10d downstream of the needle tip c) 15d downstream of the needle tip	137
6.8	Comparison between experimental and computational velocity profiles from the arterial needle in the retrograde orientation at a blood flow rate of 300 ml/min. The needle tip is placed in the middle of the vein at an angle of 20°. a) Needle tip b) 5d downstream of the needle tip c) 10d downstream of the needle tip	139
6.9	Comparison between experimental and computational velocity profiles from the venous needle at a blood flow rate of 300 ml/min. The needle tip is placed in the middle of the vein at an angle of 20°. a) Needle tip b) 20d downstream of the needle tip c) 40d downstream of the needle tip c) 60d downstream of the needle tip	141
6.10	Pathlines and velocity contours on cross-sectional planes for the arterial needle in an antegrade orientation during diastole. Arrows indicate predominate direction of blood flow. a-c) Variation in blood flow rate (200 ml/min, 300 ml/min, 400 ml/min). Needle tip is placed in the middle of the vein at an angle of 20°. d-f) Variation in needle angle (10°, 20°, 30°). Needle tip is placed in the middle of the vein with an equivalent blood flow rate of 300 ml/min. g-i) Variation in needle position (bottom, middle, top). Needle is placed at an angle of 20° with an equivalent blood flow rate of 300 ml/min.	144

6.11	Relative residence time (time averaged over 10 cycles) on the wall of the vein normalised by the mean wall shear stress for the arterial needle in the antegrade orientation. Only high levels of RRT (>10) have been coloured in red to emphasise regions of strong secondary flows. a-c) Variation in blood flow rate (200 ml/min, 300 ml/min, 400 ml/min). Needle tip is placed in the middle of the vein at an angle of 20° . d-f) Variation in needle angle (10° , 20° , 30°). Needle tip is placed in the middle of the vein with an equivalent blood flow rate of 300 ml/min. g-i) Variation in needle position (bottom, middle, top). Needle is placed at an angle of 20° with an equivalent blood flow rate of 300 ml/min.	145
6.12	Pathlines and velocity contours on cross-sectional planes for the arterial needle in a retrograde orientation during diastole. Arrows indicate predominate direction of blood flow. a-c) Variation in blood flow rate (200 ml/min, 300 ml/min, 400 ml/min). Needle tip is placed in the middle of the vein at an angle of 20° . d-f) Variation in needle angle (10° , 20° , 30°). Needle tip is placed in the middle of the vein with an equivalent blood flow rate of 300 ml/min. g-i) Variation in needle position (bottom, middle, top). Needle is placed at an angle of 20° with an equivalent blood flow rate of 300 ml/min.	147

6.13	Relative residence time (time averaged over 10 cycles) on the wall of the vein normalised by the mean wall shear stress for the arterial needle in the retrograde orientation. Only high levels of RRT (>10) have been coloured in red to emphasise regions of strong secondary flows. a-c) Variation in blood flow rate (200 ml/min, 300 ml/min, 400 ml/min). Needle tip is placed in the middle of the vein at an angle of 20° . d-f) Variation in needle angle (10° , 20° , 30°). Needle tip is placed in the middle of the vein with an equivalent blood flow rate of 300 ml/min. g-i) Variation in needle position (bottom, middle, top). Needle is placed at an angle of 20° with an equivalent blood flow rate of 300 ml/min.	148
6.14	Velocity isosurfaces (1 m/s) visualising the venous needle jet during diastole. a-c) Variation in blood flow rate (200 ml/min, 300 ml/min, 400 ml/min). Needle tip is placed in the middle of the vein at an angle of 20° . d-f) Variation in needle angle (10° , 20° , 30°). Needle tip is placed in the middle of the vein with an equivalent blood flow rate of 300 ml/min. g-i) Variation in needle position (bottom, middle, top). Needle is placed at an angle of 20° with an equivalent blood flow rate of 300 ml/min.	151

- 6.15 Time average wall shear stress (over 10 cycles) on the wall of the vein for the venous needle. Only regions above 10 Pa have been coloured to emphasise regions of excessively high stress. The scale has also been capped at the threshold reported to cause endothelial damage (40 Pa). a-c) Variation in blood flow rate (200 ml/min, 300 ml/min, 400 ml/min). Needle tip is placed in the middle of the vein at an angle of 20°. d-f) Variation in needle angle (10°, 20°, 30°). Needle tip is placed in the middle of the vein with an equivalent blood flow rate of 300 ml/min. g-i) Variation in needle position (bottom, middle, top). Needle is placed at an angle of 20° with an equivalent blood flow rate of 300 ml/min. 153
- 6.16 Relative residence time (time averaged over 10 cycles) on the wall of the vein normalised by the mean wall shear stress for the venous needle. Only high levels of RRT (>10) have been coloured in red to emphasise regions of strong secondary flows. a-c) Variation in blood flow rate (200 ml/min, 300 ml/min, 400 ml/min). Needle tip is placed in the middle of the vein at an angle of 20°. d-f) Variation in needle angle (10°, 20°, 30°). Needle tip is placed in the middle of the vein with an equivalent blood flow rate of 300 ml/min. g-i) Variation in needle position (bottom, middle, top). Needle is placed at an angle of 20° with an equivalent blood flow rate of 300 ml/min. 154

6.17	Pathlines and velocity contours on cross-sectional planes for the arterial needle in different positions during diastole. Arrows indicate predominate direction of blood flow. The needle tip is placed in the middle of the vein at an angle of 20° with an equivalent blood flow rate of 300 ml/min. a) Arterial needle in the inserted position (antegrade orientation) b) Arterial needle in the rotated position (antegrade orientation) c) Arterial needle in the inserted position (retrograde orientation) d) Arterial needle in the rotated position (retrograde orientation)	156
6.18	Relative residence time (time averaged over 10 cycles) on the wall of the vein normalised by the mean wall shear stress for the arterial needle in different positions. Only high levels of RRT (>10) have been coloured in red to emphasise regions of strong secondary flows. The needle tip is placed in the middle of the vein at an angle of 20° with an equivalent blood flow rate of 300 ml/min. a) Arterial needle in the inserted position (antegrade orientation) b) Arterial needle in the rotated position (antegrade orientation) c) Arterial needle in the inserted position (retrograde orientation) d) Arterial needle in the rotated position (retrograde orientation)	157
6.19	Time average wall shear stress (over 10 cycles) on the wall of the vein for the venous needle in the rotated and inserted position. Only regions above 10 Pa have been coloured to emphasise regions of excessively high stress. The scale has also been capped at the threshold reported to cause endothelial damage (40 Pa). The needle tip is placed in the middle of the vein at an angle of 20° with an equivalent blood flow rate of 300 ml/min. a) Venous needle in the inserted position b) Venous needle in the rotated position	158

6.20	Relative residence time (time averaged over 10 cycles) on the wall of the vein normalised by the mean wall shear stress for the venous needle in different positions. Only high levels of RRT (>10) have been coloured in red to emphasise regions of strong secondary flows. The needle tip is placed in the middle of the vein at an angle of 20° with an equivalent blood flow rate of 300 ml/min. a) Venous needle in the inserted position b) Venous needle in the rotated position	159
7.1	Locations (denoted by X) on the extracorporeal circuit where Doppler ultrasound measurements were conducted. a) between the arterial needle and the roller pump b) between the roller pump and arterial air trap c) between the arterial air trap and dialyser d) between the dialyser and venous air trap e) between the venous air trap and venous needle	177
7.2	Colour Doppler imaging of the extracorporeal tubing and blood flow	178
7.3	Isosurface of Vapour Pressure (-95000 Pa) in the arterial needle at different times in the sinusoidal inlet condition when the needle is placed in the antegrade orientation. a) 0 seconds b) 0.1 seconds c) 0.2 seconds d) 0.3 seconds e) 0.4 seconds f) 0.5 seconds g) 0.6 seconds h) 0.7 seconds	181
7.4	Isosurface of Vapour Pressure (-95000 Pa) in the arterial needle at different times in the sinusoidal inlet condition when the needle is placed in the retrograde orientation. a) 0 seconds b) 0.1 seconds c) 0.2 seconds d) 0.3 seconds e) 0.4 seconds f) 0.5 seconds g) 0.6 seconds h) 0.7 seconds	182

7.5	Range of pressures at the needle opening over two periods of the sinusoidal waveform. As the blood flow rate increases the pressure in both the antegrade and retrograde positions falls below the vapour pressure of blood; providing an environment for cavitation	183
7.6	Velocity waveform as measured by Doppler ultrasound in the haemodialysis extracorporeal circuit. a) between the arterial needle and the roller pump b) between the roller pump and arterial air trap c) between the arterial air trap and dialyser d) between the dialyser and venous air trap e) between the venous air trap and venous needle	185
7.7	Instantaneous roller motion of the peristaltic pump (High Pressure - HP, Low Pressure - LP) a) Tubing is occluded b) Release of occluded tubing (water hammer effect) c) Smooth rotation producing maximum flow d) Velocity waveform measured after the roller pump	187
8.1	a) 15G Argyle™ Safety Fistula Cannula with Anti-Reflux Valve with insertion needle pulled back b) Cross-sectional cut depicting the cannula tip geometry and structured mesh . . .	197
8.2	Monitor points of the velocity within the cannula	198
8.3	Comparison of cannula pressures calculated computationally compared to experimental data	199
8.4	Velocity isosurface (1 m/s) depicting blood exiting the cannula through the central bore and side holes. First column: 200 ml/min. Second column: 300 ml/min. Third column: 400 ml/min. a-c) Upper d-f) Centre g-i) Lower	201

8.5	Monitor points of the velocity within the cannula. Blue line represents a blood flow rate of 200 ml/min. Green line represents a blood flow rate of 300 ml/min. Red line represents a blood flow rate of 400 ml/min. Left hand column: cannula position near the roof of the vein. Middle column: cannula position in the centre of the vein. Right hand column: cannula position near the floor of the vein. a-c) Monitor point inside cannula d-f) Monitor point at outlet of cannula g-i) Monitor point 5d downstream of cannula outlet	202
8.6	Time averaged wall shear stress (TAWSS) on the vein wall highlighting regions of high WSS. Only regions above 10 Pa have been coloured to emphasise regions of excessively high stress. The maximum WSS is cut at 40 Pa, which is the threshold in which endothelial denudation can occur. First column: 200 ml/min. Second column: 300 ml/min. Third column: 400 ml/min. a-c) Upper d-f) Centre g-i) Lower	204
8.7	Relative residence time (RRT) on the vein wall highlighting regions at risk of developing IH. The scale has been normalised by the mean wall shear stress. Only high levels of RRT (>10) have been coloured in red to emphasise regions of strong secondary flows. First column: 200 ml/min. Second column: 300 ml/min. Third column: 400 ml/min. a-c) Upper d-f) Centre g-i) Lower	207
8.8	Velocity isosurfaces (1 m/s) visualising the jet exiting the cannula and needle. Left column displays the cannula. Right column displays the needle. a-b) Blood flow rate of 200 ml/min. c-d) Blood flow rate of 300 ml/min. e-f) Blood flow rate of 400 ml/min.	209

8.9	Monitor points of the velocity within the cannula. Blue line represents the cannula. Red line represents the needle. Left column displays the monitor point inside device. Middle column displays the monitor point at the outlet of the device. Right column displays the monitor point 5d downstream of the device outlet. a-c) Blood flow rate of 200 ml/min. d-f) Blood flow rate of 300 ml/min. g-i) Blood flow rate of 400 ml/min.	210
8.10	Time averaged wall shear stress (TAWSS) on the vein wall highlighting regions of high WSS. Only regions above 10 Pa have been coloured to emphasise regions of excessively high stress. The maximum WSS is capped at 40 Pa, which is the threshold at which endothelial denudation can occur. Left column displays the cannula. Right column displays the needle. a-b) Blood flow rate of 200 ml/min. c-d) Blood flow rate of 300 ml/min. e-f) Blood flow rate of 400 ml/min.	212
8.11	Relative residence time (RRT) on the vein wall highlighting regions at risk of developing IH. The scale has been normalised by the mean wall shear stress. Only high levels of RRT (>10) have been coloured in red to emphasise regions of strong secondary flows. Left column displays the cannula. Right column displays the needle. a-b) Blood flow rate of 200 ml/min. c-d) Blood flow rate of 300 ml/min. e-f) Blood flow rate of 400 ml/min.	213
8.12	B-Flow images of the Argyle™Safety Fistula Cannula in-situ (Image Courtesy of Dr Tim Spicer, Renal Medicine, Campbelltown Hospital, Sydney, Australia)	217
A.1	Temperature Calibration	240
A.2	Viscosity variation with temperature	245

B.1	Random error for variations in particle image diameter	254
B.2	Random error from particle image displacements	255
B.3	Bias error from particle image displacements	256
B.4	Probability of calculating the correct particle displacement as a function of particle image density	257
B.5	Random error due to particle image density	258
B.6	Random error from image quantisation	259
B.7	Random error due to background noise	260
B.8	Random error due to displacement gradients	261
C.1	Maximum WSS produced by the venous needle for different sizes	263
C.2	Velocity at the outlet for different mesh sizes	265
C.3	Velocity downstream of the venous needle (20d) where the jet and core flow mix for different mesh sizes	265
C.4	Velocity downstream of the venous needle (20d) where the jet and core flow mix for different time step sizes	268
D.1	Comparison between experimental and computational velocity profiles from the arterial needle in the antegrade orientation at a blood flow rate of 200 ml/min. a) Needle tip b) 5d downstream of the needle tip c) 10d downstream of the needle tip c) 15d downstream of the needle tip	270
D.2	Comparison between experimental and computational velocity profiles from the arterial needle in the antegrade orientation at a blood flow rate of 400 ml/min. a) Needle tip b) 5d downstream of the needle tip c) 10d downstream of the needle tip c) 15d downstream of the needle tip	271

D.3	Comparison between experimental and computational velocity profiles from the arterial needle in the antegrade orientation at a needle angle of 10°. a) Needle tip b) 5d downstream of the needle tip c) 10d downstream of the needle tip c) 15d downstream of the needle tip	272
D.4	Comparison between experimental and computational velocity profiles from the arterial needle in the antegrade orientation at a needle angle of 30°. a) Needle tip b) 5d downstream of the needle tip c) 10d downstream of the needle tip c) 15d downstream of the needle tip	273
D.5	Comparison between experimental and computational velocity profiles from the arterial needle in the antegrade orientation at the bottom of the vein. a) Needle tip b) 5d downstream of the needle tip c) 10d downstream of the needle tip c) 15d downstream of the needle tip	274
D.6	Comparison between experimental and computational velocity profiles from the arterial needle in the antegrade orientation at the top of the vein. a) Needle tip b) 5d downstream of the needle tip c) 10d downstream of the needle tip c) 15d downstream of the needle tip	275
D.7	Comparison between experimental and computational velocity profiles from the arterial needle in the retrograde orientation at a blood flow rate of 200 ml/min. a) Needle tip b) 5d downstream of the needle tip c) 10d downstream of the needle tip	276
D.8	Comparison between experimental and computational velocity profiles from the arterial needle in the retrograde orientation at a blood flow rate of 400 ml/min. a) Needle tip b) 5d downstream of the needle tip c) 10d downstream of the needle tip	277

D.9	Comparison between experimental and computational velocity profiles from the arterial needle in the retrograde orientation at a needle angle of 10°. a) Needle tip b) 5d downstream of the needle tip c) 10d downstream of the needle tip	278
D.10	Comparison between experimental and computational velocity profiles from the arterial needle in the retrograde orientation at a needle angle of 30°. a) Needle tip b) 5d downstream of the needle tip c) 10d downstream of the needle tip	279
D.11	Comparison between experimental and computational velocity profiles from the arterial needle in the retrograde orientation at the bottom of the vein. a) Needle tip b) 5d downstream of the needle tip c) 10d downstream of the needle tip	280
D.12	Comparison between experimental and computational velocity profiles from the arterial needle in the retrograde orientation at the top of the vein. a) Needle tip b) 5d downstream of the needle tip c) 10d downstream of the needle tip	281
D.13	Comparison between experimental and computational velocity profiles from the venous needle at a blood flow rate of 200 ml/min. a) Needle tip b) 20d downstream of the needle tip c) 40d downstream of the needle tip c) 60d downstream of the needle tip	282
D.14	Comparison between experimental and computational velocity profiles from the venous needle at a blood flow rate of 400 ml/min. a) Needle tip b) 20d downstream of the needle tip c) 40d downstream of the needle tip c) 60d downstream of the needle tip	283

D.15 Comparison between experimental and computational velocity profiles from the venous needle at a needle angle of 10°. a) Needle tip b) 20d downstream of the needle tip c) 40d downstream of the needle tip c) 60d downstream of the needle tip	284
D.16 Comparison between experimental and computational velocity profiles from the venous needle at a needle angle of 30°. a) Needle tip b) 20d downstream of the needle tip c) 40d downstream of the needle tip c) 60d downstream of the needle tip	285
D.17 Comparison between experimental and computational velocity profiles from the venous needle placed at the bottom of the vein. a) Needle tip b) 20d downstream of the needle tip c) 30d downstream of the needle tip c) 60d downstream of the needle tip	286
D.18 Comparison between experimental and computational velocity profiles from the venous needle placed at the top of the vein. a) Needle tip b) 20d downstream of the needle tip c) 40d downstream of the needle tip c) 60d downstream of the needle tip	287

List of Tables

1.1	Classification of the five stages of Chronic Kidney Injury	3
3.1	Patient demographics based on fistula age classification	46
3.2	Patient demographics based on comorbidity classification	47
3.3	Number of complications occurring in each patient group	48
3.4	Mean +/- standard deviation and statistical significance of pressure in the arterial line categorised by fistula longevity . .	52
3.5	Mean +/- standard deviation and statistical significance of pressure in the venous line categorised by fistula longevity . .	52
3.6	Mean +/- standard deviation and statistical significance of blood flow rate categorised by fistula longevity	53
3.7	Mean +/- standard deviation and statistical significance of dialysis frequency categorised by fistula longevity	53
3.8	Mean +/- standard deviation and statistical significance of fistula maturation time categorised by fistula longevity	54
3.9	Mean +/- standard deviation and statistical significance of fistula age as measured from the time of first cannulation to the time of first intervention	54
4.1	Parameters and variables of all test cases. Blood flows are listed as physiologically equivalent (not scaled)	71

4.2	Summary of flow rates and Reynolds numbers after dimensional scaling	72
4.3	Summary of pulse separation time and trigger rates for each section and flow rate of the venous needle. Blood flows are listed as physiologically equivalent (not scaled)	81
4.4	Summary of pulse separation time and trigger rates for each section and flow rate of the arterial needle. Blood flows are listed as physiologically equivalent (not scaled)	81
4.5	Summary of experimental uncertainty	87
4.6	Summary of PIV uncertainty	90
5.1	Summary of experimental cases	95
6.1	Summary of differences between computational and experimental results for the arterial needle in the antegrade orientation	138
6.2	Summary of differences between computational and experimental results for the arterial needle in the retrograde orientation	140
6.3	Summary of differences between computational and experimental results for the venous needle	142
6.4	Summary of back eye flow and area of high RRT for all tested parameters of the arterial needle in the antegrade orientation .	146
6.5	Summary of back eye flow and area of high RRT for all tested parameters of the arterial needle in the retrograde orientation	149
6.6	Summary of back eye flow and area of high RRT and high TAWSS for all tested parameters of the venous needle	150
6.7	Summary of the area of high RRT and high TAWSS for different needle positions	159
6.8	Summary of back eye flow for different needle positions	160

7.1	Summary of maximum, minimum and the standard deviation over 10 cycles of the roller pump	186
8.1	Summary of the area of high TAWSS produced by the plastic cannula	205
8.2	Summary of the area of high RRT produced by the plastic cannula	206
8.3	Comparison in the area of high RRT and high TAWSS produced by the plastic cannula and needle	214
A.1	Summary of measurements during mixing of the blood analogue solution	235
C.1	Grid Convergence Index on maximum WSS produced by the venous needle	264
C.2	Summary of Time Step Analysis	267

Nomenclature

Roman Symbols

$A_{average}$	Average cell area
$A_{>threshold}$	Vein area larger than the threshold value which can cause endothelial damage
CoC	Circle of confusion
d	Diameter of needle
d_p	Particle diameter
D	Diameter of vein
DOF	Depth of Field
D_h	Hydraulic diameter
FP	Far Point
F_d	Focal distance
F_l	Focal length
H_fL	Hyperfocal length
NP	Near Point
$N_{>threshold}$	Number of cells above the set threshold value
P	Pressure
Re	Reynolds number
Stk	Stokes number
T	Duration of the cardiac cycle
U	Average velocity through pipe
\vec{u}	Velocity vector
V	Maximum velocity through pipe

Greek Symbols

α	Womersley number
μ	Dynamic viscosity
ρ	Density
$\vec{\tau}$	Shear stress tensor
τ_w	Wall shear stress vector
ω	Angular velocity

Acronyms

AN	Arterial Needle
AP	Arterial Pressure
AVF	Arteriovenous Fistula
AVG	Arteriovenous Graft
CAD	Computer Aided Design
CFD	Computational Fluid Dynamics
CFL	Courant-Friedrichs-Lewy Condition
CKI	Chronic Kidney Injury
CT	Computerised Tomography
ESRD	End Stage Renal Disease
FSI	Fluid Structure Interaction
GCI	Grid Convergence Index
GFR	Glomerular Filtration Rate
IH	Intimal Hyperplasia
LES	Large Eddy Simulation
LDA	Laser Doppler Anemometry
MRA	Magnetic Resonance Angiogram
MRI	Magnetic Resonance Imaging
NO	Nitric Oxide

OSI	Oscillatory Shear Index
PIV	Particle Image Velocimetry
PMMA	Poly(methyl methacrylate)
SD	Standard Deviation
S-PIV	Stereoscopic Particle Image Velocimetry
TAWSS	Time Averaged Wall Shear Stress
USB	Unicersal Serial Bus
VN	Venous Needle
VNJ	Venous Needle Jet
VP	Venous Pressure
VSMC	Vascular Smooth Muscle Cell
WSS	Wall Shear Stress

Chapter 1

Introduction

This chapter begins with an overview of kidney failure and introduces the concept that the needles play an important role in vascular access failure; the main focus of this thesis. This is followed by an introduction into the treatment of haemodialysis and the requirement for a functioning vascular access is explained. For completeness, the major complications which can occur in dialysis patients are summarised. The chapter concludes by outlining the structure of this thesis.

1.1 Overview

Chronic kidney injury (CKI) is a severe condition in which the body is unable to filter toxins and waste from the blood. Haemodialysis is the most common treatment for CKI, which involves creating a vascular access so that the blood can be filtered outside the body. Dialysis needles are the crucial components that bridge the gap between the vascular system and the dialyser. Unfortunately, high rates of complications in the vascular

access are prevalent.

The most common complication is thrombosis which usually occurs due to reduced blood flow in the access or the rupture of stenotic lesions [1, 2]. Damage to the blood vessels and blood cells by haemodynamic forces is hypothesised to be a primary factor leading to morphological changes in the structure of the blood vessel, which can result in stenosis and subsequent thrombosis [3–6].

Despite their importance in delivering blood to the dialyser, dialysis needles may also be responsible for causing stenosis due to the high blood flow rates (200-400 ml/min) passing through them which create a complex flow environment within the vein. This complex flow environment consists of: jet flow phenomena, high levels of turbulence, secondary flows and regions of disturbed flows with high particle residence times [7]. These haemodynamic forces can promote the development of stenosis, which may require surgical intervention, further increasing the cost of treatment. As haemodialysis is conducted 3-4 times per week, any damage to the vascular access can have an accumulative effect on patient health. Furthermore, the efficiency in which blood is passed through the extracorporeal circuit can be reduced under these conditions, consequently failing to alleviate the initial symptoms, leading to a reduced quality of life.

The vascular access is referred to as the lifeline for haemodialysis patients. Many of the complications that plague dialysis patients arise in the vascular access and affect the machines ability to filter the blood. The vascular access has subsequently received much attention in attempts to improve its' long term patency. However, research regarding the influence of the needles has received less interest, as complications arising from their application are usually secondary to those originating in the vascular access. This thesis will focus on the haemodynamic flow field produced by the dialysis needles

and their influence on the formation of venous stenosis.

1.2 Haemodialysis

The kidneys are vital organs that receive approximately 20% of the total cardiac output. Their main purpose is the filtering of waste from the blood. Other functions they perform include: the regulation of the acid-base balance of blood, regulation of plasma ionic composition through the absorption and storage of ions and regulation of blood pressure by controlling the total blood volume [8]. CKI is diagnosed as a progressive and irreversible loss in renal function and is identified when high serum creatinine levels exist in either the blood or urine, indicating a falling glomerular filtration rate (GFR) as shown in Table 1.1. End stage renal disease (ESRD) is the final stage and occurs when the GFR falls below 15 ml/min/1.73 m² [9]. At this level of kidney function, dialysis is crucial for survival.

Table 1.1: Classification of the five stages of Chronic Kidney Injury [10, 11]

Stage	Description	GFR (ml/min/1.73 m ²)
0	Healthy Kidney	125
1	Kidney damage with normal or decreased GFR	≥ 90
2	Kidney damage with mild or decreased GFR	60-89
3	Moderate decrease in GFR	30-59
4	Severe decrease in GFR	15-29
5	Kidney Failure	< 15 (or dialysis)

The dialysis process normally occurs 3-4 times per week, with each session running for 5-6 hours depending on the health of the patient. The needle removing blood from the body is referred to as the arterial needle (AN) whilst the needle returning the filtered blood is called the venous needle

(VN). Needles ranging from 14G to 17G are commonly used, where smaller sizes and blood flow rates (200 ml/min) are preferred during the initial use of the vascular access. Once the vascular access has become accustomed to frequent cannulation larger needles are used as they facilitate higher blood flow rates (400 ml/min). This increases the efficiency of the blood filtration and reduces treatment time. The general setup for haemodialysis is displayed in Figure 1.1.

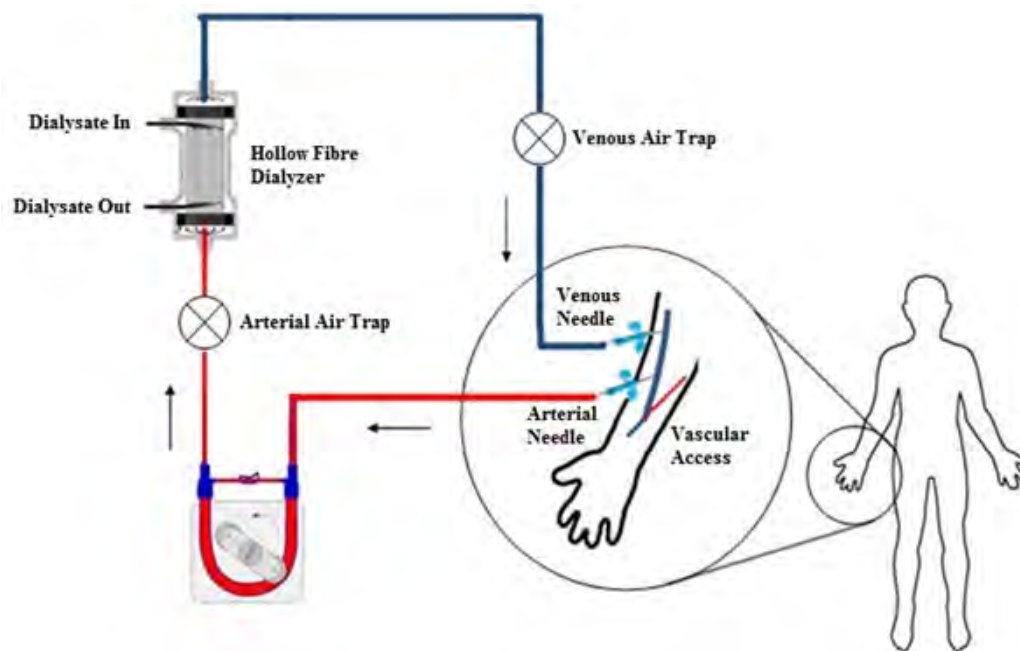


Figure 1.1: Haemodialysis Setup

1.3 Vascular Access

Vascular access is the crucial component that provides an access point to the dialyser, the component which filters toxins and waste from the blood. It must maintain high blood flow rates for efficient filtration, high patency

rates, have a low incidence of complications and provide flexibility for future options should the fistula become unusable. Currently three methods of creating a vascular access exist; catheter access, arteriovenous graft (AVG) or an arteriovenous fistula (AVF), as displayed in Figure 1.2.

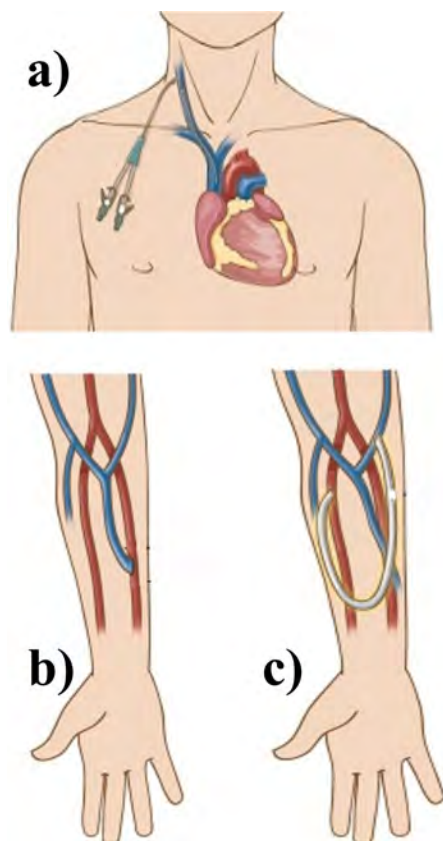


Figure 1.2: a) Central Venous Catheter b) Arteriovenous Fistula c) Arteriovenous Graft [12]

An AVF or AVG is created by surgically connecting a vein and artery which results in a low resistance, high compliance pathway in which the blood can flow from the high pressure arterial system into the low pressure venous system. A catheter is an ideal short term solution whilst patients wait for an AVF or AVG to be surgically created. Catheters are not considered a

long term solution as they have a higher risk of displacement and infection [13]. Although the two needle system in AVFs and AVGs can fail in a similar fashion, catheters have reported infection rates greater than 10% [13, 14], whilst infections in AVFs and AVGs only account for 2-3% of complications [15].

A major advantage of an AVG is that it can be cannulated within 24 hours of creation [16]. Transplanted material provides a higher compliance and reduces the chance of thrombosis compared to artificial material but also increases the chance of disintegration and haemorrhage if infection occurs [17]. Upon creation, AVFs react to elevated pressures and blood flows and increase in luminal diameter. A maturation period of approximately 4 weeks is required to allow the blood vessel wall to thicken in preparation for cannulation, hence catheters and AVGs are sometimes preferred due to their immediate availability [18]. The primary advantage of AVFs is their superior patency rates, with reported two year patency as high as 70% compared to 40% found in prosthetic grafts [19]. For this reason, as well as fewer incidents of complications the AVF is the preferred choice of vascular access [10, 13, 20].

Despite the advantages that each vascular access holds, long term patency is not high. Even AVFs, the preferred choice of vascular access, have four year primary patency rates of 48% [21]. This means that within four years over half the AVF patient population will require some form of intervention or creation of a new access; a statistic that is uncommon in other areas of medicine. The process of artificially filtering the blood frequently and effectively is complex. Various complications can arise due to: the underlying morbidities present in CKI patients, open wounds created when connecting the blood system to the dialyser, relative simplicity of the dialysis machine in replicating the complex function of the kidney or the morphological changes to the vascular system which occur upon creation of the fistula.

1.4 Vascular Access Related Complications

Vascular access related complications account for 14-17% of hospitalisations per year in dialysis patients in the United States [2]. In 2013, these vascular complications accounted for US\$30.9 billion of the total Medicare expenditures; rising 1.6% from the previous year [22]. Despite it being the preferred and most common treatment of ESRD, haemodialysis remains the most expensive renal replacement therapy as seen in Figure 1.3, equated to an annual cost of US\$84,550 per person [22].

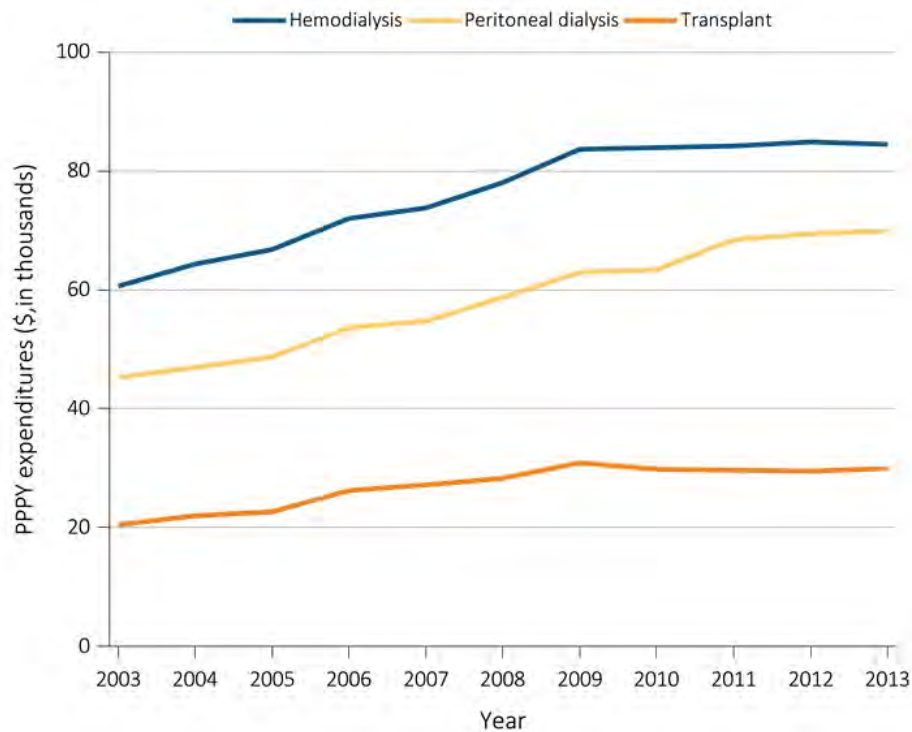


Figure 1.3: Cost of ESRD Treatments per patient per year (PPPY) [22]

1.4.1 Thrombosis

It is estimated that thrombosis is responsible for 16-23% of hospitalisations in dialysis patients [23]. The risk of hospitalisation is even higher in uraemic patients [24, 25]. Early thrombosis is usually due to twisting of the access, poor selection of anticoagulants during surgery or early cannulation before the blood vessel wall has sufficiently matured [2, 13]. Late thrombosis is generally caused by the presence of stenosis, which is clinically defined when the blood vessel narrows to more than 50% of the lumen diameter [1].

1.4.2 Stenosis

Stenosis can lead to thrombosis as the flow through the fistula is reduced which can lead to increases in access recirculation and a higher chance of clotting, or when a stenotic lesion ruptures initiating an inflammatory reaction. Early detection and treatment of stenosis is paramount in order to minimise the risk of thrombosis and potential loss of the vascular access. This is achieved by monitoring pressures within the extracorporeal circuit, routine checks for access recirculation or a vascular screening program using Doppler ultrasound [26]. Angioplasty or stenting are the most common procedures of treating stenosis as they preserve the access site and are minimally invasive. Stenosis commonly develop at the anastomosis and swing segment, accounting for 50-70% of incidents, followed by the drainage vein in 20-50% of cases, as displayed in Figure 1.4 [27–33]. Two main pathways in the development of stenosis exist; atherosclerosis or intimal hyperplasia (IH).

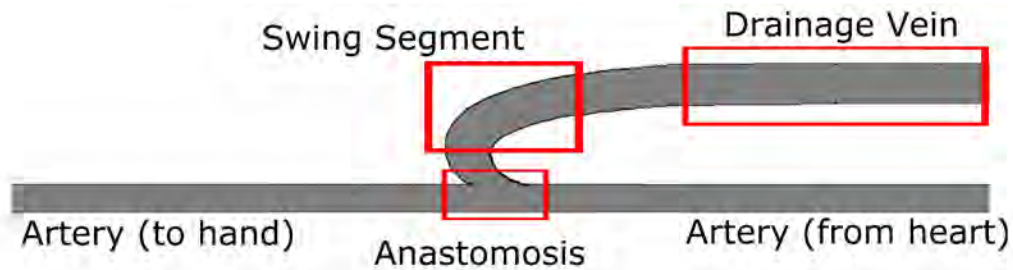


Figure 1.4: Common locations of stenosis formation in arteriovenous fistulae

Atherosclerosis is the deposition of fatty products called plaques into the walls of blood vessels. The formation of atherosclerotic stenosis is complex and is a much slower process than a stenosis formed via the IH pathway. As the plaque is deposited into the lumen of the vessel it forms a growth which reduces blood flow. In response, the blood vessel will increase its cross sectional area to preserve blood flow, in a process called outward remodelling. Over time, calcium and collagen deposits cause the plaque to stiffen which hinders the outward remodelling process. Several studies have reported a high correlation between blood flow and plaque deposition throughout the vasculature [34–36]. Wall shear stress (WSS), a measure of the stress imposed by flowing blood at the vessel wall, has been shown to be a good indicator of plaque development. In particular, low and oscillating WSS [37–40], disturbed flow [41–43], stagnant flows [38, 44] and high residence times [45] have been shown to correlate with the localisation of atherosclerotic plaques. It takes several years for an atherosclerotic stenosis to reach a stage in which they are considered clinically significant. Interventional treatment of stenosis (resulting from atherosclerosis) in dialysis patients is uncommon. Conversely, IH can develop into a clinically significant stenosis within several weeks. This leaves the vascular access at a much higher risk of failure as the time frame to detect and treat this complication is much shorter.

The IH pathway begins as a ‘response to injury’ in which the blood vessel reacts through inflammatory mechanisms. Fistulae which fail within a few weeks of creation are mainly due to vascular injury incurred during surgery, or patient characteristics such as vascular health or inadequate blood vessel size which limits the growth of the fistula [46, 47]. In contrast, haemodynamics lead to morphological changes of the blood vessel and are the primary reason for fistulae which fail months or years after creation [3–6].

IH progresses in three distinct stages; vascular smooth muscle cell (VSMC) proliferation, VSMC migration and finally intimal expansion through matrix production [48]. These stages affect all layers of the blood vessel, with VSMC migrating into the intima whilst fibroblasts move from the adventitia to the inner surface [49, 50]. A key role in the development of IH is the decrease of available nitric oxide (NO), which is a chemical that maintains homeostasis by inhibiting inflammation, maintaining cell structure, inhibiting VSMC proliferation and platelet aggregation whilst also promoting vasodilation and endothelial regrowth [48, 51–53]. Similar to the localisation of atherosclerotic stenosis, several studies have also reported a high correlation between WSS and IH development. In particular, turbulence [54], low WSS [55–59], oscillatory WSS [4, 58, 59] and excessively high WSS [60–62] have been shown to induce ‘injury’ to the endothelial layer which can lead to intimal thickening in AVFs and AVGs.

1.4.3 Aneurysm

The opposite effect to stenosis is an aneurysm, which is a localised pathological enlargement of the blood vessel. Aneurysm formation stems from damage to the endothelial layer and normally occurs where regions of high blood flow exist in the vasculature [60, 63]. In dialysis patients, they

are commonly found in the anastomotic region of the fistula as the high velocity blood flow enters the venous segment, or in the downstream vein where the blood vessel wall has weakened by repeated needle punctures [1, 26, 64].

1.4.4 Infection

The second most common complication in dialysis patients is infection, which is responsible for approximately 20% of all hospitalisations [65]. *Staphylococci aureus* is the most common organism found in patients who suffer from infection, occurring in over 70% of graft infections and over 90% of fistula infections [66]. The insertion of the needle leads to four pathways in which infection can occur; the exit site on the skin, lumen of the needle, contamination prior to insertion or an infection from elsewhere in the body, carried by the blood to the fistula [65]. Most preemptive measures involve keeping the puncture site clean and the needles sterile.

1.4.5 Microbubbles

Long term exposure to microbubbles is another problem which can lead to several complications. Some studies have identified the presence of air emboli or microbubbles within the extracorporeal circuit [67–72]. Arterial and venous air traps are used to measure pressures within the extracorporeal circuit and to prevent large air bubbles and emboli from entering the patient. However, microbubbles ranging from 5-200 μm have been shown to pass through the venous air trap without activating the alarm and enter the blood stream [68, 69, 72, 73]. The presence of microbubbles within the circulation can lead to many pathophysiological implications, of which the most severe is tissue ischaemia where the

microbubble blocks blood flow, preventing the nearby tissue from receiving nutrients and oxygen. Several in-vivo studies have shown that microemboli can pass through the pulmonary circulation and deposit in the lungs [74–76]. Fairshter et al. [77] reported that 95.7% of haemodialysis patients had acute lung disease whilst 80.4% had chronic lung disease in a post mortem examination, indicating that microbubble deposition in the lungs may lead to chronic complications. Microbubble deposition in the brain has also been hypothesised to contribute to the deterioration of neurological function in long term haemodialysis patients [78, 79]. Cerebral atrophy [80] and neurocognitive dysfunctions [81] in chronic haemodialysis patients is also a recognised problem. Cavitation at the VN due to turbulence and pressure changes has been suggested as a potential source of microbubble formation [67, 68]. However, this remains to be confirmed as other sources of microbubble formation have also been proposed [68, 71, 82, 83].

1.4.6 Minor Complications

The aforementioned complications are the most pertinent in the haemodialysis population whilst thrombosis and infection undoubtedly pose the highest risk to the patients health [66, 84]. Several other complications can also arise due to the creation of the vascular access such as: vascular steal syndrome, vascular access neuropathy and cardiovascular problems. However, none of these have been linked to dialysis needles.

All of these complications contribute to the high cost of haemodialysis and the high failure rate of the vascular access. Dialysis needles have been cited to contribute to: higher rates of infection as they create an open path from the skin [85], aneurysm formation due to a weakened blood vessel from repeated puncture [86], potential microbubble formation from cavitation [67, 68], stenosis formation through IH [48] and thrombosis due to stenosis

rupture [1] or needle infiltration [87]. In order to minimise associated costs and improve fistula patency in the haemodialysis population, it is imperative that the impact of the needles must be more clearly understood. As mentioned, thrombosis is the most frequent complication leading to vascular access failure [2], and usually arises from stenosis rupture [1, 27]. Thus, the major focus of this thesis is to examine the relationship between haemodynamic forces and intimal thickening, which can subsequently lead to stenosis formation and potential thrombosis.

1.5 Thesis Outline

This thesis aims to investigate the haemodynamics surrounding the AN and VN during standard haemodialysis and assess potential mechanisms to minimise damage to the vascular access which will reduce the cost of treatment and improve quality of life. The relationship between haemodynamics and vascular response is outlined in Chapter 2. As will be shown, a substantial amount of research has been dedicated to improving the function of the vascular access itself, however there has been little research dedicated to understanding the influence of the needles. Chapter 3 analyses common complications in late fistula failure and where they occur anatomically. The influence of current clinical practices and their ability to predict vascular access failure is also investigated. Chapter 4 provides a thorough description of the experimental procedure which is used to validate the CFD models used in subsequent chapters. The experiment employs stereo PIV to obtain three dimensional velocities along the centre plane around the needles. Chapter 5 presents the experimental results. Chapter 6 displays the validation between the PIV measurements and steady state CFD simulations. The steady state computational model is then translated to transient simulations to incorporate the pulsatile nature

of flow in the cardiac cycle. Metrics are also introduced to assess the haemodynamics produced by the needles and examine how vascular access patency can be improved. Chapter 7 determines the potential of cavitation occurring in the extracorporeal circuit to ascertain the source of microbubbles in haemodialysis. Chapter 8 compares the haemodynamics of the standard haemodialysis needle with a new product entering the market; the Argyle™ Safety Fistula Cannula with Anti-Reflux Valve. Finally, Chapter 9 concludes the key findings of this thesis and summarises the methods in which vascular access patency can be improved. Avenues of future work are also discussed. Appendix A provides a comprehensive breakdown of the experimental error which exists within the setup. Errors within the PIV setup and post processing are included in Appendix B. Appendix C presents the analysis on the convergence of the computational mesh and time step size.

Chapter 2

Literature Review

Following from the previous chapter, the common complications which plague haemodialysis patients have been outlined and the requirement for a long lasting and functioning vascular access should be apparent. This chapter begins by defining the relationship between haemodynamics and stenosis formation; one of the major causes of vascular access failure. The metrics used to predict endothelial damage and subsequent IH are defined. The influence of the needles on vascular access patency is described in detail with focus on the haemodynamics they produce and how this can lead to stenosis. Following this, an extensive review into methods of examining haemodynamics specifically within the vascular access is provided.

2.1 The Role of Haemodynamics in Vascular Access Failure

It is well accepted that the endothelium actively participates in homeostasis by responding to changes in blood flow [52]. This originates from the ability of the endothelium to transduce mechanical forces into a biological signal in a process called mechanotransduction. With respect to the vascular system, the endothelial layer is the key component of mechanotransduction as it forms the barrier between blood and tissue. It has been shown that endothelial cells exist in a pre-stressed state between each other and the extracellular matrix [25, 51, 88] and that externally applied forces are directly transmitted through the endothelial cell and extracellular matrix[88–90]. Because of this ability, blood vessels function within a physiological range of WSS. In veins this has been reported to be 0.1-0.6 Pa whilst in arteries it is approximately between 1-7 Pa [91]. Mechanotransduction also extends to the vascular wall where stresses produced by the pressure pulse also influence adaption and remodelling. The blood vessel responds by either constriction or dilation when the WSS falls outside of this physiological range, in an attempt to return blood flow to normal levels.

2.1.1 Metrics of Predicting Vascular Complications

Haemodynamic forces and their interaction with the endothelial layer have a direct impact on vascular access patency. Examining boundary layer flows near the endothelial layer in blood vessels is critical in understanding vascular responses. The purpose of an AVF is to elevate blood flow to increase the efficiency of blood filtration and to provide a site for frequent access to the blood. The large increase in blood flow introduces complex

haemodynamics which leads to morphological changes of the blood vessel. Unfortunately, one response of the blood vessel is intimal thickening which can result in vascular access failure [3–6]. Certain haemodynamic metrics have been identified which can predict the development of stenosis.

2.1.2 Shear Stress

In healthy blood vessels high WSS is invariably linked with increased blood flow. As such, high WSS has been associated with the outward remodelling process, as the blood vessel expands in an attempt to reduce high velocities [60]. Exposure to high WSS in excess of 40 Pa, above the normal physiological range, can result in endothelial cell damage within one hour, which can trigger the ‘response to injury’ pathway to stenosis [61]. Furthermore, extensive cell damage occurs at levels above 150 Pa [92]. High WSS causes cells to elongate within 24 hours, resulting in increased endothelial permeability as endothelial gap junctions are stretched apart, which can lead to reduced endothelial function [60]. Prolonged exposure to impinging jets producing high levels of WSS has been shown to cause endothelial denudation, an injury to the blood vessel wall which can trigger the inflammatory pathway to intimal thickening [62]. High WSS has also been correlated to aneurysm formation and atherosclerotic plaque instability which can eventuate in thrombosis [60, 63]. High WSS exists within the flow field near the needles due to the high flow rates required for efficient blood filtration. However, quantification of these haemodynamic forces remains to be examined.

In low flow conditions the blood vessel will constrict and thicken in an attempt to restore WSS to normal levels. Intimal thickening is the response to decreases in blood flow, where low WSS stimulates VSMC migration and proliferation [56]. As such, low WSS has a high correlation with IH [55–58]. Interestingly, Keynton et al. [4] reported that IH has a higher correlation to

the mean WSS (averaged in time) rather than extreme values. This observation has led to several studies using a time averaged wall shear stress (TAWSS) metric to predict intimal thickening. The TAWSS is defined as:

$$TAWSS = \frac{1}{T} \int_0^T |\tau_w| dt \quad (2.1)$$

where T represents the period of one cardiac cycle and τ_w is the wall shear stress vector.

Recently, oscillatory flow has been identified as a more effective predictor of intimal thickening as it was shown that the endothelial layer is sensitive to flow reversal and therefore a unidirectional high or low WSS may not be an accurate metric in predicting intimal thickening [4, 45, 58]. Chien [41] showed that endothelial cell structure changes from regular striated patterns to random orientations in disturbed flow conditions. This random orientation increases vascular permeability making the blood vessel highly susceptible to deposition of inflammatory mediators [45]. Furthermore, regions of disturbed flow enhance endothelial cell turnover, which further increases vascular permeability [41]. The oscillatory shear index (OSI) first proposed by Ku et al. [40], measures the oscillatory nature of the flow and is defined as:

$$OSI = \frac{1}{2} \left(1 - \frac{\left| \int_0^T \tau_w dt \right|}{\int_0^T |\tau_w| dt} \right) \quad (2.2)$$

This metric falls within the range of 0-0.5, where a value of 0.5 indicates pure oscillatory flow with no net forward motion and a high possibility of endothelial dysfunction. Conversely, a value of zero indicates purely

forward motion with no oscillatory flow. The presence of haemodialysis needles within the vascular access creates complex secondary flows. Quantifying the oscillatory nature of the flows around the needle may indicate potential sites of intimal thickening in the vascular access.

2.1.3 Residence Time

High particle residence time can increase the chance of blood particle interactions and contact with the endothelium; resulting in higher rates of coagulation and deposition of inflammatory mediators [1, 45, 93]. High residence times are inherently associated with low and oscillatory shear conditions, which has led to a relative residence time (RRT) metric incorporating the OSI and taking into account the WSS magnitude through TAWSS. This metric was first proposed by Himburg et al. [45] and is defined as:

$$RRT = [(1 - 2 \times OSI) |TAWSS|]^{-1} \quad (2.3)$$

Due to the sensitivity to both direction and magnitude of WSS, the RRT metric has been reported to be the most effective indicator of intimal thickening due to its robustness [38] and accuracy [44].

2.1.4 Turbulence

The significance of turbulent flow stems from its characteristics within the boundary layer. Unlike a laminar boundary layer where the flow consists of adjacent layers, a turbulent boundary layer consists of chaotic, swirling flow [94]. The thickness of the boundary layer also increases in turbulent flow.

The multi-directional turbulent eddies produced by the energy cascade in the boundary layer directly impair endothelial cell function. Turbulence within the vasculature is highly dependent on geometry and the pulsatility of blood flow [48, 95–97]. Within AVF junctions, the vein diameter and flow split ratio has also been shown to contribute to turbulent generation, indicating that turbulent structures can exist well below the critical Reynolds number of 2300 for pipe flows [97]. Flow within AVFs and AVGs has subsequently been identified as transitional with strong secondary flows present throughout the cardiac cycle [7, 54, 97–99]. This transitional flow develops in the anastomotic region of the fistula and dampens towards the venous outflow [99]. Turbulent flows have also been shown to exist in the downstream vein due to the jet flows exiting the VN during dialysis [7]. This turbulent flow inhibits NO production, affecting the anti-proliferative and anti-inflammatory response of the endothelial layer [48]. Turbulent flows also induce random alignment of endothelial cells and promote cell turnover within 24 hours, which increases endothelial permeability, leaving the blood vessel susceptible to the deposition of inflammatory mediators, such as clotting factors, thrombin and chemokines, which can also trigger intimal thickening [42, 48].

2.1.5 Alternative Indices

Other indices have also been employed alongside computational models in order to predict regions of stenosis formation. The transverse WSS metric was introduced by Peiffer et al. [100] and characterises the multidirectional nature of the WSS vector. This metric cannot distinguish between purely forward or reverse flow and must subsequently be used in conjunction with TAWSS, OSI or RRT. Gradients of WSS in space and time have also been correlated with vascular dysfunction. Keynton et al. [4] showed a good

correlation between intimal hyperplasia formation at the anastomosis in distal bypass grafts and shear rates below 100 s^{-1} . However, gradients of WSS (in space and time) have become redundant due to practical difficulties in their physical measurement and are limited to the direction of the WSS vector, an issue which has been overcome by the newer metrics [38]. Circumferential strain has also been shown to influence vascular regulation, particularly when in phase with oscillatory shear [101]. However, measurement of circumferential strain physically or computationally is difficult, making this metric less common.

2.2 Current Research into Haemodialysis Haemodynamics

It is evident that components of wall shear can serve as metrics to predict locations of intimal thickening and potential vascular access failure. Accurately measuring flow conditions and WSS is a challenging task. Computational fluid dynamics (CFD) has proved an invaluable tool in obtaining both qualitative and quantitative information of the flow conditions in the vascular access. Additionally, particle image velocimetry (PIV), laser doppler anemometry (LDA) and flow visualisation are some of the available techniques which are used to examine the haemodynamics using in-vitro flow models. These techniques also serve to validate computational models. In-vivo experiments involving either animals or humans have been used to link flow conditions with vascular response.

2.2.1 Haemodialysis Cannulation

Three methods of cannulation exist; the area technique, the rope ladder technique and the button hole technique. The rope ladder technique involves rotating the insertion point along the vascular access to minimise trauma to the blood vessel, whilst the area technique involves rotating the insertion site within a confined area. The button hole technique uses the same puncture site repetitively so that a scar tissue tract is formed. The button hole technique has been shown to reduce the incidence of thrombosis, aneurysms and vascular intervention [86, 102], but is also associated with a higher incidence of infection [65]. The puncture sites for each technique are displayed in Figure 2.1.

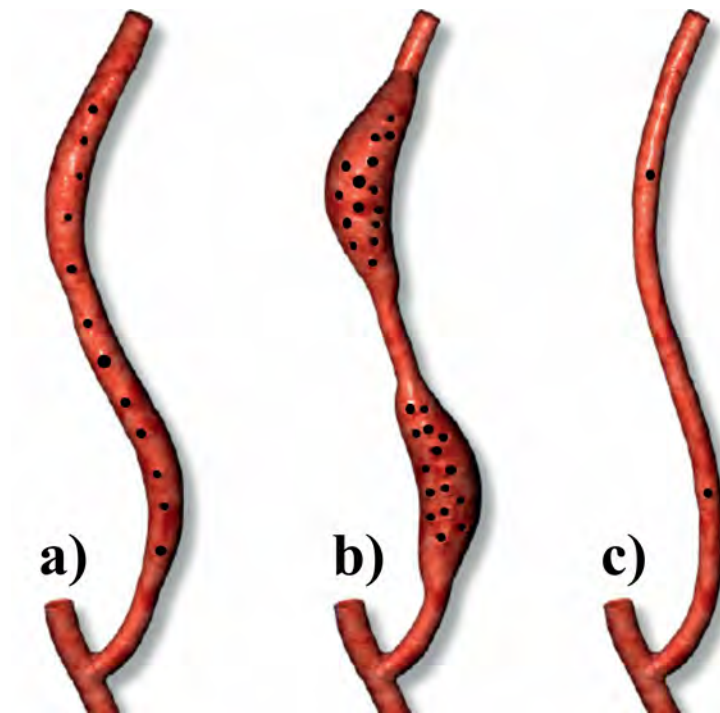


Figure 2.1: Puncture sites for various methods of cannulation. a) Rope Ladder b) Area c) Button hole

Guidelines recommend that fistulae be allowed one month to mature before cannulation [10], whilst others have indicated that the AVF can theoretically be used 14 days after creation [103, 104]. This allows the vein wall to thicken during the maturation process, reducing the chance of thrombosis. Once frequent cannulation has begun the access is not usually monitored unless problems with dialysis clearance or health of the access arise. However, this can sometimes be too late and potentially lead to a loss of the access, increased costs of treatment and a decline in patient wellbeing. It would be ideal to understand why vascular access failure is occurring and to identify sites at higher risk and mechanisms in which this risk can be reduced.

As previously explained, flow instabilities and secondary flows have a high predisposition to intimal thickening. In regards to dialysis needles, the foremost study to link these flow features with IH employed bench top flow rigs to replicate in-vivo conditions in a controlled setting. Flow instabilities and turbulence produced by the VN inserted in an AVG were measured up to 8 cm from the needle tip using LDA [7]. These flows were attributed to the boundary layer interaction between the jet exiting the VN and the graft flow. The jet flow was entrained into the core flow resulting in energy dissipation through the creation of secondary flows. The jet structure exiting the VN was measured to have velocities up to 3.5 m/s when a standard haemodialysis flow rate of 300 ml/min was tested. The turbulence and pressure changes produced by the VN jet has been suggested as a potential source of microbubble formation from cavitation which can lead to tissue ischaemia if deposited in the body [67, 68]. This may account for the high incidence of chronic lung complications and deterioration of neurological function in long term haemodialysis patients, however this hypothesis has yet to be examined.

Huynh et al. [48] extended the work of Unnikrishnan et al. [7] by placing cultured bovine aortic endothelial cells on the inner surface of a compliant

tube in the region where the flow instabilities were measured. Endothelial denudation occurred in the presence of the VN jet in six hours, which would leave the vascular wall vulnerable to platelet adhesion and aggregation and potential development of IH. Endothelial cells within the turbulent region were found to be randomly aligned, reducing endothelial integrity and further compounding the blood vessels ability to maintain homeostasis. Furthermore, NO was found to be inhibited by the downstream turbulence, reducing the ability of the blood vessel to adapt to the dynamic flow conditions.

A limitation of the LDA measurements conducted by Unnikrishnan et al. [7] is that only point measurements were made. The previous studies did not visualise or measure the three dimensional flow field produced by the VN. Qualitative information on the jet break down and subsequent flow instabilities has also not been investigated. Furthermore, approaches to reduce the risk of IH in the downstream vein have not been explored despite the evidence that the exiting jet structure affects endothelial function.

The design of dialysis needles has remained relatively unchanged in the last 50 years. The main area of innovation has been through needle tip design to reduce the bevel length and required insertion force [105]. Zarate [106] proposed a new needle design which includes two lateral openings with internal flow diverters. This design reduces the velocity of the jet exiting the central bore of the VN, subsequently decreasing the downstream turbulence and shear stresses. When used in the setting of an AN, this design lowers the negative pressure surrounding the needle tip. A similar design utilizing two side eyes was also proposed by Van Tricht [107] as displayed in Figure 2.2, with common aims to optimise flow division and reduce WSS values. Evidently, the primary drive to improve vascular access patency is to reduce the haemodynamic forces that can lead to IH. Unfortunately, these designs do not appear to have been commercialised,

with the existing design including a back eye and double bevel point remaining the current standard.

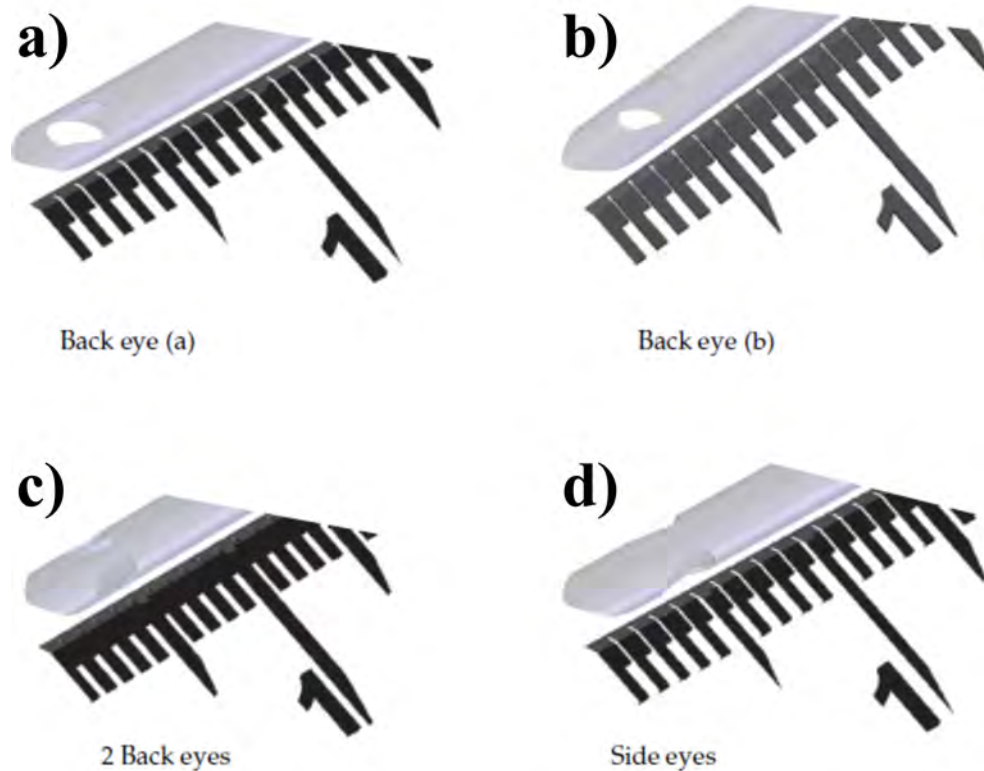


Figure 2.2: Various needle designs [107]. a) Oval Back Eye b) Ellipse Back Eye c) Two Back Eyes d) Side Eyes

On the other hand, much research has been dedicated to the design of cannulae in ventricular assist devices [108–110], cardiopulmonary bypass [111–113] and central venous catheters [114–116]. It has been shown that the geometry and position of the inlet port is fundamental in determining the amount of flow supplied to the dialysis machine [117]. The outcomes of these studies have resulted in an optimised geometry where more than 50%

of blood flow enters through the side holes [114, 116, 118]. Computational models have indicated that increasing the number of side holes can reduce high WSS which may reduce haemolysis levels [109, 110].

Looking at the effects of both the AN and VN placed in proximity to each other is important for investigating decreases in dialysis efficiency due to access recirculation. Rothera et al. [119] conducted such a study by examining the influence of needle separation distance in a clinical setting. Traditional practice recommends a minimum distance of 5 cm between the needles to minimise access recirculation. However, the study by Rothera et al. [119] found that needles placed within 2.5 cm of each other did not result in access recirculation, indicating that a large cannulation segment may not be required. Weitzel et al. [120] reported similar results when measuring the differential pressure between the needles and showed that needle induced flow effects are evident within 1 cm of the AN and several centimetres of the VN, which is in agreement with the previous assessment of VN turbulence [7].

Interestingly, in the study by Rothera et al. [119] both needles were pointed in the same direction as the blood flow through the access. Guidelines exist in regards to cannulation practice but haemodialysis treatment is usually tailored to the requirements of the patient in regards to dialyser clearance and vascular access preservation. As such, there is much variation in cannulation practice between dialysis wards and even patients. Orientation of the AN is one area which has received much debate. The VN must always point in the direction of the blood flow, however the AN may be placed in the retrograde orientation or antegrade orientation, as demonstrated in Figure 2.3 [121]. The VN is always placed downstream of the AN, closer to the heart, to facilitate the return of filtered blood to the body. The antegrade orientation has been associated with greater access flows [122], however no difference was observed for dialysis clearance [123]. Conversely, Parisotto et al. [124]

reported lower access survival and a higher risk of aneurysm formation with the AN in the retrograde orientation as the tract at the puncture site can be kept open through fistula flow forces, thereby weakening the blood vessel wall further and leaving it susceptible to blood particle deposition.

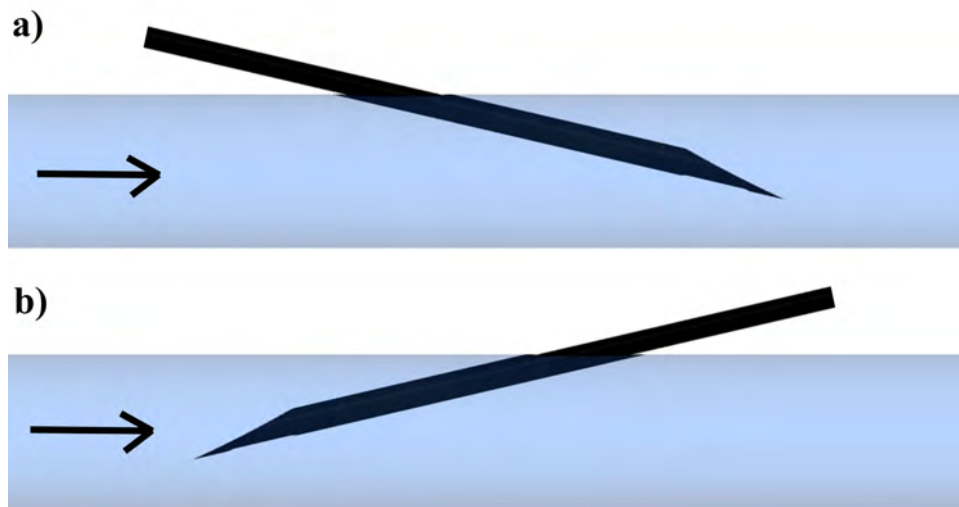


Figure 2.3: Needle orientation where the arrow indicates the direction of blood flow in the vein. a) Antegrade b) Retrograde

Another area which is controversial is the technique of rotating the needle 180° about its cylindrical axis after insertion. This is done to alleviate pressure in the AN if the bore becomes attached to the vessel wall [121]. This technique is also performed to minimise the risk of infiltration which can result in thrombosis [87]. However, it has been identified that infiltration can occur during the rotation process itself [85]. Parisotto et al. [124] concluded that needle rotation is an unnecessary practice as it may cause damage to the vascular access, yet this practice is still conducted by some.

Evidently, the application of dialysis needles within the blood vessel play an important role in vascular access patency. The needles have been shown to

produce complex haemodynamics which can lead to IH, however qualitative and quantitative information regarding the haemodynamics produced by dialysis needles in an AVF remains to be investigated. Understanding the haemodynamic forces produced by the needles will reveal sites at higher risk of IH or mechanisms in which this complication can be minimised.

2.2.2 Arteriovenous Fistulae and Arteriovenous Grafts

Thrombosis usually occurs in the anastomosis of the vascular access due to the high prevalence of stenosis in this region [27–33]. Much research in the field of haemodialysis has been dedicated to understanding the pathophysiology of intimal hyperplasia in AVFs and AVGs. In-vivo studies have elucidated the cascade of events involved in intimal thickening and shown its formation to be highly localised. These studies have helped validate the theory that haemodynamics plays an influential role in the development of IH.

2.2.2.1 In-vivo Experiments

Examination of grafts implanted in canines revealed that IH was found to be localised at the heel and toe of the graft and consisted mainly of VSMC proliferation, degenerating myocytes, active myofibroblasts and dense collagen fibres [57, 125]. Similar cellular phenotypes have also been identified in human tissue samples [3, 126]. Jackson et al. [127] found similar results when examining end-to-side AVFs in rabbits. Varying anastomotic angles were created resulting in varying responses of intimal thickening which coincided with a stagnation point that migrated during the cardiac cycle. The migration of the stagnation point in grafts was also

examined by Bassiouny et al. [58] using flow visualisation, as displayed in Figure 2.4.

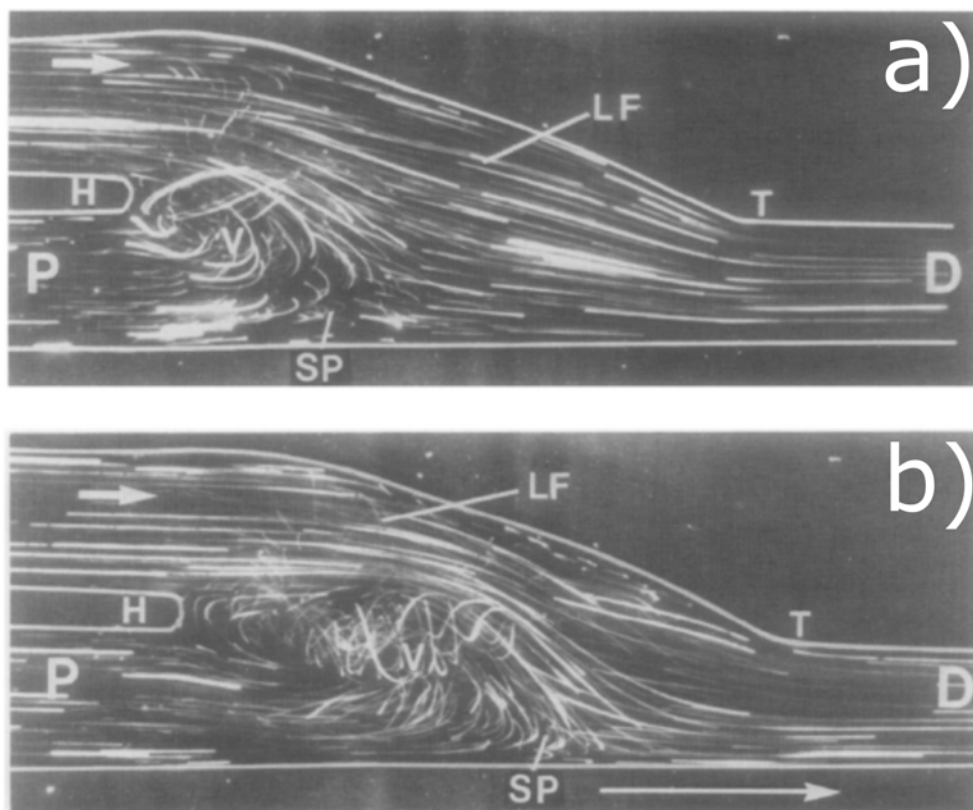


Figure 2.4: Movement of the stagnation point throughout the cardiac cycle in vascular grafts. The figures are labelled as: heel (H), toe (T), proximal (P), distal (D), laminar flow (LF), stagnation point (SP). a) Early Systole b) Mid-Systole [58]

Interestingly, intimal thickening coincided with regions of low WSS [57, 58], with accelerated VSMC proliferation found in regions of extremely low WSS (<0.2 Pa) [56]. In this case, the WSS was approximated from an empirical formula using velocity measurements taken with an ultrasonic flow transducer. Keynton et al. [4] also utilised an ultrasonic flow

transducer to measure temporal and spatial gradients in grafts implanted in dogs to examine transient effects. It was observed that over 75% of IH occurred at shear rates below 100 s^{-1} and that 92% occurred when the shear rate was below 346.5 s^{-1} . Furthermore, no intimal thickening was observed for shear rates greater than 950 s^{-1} . Analysis of the oscillatory flow component led to the conclusion that IH is more prone to develop in regions of flow reversal. This observation has also been reported by others [58, 59].

However, the spatial resolution of ultrasonic flow transducers is a major limitation affecting the accuracy of the velocity measurements. Furthermore, calculation of WSS relies on the application of the Hagen-Poiseuille equation, a generalised approach based on the assumption of laminar flow. This methodology is limited by the fact that the flow in the vascular access is thought to be transitional to turbulent [54, 97–99]. Remuzzi et al. [128] developed a method of measuring WSS in-vivo, that takes into account the pulsatile nature of blood flow and variations in blood viscosity. They measured WSS in the range of 6-11 Pa in a human radial artery, seven days after creation of the AVF. These findings concur with those of Kohler et al. [129], who calculated values of approximately 7.8 Pa in baboon grafts.

2.2.2.2 In-vitro Experiments

Despite the general agreement in WSS measurements, spatial resolution remains a limiting factor. In-vitro experiments utilising bench top models are an effective way of replicating in-vivo conditions in a controlled environment and can overcome the limitations of spatial resolution and empirical approximations. Qiu and Tarbell [101] used a piston pump to impose sinusoidal flow over cultured bovine aortic endothelial cells on a

compliant tube. Pressure transducers and CCD cameras were employed to measure the diameter and pressure waveforms in the elastic tubes simultaneously. In this study, the photochromic method was used to calculate the wall shear rate. Over a period of four hours, oscillatory WSS was found to cause the highest production of vasoconstrictors, whereas vasodilators were upregulated under steady WSS. Davies et al. [42] also examined the effects of turbulent flow on cultured bovine aortic endothelial cells using flow visualisation and hot wire gauges to measure the WSS. Turbulent flow coupled with low WSS in the range of 0.15-1.4 Pa resulted in a higher rate of endothelial turnover than that of the same range in laminar flow, demonstrating the damaging nature of a turbulent flow field. Chien [41] reported similar findings, in that complex flow patterns, oscillatory WSS and negative WSS increased the permeability of cultured endothelial cells. This affected communication between neighboring cells, resulting in heightened endothelial cell turnover and an inability of the endothelium to maintain vascular integrity.

Several studies have employed either flow visualisation [98], LDA [54, 130–133] or PIV [134–137] to analyse the haemodynamics in bench top models of AVFs and AVGs. A crucial component when using lasers for flow measurement is the creation of a transparent flow phantom with a refractive index matched working fluid [138]. Rigid models are generally more common as they are easier to construct, although compliant models are also possible [138]. The rigid models are commonly cast from silicon derivatives such as sylgard 184 [131] or silastic rubber [98] but can also be machined from acrylic [130]. Refractive index matching prevents optical distortion at the fluid-solid interface, improving the accuracy of measurements. The effects of refractive index matching are shown in Figure 2.5.

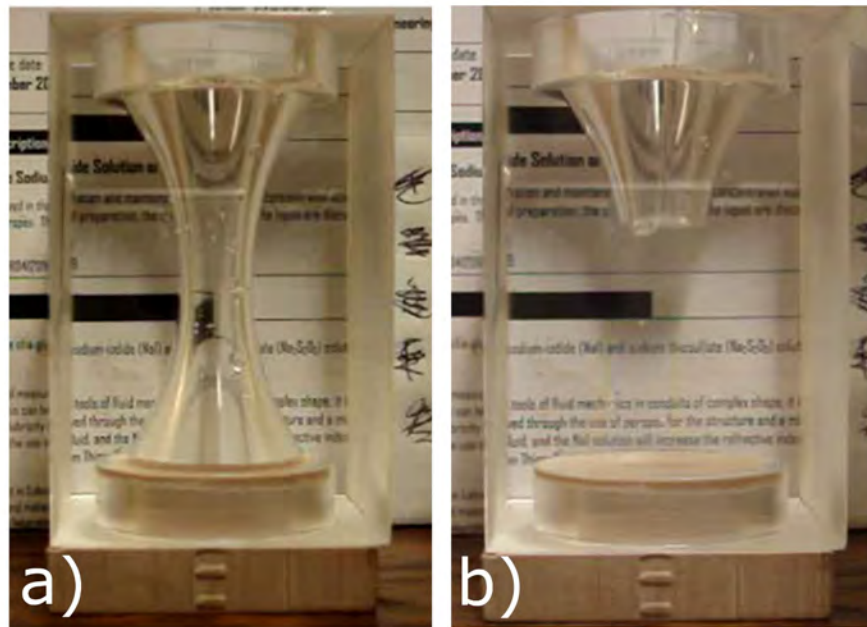


Figure 2.5: Effects of refractive index matching on acrylic models. a) No refractive index matching fluid b) Refractive index matching fluid

A mixture of glycerol and water at a ratio of approximately 40:60 is commonly used as it yields a viscosity similar to that of blood (≈ 0.003 Pa.s). Dynamic similarity can also be employed to assist in laser alignment and increase the spatial resolution of the flow field. A common finding in the studies investigating flows in AVGs was the existence of a stagnation point on the floor of the artery consisting of low and oscillating WSS [54, 55, 130–133]. The stagnation point coincided with regions of IH, highlighting the power of laser measurements in predicting disease formation. Similar results were also discovered in AVFs [136].

Despite the high accuracy and improved spatial resolution lasers offer compared to other measurement devices, they are still generally limited to point or planar measurements. This can be overcome by using a tomographic system, however this exponentially increases the complexity

and cost of the experiment. Furthermore, measurement of WSS is still difficult due to: reflections at the fluid-wall interface, high gradients near the boundary and the three dimensionality of flow structures in this region [139]. A common application of laser measurements is the validation of bulk flow quantities for CFD models [132, 134, 135, 140]. Advances in computational power have allowed the complex three dimensional flow fields in blood vessels to be resolved with a high resolution. Subsequently, the WSS vector is easily calculated with great accuracy. Validated computational models have thus proven to be an invaluable tool when investigating disease progression in blood vessels.

2.2.2.3 Numerical Modelling

Several studies have employed the power of computational models to numerically examine the haemodynamics in AVGs [93, 97, 132, 140–143] and AVFs [97, 99, 134, 135, 144–148]. The validity of these models is primarily determined by the choice of boundary conditions, whilst the mesh quality, choice of solvers and numerical discretisation scheme also influence the quality of the simulations. The temporal nature of blood flow is easily examined by applying transient boundary conditions as measured by Duplex ultrasound [144]. Transient analysis of AVF flows has shown that transitional flow vortices originating in the anastomosis are most pronounced during systole and often persist through to diastole, as shown in Figure 2.6 [99]. These transitional flow vortices persist within the venous outflow and only begin to re-laminarise several centimeters from the anastomosis [147]. Broderick et al. [97] examined the influence of various factors on the production of instabilities within an AVG. Large eddy simulations (LES) were conducted to resolve these high fluctuations and instabilities originating in the anastomosis. Vein diameter and flow split ratio were shown to be the greatest contributors to turbulent generation at

the anastomosis, with fluctuating and chaotic flows existing well below the critical Reynolds number of 2300 for pipe flows. Lee et al. [143] also highlighted the influence of flow split ratio and revealed that transitional flows exist at Reynolds numbers as low as 800.

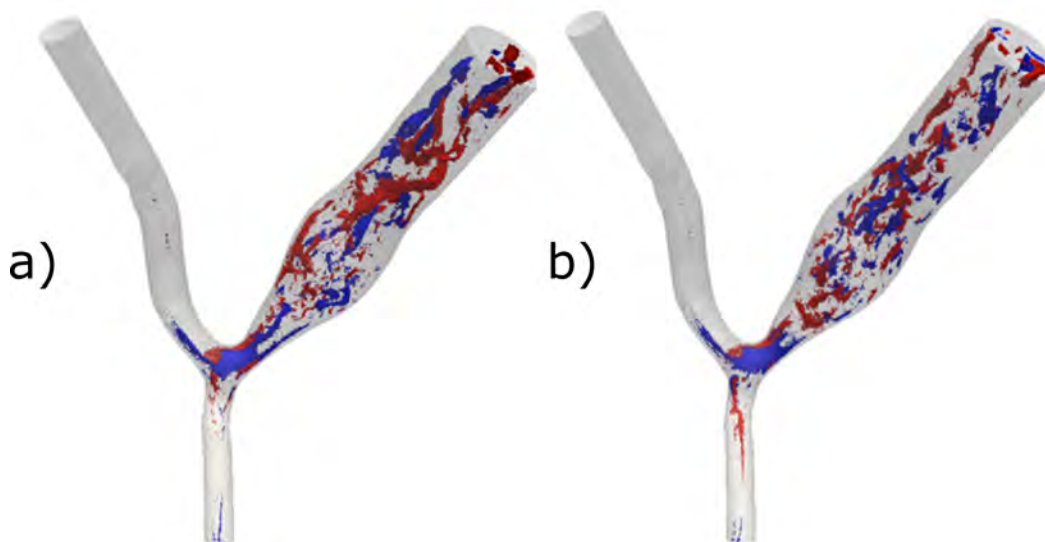


Figure 2.6: Isosurfaces of helicity showing the development of transitional flow at the anastomosis. a) Systole b) Diastole [99]

Idealised geometries have previously been used to examine the haemodynamics within the vascular access [132, 140–142, 145]. Geometries created using computer aided design software (CAD) can decrease the complexity of parametric design as they allow specific variables to be analysed in a controlled setting. This method is evident in the study by Van Canneyt et al. [141], who explored the effect of helical graft designs in minimising low and oscillatory flow conditions. Idealised geometries also allow the application of fully structured hexahedral grids which increases mesh quality and numerical accuracy whilst also reducing computational time. The use of hexahedral grids in vascular access studies has been shown

to produce errors in WSS calculation as low as 2% [132, 141]. Furthermore, idealised geometries allow the use of symmetry assumptions, which further reduces computation time [142].

Idealised geometries have also allowed the effects of non-Newtonian blood modelling to be examined. Blood is a shear thinning fluid, in that its viscosity is shear dependent. However, at shear rates greater than 100 s^{-1} blood acts as a Newtonian fluid, thus the application of non-Newtonian models is questionable in vessels with high flows such as AVFs and AVGs. Furthermore, blood viscosity depends on many factors such as: haematocrit, temperature, plasma composition and pathological conditions, making the application of a universal blood model difficult. O’Callaghan et al. [149] compared various blood models in a distal vascular bypass graft; whose geometry is similar to that of an AVG. Little difference in WSS was found between the blood models at high shear rates, however variations up to 300% were evident under low shear conditions. Decorato et al. [135] reported values much lower, with the mean difference in WSS at the anastomosis and downstream vein of an AVF approximately 10% and 13%, respectively. Both studies concluded that the application of a non-Newtonian model is case dependent and is not necessary in cases with high blood flows.

Blood vessels have elastic properties and deform under the influence of blood pressure, yet the rigid wall assumption is commonly made for simplification and to reduce computation time. Fluid structure interaction (FSI) models combine the effects of blood pressure and the elastic properties of blood vessels to obtain a more complete picture of the vascular access. McGah et al. [148] compared WSS measurements between a rigid and fully coupled FSI simulation of an end-to-side fistula. Variations in WSS up to 50% were measured at the anastomosis, however differences in the downstream vein were only 10%. These values are comparable to Decorato et al. [135] who reported a 15% variation in peak WSS and 20%

in maximum velocity. Shear stresses in FSI simulations are generally lower than rigid models as the elasticity of the walls dampens the velocity in the blood vessel. Thus the rigid wall assumption will overestimate the WSS in the vascular access. Several limitations in the flexible wall approach were noted by McGah et al. [148], most importantly an uncertainty of approximately 25% in the value of the elastic modulus and an uncertainty of 10-15% in measuring the exact wall thickness of the blood vessels. Another limitation is the non-homogeneity of the blood vessel wall and the variation of its properties between patients, making the application of an FSI model case dependent. Both studies also noted that FSI models are much more computationally expensive than their rigid wall equivalents.

Recently, patient specific geometries of AVFs have been realised from 3D laser scans of vascular casts [93] or image segmentation from: 2D ultrasound images [147, 148], computerised tomography scans (CT) [135, 143], angiograms [144], magnetic resonance angiograms (MRA) [99] or magnetic resonance imaging (MRI) scans [146, 147]. A common finding in the patient specific geometries is the presence of strong secondary flows due to the curvature of the anastomosis and the adjoining vein. As the blood flow exits the anastomosis it impinges on the far surface of the vein and becomes highly skewed causing flow separation, disturbed flows and flow reversal. These secondary flows coupled with the transient nature of blood flow result in regions of oscillating WSS on the anastomosis floor and inner surface of the juxta-anastomotic vein. These flows contribute to the high incidence of IH in the anastomotic region [27–33]. Figure 2.7 compares CFD and PIV data on the flow through a patient specific AVF and represents the power of these two methods in examining biological blood flows.

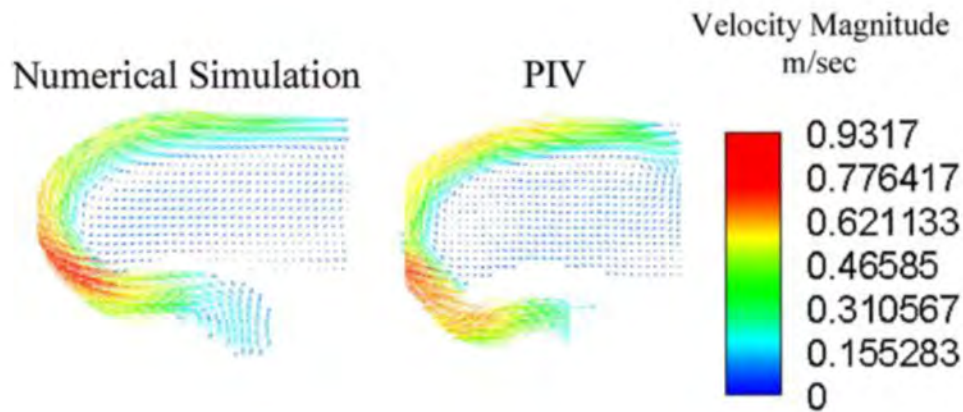


Figure 2.7: CFD and PIV data on flow through a patient specific AVF [134]

2.3 Summary of Literature

- The vascular access is referred to as the lifeline for haemodialysis patients. An AVF is the preferred choice of access due to superior patency rates and fewer incidents of complications, which reduces the long term cost of haemodialysis.
- Thrombosis as a result of low flow conditions or rupture of stenosis is the most common complication in haemodialysis patients. Stenosis formation is highly localised within the vasculature, commonly forming at the anastomosis or downstream vein. Intimal thickening has been shown to have a strong correlation with haemodynamics, in particular low WSS, oscillatory WSS, disturbed flows, stagnant flows and excessively high WSS.
- Accurately measuring WSS has proven difficult. Laser diagnostic techniques have been proven to have the highest accuracy when measuring bulk flow quantities on bench top models. Measurement of

WSS using lasers is also difficult due to: reflections at the fluid-wall interface, high gradients near the boundary and the three dimensionality of flow structures in this region. Laser techniques have thus far mainly been used to validate computational models.

- Computational models are able to resolve the haemodynamics with high three dimensional resolution and can accurately calculate WSS. The accuracy of the model is highly dependent on the choice of boundary conditions. Assumptions on geometry, blood rheology model and wall elasticity are usually made to reduce the complexity and computational time of the simulation.
- Dialysis needles have a direct influence on vascular patency. With reference to haemodynamics, the jet exiting the VN produces highly disturbed flow. The flow field around the AN is thought to be much smaller as the blood is withdrawn from the vein. Needle geometry and position within the vessel also influence vascular patency.
- The majority of research has focused on the haemodynamics of AVFs and AVGs, justifiably as intimal thickening most frequently occurs at the anastomosis. However, intimal thickening in the downstream vein is also common, and investigation into the haemodynamics produced by the needles has received little attention.

2.4 Thesis Objectives

The vascular access is a crucial component in haemodialysis treatment but does not have high long term success. Extensive examination of the haemodynamic forces produced by blood entering and exiting dialysis needles has not been conducted. The primary objective is to determine the

extent that dialysis needles contribute to IH in the downstream vein. A secondary objective is to determine the role of dialysis needles in microbubble formation from cavitation. From these objectives, the aim is to determine methods of identifying and minimising the risk of vascular access failure.

It is hypothesised that blood flow through the VN causes damage to the endothelium through high WSS and secondary flows produced by the exiting jet structure. Conversely, the flow field surrounding the AN is small relative to the VN and its role in intimal thickening is minimal. In regards to microbubble formation, it is hypothesised that cavitation is more likely to occur at the AN due to the lower negative pressures that are produced when the blood is extracted from the vein.

The most relevant parameter in predicting IH is WSS. Numerical models will be employed to accurately assess this parameter whilst also providing high resolution three dimensional data of the flow field surrounding the needles. Qualitative and quantitative information on the flow field produced by the needles is required to identify regions at risk of intimal thickening. This can aid in vascular screening and treatment of stenosis. Furthermore, methods to minimise the harmful haemodynamics will be explored by determining the effect of needle position, blood flow rate and alternate designs. These solutions may minimise the incidence of stenosis in the downstream vein, thereby increasing the useful life of the fistula whilst also reducing the cost of treatment. The potential of microbubble formation from cavitation is also explored through computational models and clinical examination of the pulsatility within the extracorporeal system and subsequent pressures.

As highlighted above, computational models are highly dependent on boundary conditions and require validation. Stereoscopic PIV will be employed to validate the three dimensional bulk flow velocities along the

central plane in the computational models under steady conditions. Steady state boundary conditions are selected to provide an extra degree of control in the experiment and allow the use of time averaged quantities to maximise the accuracy of the validation. Improved experimental techniques such as refractive index matching and high precision machining are also utilised.

From a clinical stand-point, analysis of variables measured during haemodialysis may reveal a relationship between the haemodynamics produced by the needles and AVF failure. From this data, predictors of late failure might be elucidated from variables which are already collected during routine treatment. This offers an alternate approach from the aforementioned methods to improve patient care. A clinical study also provides the link between biological responses and bench top/computational modelling.

Chapter 3

Clinical Study: Correlation between haemodynamics and late fistula failure

Despite the advantages of AVFs over other forms of vascular access, late failure is still common and contributes to an increased cost of care. This chapter investigates the relationship between haemodynamic variables and late failure by retrospectively examining patients with mature radiocephalic fistulae from the time of first cannulation until an intervention was required. The influences of hemodialysis practices and the effects of comorbidities (diabetes and age) were measured to assess the influence of cannulation on AVF survival, with the aim of using clinical variables to predict the development of complications within the vascular access. The results of this study form an exploratory analysis into current trends of clinical care for a specific patient cohort.

3.1 Introduction

The prevalence of ESRD within the United States in 2012 was roughly 637,000; increasing 3.7% from the previous year [150]. At this time, haemodialysis remained the most popular form of treatment accounting for approximately 64% of the ESRD population, as shown in Figure 3.1 [150]. Although kidney transplantation is the preferred treatment due to the greater social and physical benefits it offers, haemodialysis is more common in Australia and the United States due to the limited availability of transplantation kidneys [151].

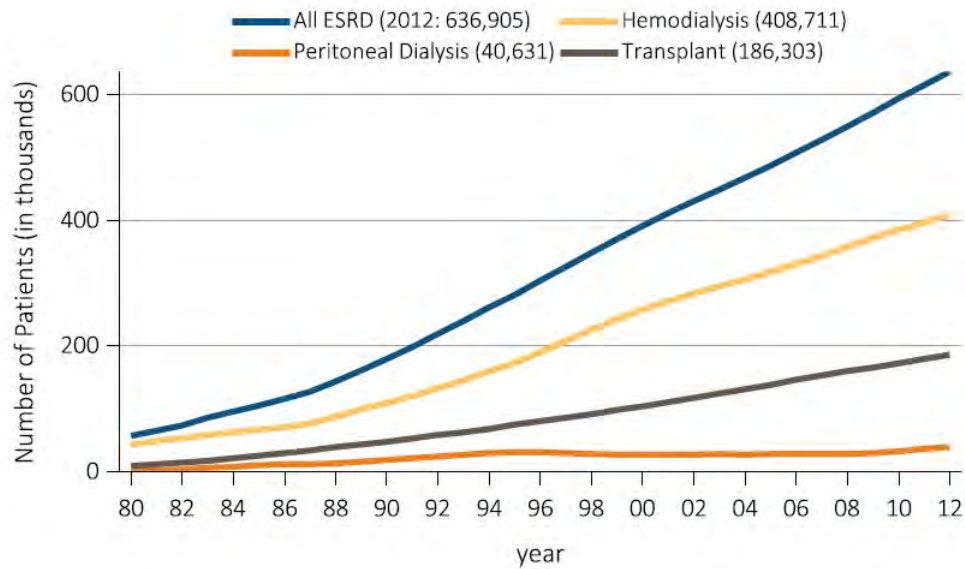


Figure 3.1: Prevalence of End Stage Renal Disease in the United States [22]

Diabetes and hypertension are major causes of ESRD, accounting for 50% and 20%; respectively [9]. Two other major causes are glomerulonephritis and cystic kidneys; diseases which target the kidneys. The number of incident cases per year for the four main causes of ESRD in the United States is

displayed in Figure 3.2. Incident rates of ESRD have been declining since 1996 due to improved kidney management in regards to the primary causes, as well as better survival of ESRD patients. Due to the high prevalence of haemodialysis the requirement to create a long lasting vascular access is increasingly important.

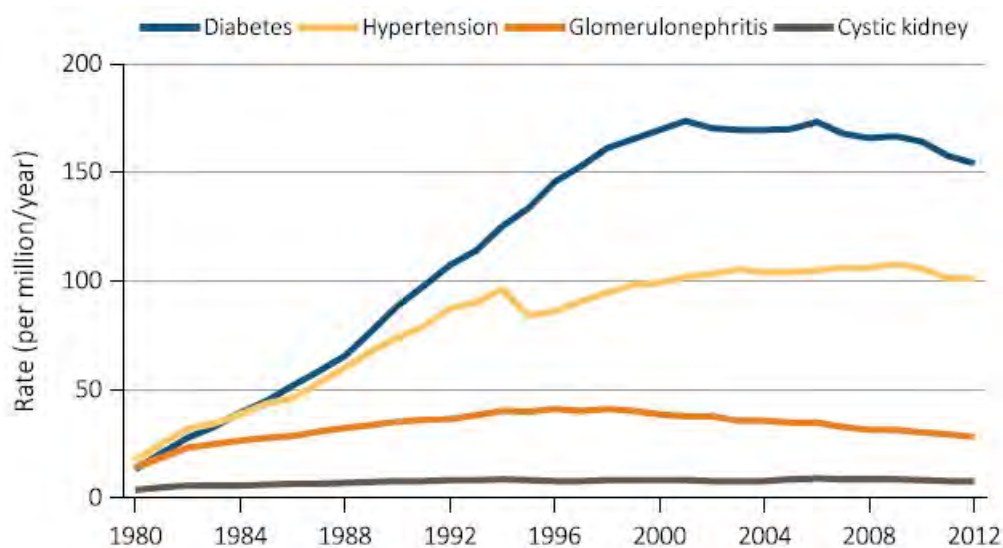


Figure 3.2: Incident rates in the United States of primary causes of ESRD in 2012 [22]

Long term preservation of the haemodialysis vascular access is a primary objective for patients suffering from ESRD. AVFs are the first choice of vascular access because they have the highest patency rates, fewest complications and lowest cost compared to graft and catheter access [10]. In particular, AVFs have been reported to have two year patency rates up to 70% compared to 40% in grafts [19]. However, AVFs are prone to developing complications, with unsuccessful maturation accounting for 53% of failures [152], whilst 30% may fail within the first three months [153]. Conversely, late failure can also occur after the AVF has matured and is cannulated regularly, with one and four year patency rates reported to be

approximately 70% and 48%, respectively [21].

Early failure of the vascular access is mainly due to patient characteristics such as vascular health or small blood vessel size which limits the high blood flow required for efficient dialysis [46, 47], whereas late failure commonly occurs due to morphological changes to the structure of the blood vessel initiated by haemodynamic changes [3–6]. Despite the mechanisms of failure being well defined, predicting its occurrence remains a challenge.

To aid in the long term preservation of the vascular access this chapter set out to investigate the specific factors that lead to late AVF failure in matured radiocephalic fistulae. Haemodynamic clinical variables, as well as underlying comorbidities of age and diabetes were examined to determine their ability to predict the occurrence of late failure.

3.2 Methods

3.2.1 Study Design

A retrospective examination was conducted on a range of haemodynamic clinical measurements (maturation time, arterial pressure, venous pressure, blood flow rate and frequency of dialysis sessions) in haemodialysis patients with matured radiocephalic fistulae and of the relationship between these variables pertaining to cannulation and AVF failure. Correlations between time to failure (useful fistula age) and the haemodynamic variables of pressure and blood flow rate were also examined to determine their potential at predicting late failure. The effects of underlying comorbidities of age and diabetes on fistula age were also investigated.

In this study, early failure was defined as an AVF which does not mature and cannot be cannulated whilst late failure was defined as an AVF that has fully matured and is being regularly cannulated until it reaches a point where efficient dialysis is no longer achievable and interventional surgery is required. Maturation time was defined as the time between surgical creation of the fistula and first cannulation.

Data was obtained from thirty-one patients who were using a radiocephalic fistula and successfully dialysing at the Prince of Wales Hospital, Sydney, Australia, from January 2006 to January 2015. Ethical approval was provided by the Human Research Ethics Committee at the Prince of Wales Hospital (HREC Number: 14/255, SSA Number: 14/G/358). Patient data was selected from the time of first cannulation until the first surgical intervention, thereby removing any post-surgical effect on the health of the AVF. The inclusion criteria were:

- Patients are dialysing with a radiocephalic fistula
- No surgical intervention was performed to aid in maturation
- Patients are over 18 years of age
- Late failure (as defined above) must have occurred
- The access is the patient's first fistula

3.2.2 Data Analysis Methodology

Predictors of late failure were identified by plotting the haemodynamic variables of pressure and blood flow rate vs time to failure (useful fistula age) for each patient individually. Blood flow rate is set by the blood pump speed and is a controlled variable that indicates vascular health from the

nurses' experience. Measurement of the arterial and venous pressure represents the ability to withdraw and return blood to the fistula and provides an indication of vascular resistance from potential stenosis or thrombosis. Blood pressure and blood flow rate were recorded once during treatment from the pressure gauge and blood flow setting on the AK200S dialysis machine (Gambro, Lund, Sweden). To identify the cause of late AVF failure, the patients were classified into groups based on the length of time in which successful cannulation was conducted until an intervention was required (useful fistula age). The influence of haemodynamic variables pertaining to cannulation were then measured against fistula age groupings: 0-99 days; 100-499 days; 500-999 days; 1,000-1,999 days and 2,000+ days. The demographics of fistula age classification are displayed in Table 3.1. The mean age is calculated based on the patient age at the end of the study period (January 2015).

Table 3.1: Patient demographics based on fistula age classification

Fistula Life (days)	Mean Age (SD)	Men/Women
2,000+	75 (2) years	2/0
1,000-1,999	74 (12) years	3/2
500-999	49 (9) years	3/0
100-499	67 (11) years	12/2
0-99	58 (15) years	12/2

Control of poor vascular health were also imposed by dividing the patients into four groups based on comorbidities of age (>65 years) and diabetes mellitus as displayed in Table 3.2.

Table 3.2: Patient demographics based on comorbidity classification

Group No.	Diabetes	Age (years)	Mean Age (SD)	Men/Women
1	No	<65	50 (14) years	4/2
2	Yes	<65	57 (4) years	7/2
3	No	>65	78 (8) years	7/1
4	Yes	>65	73 (5) years	6/2

Radiocephalic fistulae were predominantly located in the left arm in 27/31 (87%). Locations of failure were classified as the inflow artery, anastomosis region including the swing segment of the fistula and the outflow region which includes the cannulation segment and drainage vein, which are similar to that used by Sivanesan et al. [28]. All patients were dialysed using an AK200S device (Gambro, Lund, Sweden), Gambro BL 208BD bloodlines and a high-flux Revaclear 400 dialyser (Gambro, Lund, Sweden).

3.2.3 Statistical Analysis

All statistical analyses were conducted in MATLAB (Mathworks Inc, Massachusetts, United States). A standard least-squares regression analysis was conducted on the haemodynamic variables of pressure and blood flow rate to determine a correlation with late failure. The coefficient of determination (R^2) is used to fit the data with the regression line. The significance of group differences were assessed using a two-way unbalanced ANOVA, where a p-value less than 0.05 was considered significant. The two way ANOVA was performed against the group whose patients had the longest fistula survival (2000+ days), as these patients were able to remain on dialysis successfully for a longer time without requiring an intervention. It was also performed on patients without comorbidities of diabetes or age as these patients historically have greater fistula survival. The data for each

group is presented in terms of the mean and standard deviation (SD). Fistula life was assessed using the Kaplan-Meier survival analysis.

3.3 Results

3.3.1 Complications

There were a total of 39 complications in 31 patients that resulted in an intervention, displayed in Table 3.3. Stenosis was the most common complication accounting for 37 (95%) incidents, with five patients exhibiting stenosis in two areas and one patient showing stenosis in all three locations. Steal syndrome accounted for the other two complications in two patients with diabetes. Both cases of steal syndrome were treated by collateral vein ligation. Stenosis at the anastomosis was the most common complication accounting for 19 incidents, closely followed by outflow stenosis (14 incidents) with inflow stenosis being less common (4 incidents).

Table 3.3: Number of complications occurring in each patient group

Group No.	Inflow stenosis	Anastomosis stenosis	Outflow stenosis	Steal syndrome
1	1 (14%)	3 (43%)	3 (43%)	0 (0%)
2	1 (8%)	7 (54%)	4 (31%)	1 (8%)
3	0 (0%)	4 (50%)	4 (50%)	0 (0%)
4	2 (18%)	5 (45%)	3 (27%)	1 (9%)

3.3.2 Standard least-squares regression analysis

The relationship between blood flow rate and time to failure is displayed in Figure 3.3. Standard practice on new fistulae is to cannulate conservatively by using lower blood flow rates during initial dialysis sessions. This trend is highlighted in the data where the average blood flow rate was found to be lower in patients who required an intervention soon after dialysis treatment commenced. Regression analysis shows that after the first few months the blood flow rate remained between 300-360 ml/min. This result displays standard practice rather than indicating that fistulae with higher blood flow tend to last longer.

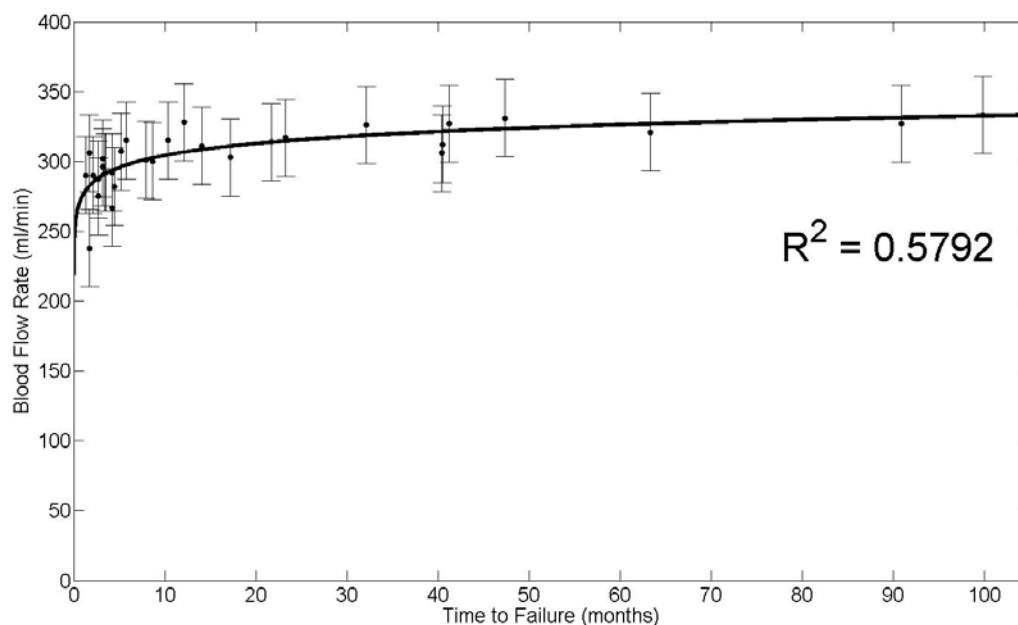


Figure 3.3: Relationship between average blood flow rate averaged over all sessions per patient and time to failure (useful fistula age). Standard deviation is the average across all measurements for the cohort of patients.

The average arterial pressure for each patient is plotted against time to failure in Figure 3.4. Higher arterial pressures were associated with fistulae which required an intervention within the first year but continued to decrease over time, albeit at a small rate. The correlation between arterial pressure and failure was not strong.

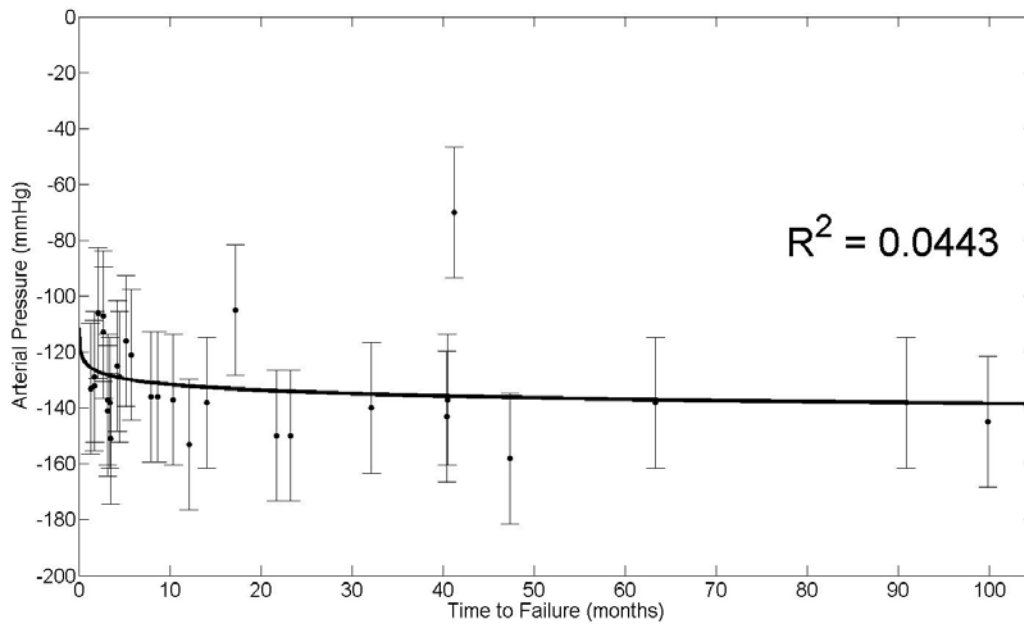


Figure 3.4: Relationship between average arterial pressure averaged over all sessions per patient and time to failure (useful fistula age). Standard deviation is the average across all measurements for the cohort of patients.

The average venous pressure is plotted against time to failure for each patient in Figure 3.5. Similar to the trend with arterial pressure, the venous pressure was lower for patients who required an earlier intervention and continued to rise over time. No strong correlation between venous pressure and failure was found.

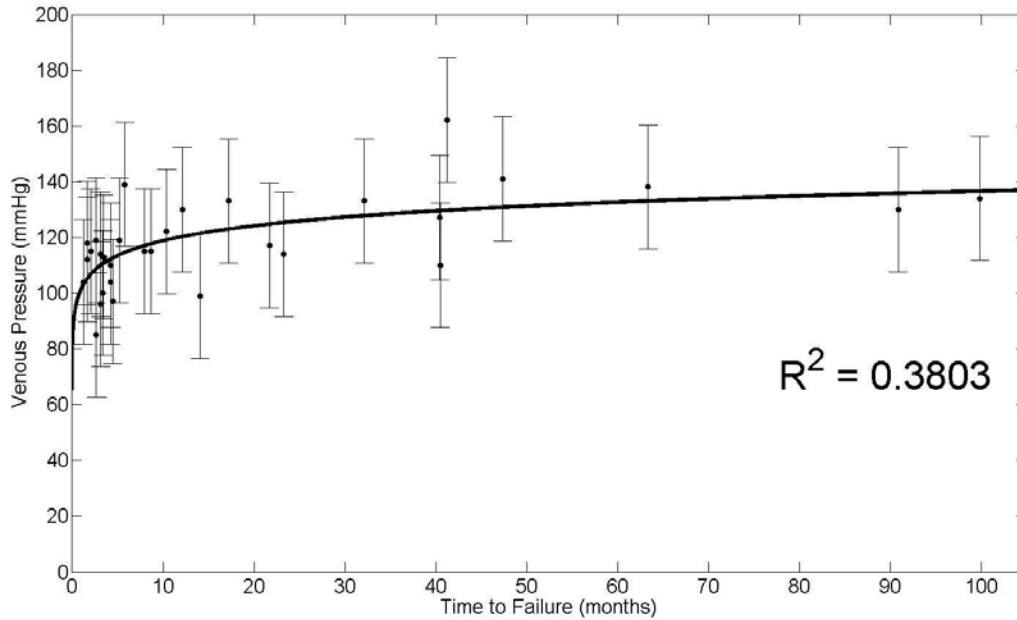


Figure 3.5: Relationship between average venous pressure averaged over all sessions per patient and time to failure (useful fistula age). Standard deviation is the average across all measurements for the cohort of patients.

3.3.3 Effects of Fistula Survival

Table 3.4 displays the average arterial pressures for different fistula ages. A lower average arterial pressure, around -140 mmHg, was associated with longer AVF use. In particular, patients who required an intervention within 100 days of cannulation tended to have a higher arterial pressure around -120 mmHg although this relationship was not significant ($P = 0.12$).

Table 3.4: Mean +/- standard deviation and statistical significance of pressure in the arterial line categorised by fistula longevity

Fistula Life (days)	Mean AP (mmHg)	SD (mmHg)	P-value
2,000+	-141	16	-
1,000-1,999	-129	24	0.65
500-999	-147	19	0.38
100-499	-132	24	0.33
0-99	-123	24	0.12

Table 3.5 displays the venous pressure for each fistula life group. The data shows that patients whose AVF functioned for a longer time had a higher venous pressure around 130 mmHg, compared with patients whose AVF failed within the first 100 days of cannulation who had an average venous pressure of approximately 110 mmHg, which was statistically significant.

Table 3.5: Mean +/- standard deviation and statistical significance of pressure in the venous line categorised by fistula longevity

Fistula Life (days)	Mean VP (mmHg)	SD (mmHg)	P-value
2,000+	132	18	-
1,000-1,999	135	20	0.81
500-999	121	19	0.26
100-499	115	23	0.09
0-99	107	26	0.03

Table 3.6 shows the average blood flow rate for each fistula life group. The trend to cannulate conservatively by using lower flow rates during initial dialysis sessions is highlighted, where the average blood flow rate was found to be lower in patients who required an intervention soon after dialysis treatment commenced. Interestingly, flow rates below 300 ml/min were found to be statistically related to those whose fistula failed within 500 days.

Table 3.6: Mean +/- standard deviation and statistical significance of blood flow rate categorised by fistula longevity

Fistula Life (days)	Mean BFR (ml/min)	SD (ml/min)	P-value
2,000+	330	20	-
1,000-1,999	320	23	0.65
500-999	319	21	0.12
100-499	300	29	0.02
0-99	283	33	0.02

Table 3.7 shows the average frequency of treatment for each fistula life group. The mean time between sessions remained consistent, with patients receiving dialysis every 2-3 days, as noted by the small standard deviation. A statistical significance was found for late failure and a shorter time interval between sessions however this was within the range of all measurements.

Table 3.7: Mean +/- standard deviation and statistical significance of dialysis frequency categorised by fistula longevity

Fistula Life (days)	Mean Dialysis Frequency (days)	SD (days)	P-value
2,000+	2.44	0.8	-
1,000-1,999	2.43	0.79	0.65
500-999	2.33	0.67	0.02
100-499	2.41	0.77	0.75
0-99	2.38	0.78	0.68

The mean and standard deviation for fistula maturation times are displayed in Table 3.8. Generally the fistulae that survived longer without an intervention had been given more time to mature, although this was not significant ($P = 0.91$).

Table 3.8: Mean +/- standard deviation and statistical significance of fistula maturation time categorised by fistula longevity

Fistula Life (days)	Mean Maturation Time (months)	SD (months)	P-value
2,000+	9.0	8.6	-
1,000-1,999	5.4	3.4	0.42
500-999	1.5	0.1	0.20
100-499	9.8	8.9	0.91
0-99	3.3	3.2	0.15

3.3.4 Effects of Vascular Health

The mean and standard deviation for fistula age (as measured from the time of first cannulation to the time of first intervention) for each group are displayed in Table 3.9. Patients over the age of 65 and those who were also diagnosed with diabetes had a longer time of successful cannulation without requiring an intervention compared to those with a healthy vasculature (<65, no diabetes). Although there was a trend between these comorbidities and longer fistula survival the relationship was not significant (P = 0.38).

Table 3.9: Mean +/- standard deviation and statistical significance of fistula age as measured from the time of first cannulation to the time of first intervention

Group No.	Mean Age (months)	SD (months)	P-value
1	12.7	16.2	-
2	10.5	10.4	0.75
3	29.8	33.4	0.27
4	29.1	32.4	0.38

Figure 3.6 displays a Kaplan-Meier survival curve for the different groups based on classification of vascular health. Patients over the age of 65 and those who also have diabetes have a higher probability of longer fistula use, which mirrors the data displayed in Table 7. Figure 3.6 also shows that elderly patients outperformed the younger cohort, with elderly patients whom were also diagnosed with diabetes outperforming their counterparts without diabetes. Interestingly, regardless of vascular health status, all four groups display similar survival probabilities within the first 6 months of AVF use, with approximately 50% of patients requiring an intervention.

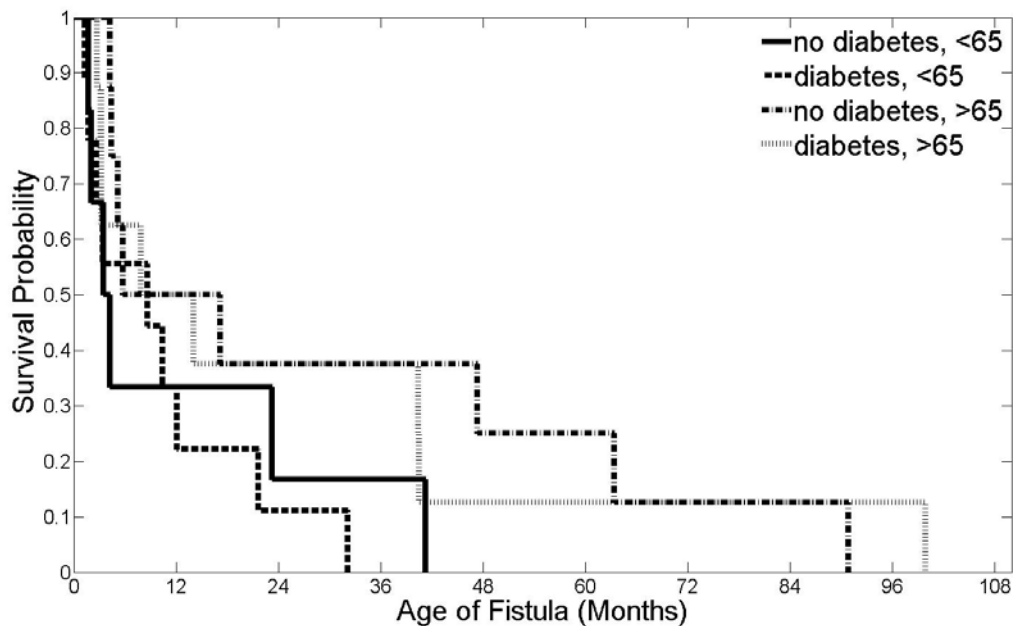


Figure 3.6: Kaplan Meier Survival Analysis for each patient group

3.4 Discussion

Despite the radiocephalic fistula being the preferred choice of access, its long term use is still plagued by a wide range of complications which usually require intervention and can occasionally leave the access unsalvageable [15, 23].

Thrombosis as a result of reduced blood flow or stenotic lesion rupture is the most common complication in haemodialysis patients [1, 2] and is more common in older fistulae [153]. While no episodes of thrombosis occurred in patients in this study, stenosis was the most common complication accounting for 37/39 (95%) of incidents in 30/31 (97%) patients. This reflects the routine fistula screening conducted for this cohort of patients that aimed to minimise the risk of thrombosis through the use of planned intervention on stenosis development. Konner [154] reported similar results, where an emergency intervention to correct for thrombosis occurred in 31.8% of patients with an AVF, whilst 66.4% chose to have an elective revision to correct a developing stenosis before thrombosis occurred that would have left the fistula unusable.

This study found that elderly patients with and without diabetes had longer use of their fistulae before requiring an intervention. Furthermore, the effects of age and diabetes were not found to be statistically significant, indicating that vascular health was not a primary factor in predicting late AVF failure in this cohort. This finding is supported by other studies that have also reported no statistical relationship between these comorbidities and AVF patency [21, 33, 155]. To remove the influence of previous access on vascular health, this study was designed so that only patients with a radiocephalic fistula were selected. As this is the most distal access, only elderly and diabetic patients with good vascular health would have been

selected to receive this type of fistula, which places a level of bias in the data. Conversely, radiocephalic fistulae have been shown to have higher one and two year patency rates in patients younger than 65 years old, which indicates that other factors may also influence AVF survival [156]. Vessel diameter before AVF creation in particular has been shown to have a strong statistical relationship to AVF survival [6, 42, 145]. This result, which manifests from the controls used in this study emphasises that elderly or diabetic patients should not be discarded for radiocephalic fistula creation based on these comorbidities, as other variables such as blood vessel diameter may be more influential.

Interestingly, patients with diabetes whom are younger than 65 showed the poorest fistula survival. This result mimics our observation above, in that vascular health is not a primary factor in predicting late AVF failure. On the other hand, the result may manifest from a bias due to the controls for vascular health, as young diabetic patients may have poorer vascular health due to the expression of the disease at an early age. This observation echoes the findings of others whom report poorer long term vascular access survival in diabetics [154]. At the other end of the spectrum, the data showed that elderly patients whom were also diagnosed with diabetes outperformed their counterparts without diabetes. This may be attributed to the age difference (5 years) between both groups of elderly patients. This result indicates that the effects of diabetes on vascular health manifest at various severities and are dependent on the age of the patient. This implies that vascular health should not be a primary factor in patient selection for radiocephalic fistula creation.

An interesting trend present in all groups was the high failure rate within the initial six months of fistula use, with approximately 50% of patients requiring an intervention. Several studies have identified a higher risk of AVF failure in the period following its creation [6, 56], with one month primary patency

rates reported to be as low as 57.6% [157]. However, interventional measures can mitigate these initial problems, where secondary patency rates above 80% have been reported following balloon fistuloplasty and stent placement [29]. This result emphasises the importance of frequent monitoring within the first six months of cannulation as the risk of developing complications during this period is higher.

The anastomosis was the most common location for stenosis, accounting for 49% of incidents, whilst 38% occurred at the outflow segment. Similar figures have been reported in radiocephalic fistulae with 49% of cases forming at the anastomosis and 45% in the outflow segment [27]. Intimal hyperplasia is the primary process leading to stenosis in haemodialysis patients and develops under a complex pathway which is not yet fully understood [3, 6]. Possible mechanisms of activation include surgical injury [58], oxidative and inflammatory stress [158] or the most popular theory, which suggests morphological changes occur in the blood vessel under changed flow conditions following AVF creation [4]. Several studies have shown a relationship between disturbed flow and stenosis formation at the anastomosis of AVFs and AVGs [42, 56, 145]. However, the disturbed flow generated within the AVF has been shown to dissipate in the venous outflow segment [145]. This study measured a high incidence of stenosis in the outflow segment, which has also been reported by others [27, 28, 33]. This high incident rate indicates the potential damage exerted on the blood vessel after the introduction of the needles in the AVF circuit.

Cannulation technique has previously been shown to influence AVF survival [124]. To ascertain the influence of cannulation on AVF survival, the related haemodynamic clinical variables of arterial pressure, venous pressure, blood flow rate, maturation time and frequency of dialysis sessions were measured. Pressure in the arterial and venous lines measure resistance at the needles and can be used to identify underlying stenosis within the fistula [85, 124].

Clinical practice guidelines for vascular access recommend that pressure in the arterial line should not fall below -250 mmHg as this can decrease the delivery of blood to the dialyser, thereby decreasing the efficiency of the treatment [10]. It has also been reported that haemolysis can occur at arterial pressures lower than -150 mmHg [159]. The blood flow rate is set by the clinician and determines the treatment time and filtration efficiency whilst the pressure is a function of vascular resistance (ability to withdraw and return blood to the fistula). The arterial operating pressures in the AK200S Gambro dialysers were set to -100 mmHg to -200 mmHg, whilst the venous operating pressures were set at 100 mmHg to 200 mmHg. The machine will alarm if the pressure falls beyond this range, indicating increased resistance in supplying blood to the dialyser. The data showed that fistulae which had a better survival rate were associated with lower arterial pressures around -140 mmHg, although this was not considered statistically significant.

Conversely, a significant statistical relationship was found between lower venous pressures (110 mmHg) and a lower survival rate. Higher risk of failure has been reported when venous pressures exceeded 150 mmHg or fell below 100 mmHg [124]. This trend may manifest from the intimal thickening occurring in the drainage vein. This process changes the morphological structure of the blood vessel wall, resulting in an increase in the number of smooth muscle cells which intrinsically decreases the compliance, hereby increasing the resistance of the circuit. Hence, patients who have been dialysing for a short time will have a lower vascular resistance. The standard least-squares regression analysis showed a similar trend in arterial and venous pressure, with a more dynamic variation in the early life of the fistula. The average pressures recorded in this study still fall within the safe operable limits, despite the transient change in pressures. In particular, the standard least-squares regression analysis showed that the arterial and venous pressure changes were minimal after the first 12 months. As these pressures can be used to indicate underlying

stenosis, the operating limits should be monitored frequently, especially within the first year of dialysis.

Fistula maturation time was found to be slightly higher in fistulae that survived longer although this finding was not significant. Guidelines recommend that fistulae be allowed one month to mature before cannulation [10], whilst others have indicated that the AVF can theoretically be used 14 days after creation [103, 104]. These dynamic fistula conditions are further demonstrated in the standard least-squares regression analysis which identified a greater range of arterial and venous pressures in early fistula use. Furthermore, these pressures were shown to continually change over the life of the fistula, emphasising the continual maturation process of the vein. This study indicates that a longer maturation time, of up to 6 months, when clinically feasible, may be beneficial for access survival, as it allows the fistula more time to adapt to the new haemodynamic conditions and reduces the trauma of cannulation.

Previous studies have shown that high blood flow rates in haemodialysis produces high levels of turbulence and shear stresses in the range reported to cause endothelial damage, which can initiate mechanisms leading to intimal thickening [7, 48]. This contradicts the results in this study, where flow rates below 300 ml/min were statistically related to fistulae that failed within the first 500 days. Similar findings have been reported in patients with blood flows below 310 ml/min, where the higher risk of failure was attributed to the underlying complications that limited the flow through the AVF, thus making the required flow rates unattainable [160]. A similar bias may also have occurred in this study. Furthermore, as mentioned previously, patients begin dialysis on lower flow rates to minimise the initial trauma. The standard least-squares regression analysis highlighted this standard practice rather than indicating failure, as fistulae that failed early

inevitably used lower blood flow rates whilst fistulae that survived longer were consistently dialysed at flow rates between 300-360 ml/min. This subsequently places a bias towards lower blood flow rates in fistulae that fail soon after cannulation begins. The effects of excessively high or low blood flow rates on fistula survival cannot be addressed in this study as all flow rates remained within standard clinical limits.

A statistical relationship was also found in patients who dialysed more frequently. However, the standard deviation was small in all groups, where patients received dialysis on average every 2-3 days. This follows standard practice and likely manifests from the low power in the analysis, which is a limitation of this study and therefore this result is deemed negligible.

3.5 Limitations

The main limitation of this study was the small number of available patients due to the specific controls used. Hard control points were used to isolate the effects of cannulation (successful primary maturation, no history of previous access, only examining patients with radiocephalic fistulae) which limited the number of applicable patients to the study. These controls were necessary to specifically analyse the modalities of late failure, removing the influence of secondary complications from interventions or previous access. Data was simply not available for patients with long term fistula use (>8 years with no major complications) as such patients are extremely rare. Data pertaining to each cannulation session was also limited to the variables collected during standard practice.

An ANOVA test was used to test for differences between groups, which requires the assumption of a normal distribution. Although the patient numbers in each group were small, the number of sample collections for the

two patients whose fistula functioned the longest without a complication were high and a normality test conducted on the raw data for these two patients revealed a normal distribution. Furthermore, Type 1 errors are common if t-tests are run multiple times on the same data, as would be the case in this study. ANOVA was chosen to remove the chance of a Type 1 error occurring in the analysis.

3.6 Conclusion

Haemodialysis patients have a high risk of late fistula failure, with the most common complication observed in this study being stenosis at the anastomosis and outflow segment. The risk of failure is elevated within the first six months as the fistula adjusts to dialysis conditions, indicating the importance of routine screening for vascular complications during this time. Diabetes and age were not statistically related to late failure indicating that these patients should not be discarded for radiocephalic fistula. While arterial and venous pressures reflect the vascular resistance of the dialysis circuit, no model to predict failure based on blood flow rate or arterial and venous pressures was established. Vascular resistance was found to change over the life of the AVF, which signifies that operating pressures should be monitored frequently, especially within the first year of dialysis as the fistula adapts to dialysis treatment. Finally, a maturation time of up to six months may reduce the trauma of cannulation, highlighting the importance of advanced access planning in renal failure patients.

Chapter 4

Experimental Study of Cannulation Technique: Methods

This chapter details the design and specifications of the optical bench top flow rig used to validate the computational models. Specifics of the experimental setup, blood analog fluid and stereo-PIV processing methodology are explained. An analysis of the experimental errors is also provided.

4.1 Introduction

Particle image velocimetry is an effective tool for measuring high speed flows instantaneously without intruding on the flow field. As such, this method has been used to investigate jet turbulence and vortices [161, 162], and has also been extended to measure physiological flows using bench top flow models of aneurysms [163] and stents [164]. Studies focusing on jet dynamics have

identified four distinct regions of the flow field for an impinging jet model: the potential core, impingement region, impingement boundary layer and the wall jet region [165].

The characteristic regions of the impinging jet and its interaction with the wall and subsequent turbulent structures is a key area of focus in jet dynamic studies [166–169]. The impingement point is a focal point at which the impinging jet transforms into a wall jet. A large reduction in momentum also occurs when a jet impinges on a surface which can lead to complex flows. Rajaratnam et al. [169] found that turbulence within the jet near the location of impingement diminishes and deduced that this could aid in the initiation of erosion. Vaishnav et al. [62] displayed this effect with an impinging jet onto ex-vivo thoracic aorta from dogs. A limitation in extending these findings is that these studies were conducted at Reynolds numbers much larger than found in-vivo and for an impingement normal to the boundary, while an impinging jet at incidence for low Reynolds numbers is more relevant to the flow field produced by the venous needle jet (VNJ). The main features of the impinging VNJ are displayed in Figure 4.1.

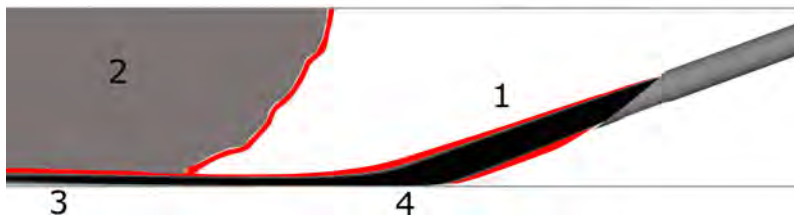


Figure 4.1: Features of the impinging VNJ including: free stream jet (1), recirculation zone (2), wall jet (3) and impingement zone (4). Regions in red show the boundary layer between the various flow zones

The flows produced by the AN may also influence endothelial function and subsequent intimal thickening. Little research has investigated the flows around the AN, setting a requirement for the work in this chapter. Instead,

research has focused on the design of cannulas to improve their ability to extract blood without damaging blood cells. Mareels et al. [114] used PIV to validate various designs of cannula tips using computational models. The direction of flow through the cannula bore and side holes was optimised to reduce WSS and particle residence time, in order to reduce the risk of thrombosis. De Bartolo et al. [118] had a similar approach using flow sensors and pressure transducers to validate the numerical models. Disturbed flow regions were measured around the cannula tip as blood was extracted from the vein, which may contribute to thrombosis formation. These studies imply that similar disturbed flow regions may exist around the AN, however it is unknown if the disturbed flow extends to the walls of the blood vessel.

The aim of this chapter is to investigate the three dimensional flow structures produced by the VN and AN under normal haemodialysis conditions using stereoscopic particle image velocimetry (S-PIV). These results will provide validation for the subsequent computational models used in Chapter 6. An idealised model of haemodialysis cannulation with constant flow conditions is utilised with a blood analogue fluid with different needle flow rates, needle positions and insertion angles tested to cover the range of normal haemodialysis conditions.

4.2 Experimental Methods

4.2.1 Bench Top Flow Rig

An idealised model of haemodialysis cannulation was constructed from poly(methyl methacrylate) (PMMA). The outflow vein was modelled as a simple cylinder with the needle placed at an angle. Two in-house designed

piston pumps were used to deliver continuous constant flow through four solenoid valves. A stepper motor was used to drive the pump and an encoder was used to control the position of the piston. Air traps and bleed valves were employed to remove bubbles in the system which can cause errors from reflections produced by the laser. The fistula pump is shown in Figure 4.2 with the key parts labeled.

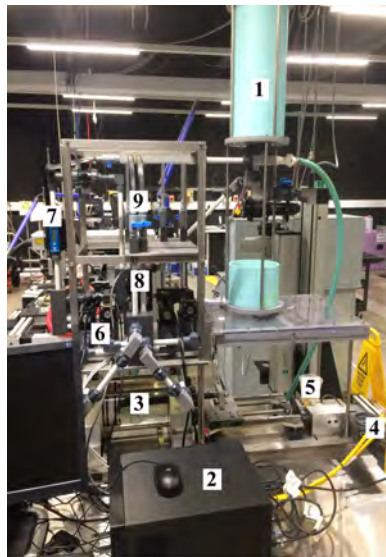


Figure 4.2: Fistula pump used in the experiments. 1) Reservoir 2) Control unit 3) Cylinder and piston 4) Stepper Motor 5) Encoder 6) Four solenoid valves 7) Atrato Ultrasonic flow meter 8) MRC22 PT100 pressure transducer and Monel Thermowell PT100 temperature transducer 9) Bleed system

The flow and pressure produced by the pump were monitored using an Atrato Ultrasonic flow meter (Titan Enterprise Ltd, Dorset, United Kingdom) and an MRC22 pressure transducer (MeasureX Pty Ltd, Melbourne, Australia). The flow remained within 1.16% of the set value whilst the pressure varied less than 13.95% of the mean as displayed in Figure 4.3 and Figure 4.4. Variability in pressure and flow is due to friction from the piston pump and pressure losses produced by the air bleed system.

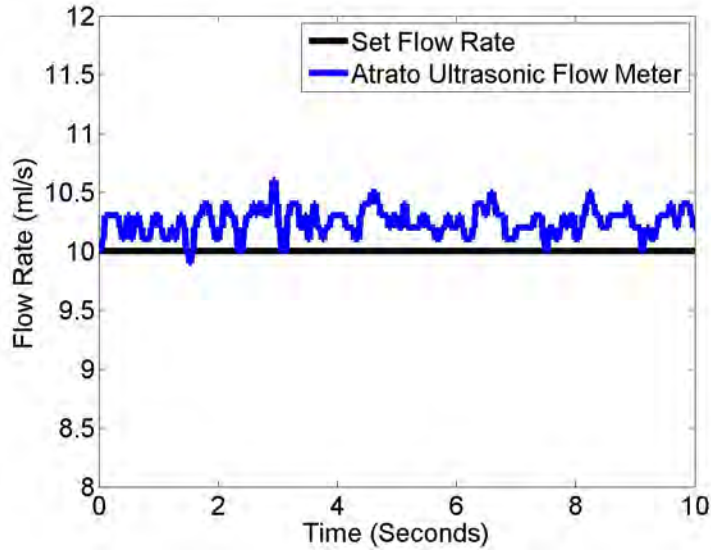


Figure 4.3: Flow meter data (measured at the outlet of the pump) from one cycle of the fistula pump

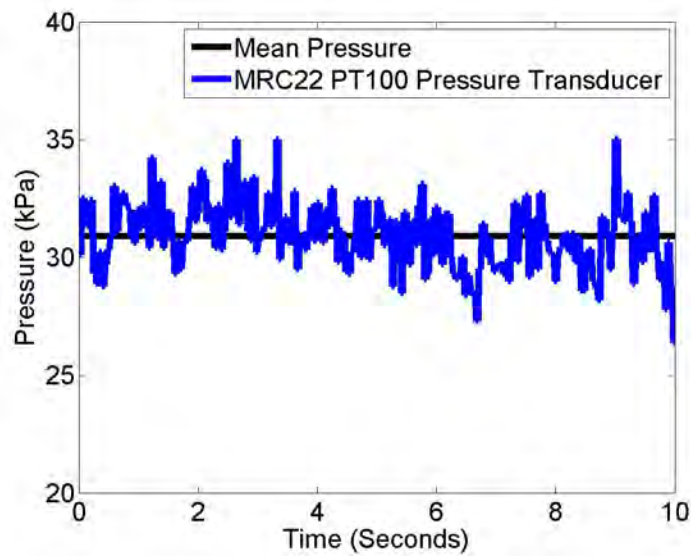


Figure 4.4: Pressure data (measured at the outlet of the pump) from one cycle of the fistula pump

The laser was mounted on a single axis micrometre traverse system whilst the cameras were mounted on a three axis motorised traverse (LaVision GmbH, Goettingen, Germany) with a precision up to 0.1 mm. The experimental flow rig, laser system and cameras were mounted on self-leveling feet which also dampened the vibrations produced by the pump as displayed in Figure 4.5.

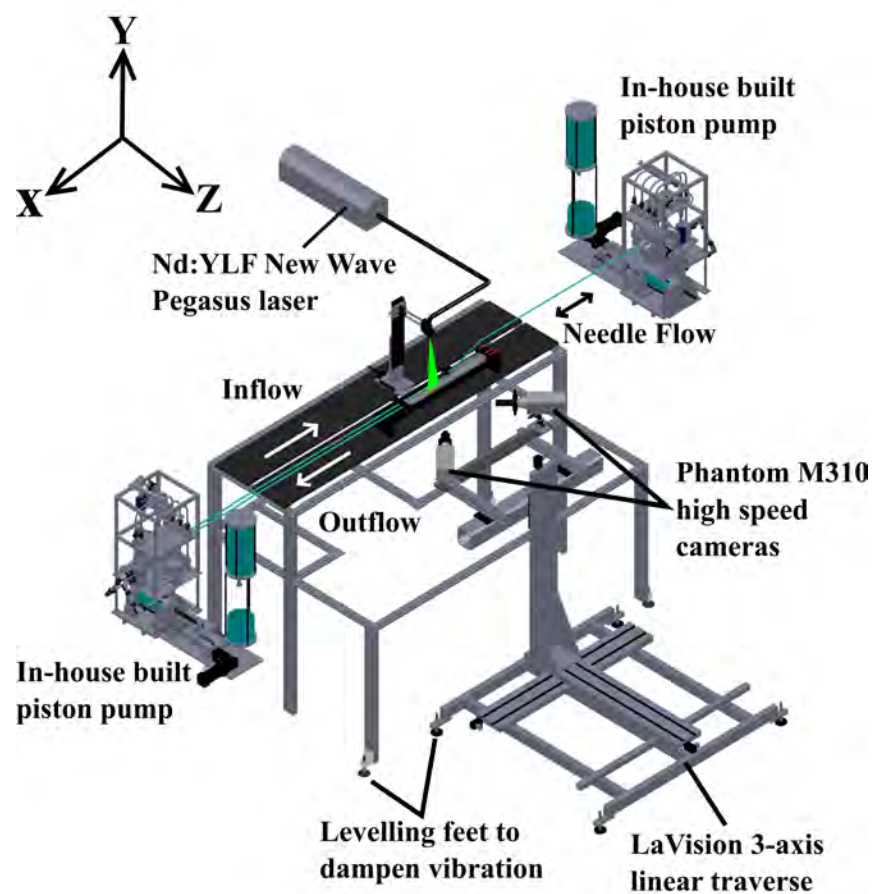


Figure 4.5: Experimental Setup

The diameter of the vein is scaled (by a factor of two) to 20 mm (D), with the downstream portion extended to $20D$ to prevent any back pressure from affecting the flow around the needle and the upstream portion is extended $50D$ to ensure fully developed flow before the needle. Only a single needle was examined so the flow field could be viewed in isolation as shown in the schematic in Figure 4.6.

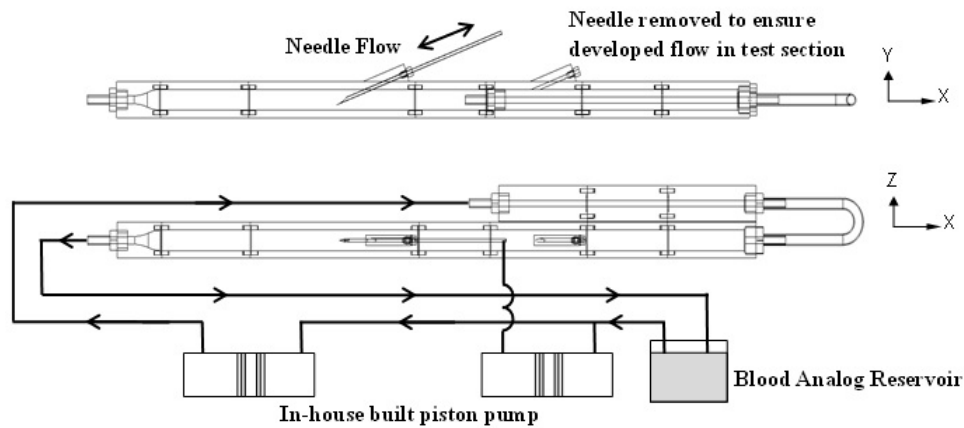


Figure 4.6: Schematic of the Experimental Setup

Figure 4.7 shows the needle placed within the PMMA block. The locating pins are displayed, as well as the mechanism (nut and ferrule) used to seal the needle within the rig. The locating pins were placed at two corners of each block and allowed the modular units to form a continuous smooth test section. The ferrule formed a tight seal around the needle body when the nut was screwed in which minimised leaking and maintained a sealed environment within the rig.

The twice scaled needles were manufactured from 10G stainless steel tubing with an inner diameter of 2.692 mm (d) and outer diameter of 3.404 mm. The scaling was based on standard 15G needles commonly used in clinical practice, which have an inner diameter of 1.372 mm and outer diameter of

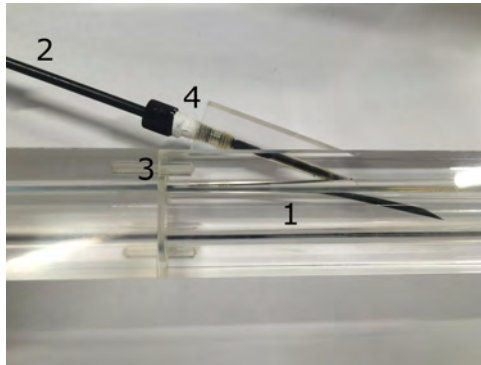


Figure 4.7: Needle placed within the PMMA block. 1) Vein 2) Needle 3) Locating Pin 4) Nut and Ferrule

1.830 mm. The scaled needle also contained a back eye with position and dimensions displayed in Figure 4.8.

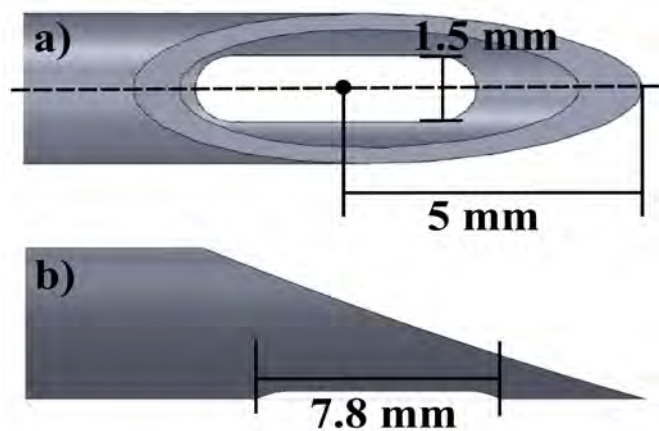


Figure 4.8: Back eye dimensions in the scaled 10G needle

The rig was designed in modular blocks and sealed with o-rings to test a range of parameters. Needle angles of 10° , 20° and 30° were tested whilst the position of the needle bore was also shifted to sit within the centre and in the upper and lower thirds of the vein. Standard haemodialysis blood flow rates of 200 ml/min, 300 ml/min, 400 ml/min were forced through the needle whilst a constant flow rate of 666 ml/min was pumped through the venous

circuit, providing the core flow. For the three tested parameters (needle flow rate, needle angle, needle position), there were three separate variables, which constituted nine different cases per needle as displayed in Table 4.1. The arterial needle was examined in the antegrade and retrograde orientation whilst the venous needle was placed in the antegrade position, conforming to standard practice.

Table 4.1: Parameters and variables of all test cases. Blood flows are listed as physiologically equivalent (not scaled)

Parameter	Variable	Constants
Needle Flow Rate	200 ml/min	20°
	300 ml/min	Middle
	400 ml/min	
Needle Angle	10°	300 ml/min
	20°	Middle
	30°	
Needle Position	Top	300 ml/min
	Middle	20°
	Bottom	

4.2.2 Dimensional Scaling

Dynamic similarity was achieved by scaling the diameters of the needle and vein by a factor of two whilst maintaining Reynolds number, defined as:

$$Re = \frac{\rho U D_h}{\mu} \quad (4.1)$$

where ρ is the density, U is the average velocity through the pipe, D_h is the hydraulic diameter and μ is the dynamic viscosity.

It was assumed that blood behaves as a Newtonian fluid under the high shear rates created by the needle and core flow, and that the density and dynamic viscosity of blood is 1045 kg/m^3 and $0.0035 \text{ Pa}\cdot\text{s}$ respectively. The resultant flow rates are displayed in Table 4.2 with their associated Reynolds numbers.

Table 4.2: Summary of flow rates and Reynolds numbers after dimensional scaling

Inlet Type	Physiological Flow Rate (ml/min)	Scaled Flow Rate (ml/min)	Reynolds Number
Vein	654	666	740
Needle	200	291	924
Needle	300	436	1385
Needle	400	581	1847

4.2.3 Blood Analogue Fluid

A blood analogue fluid was used which contained a mixture of aqueous sodium iodide (76.5 %) and glycerol (23.5 %). Sodium thiosulfate (0.1 % w/w) was added to minimise the effects of discolouration which occurs when the test fluid contacts UV light. The ratio of this mixture was controlled to match the refractive index of the PMMA (1.49), which minimised any light distortion occurring at the fluid-solid interface. A Cannon-Fenske viscometer (Cannon Instrument Company, Pennsylvania, USA) was used to monitor the viscosity of the blood analogue during mixing. The subsequent test fluid has a dynamic viscosity of $0.00706 \text{ Pa}\cdot\text{s}$, which is within the range of blood viscosity ($0.01\text{-}0.08 \text{ Pa}\cdot\text{s}$), and a density of 1652 kg/m^3 at 20°C . The viscosity of the test fluid was not able to be matched to that of healthy blood ($0.0035 \text{ Pa}\cdot\text{s}$), as this was unachievable with the ratio of the constituents whilst also matching the refractive index, which was the main criteria.

The test fluid was seeded with spherical fluorescent polymer particles made from PMMA labeled with Rhodium B. The particles were seeded at a concentration of approximately 5 mg/L based on the work by Melling [170]. The largest particle diameter allowable for optimal flow tracking was calculated based on Stokes number (Stk), defined as:

$$Stk = \frac{\rho d_p^2 V}{18\mu D} \quad (4.2)$$

where d_p is the particle diameter and V is the maximum velocity through the pipe. The particle is unaffected by the fluid velocity when $Stk < 1$. Approximating the maximum velocity in the VNJ as 3 m/s, the maximum particle diameter is:

$$d_p^2 = \left(\frac{18\mu D}{\rho V} \right) Stk \quad (4.3)$$

$$d_p^2 = \left(\frac{18 \times 0.00409 \times 0.02}{1652 \times (10^3) \times 3} \right) \times 1$$

$$d_p = 16.19 \mu m$$

Subsequently, particles with a mean diameter of 10 μm (range: 1-20 μm) and density of 1190 kg/m^3 were used to obtain optimum light scattering and particle tracking. The fluid was seeded at a concentration of 0.1% V/V based on the work by Melling [170]. All experiments were conducted in a controlled environment at 20°C to maintain constant viscosity across measurements. A Monel Thermowell PT100 temperature transducer (Pyrosales Pty Ltd, Sydney, Australia) was placed at the inlet and outlet of the pump system and confirmed that the temperature remained constant over a 4 hour operating period.

4.2.4 Stereo-PIV Setup

The S-PIV system consists of two Phantom M310 high speed cameras of $1280 \times 800 \text{ pixels}^2$, and an Nd:YLF New Wave Pegasus laser (New Wave Research, California, USA) with a wavelength of 527 nm and 10 mJ of energy. The laser was situated to illuminate particles on the x-y plane along the centre of the rig as depicted in Fig 4.9.

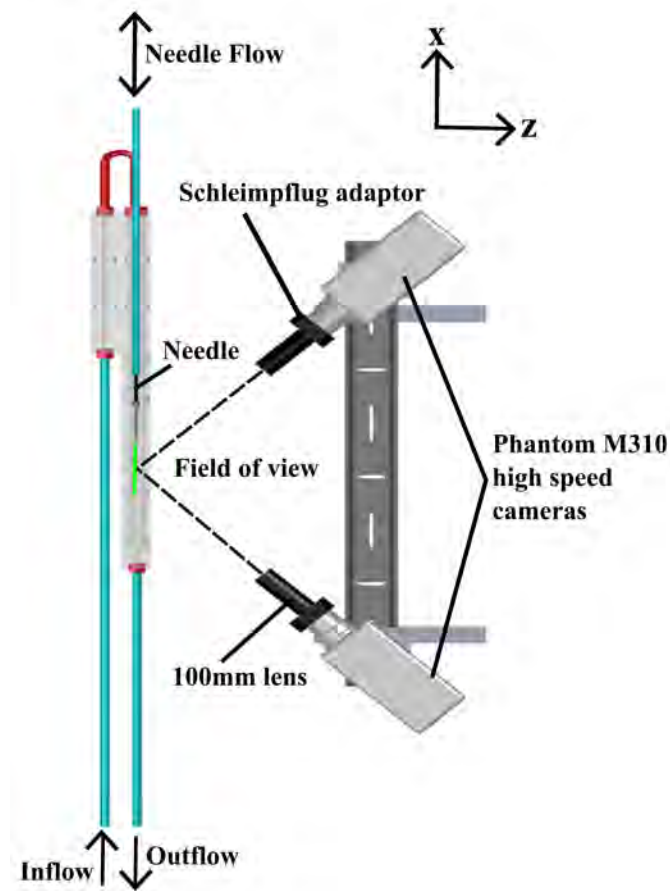


Figure 4.9: Camera Setup

To capture the three components of velocity two cameras were placed on the same plane at incidence to the laser sheet. Utilising two cameras enables particle motion tracking on the laser sheet in the x-y plane, as well as out of plane motion in the z-direction. The S-PIV method matches the two views from each camera to reconstruct the three components of the velocity vector. The general schematic of the S-PIV technique is displayed in Figure 4.10.

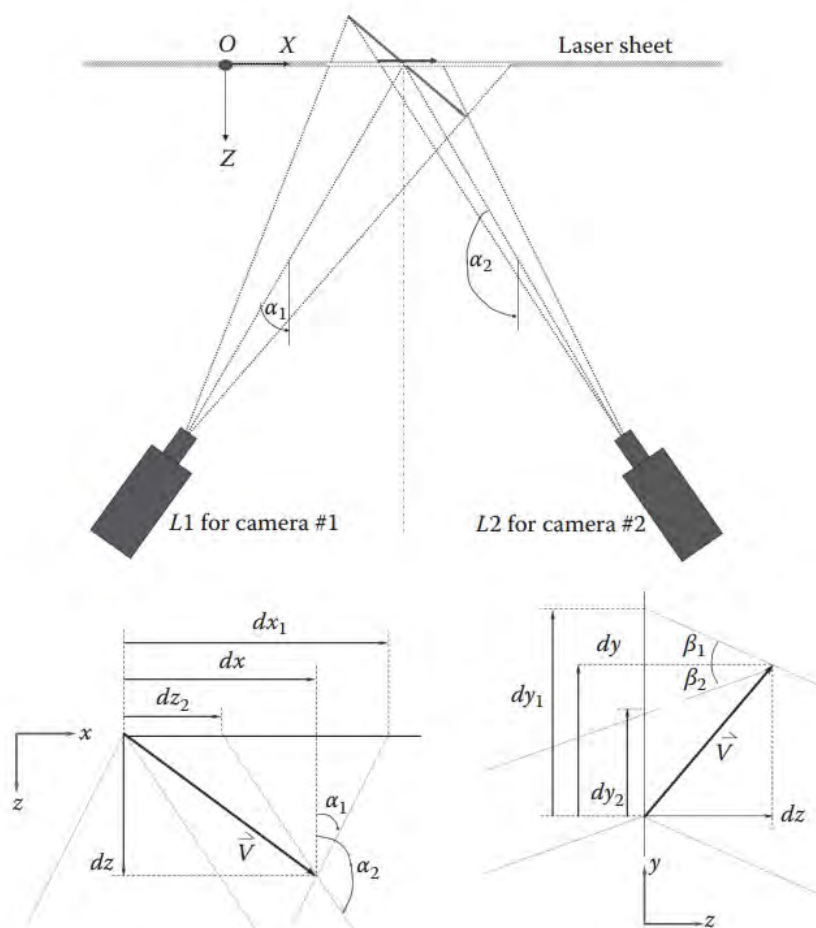


Figure 4.10: Schematic for the reconstruction of three components of the velocity vector for stereoscopic PIV measurements [171]

The origin represents a point visible by both cameras, whilst the location of the cameras is denoted as $L_1 (x_1, y_1, z_1)$ and $L_2 (x_2, y_2, z_2)$. The measurement displacement on the laser sheet is (dx_1, dy_1) and (dx_2, dy_2) . The angle on the x-z plane created by the reflected light in relation to the z-plane is α_1 and α_2 . The angles β_1 and β_2 are similar but lie on the y-z plane. The three components of the velocity vector can therefore be calculated using the following equations:

$$dx = \frac{dx_2 \tan \alpha_1 - dx_1 \tan \alpha_2}{\tan \alpha_1 - \tan \alpha_2} \quad (4.4)$$

$$dy = \frac{dy_1 + dy_2}{2} + \frac{dx_1 + dx_2}{2} \left(\frac{\tan \beta_2 - \tan \beta_1}{\tan \alpha_1 - \tan \alpha_2} \right) \quad (4.5)$$

$$dz = \frac{dy_2 - dy_1}{\tan \beta_1 - \tan \beta_2} \quad (4.6)$$

However, this setup will induce focusing issues because the lens plane is not parallel to the image plane. To satisfy this condition, also known as the Scheimpflug condition, a Scheimpflug adaptor is used which tilts the image sensor plane as shown in Figure 4.11

The cameras were mounted at an angle of 30° to the laser sheet to minimise the error in the three component velocity calculations [172]. A Nikkor 105 mm lens was attached to the cameras with an aperture of f/2.8 to capture the region of interest and allow sufficient light to accurately track the illuminated particles. The depth of field (DOF) is calculated using the following equation:

$$DOF = FP - NP \quad (4.7)$$

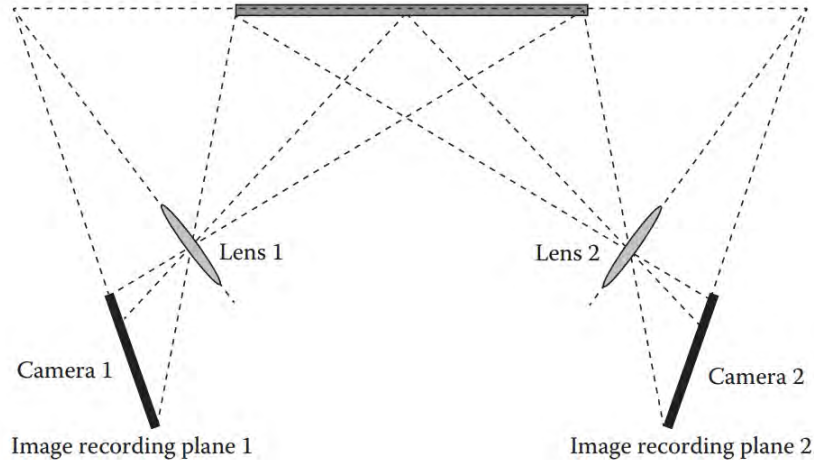


Figure 4.11: Angle displacement arrangement of the Scheimpflug condition [171]

where FP is the far point and NP is the near point defined by:

$$NP = \frac{H_f L F_d}{H_f L} + (F_d - F_L) \quad (4.8)$$

and

$$FP = \frac{H_f L F_d}{H_f L} - (F_d - F_L) \quad (4.9)$$

where $H_f L$ is the hyperfocal length, F_d is the focal distance and F_L is the focal length of the camera.

The hyperfocal length is defined as:

$$H_f L = \frac{F_d^2}{Aperture \times CoC} \quad (4.10)$$

where CoC is the circle of confusion and is calculated using the Ziess formula as follows:

$$CoC = \frac{\text{diagonal length of camera sensor}}{1730} \quad (4.11)$$

The Phantom M310 high speed cameras have a sensor size of 25.6×16 mm. Therefore the circle of confusion is:

$$CoC = \frac{30.2}{1730} \quad (4.12)$$

$$CoC = 0.017 \text{ mm}$$

The hyperfocal length is therefore:

$$H_f L = \frac{105^2}{2.8 \times 0.017} \quad (4.13)$$

$$H_f L = 225,645 \text{ mm}$$

The near point and far point are subsequently 499.126 mm and 500.877 mm, respectively and the depth of field is calculated to be 1.75 mm.

The laser sheet was focused to an approximate thickness of 2 mm, indicating that most of the laser sheet remains in focus. Care was taken during camera focus to ensure that the centre of the laser sheet was in focus providing maximum illumination of the particles. The camera and laser setup is shown in Figure 4.12 with the key parts labeled.

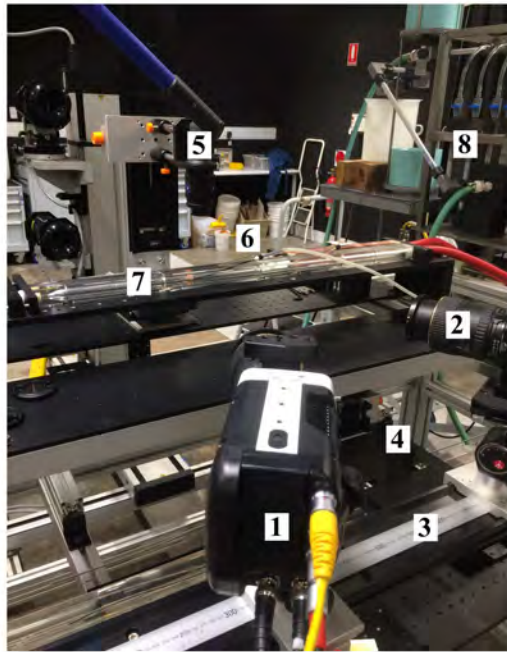


Figure 4.12: Laser and camera setup for stereoscopic particle image velocimetry measurements. 1) Phantom M310 high speed camera 2) Nikkor 105 mm lens 3) Mounting on traverse system 4) 058-5 calibration plate 5) Laser head to the Nd:YLF New Wave Pegasus laser 6) Needle 7) PMMA Rig 8) Pump

Double frame images were captured in four downstream sections along the x-axis for the VN case so that the VNJ and resultant disturbed flows could be properly imaged, whilst the AN in antegrade was captured in two downstream sections as the flow field was smaller. The camera sections for each needle configuration are displayed in Figure 4.13. The presence of the needle blocked the laser sheet and prevented imaging in the downstream portion of the AN placed in retrograde. Instead, the portion around the needle tip was imaged in two upstream sections. Due to the unsteadiness of the flow field, a slight mismatch in the contour plots occurs along the border of each section. This feature is unavoidable when presenting the entire flow domain produced by the needles.

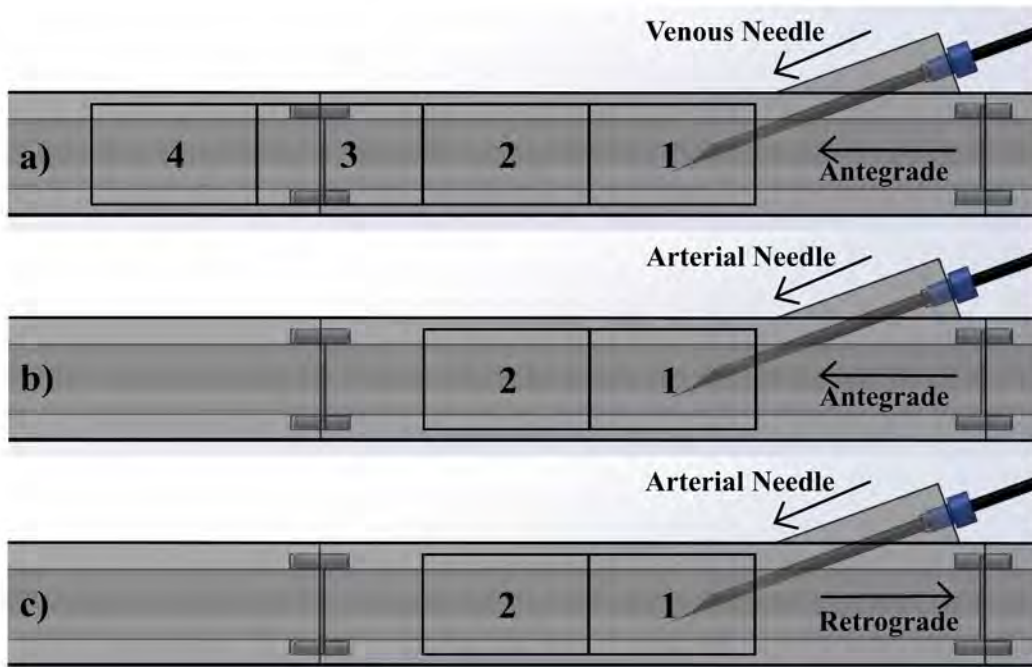


Figure 4.13: Schematic displaying the sections captured around the needle. a) Venous needle b) Arterial needle in antegrade c) Arterial needle in retrograde

The pulse separation and trigger rate were adjusted for each section due to the dynamic range of velocities in the flow field. The pulse separation and trigger rates were calculated on the condition of achieving a particle displacement of $1/4$ of the interrogation window based on the work by Raffel et al. [173]. The pulse separation and trigger rate for the VN and AN are displayed in Table 4.3 and Table 4.4; respectively.

For every case 400 double frame images were captured by each camera to ensure repeatability in measurements, as discussed in Section 4.3.5. All processing was conducted using DaVis 8.2 (LaVision, Goettingen, Germany). Raw images were preprocessed using a high pass filter function which subtracted the average background light intensity from each image,

Table 4.3: Summary of pulse separation time and trigger rates for each section and flow rate of the venous needle. Blood flows are listed as physiologically equivalent (not scaled)

Section	Needle Flow Rate (ml/min)	Pulse Separation (μ s)	Trigger Rate (kHz)
1	200	180	1
	300	100	1
	400	80	1
2	200	270	1
	300	180	1
	400	120	1
3	200	900	0.5
	300	550	0.5
	400	390	0.5
4	200	2500	0.2
	300	2500	0.2
	400	2500	0.2

Table 4.4: Summary of pulse separation time and trigger rates for each section and flow rate of the arterial needle. Blood flows are listed as physiologically equivalent (not scaled)

Section	Needle Flow Rate (ml/min)	Pulse Separation (μ s)	Trigger Rate (kHz)
1	200	2500	0.2
	300	2500	0.2
	400	2500	0.2
2	200	2500	0.2
	300	2500	0.2
	400	2500	0.2

which produced a consistent intensity between all images and reduced the effects of reflections on the surface of the rig and needle. An algorithmic mask was applied in conjunction with a geometric mask to further minimise the effects of reflections. An adaptive multi-pass cross-correlation algorithm

was utilised, where the size of the interrogation window was iteratively adjusted from an initial interrogation window of 48 X 48 pixels to a final size of 24 X 24 pixels with a 50% overlap. This algorithm was used to measure the velocity gradients created between the VNJ and core flow. No vector post processing was conducted to ensure a realistic estimate of the true velocity was calculated.

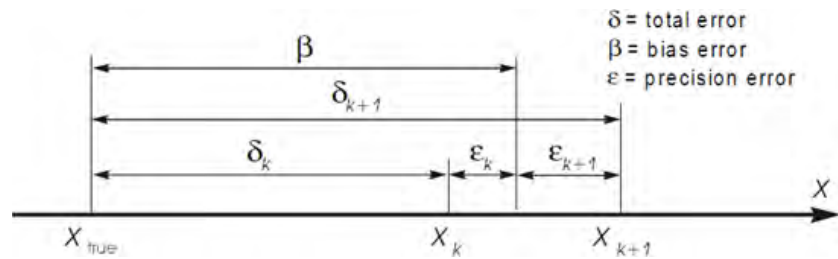
Results are presented as contours of out of plane velocity (z-direction) with normalised vectors superimposed to show the direction of flow and its three dimensional nature. Measurements from the different regions were stitched together using Inkscape (Inkscape, New York, United States) to show the entire flow domain for both the AN and VN. Velocity profiles are also presented to show the influence of the flow entering and exiting the needles.

4.3 Experimental Uncertainty

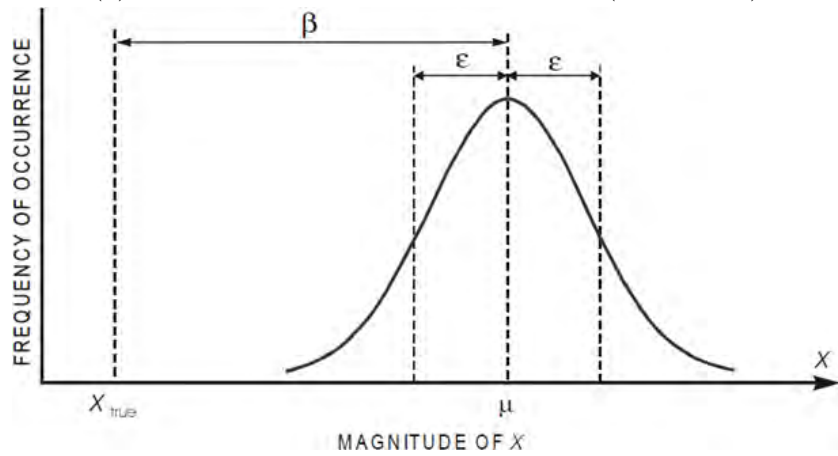
4.3.1 Methodology

The total error within an experiment can be quantified as the combination of a precision (random) error which contributes to the scatter of the data and a bias (systematic) error which is dependent on the experimental setup. Bias errors remain consistent regardless of the number of measurements, whereas precision errors are dependent on the number of measurements taken, as displayed in Figure 4.14.

Measurement of the experimental uncertainty (to 95% confidence) in this thesis is based on Coleman and Steele [174], using the thesis by Stanley [175] as a guide. The total error is estimated where the precision and bias error



(a) Uncertainty with two measurements (k and k+1)



(b) Uncertainty for an infinite number of measurements

Figure 4.14: Uncertainty comprised of precision and bias errors [174]

of the individual variables within the experiment is accounted for using the data reduction equation:

$$r = r(X_1, X_2, \dots, X_i) \quad (4.14)$$

where r is the experimental result determined from i measured variables X_i . The total uncertainty (U_r) can then be estimated as the root sum square of the bias and precision errors:

$$U_r = B_r^2 + P_r^2 \quad (4.15)$$

where B_r is the bias error and P_r is the precision error.

4.3.2 Bias Error

When the number of readings per sample is larger than 10 the bias error can be defined as:

$$B_r^2 = \sum_{i=1}^J \theta_i^2 B_i^2 + 2 \sum_{i=1}^{J-1} \sum_{k=i+1}^J \theta_i \theta_k B_{ik} \quad (4.16)$$

where θ_i is the sensitivity coefficient defined as:

$$\theta_i = \frac{\partial r}{\partial X_i} \quad (4.17)$$

and B_i is the bias error for variable X_i and B_{ik} is the correlated bias error for the correlated variables X_i and X_k . The correlated bias limit (B_{ik}) must be approximated as it is difficult to determine the covariance of the bias errors in multiple variables. The correlated bias limit is estimated as:

$$B_{ik} = \sum_{\alpha=1}^L (B_i)_\alpha (B_k)_\alpha \quad (4.18)$$

where L is the number of correlated bias error sources that are common for measurements of variables X_i and X_k . Correlated bias errors arise from different variables sharing a source of error, such as using the same calibration instrument or the same measurement device for a number of variables.

When several bias errors exist for an individual variable it is useful to

separate all sources into separate categories and estimate the bias within each category. The bias error for all sources can then be estimated as the root sum square of each category using:

$$B_i^2 = \sum_{k=1}^J (B_i)_k^2 \quad (4.19)$$

4.3.3 Precision Error

In engineering experimentation it is preferable to measure certain parameters numerous times to ensure statistical certainty. If a test is performed on M sets of measurements (X_1, X_2, \dots, X_J) an average result \bar{r} is calculated using:

$$\bar{r} = \frac{1}{M} \sum_{k=1}^M r_k \quad (4.20)$$

The precision error for a single result of the M measurements is:

$$P_r = tS_{\bar{r}} \quad (4.21)$$

where t is M-1 degrees of freedom and can be approximated as 2 if more than 10 measurements are taken ($M > 10$), and $S_{\bar{r}}$ is the standard deviation of the results defined as:

$$S_{\bar{r}} = \left[\frac{1}{M-1} \sum_{k=1}^M (r_k - \bar{r})^2 \right]^{\frac{1}{2}} \quad (4.22)$$

The precision error for the average result can therefore be calculated using:

$$P_{\bar{r}} = \frac{P_r}{\sqrt{M}} \quad (4.23)$$

However, sometimes making repeat measurements can be time consuming and costly. Therefore, when single measurements are conducted and the M set of measurements are measured over an appropriate time the precision error can be determined by:

$$P_r = tS_r \quad (4.24)$$

where t is the statistical coverage from the two tailed t-distribution and S_r is the standard deviation for N readings. The precision error can also be estimated as the root sum square of the elemental error source (if known), assuming no correlation exists with the precision uncertainties. This is defined by:

$$P_r^2 = \sum_{i=1}^J \theta_i^2 P_i^2 \quad (4.25)$$

where θ_i is the sensitivity coefficient defined above and P_i is the precision error for the variable X_i ($P_i = tS_i$).

A summary of the level of uncertainty to 95% confidence in each measured parameter is displayed in Table 4.5. A comprehensive uncertainty analysis for each measured parameter is attached in Appendix A. The low levels of uncertainty acknowledge the attention directed at constructing an accurate experiment.

Table 4.5: Summary of experimental uncertainty

Parameter	Nominal Value	Bias Error	Precision Error	Uncertainty	
				Value	%
Vein Diameter (mm)	20	0.005	0.122	0.122	0.608
Needle Diameter (mm)	2.692	0.005	0.048	0.048	1.777
Temperature ($^{\circ}$ C)	20	0.406	0.280	0.493	2.463
NaI Concentration %(w/w)	76.5	0.073	0.073	0.104	0.135
Viscosity (Pa.s)	0.00706	0.0002	0.0002	0.00028	3.901
Density (kg/m^3)	1651.65	14.166	15.687	21.137	1.280
Fistula pump piston velocity (m/s)	0.000858	0.0000293	0.0000111	0.0000313	3.652
Needle pump piston velocity (m/s)	0.0023	0.000076	0.00003	0.000082	3.539

4.3.4 PIV Error

The overall measurement accuracy of PIV is dependent on several aspects extending from the recording of the raw images to the statistical methods of evaluation. The error of a single displacement vector can be quantified as:

$$\epsilon_{total} = \epsilon_{systematic} + \epsilon_{residual} \quad (4.26)$$

where a systematic error arises due to the inadequacy of the statistical method in the cross correlation algorithm. An example of a systematic error is in application to flows with high gradients or in estimating the pixel intensity in an interrogation window. A residual error is the uncertainty in the measurement and exists even when systematic errors are removed. However, in practice it is difficult to separate these two forms of error. Following the statistical methods outlined above, the uncertainty in the PIV measurements is quantified using:

$$\epsilon_{total} = \epsilon_{bias} + \epsilon_{rms} \quad (4.27)$$

where the bias error quantifies the over or under estimation in the measurement and the rms error quantifies the random error in the PIV setup.

It is both expensive and difficult to quantify the uncertainty that exists in PIV for every single case. Therefore, the uncertainty in the PIV measurements in this thesis are based on the Monte Carlo simulations presented by Raffel et al. [173], which encompasses the raw effects of different variables in PIV and their influence on uncertainty in PIV. The

variables deemed to influence the total uncertainty in PIV include: perspective error from the lens, image distortion, particle image diameter, particle image displacement or shift, particle image density, variation of image quantisation, background noise and the variation of displacement gradients in the flow. A further error exists from the calibration process of the stereo PIV in relation to the Scheimpflug principle. The bias error from calibration is calculated automatically in the software using the pinhole calibration method and a standard 058-5 calibration plate (LaVision, Goettingen, Germany). The maximum bias from stereo PIV calibration was maintained below 1 pixel.

A summary of the uncertainty in each variable is displayed in Table 4.6. A comprehensive analysis of the uncertainty in each variable is attached in Appendix B. Great care was taken in the setup of the PIV experiments which is reflected in the results of the uncertainty. Furthermore, both the laser sheet and camera were mounted on micrometre traverses allowing repeatable measurements of the regions of interest up to ± 0.01 mm. A total uncertainty of 0.333 pixels was estimated in the PIV measurements based on the study by Raffel et al. [173]. For optimum PIV settings a 24X24 pixel window was used with a particle travelling approximately 8 pixels. Hence, the maximum estimated uncertainty in each measured displacement is approximately 1.333 pixels (16.7%). This uncertainty will be smaller for particles travelling outside the VNJ and the disturbed flows.

4.3.5 Repeatability

Velocity profiles were compared for a range of images in order to determine the required number of double frame images to achieve an accurate solution. Tests were conducted for the baseline case on the VN (300 ml/min, needle

Table 4.6: Summary of PIV uncertainty

Parameter	Bias Error	RMS Error	Uncertainty
Image distortion (pixel)	0	N/A	0
Particle image diameter (pixel)	N/A	0.05	0.05
Particle image displacement (pixel)	-0.02	0.05	0.03
Particle image density (pixel)	N/A	0.03	0.03
Image quantisation (pixel)	N/A	0.011	0.011
Background noise (pixel)	N/A	0.012	0.012
Displacement gradient (pixel)	N/A	0.2	0.2
Stereo Calibration (pixel)	1	0	1
	Total	(pixel)	8 +/- 1.333
	Total	(%)	16.7%

angle of 20° , needle tip in the middle of the vein). Figure 4.15 shows the velocity profile 5d downstream of the needle tip. The velocity profile remains very similar with the number of images ranging from 200-1000.

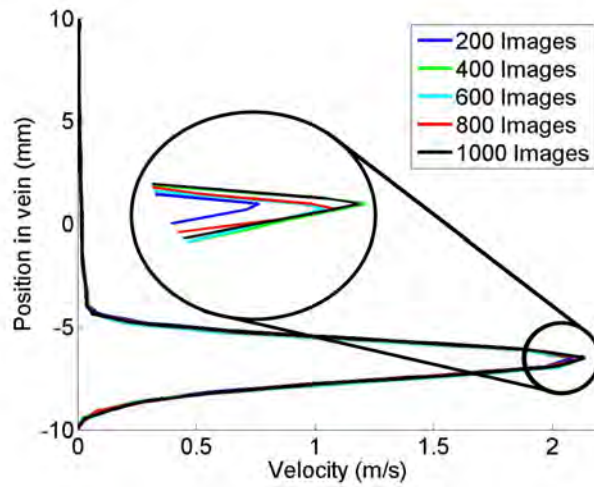


Figure 4.15: Convergence of the number of images required to achieve a repeatable time averaged result. Velocity profile measured 5d from the venous needle tip.

The maximum velocity in the jet was also measured. Figure 4.16 shows that the maximum velocity reaches a constant value when more than 400 double frame images are averaged. The percentage difference in the average and maximum velocity for 400 image compared to 200 images were $<0.1\%$ and $<1\%$, respectively. Comparatively the percentage difference between 1000 images to 400 images was insignificant, where the average and maximum percentage difference in velocity was 0.22% and 0.16% , respectively. Therefore, 400 images were captured in each experiment to ensure an accurate solution was attained.

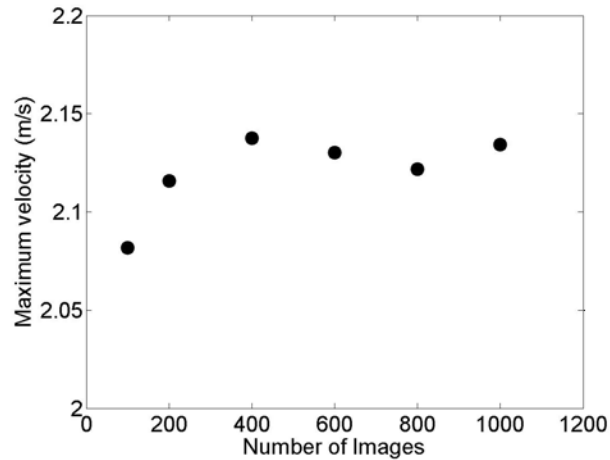


Figure 4.16: Convergence of the number of images required to achieve a repeatable time averaged result. Maximum velocity in the jet as measured 5d from the venous needle tip.

A series of tests was also conducted to determine the repeatability of the measurements and processing method. Three measurements of the velocity profile 5d downstream of the VN placed centrally at an angle of 20° with a needle flow rate of 300 ml/min is displayed in Figure 4.17. The variance in the average and maximum velocity between the three sets of measurements was 0.2% and 0.8% respectively, ensuring repeatability.

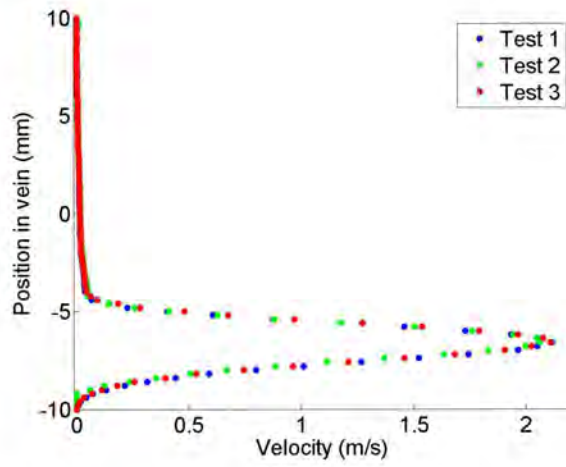


Figure 4.17: Repeatability of PIV results. Velocity profile measured 5d from the venous needle tip.

Chapter 5

Experimental Study of Cannulation Technique: Results and Discussion

This chapter presents the results of the S-PIV measurements, followed by a discussion of the important flow features. Results are presented as contours of out of plane velocity with superimposed vectors and velocity profiles measured at regular intervals within the vein. A summary of all cases is presented at the start for completeness.

5.1 Summary of Cases

The flow domain was split into different sections to maximise the resolution of each respective region. Four sections were required to sufficiently capture the effects of the VNJ. The flow field around the AN was more localised, requiring only two sections. The cameras were mounted on a three axis

motorised traverse which shifted the cameras to specified increments with a precision up to 0.1 mm. The pulse separation time and trigger rate for each section and flow rate was adjusted to optimise the particle displacement in each interrogation window. This ensured that the jet and secondary flows were accurately captured throughout the domain.

Table 5.1 presents all the experimental cases and variables. A total of 27 cases were conducted, where the flow rate, needle position and needle angle was varied. Three flow rates (200 ml/min, 300 ml/min, 400 ml/min), needle positions (needle bore located in the bottom third of the vein, needle bore located in the middle of the vein, needle bore located in the top third of the vein) and needle angles (10° , 20° , 30°) represent a range of clinical conditions. The AN is examined in both antegrade and retrograde orientations whilst the VN is placed in antegrade, according to standard clinical practice. The number of sections required to capture the flow domain for each case is also included.

Table 5.1: Summary of experimental cases

Needle	Orientation	Variable	Blood Flow Rate	Blood Flow Rate	Needle Position	Needle Angle	PIV ROI's
Arterial	Antegrade	Blood Flow Rate	200 ml/min	Middle	20°	1, 2	
			300 ml/min	Middle	20°	1, 2	
			400 ml/min	Middle	20°	1, 2	
		Needle Angle	300 ml/min	Middle	10°	1, 2	
			300 ml/min	Middle	20°	1, 2	
			300 ml/min	Middle	30°	1, 2	
	Retrograde	Needle Position	300 ml/min	Bottom	20°	1, 2	
			300 ml/min	Middle	20°	1, 2	
			300 ml/min	Top	20°	1, 2	
		Blood Flow Rate	200 ml/min	Middle	20°	1, 2	
			300 ml/min	Middle	20°	1, 2	
			400 ml/min	Middle	10°	1, 2	
Venous	Antegrade	Needle Angle	300 ml/min	Middle	20°	1, 2	
			300 ml/min	Middle	20°	1, 2	
			300 ml/min	Middle	30°	1, 2	
		Needle Position	300 ml/min	Bottom	20°	1, 2	
			300 ml/min	Middle	20°	1, 2	
			300 ml/min	Top	20°	1, 2	
	Retrograde	Blood Flow Rate	200 ml/min	Middle	20°	1, 2	
			300 ml/min	Middle	20°	1, 2	
			400 ml/min	Middle	20°	1, 2	
		Needle Angle	300 ml/min	Middle	10°	1, 2	
			300 ml/min	Middle	20°	1, 2	
			300 ml/min	Middle	30°	1, 2	
Retrograde	Needle Position	300 ml/min	Bottom	20°	1, 2		
		300 ml/min	Middle	20°	1, 2		
		300 ml/min	Top	20°	1, 2		
	Blood Flow Rate	200 ml/min	Middle	20°	1, 2		
		300 ml/min	Middle	20°	1, 2		
		400 ml/min	Middle	20°	1, 2		

5.2 Results

5.2.1 Arterial Needle

5.2.1.1 Antegrade Orientation

Figure 5.1 displays velocity contours of out of plane flow for a range of needle flow rates with normalised vectors superimposed for the AN in the antegrade orientation. The flow field is highly focused around the needle with a disturbed flow region occurring above the needle tip, where a reverse flow component (against the predominant axial flow direction) occurs on the roof of the vein. The size of the disturbed flow region increases slightly as the needle flow rate increases, however the magnitude of the out of plane flow entering the needle remained similar for all cases.

Figure 5.2 displays velocity profiles downstream of the AN when placed in the antegrade orientation for a range of needle flow rates. Higher needle flow rates result in a lower velocity of the core flow, as this is invariably linked to the greater amount of blood being extracted by the AN. The M-shape of the velocity profile at the needle tip further shows that the flow entering the needle is highly localised around the tip. The upper and lower component represents flow entering the central bore and through the back eye, whilst the rapid drop in velocity represents the position of the needle tip. The velocity profiles approach a parabolic shape downstream of the needle tip, further indicating that the flow field is highly focused around the needle for all needle flow rates.

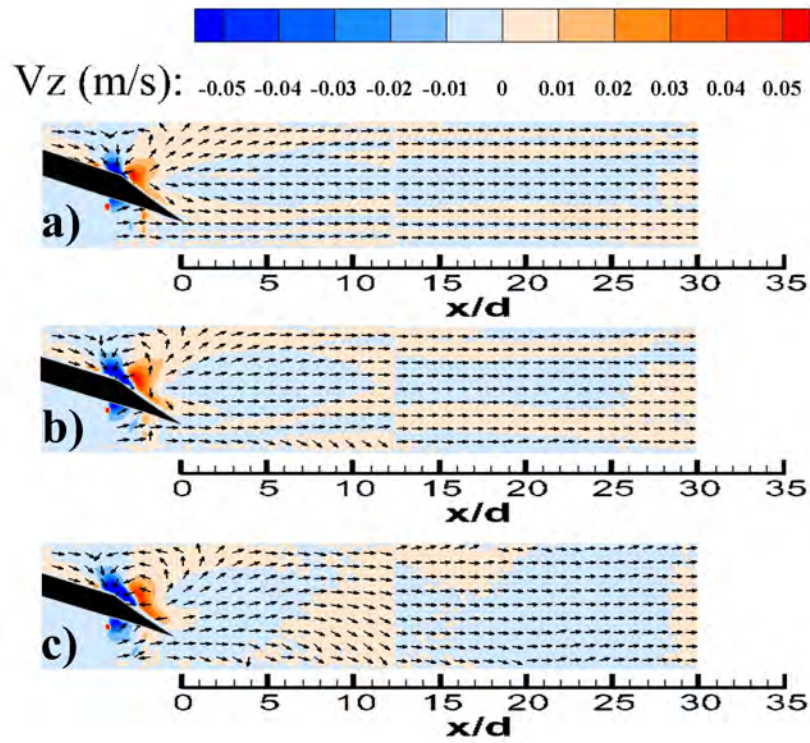


Figure 5.1: Contours of time averaged z-velocity with vectors of normalised velocity for the arterial needle in the antegrade orientation with different needle flow rates. The needle tip is placed in the middle of the vein at an angle of 20° . A steady flow rate of 666 ml/min is passed through the vein. a) 200 ml/min b) 300 ml/min c) 400 ml/min

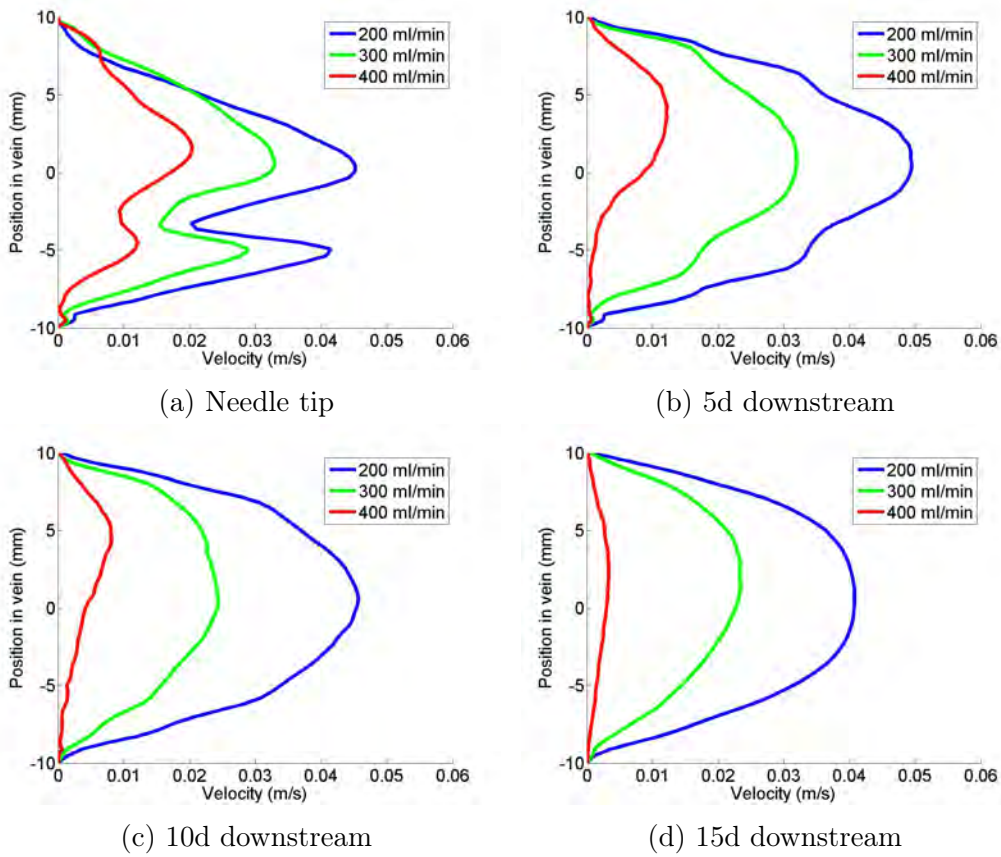


Figure 5.2: Velocity profiles from the arterial needle in the antegrade orientation for different needle flow rates. The needle tip is placed in the middle of the vein at an angle of 20° . A steady flow rate of 666 ml/min is passed through the vein. a) Needle tip b) 5d downstream of the needle tip c) 10d downstream of the needle tip d) 15d downstream of the needle tip

Contours of out of plane velocity with normalised vectors superimposed for the AN at a range of needle depths in the antegrade orientation are presented in Figure 5.3. When the needle is near the floor of the vein a disturbed flow region forms along the roof of the vein downstream. Conversely, when the needle is near the roof of the vein a disturbed flow region forms along the floor of the vein downstream. Disturbed flows also occurs when the needle

is placed in the centre of the vein, although this remains localised above the needle tip. All of the disturbed flows contain reversed flow (against the predominant axial flow direction) along the walls of the vein.

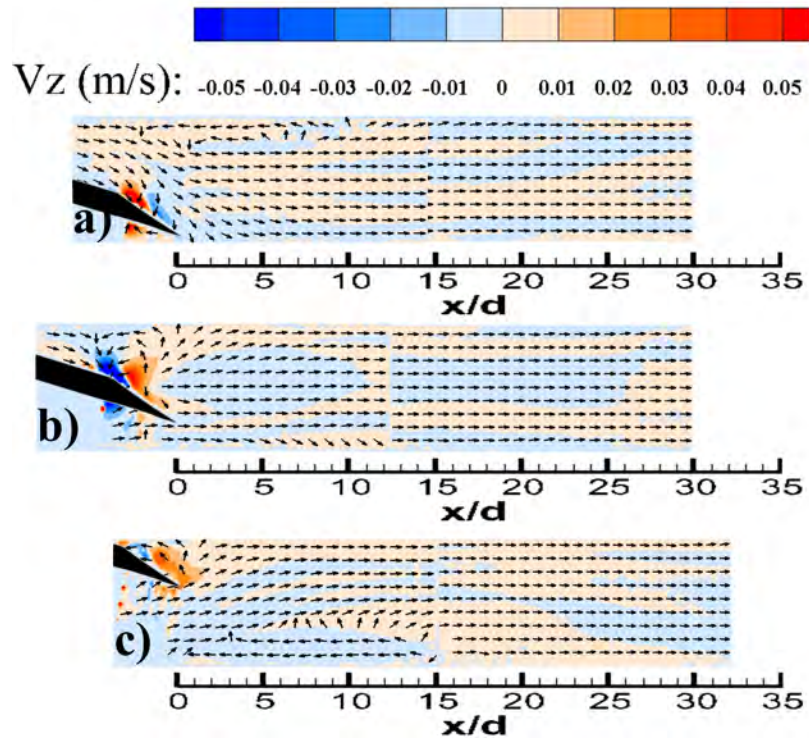


Figure 5.3: Contours of time averaged z-velocity with vectors of normalised velocity for the arterial needle in the antegrade orientation with different needle depths. The needle is placed at an angle of 20° with an equivalent blood flow rate of 300 ml/min. A steady flow rate of 666 ml/min is passed through the vein. a) bottom b) middle c) top

Velocity profiles downstream of the AN when placed in the antegrade orientation for a range of needle positions are presented in Figure 5.4. The velocity profiles are highly skewed based on the position of the needle. A parabolic profile returns 10d downstream when the needle is placed centrally within the vein indicating developed flow. However the effects of

the needle are evident up to 15d downstream when the needle is placed closer to the vein wall.

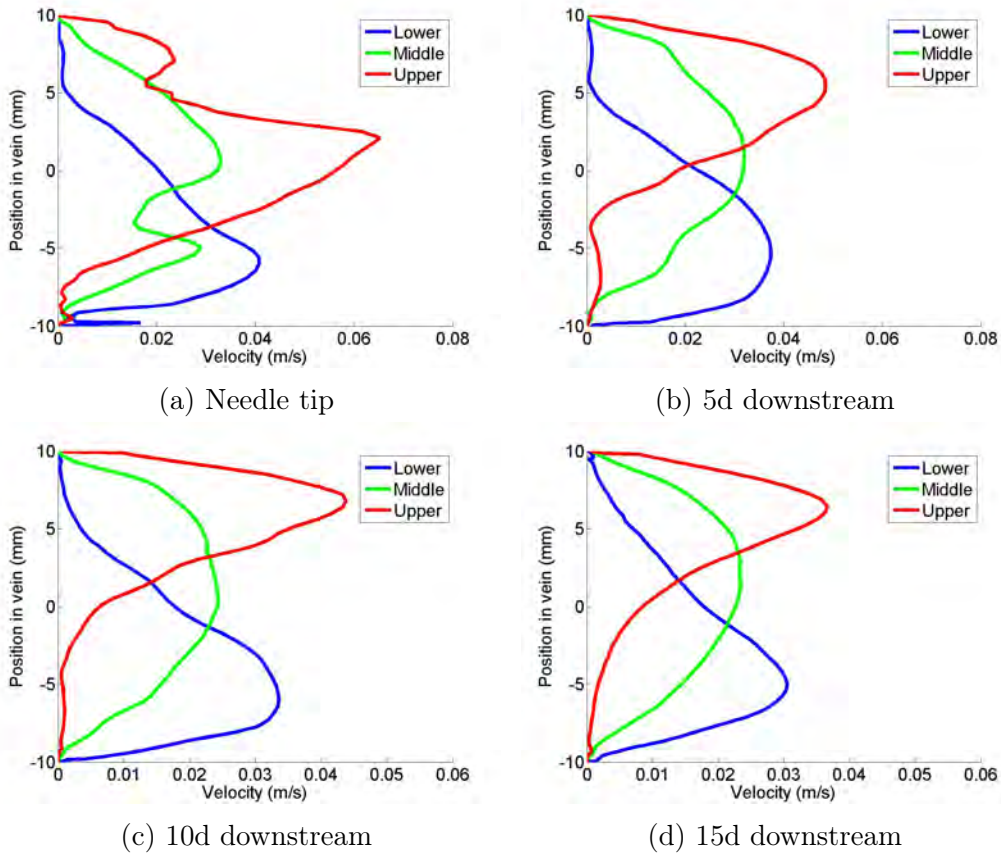


Figure 5.4: Velocity profiles from the arterial needle in the antegrade orientation for different needle depths. The needle is placed at an angle of 20° with an equivalent blood flow rate of 300 ml/min. A steady flow rate of 666 ml/min is passed through the vein. a) Needle tip b) 5d downstream of the needle tip c) 10d downstream of the needle tip d) 15d downstream of the needle tip

The effect of the AN angle when placed in the antegrade orientation is presented in Figure 5.5. The normalised vectors show the presence of disturbed flows above the needle tip which extends to the roof of the vein.

Needle angle has little effect on the size of the disturbed flow region, however the magnitude of the out of plane flow decreases with sharper angles. The flow field is also highly localised around the needle tip as the core flow remains relatively undisturbed downstream.

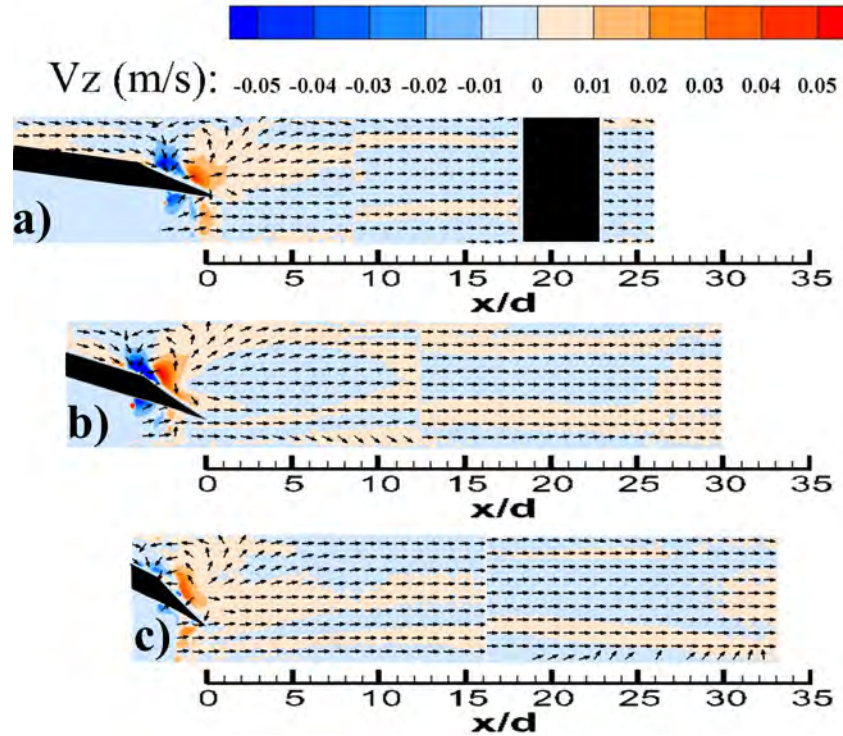


Figure 5.5: Contours of time averaged z-velocity with vectors of normalised velocity for the arterial needle in the antegrade orientation with different needle angles. The needle tip is placed in the middle of the vein with an equivalent blood flow rate of 300 ml/min. A steady flow rate of 666 ml/min is passed through the vein. The black section represents the region which was masked due to shadows produced by the o-ring and block alignment pins. a) 10° b) 20° c) 30°

Figure 5.6 displays velocity profiles downstream of the AN in the antegrade orientation with different needle angles. The M-shaped profile occurs at the needle tip, representing the flow entering the central bore and back eye.

A sharper needle angle produces a higher velocity under the needle, where the flow enters through the back eye. This is due to the back eye position in relation to the oncoming core flow. The velocity profiles are parabolic downstream, further demonstrating that the flow field is localised around the needle tip.

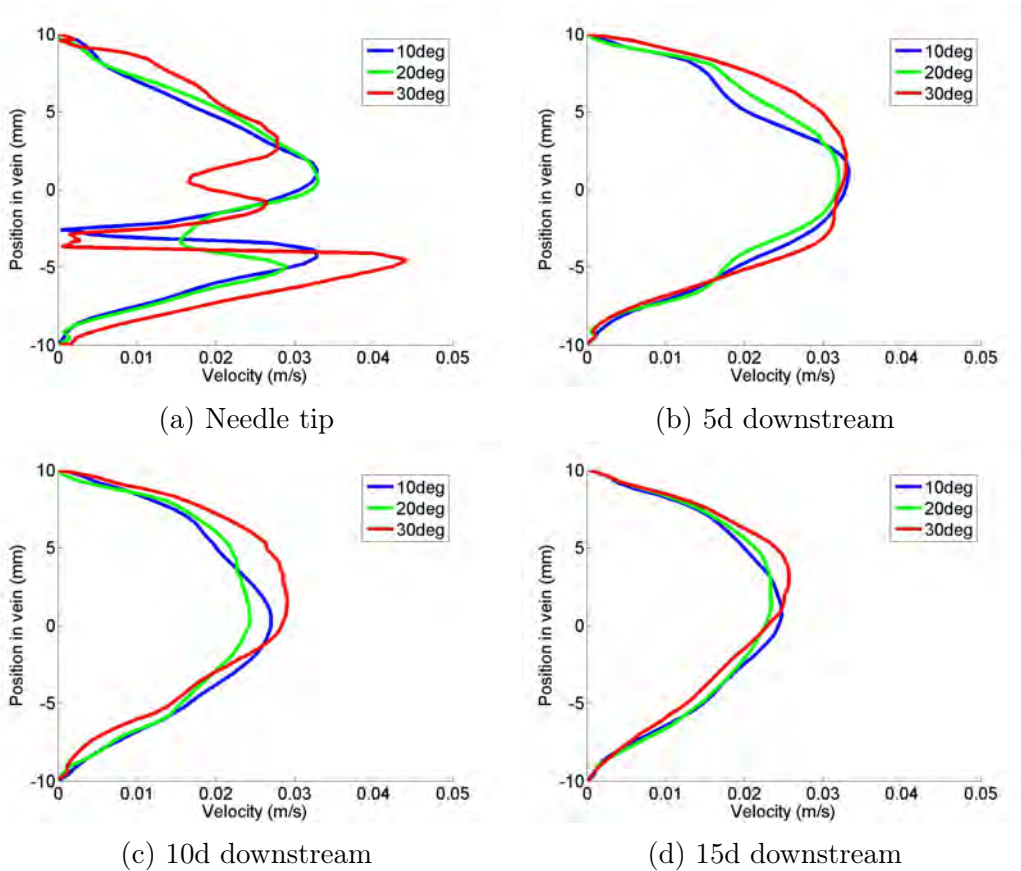


Figure 5.6: Velocity profiles from the arterial needle in the antegrade orientation for different needle angles. The needle tip is placed in the middle of the vein with an equivalent blood flow rate of 300 ml/min. A steady flow rate of 666 ml/min is passed through the vein. a) Needle tip b) 5d downstream of the needle tip c) 10d downstream of the needle tip d) 15d downstream of the needle tip

5.2.1.2 Retrograde Orientation

Figure 5.7 displays velocity contours of out of plane flow for a range of needle flow rates with normalised vectors superimposed for the AN in the retrograde orientation. The flow field is highly localised around the needle tip and the magnitude of out of plane flow around the needle is much less than that witnessed when the AN was placed in the antegrade orientation. An increase in needle flow rate only results in a slight increase in the magnitude of out of plane flow.

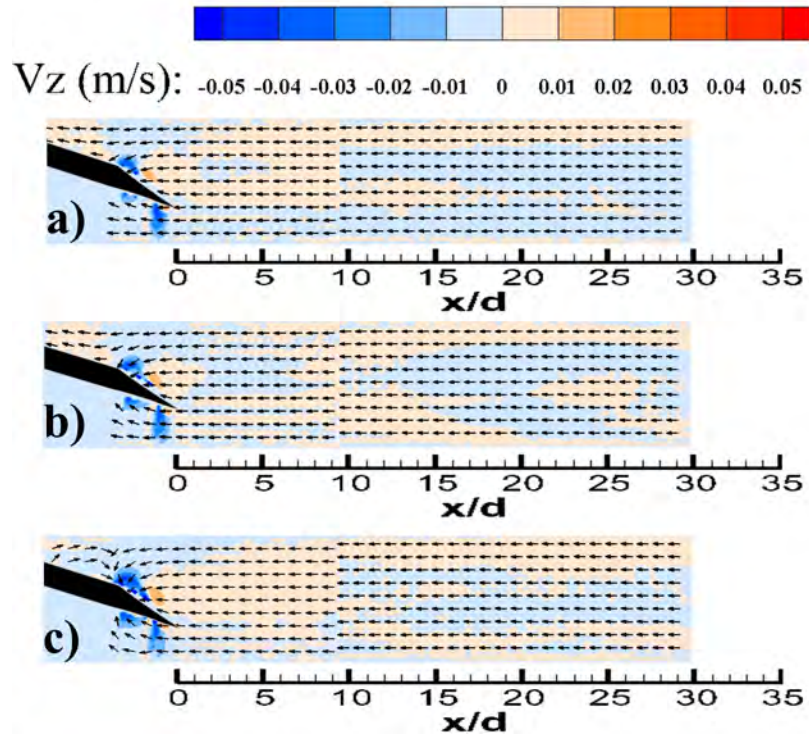
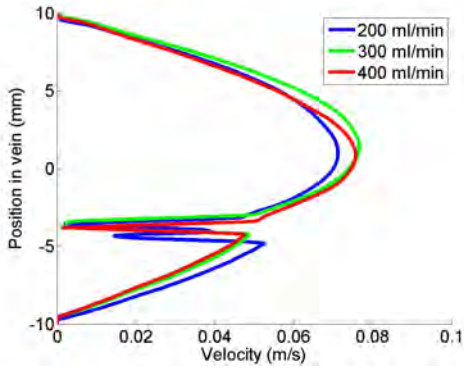


Figure 5.7: Contours of time averaged z-velocity with vectors of normalised velocity for the arterial needle in the retrograde orientation with different needle flow rates. The needle tip is placed in the middle of the vein at an angle of 20° . A steady flow rate of 666 ml/min is passed through the vein. a) 200 ml/min b) 300 ml/min c) 400 ml/min

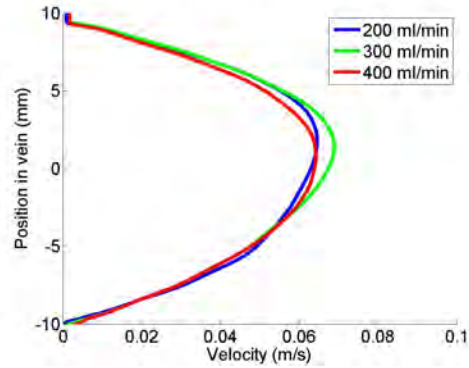
Figure 5.8 displays velocity profiles around the AN when placed in the retrograde orientation for a range of needle flow rates. The flow approaching the AN is fully developed as it approaches the needle tip, further showing that the flow entering the AN in the retrograde orientation is highly localised around the needle tip. The velocity profiles are similar for all needle flow rates, which indicates that this parameter has minimal effect on the flow field within the vein. An M-shape profile forms at the needle tip similar to previous results, where the upper and lower component represents blood entering the central bore and back eye, whilst the rapid drop in velocity represents the position of the needle tip.

Contours of out of plane velocity with normalised vectors superimposed for the AN at a range of needle depths in the retrograde orientation are presented in Figure 5.9. In all positions the flow was localised around the needle tip and no disturbed flow regions were found. The effects of needle position on the flow entering the AN was minimal when placed in the retrograde orientation.

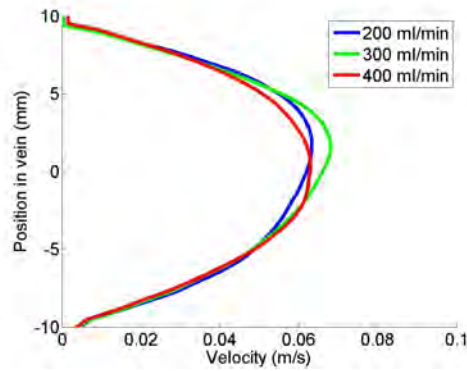
Velocity profiles around the AN when placed in the retrograde orientation for a range of needle positions are presented in Figure 5.10. The flow approaching the AN is parabolic, with the flow field highly localised around the needle tip. The effect of needle position has little effect on the magnitude of the velocity entering the needle as shown by the similar M-shape profiles at the needle tip.



(a) Needle tip



(b) 5d downstream



(c) 10d upstream

Figure 5.8: Velocity profiles from the arterial needle in the retrograde orientation for different needle flow rates. The needle tip is placed in the middle of the vein at an angle of 20° . A steady flow rate of 666 ml/min is passed through the vein. a) Needle tip b) 5d upstream of the needle tip c) 10d upstream of the needle tip

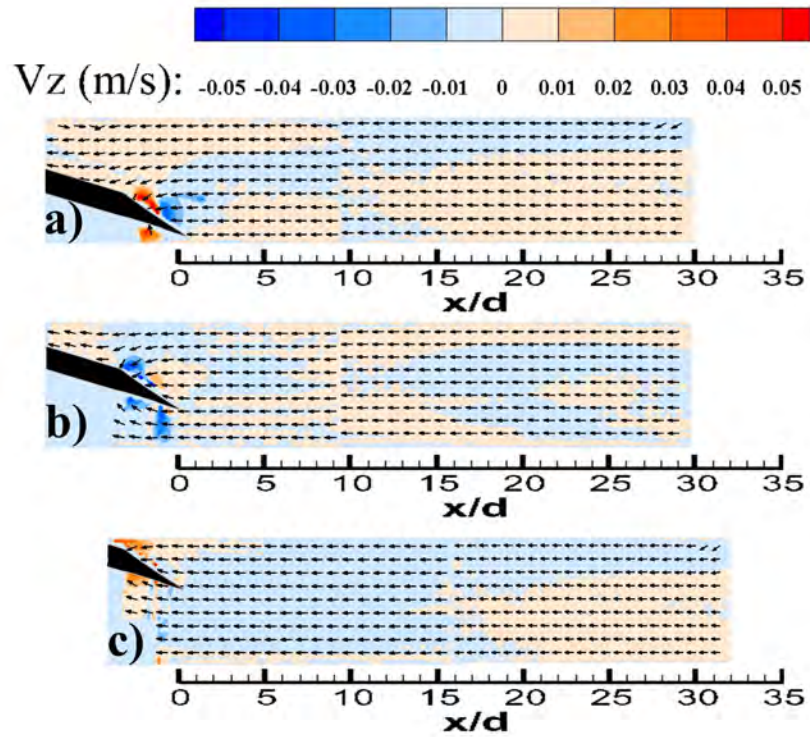


Figure 5.9: Contours of time averaged z-velocity with vectors of normalised velocity for the arterial needle in the retrograde orientation with different needle depths. The needle is placed at an angle of 20° with an equivalent blood flow rate of 300 ml/min. A steady flow rate of 666 ml/min is passed through the vein. a) bottom b) middle c) top

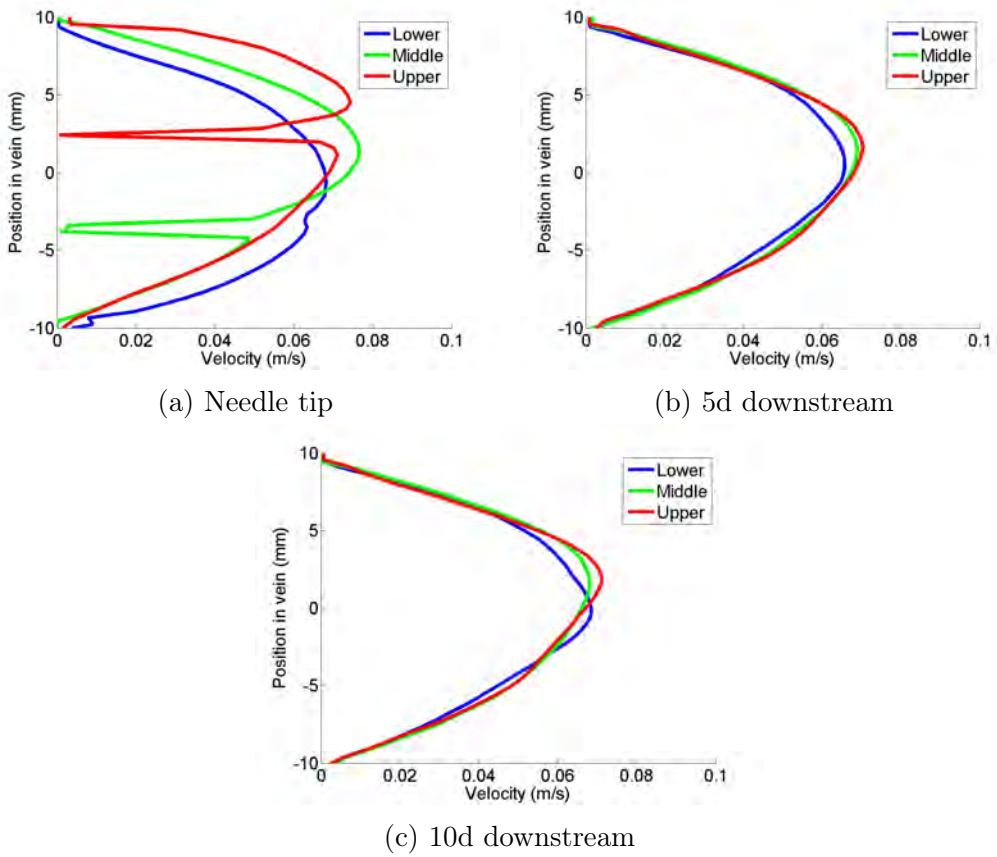


Figure 5.10: Velocity profiles from the arterial needle in the retrograde orientation for different needle depths. The needle is placed at an angle of 20° with an equivalent blood flow rate of 300 ml/min. A steady flow rate of 666 ml/min is passed through the vein. a) Needle tip b) 5d upstream of the needle tip c) 10d upstream of the needle tip

The effect of AN angle when placed in the retrograde orientation is presented in Figure 5.11. The normalised vectors show that the flow field is highly localised around the needle tip with no disturbed flow regions forming. The magnitude of the out of plane flow also remained relatively similar for all cases, indicating the effect of needle angle is minimal.

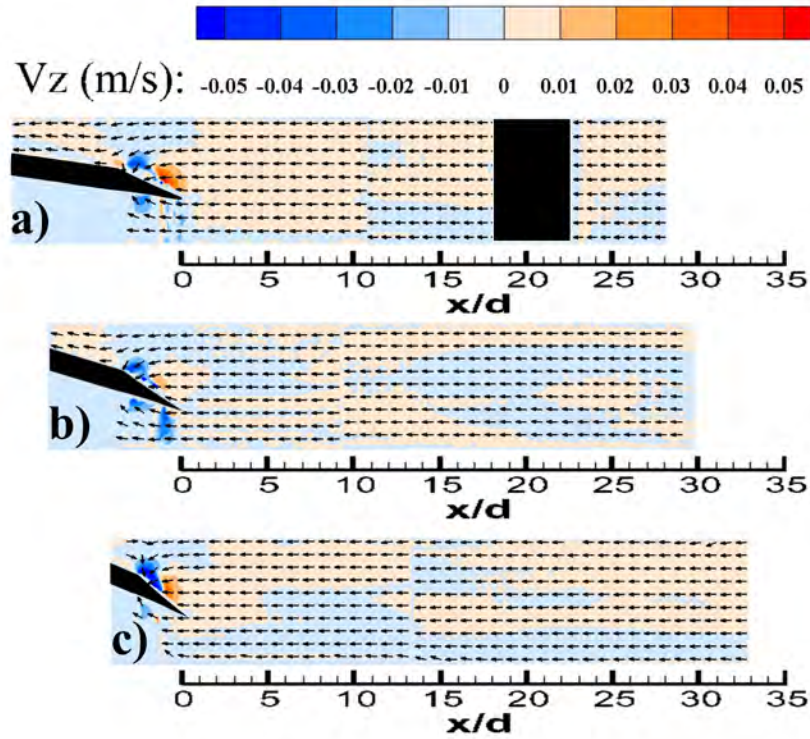


Figure 5.11: Contours of time averaged z-velocity with vectors of normalised velocity for the arterial needle in the retrograde orientation with different needle angles. The needle tip is placed in the middle of the vein with an equivalent blood flow rate of 300 ml/min. A steady flow rate of 666 ml/min is passed through the vein. The black section represents the region which was masked due to shadows produced by the o-ring and block alignment pins. a) 10° b) 20° c) 30°

Figure 5.12 displays velocity profiles upstream of the AN in the retrograde orientation for a range of needle angles. Similar to previous cases, the M-shape profile occurs at the needle tip and shows that the angle of the needle has little effect on the flow as the profiles remained similar in all cases. Consequently, the central bore is exposed to the oncoming core flow when the AN is placed in the retrograde orientation. The velocity profiles approaching the AN are developed as noted by their parabolic shape, providing further

evidence that the flow field remains localised around the needle tip.

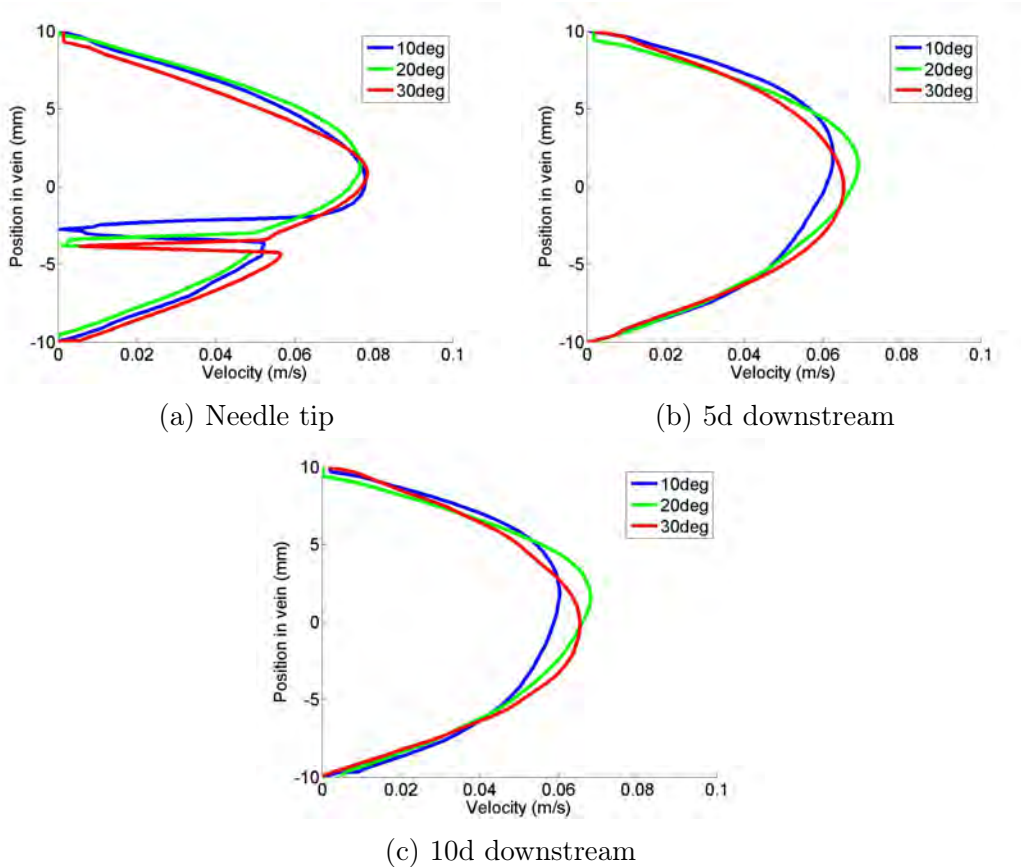


Figure 5.12: Velocity profiles from the arterial needle in the retrograde orientation for different needle angles. The needle tip is placed in the middle of the vein with an equivalent blood flow rate of 300 ml/min. A steady flow rate of 666 ml/min is passed through the vein. a) Needle tip b) 5d upstream of the needle tip c) 10d upstream of the needle tip

5.2.2 Venous Needle

The flow field with vectors of normalised velocity and out of plane velocity contours under various needle flow rates is displayed in Figure 5.13. For

all flow rates the VNJ travels unperturbed until the point of impingement where it then forms a wall jet. The core flow has minimal effect in dissipating the VNJ as no vortex shedding is observed for any of the flow rates. This also highlights the laminar nature of the jet. Contours showing out of plane velocity indicate that the jet is swirling as it exits the venous needle, with greater swirling occurring at higher needle flow rates. Upon impingement the swirling jet quickly dissipates as the jet begins to spread along the curved walls of the vein. The jet spreading results in the formation of contra rotating vortices, which converge along the centre plane forming a distinct steady secondary flow region which extends from the free shear layer of the wall jet to the upper surface of the vein. The vector field confirms that the contra rotating vortices converge on the centre plane as evidenced by the vertical direction of flow. The flow also travels in a reverse direction (against the predominant axial flow direction) along the roof of the vein. Contours of out of plane velocity also identify mixing occurring in the disturbed flow region due to the interaction between the wall jet, contra rotating vortices and core flow. For needle flow rates of 200 ml/min, the degree of mixing has almost completely dissipated by 50d, whereas a large degree of out of plane velocity still exists at the same location for needle flow rates of 400 ml/min. This indicates that the size of the disturbed flow region and degree of mixing increases with higher needle flow rates.

Velocity profiles at the needle tip and 20d, 40d and 60d from the needle are displayed in Figure 5.14. The flow exiting the venous needle is fully developed for all flow rates as made evident by the parabolic profile. The wall jet which forms after impingement is evident at 20d with all needle flow rates showing similar characteristics. At 40d from the needle tip the wall jet begins to detach from the wall and dissipate with the core flow. This is due to the angle of the needle which causes the VNJ to reflect off the lower surface of the vein after impingement. The breakdown of the wall jet increases the entrainment of the core flow and contributes to the high degree of mixing in

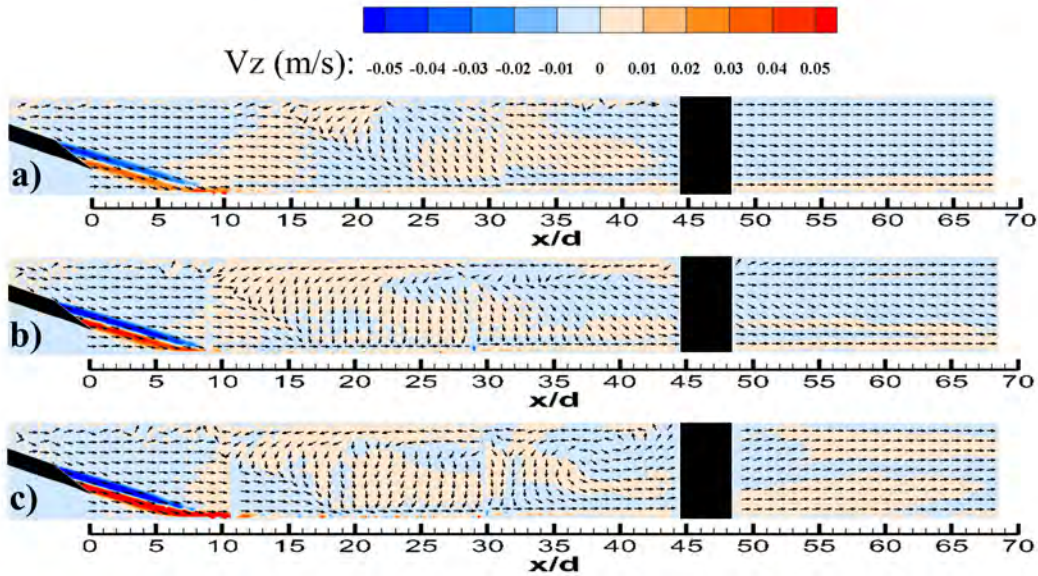


Figure 5.13: Contours of time averaged z-velocity with vectors of normalised velocity for the venous needle with different needle flow rates. The black section represents the region which was masked due to shadows produced by the o-ring and block alignment pins. The needle tip is placed in the middle of the vein at an angle of 20° . A steady flow rate of 666 ml/min is passed through the vein. a) 200 ml/min b) 300 ml/min c) 400 ml/min

the disturbed flow region. Evidence of the jet is still present 60d from the needle tip, although the velocity of the flow field is much more uniform at this point.

Figure 5.15 displays vectors of normalised velocity and out of plane velocity contours for various needle angles. A distinct change from the previous case is the location of impingement, which moves further downstream as the angle becomes shallower. At 10° the VNJ must travel a longer distance before impingement. This case shows that the influence of the core flow on the free stream jet is minimal as no vortex shedding or breakdown is observed, highlighting the laminar nature of the jet. Similar to the observations above, a wall jet is created after impingement followed by a distinct steady secondary

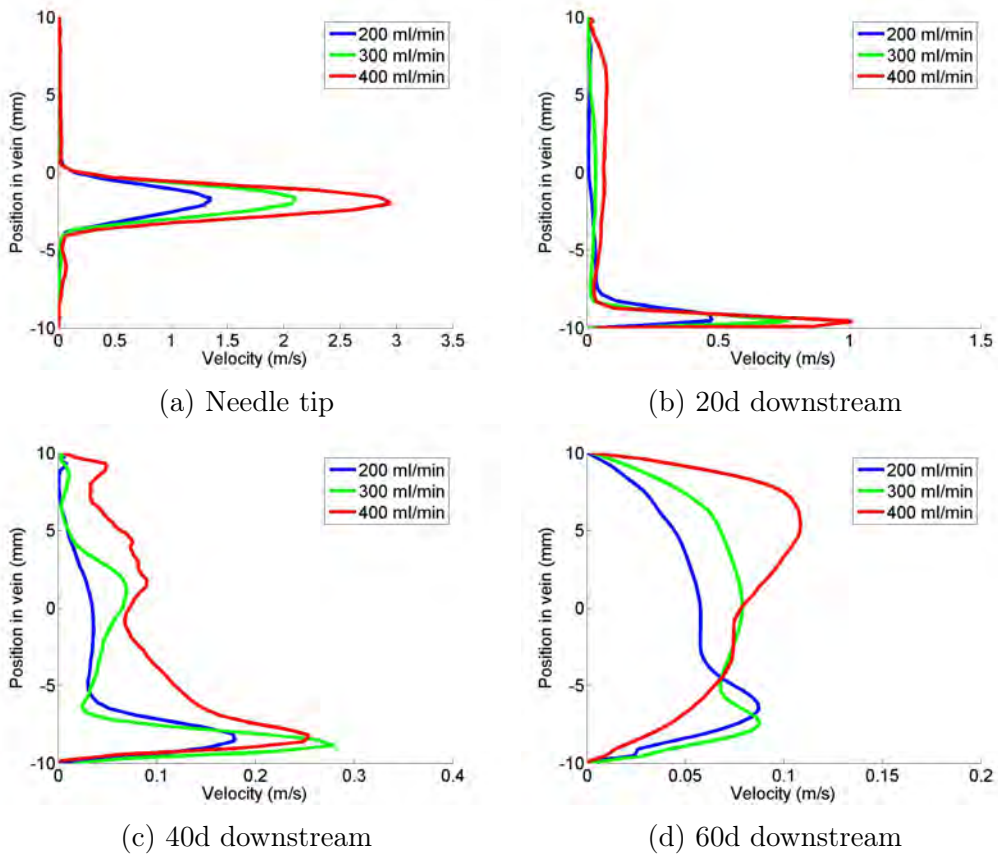


Figure 5.14: Velocity profiles from the venous needle for different needle flow rates. The needle tip is placed in the middle of the vein at an angle of 20° . A steady flow rate of 666 ml/min is passed through the vein. a) Needle tip b) 20d downstream of the needle tip c) 40d downstream of the needle tip d) 60d downstream of the needle tip

flow region as the jet spreading creates contra rotating vortices. An increase in needle angle draws the secondary flows closer to the needle, which supplies further evidence that the disturbed flow region forms from jet spreading and the subsequent creation of contra rotating vortices after impingement. The needle angle does not have a large influence on the strength of mixing within the disturbed flow region as evident by the consistent contours of z -velocity in

each case. However, as the location of impingement varies with the angle of the needle, a higher degree of mixing is evident further upstream at shallower needle angles.

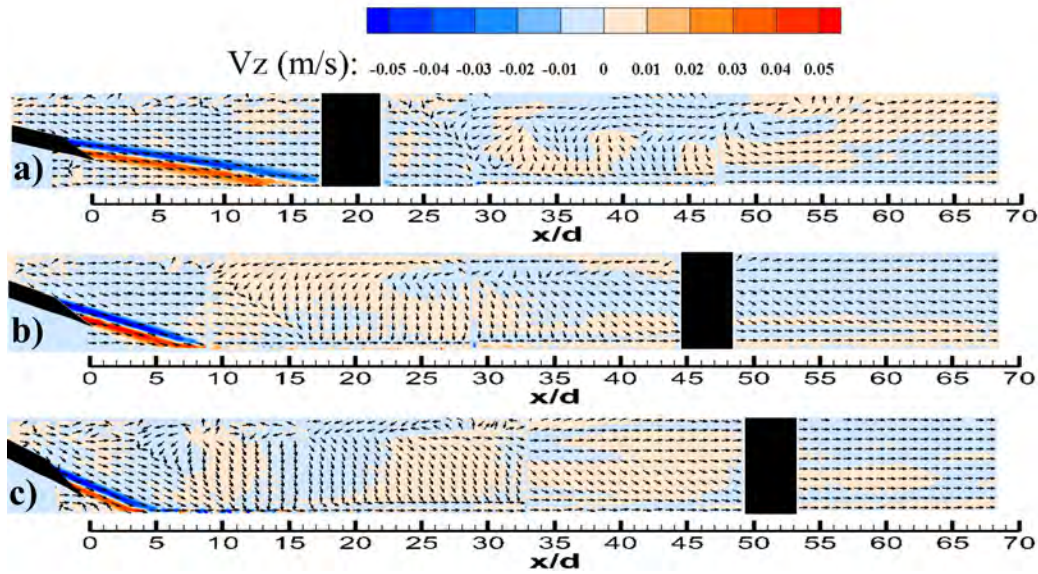


Figure 5.15: Contours of time averaged z-velocity with vectors of normalised velocity for the venous needle with different needle angles. The needle tip is placed in the middle of the vein with an equivalent blood flow rate of 300 ml/min. A steady flow rate of 666 ml/min is passed through the vein. The black section represents the region which was masked due to shadows produced by the o-ring and block alignment pins. a) 10° b) 20° c) 30°

Figure 5.16 displays velocity profiles of the VNJ downstream of the needle tip for various needle angles. Similar to the cases above, fully developed flow exits the venous needle before forming a wall jet upon impingement. Needle angle has a profound effect on the attachment of the wall jet to the vein surface as a sharper needle angle results in a greater deflection off the vein floor. Detachment of the wall jet leads to a greater level of jet dissipation and a higher degree of entrainment with the core flow. This is most evidenced by the lower velocity of the wall jet when the needle angle is set at 30°, despite the jet exiting the needle at the same velocity in every case. It is further

exemplified in Fig 5.15, where a high degree of out of plane velocity occurs in the disturbed flow region, indicating greater mixing when the needle is placed at 30° . By 40d downstream of the needle tip the jet structure has almost completely dissipated at a needle angle of 30° , whereas the structure of the jet is still present at shallower needle angles. This indicates that the disturbed flow region is influential in the process of jet breakdown and subsequent mixing.

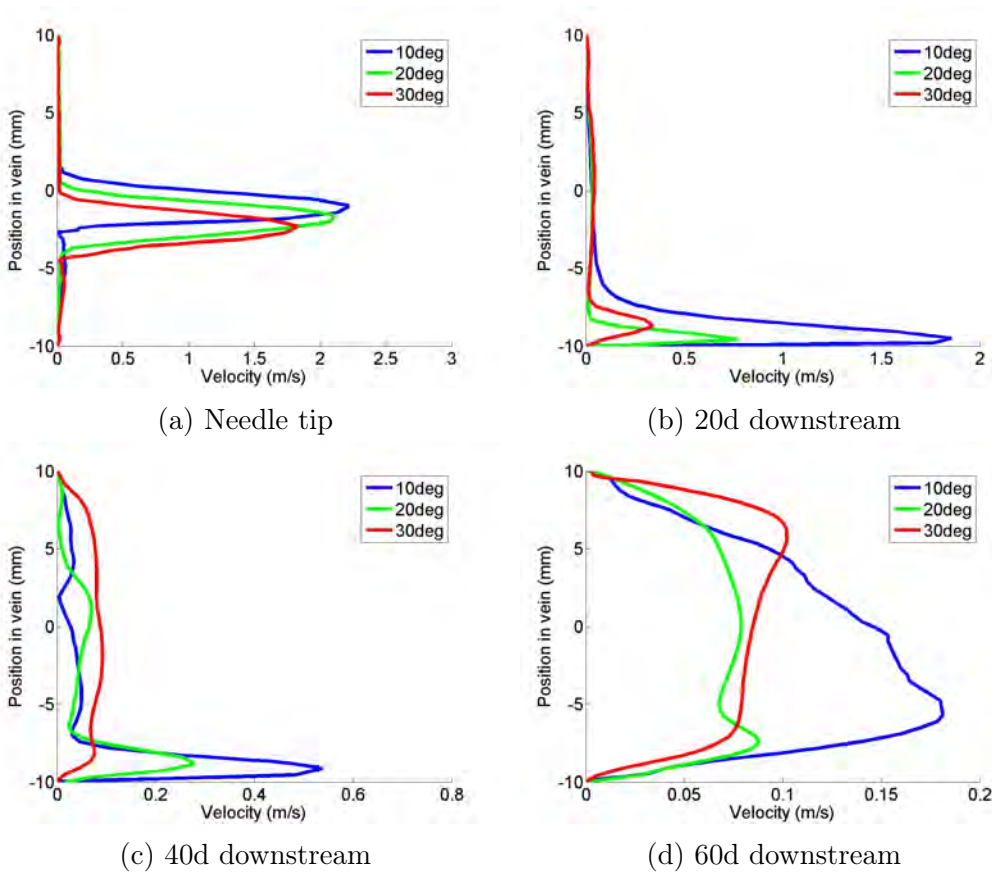


Figure 5.16: Velocity profiles from the venous needle for different needle angles. The needle tip is placed in the middle of the vein with an equivalent blood flow rate of 300 ml/min. A steady flow rate of 666 ml/min is passed through the vein. a) Needle tip b) 20d downstream of the needle tip c) 40d downstream of the needle tip d) 60d downstream of the needle tip

Out of plane velocity contours and vectors of normalised velocity for various needle depths is displayed in Figure 5.17. A needle placed close to the roof of the vein results in a longer distance in which the VNJ must travel before impingement. This has a similar effect to the cases with varying needle angles where the point of impingement shifts downstream. This inevitably affects the location of the resultant disturbed flow region which forms due to the jet spreading along the curved walls of the vein after impingement. A needle placed closer to the floor of the vein draws the secondary flows closer to the needle whilst a needle placed closer to the roof of the vein pushes the disturbed flows downstream. Similar to the case with the needle at 10° , no vortex shedding from the free stream VNJ is observed when the needle is placed closer to the roof of the vein, further highlighting the laminar nature of the jet. The secondary flow pattern also maintains the same characteristics as seen in the previous cases, which is steady in nature with a reverse flow component along the roof of the vein and the contra rotating vortices combining on the centre plane. A higher degree of velocity in the z-direction occurs when the needle tip is placed closer to the vein wall (upper or lower), indicating a higher degree of mixing occurring in these two needle positions which remains evident up to $65d$ downstream.

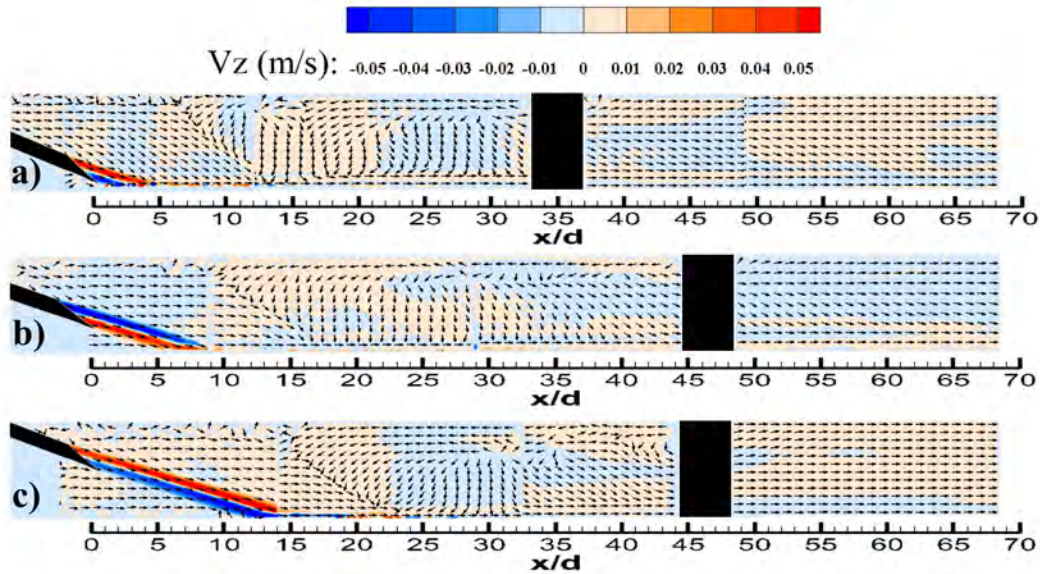


Figure 5.17: Contours of time averaged z-velocity with vectors of normalised velocity for the venous needle with different needle depths. The needle is placed at an angle of 20° with an equivalent blood flow rate of 300 ml/min. A steady flow rate of 666 ml/min is passed through the vein. The black section represents the region which was masked due to shadows produced by the o-ring and block alignment pins. a) bottom b) middle c) top

Velocity profiles downstream of the needle for different needle depths are displayed in Figure 5.18. The velocity in the wall jet is reduced when the needle is placed close to the vein floor due to the dampening effects and momentum change which occurs at impingement. Similar to the previous cases, there is evidence of wall jet detachment at $40d$ downstream for every needle depth. The detachment of the wall jet contributes to the mixing with the core flow and breakdown of the disturbed flow region. By $60d$ downstream the velocity field is more uniform, especially when the needle is placed closer to the roof or floor of the vein, due to the higher degree of jet breakdown from entrainment with the core flow when the needle is in these positions.

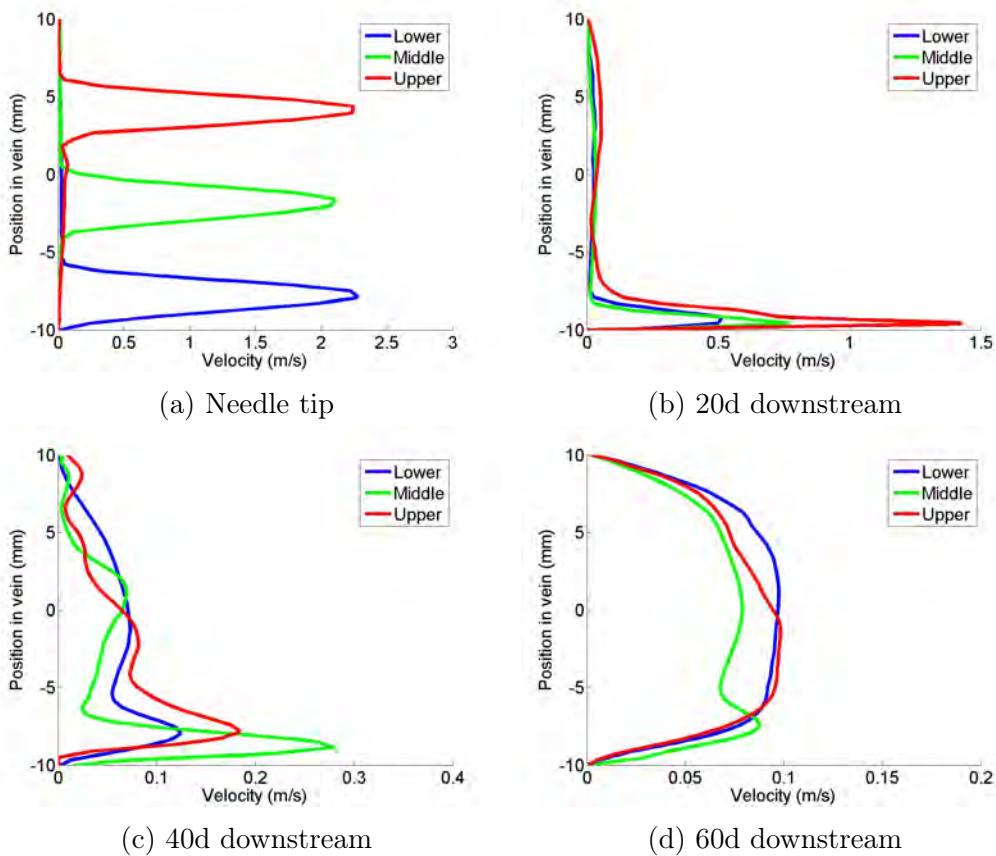


Figure 5.18: Velocity profiles from the venous needle for different needle depths. The needle is placed at an angle of 20° with an equivalent blood flow rate of 300 ml/min. A steady flow rate of 666 ml/min is passed through the vein. a) Needle tip b) 20d downstream of the needle tip c) 40d downstream of the needle tip d) 60d downstream of the needle tip

5.3 Discussion

The aim of this chapter was to examine the flow structures produced by the needles and provide validation data for numerical models, which will be used to assess the potential damage to the endothelium caused by the needles in

subsequent chapters. A high speed jet was shown to exit the VN and impinge on the floor of the vein producing disturbed flows downstream, whilst the flow structures around the AN remained localised around the needle tip.

5.3.1 Arterial Needle

Disturbed flows were visualised around the AN when placed in the antegrade orientation. The disturbed flows extended from the needle tip to the roof of the vein and contained a reverse flow component (against the predominant axial flow direction). Increased needle flow rates increased the size of the disturbed flow region slightly whilst the magnitude of out of plane flow entering the needle remained similar. Needle angle also had minimal effect on the size of the disturbed flow region, although sharper needle angles led to a decrease in out of plane flow. The position of the AN within the blood vessel when placed in the antegrade orientation had the most impact on the disturbed flow. When the needle was placed closer to the vein wall a disturbed flow region formed up to 15d downstream, whereas a centrally placed needle localised the disturbed flows above the needle tip.

On the other hand, no disturbed flows were examined when the AN was placed in the retrograde orientation. The flow field being entrained into the AN remained more localised in the retrograde orientation, extending only a few diameters around the needle. This is because retrograde placement inevitably has a lower resistance of flow entering the needle. An increase in needle flow rate resulted in a slight increase in the magnitude of out of plane flow, although the effect was minimal. Needle angle and position of the needle tip within the vein did not have a large influence on the flow field entering the AN. The presence of the AN itself had minimal effect on the flow downstream, with developed flow returning within 10d in most

cases with antegrade placement. The flow field around the AN in the retrograde orientation was also highly localised around the needle tip. The results presented in this chapter mimic those of Weitzel et al. [120], who showed that the flow effects of the AN were only evident within 1 cm of the needle tip.

5.3.2 Venous Needle

Common flow features were examined in every case which includes: the free stream jet, jet impingement, formation of a wall jet and secondary flows. The flow exiting the needle was shown to be swirling and travelled unperturbed until the point of impingement. No vortex shedding or jet breakdown was examined in the free stream component highlighting its laminar nature and the minimal influence of the core flow. Upon impingement the jet spread along the curvature of the vein and a wall jet formed on the lower surface. The jet spreading resulted in the formation of contra rotating vortices which converged on the central plane. The contra rotating vortices coupled with the wall jet resulted in disturbed flow which is steady in nature and extends from the free shear layer of the wall jet to the roof of the vein, where the flow along the roof was against the predominant axial direction which counteracted the wall jet travelling on the floor of the vein. The position of the disturbed flow region was highly dependent on the impingement region and degree of jet spreading within the vein. The final significant flow feature was wall jet detachment and subsequent breakdown through entrainment of the core flow resulting in mixing between the two streams. Wall jet detachment manifested from the angle of the needle which resulted in a reflection of the jet at the point of impingement.

Jet impingement, jet spreading and the subsequent formation of the wall jet and the formation of the contra rotating vortices were the driving factors

behind the emergence of the disturbed flow. In this experiment, the velocity of the jet is an order of magnitude larger than the core flow. In a large pressure gradient, the core flow can retard the jet, which aids in the formation of the stable secondary flow region. As the two contra rotating vortices combined on the centre plane, a downward motion onto the wall jet resulted. This motion suppressed the unsteady effects which are normally present in the free shear layer of a wall jet, which produced the steady secondary flow region.

No large scale vortex shedding was observed from either the free stream VNJ or the wall jet. Primarily this is due to the laminar and steady conditions of both the VNJ and the core flow. Furthermore, the phenomenon of wall jet detachment as described by Bajura and Catalano [176] was not observed. It is hypothesised that this event did not occur due to the forces being present in the confined pipe as well as the formation of the disturbed flow region. Gogineni and Shih [177] noted that the adverse pressure gradient between the inner and outer layers of the wall jet is the key mechanism causing detachment, as demonstrated in Figure 5.19. The confined environment within the pipe suppressed the potential for wall jet detachment as a higher pressure exists on the free shear layer compared to an open environment. Furthermore, the disturbed flow region was shown to have a vertical component on the wall jet as the contra rotating vortices converged on the centre plane. This motion suppressed any vortex detachment that can occur on the free shear layer, which dampened any events leading to detachment. Hsiao and Sheu [178] state that the most important mechanism in early wall jet detachment is the formation of the primary vortex and the induction of the secondary vortex. Hence, wall jet detachment will only occur if the shear layer becomes inherently unstable to counteract the dampening effect of the disturbed flow region.

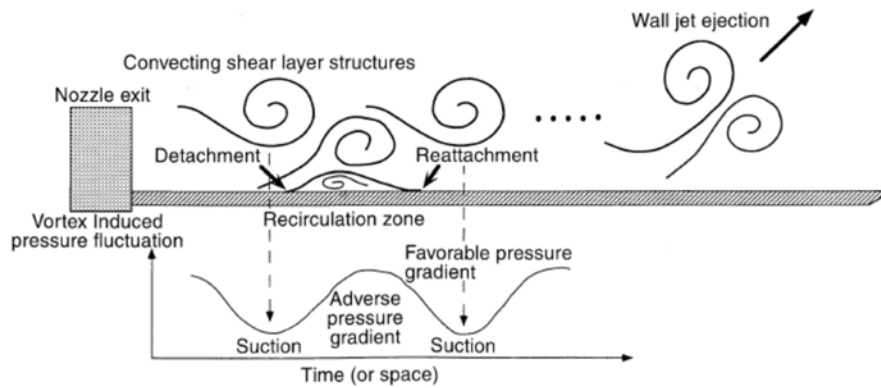


Figure 5.19: Schematic showing the mechanics of wall jet detachment [177]

The secondary flow region resulted in steady mixing of the needle flow and core flow. The location of this mixing coincided with the regions of high turbulent intensities reported by Unnikrishnan et al. [7]. Although turbulent intensities were not measured in this study, the secondary flows measured in this study were shown to be steady. The contradicting results on the VN turbulence can be attributed to the differences between the two studies. The vein in this study was 1.5 times larger than the graft examined in the aforementioned study. Additionally, the core flow was a magnitude larger which generates a larger Reynolds number and invariably elevates the turbulence produced downstream of the VN. Furthermore, the study by Unnikrishnan et al. [7] placed the needle concentrically within the vein whereas this study placed the needle at an angle. As such, the steady secondary flow regions observed in this study would not form, as jet impingement was shown to be a critical factor in its formation. However, the cell culture study conducted by Huynh et al. [48] placed the VN at an angle of 30° , which would produce a similar flow field as observed in this study. Hence, turbulent intensities may not be as elevated as first thought but endothelial function might still be impaired due to the disturbed flows produced by the VNJ.

The parameters tested in this study had various influences on the resulting flow field. Increasing the flow rate led to greater mixing downstream of the needle. Although the jet was shown to have mostly dissipated 60d downstream, remnants were still present at needle flow rates of 400 ml/min indicating that lower flow rates can minimise the effects of the VNJ.

The angle of the needle had a strong influence on the location of impingement and subsequently the position of the disturbed flow region, where higher needle angles drew the disturbed flows closer to the needle insertion site. This may be problematic as the insertion site forms a direct pathway outside the body and is frequently plagued by infection in haemodialysis patients [65]. Furthermore, a sharper needle angle caused a greater deflection of the wall jet from the vein surface which resulted in greater dissipation and entrainment of the wall jet with the core flow which leads to more mixing. The needle angle subsequently determined the level of mixing occurring far downstream. Hence, a shallower needle angle will minimise wall jet deflection, subsequently reducing the downstream mixing and shift the disturbed flow away from the needle insertion site.

Needle position was not shown to influence the size of the disturbed flow, however a greater amount of out of plane velocity was measured when the needle was placed in the upper and lower positions. A needle placed closer to the floor of the vein resulted in a larger wall jet detachment which increased the downstream mixing. Similarly, a needle placed near the roof of the vein shifted the impingement point and disturbed flow region leading to greater mixing further downstream.

Optimising the needle position within the vein can be difficult unless ultrasound is used to guide the placement. To avoid mispuncture the needle should be placed centrally within the vein as needle depth did not have a large impact on the structure of the disturbed flow region other than its

position within the vein. Therefore, high needle flow rates, sharp angles and needles placed near the surface of the vein (roof or floor) should be avoided.

5.3.3 Limitations

The purpose of the experimental work was to provide validation for the numerical models. The main issues revolving around this objective are the limitation of planar measurements and the spatial resolution of the images. A two camera S-PIV system was used to capture all components of velocity on the centre plane. Whilst central plane measurements were sufficient for validation, the flow field was found to be highly three dimensional. A great amount of data could be captured using a tomographic setup. The accuracy of the measurements could also be improved by increasing the number of cameras, which would aid in reducing the image disparity. Spatial resolution was limited by the position of the o-rings and locating pins, which produced gaps in the measurements due to shadows. The rig was designed to be modular to enable a large amount of cases to be tested with ease. Limitations in tooling also prevented the creation of long test segments. Whilst not applicable to this thesis, future work may incorporate pulsatile flows produced by the pump, patient specific vascular geometries and compliant tubing cast from silicon to create an improved physiological match with clinical conditions.

5.4 Conclusion

A twice scaled, idealised model of the AN and VN during haemodialysis was analysed using S-PIV. The primary result of this study was to generate

high resolution data on the bulk flow quantities (three component velocity measurements) under steady flow conditions to serve as validation of the computational models presented in subsequent chapters. Velocity profiles measured downstream of the needles under the various test conditions will be compared against similar scale numerical models in Chapter 6. The results also indicated the presence of secondary flows around the needles.

The flow field around the AN was highly localised around the needle tip in both antegrade and retrograde orientations. Disturbed flows were identified above the AN when placed in the antegrade orientation. Needle flow rate and needle angle had minimal effect on the flow field around the AN. However, a needle placed near the walls of the vein produced a larger disturbed flow region downstream, therefore the needle should be located in the centre of the vein when placed in the antegrade orientation.

Conversely, the flow field downstream of the VN was much larger due to the presence of the VNJ. Results showed the formation of a steady secondary flow region, which formed under all tested conditions due to the interaction of contra rotating vortices caused by jet spreading and a wall jet which formed after impingement of the VNJ. The size of the disturbed flow region was minimised under low needle flow rates and when the VN was placed at shallow angles and centrally within the vein.

Chapter 6

Numerical Study of Cannulation Technique

This chapter presents the primary results of this thesis; an assessment of the haemodynamics produced by the VN and AN with an emphasis on WSS. Qualitative and quantitative information on the flow field produced by the needles is displayed to identify regions at risk of intimal thickening. The position and blood flow rate through the needles is varied to determine an optimum cannulation technique in which the harmful haemodynamic forces can be minimised. The numerical methods used to assess the impact of the needles are outlined. This is accompanied by a numerical uncertainty analysis and validation with the experimental data presented in the previous chapter.

6.1 Introduction

Haemodialysis patients have a high predisposition to pathological narrowing of the access, which commonly occurs at the anastomosis of AVGs and AVFs and the draining vein [27, 33, 98]. Thrombosis is the most common complication leading to vascular access failure, accounting for 23% of all hospitalisations [23], and usually occurs under low flow conditions or when a stenotic lesion ruptures [1, 2]. Thrombosis can also occur in high shear flows, which cause platelet activation [179]. The risk of thrombosis is exacerbated when the activated platelets pool in low flow regions. An effective treatment of thrombosis is to prevent the formation of a clinically significant stenosis.

IH is the pathological thickening of the blood vessel wall in response to injury and is the primary cause of stenosis formation in dialysis patients [180]. Variations in flow resulting in low WSS [56], oscillatory WSS [4] or excessively high WSS [61, 62] have been shown to induce ‘injury’ to the endothelial layer, initiating the inflammatory pathway leading to IH. In particular, low WSS conditions stimulate vascular smooth muscle cell migration and proliferation [56], whilst oscillatory flows cause changes in the endothelial cell structure and orientation which increases vascular permeability [41]. Residence time has become a prime indicator of intimal thickening as blood particles caught in low and oscillatory flows inevitably have a higher probability of interacting with the endothelial layer [45]. Conversely, exposure to high WSS in excess of 40 Pa can result in cell damage within one hour [61].

The flows produced by haemodialysis needles can have a major influence on vascular health. The VNJ has been reported as one potential source of stenosis formation due to high levels of turbulence produced by jet break down [7, 48]. Unnikrishnan et al. [7] reported elevated turbulent intensities

extending up to 8cm downstream of the needle tip. These turbulent fluctuations significantly altered the function of the vessel wall, resulting in random alignment of endothelial cells and a decrease in nitric oxide production, a precursor event in stenosis formation [48]. The AN extracts blood from the fistula and its design and position is fundamental in ensuring a large supply of blood is delivered to the dialyser.

Cannulation technique also has a large influence on some of the factors that affect patency [124], but has received little attention. A key topic of debate is the effect of rotating or “flipping” the needle about its axis after cannulation. This is done to alleviate pressure in the AN if the bore becomes attached to the vessel wall. A needle containing a back eye is also used to alleviate the high pressure present at the central bore. Needle rotation at the time of initial cannulation also prevents needle infiltration by moving the tip away from the floor of the vein [121]. Needle infiltration can lead to significant damage to the vascular access, with 26% of infiltrations resulting in fistula thrombosis, suggesting that needle rotation may be beneficial in preserving the integrity of the vessel wall [87]. However, some reports suggest that infiltration could occur during the rotation process itself [85]. The orientation of the AN is also debated as antegrade orientation has been associated with greater flow to the dialyser [122], however there is no difference for dialysis clearance compared to a retrograde placement [123].

The present study uses computational models to assess the haemodynamic forces created by the AN and VN during haemodialysis. Metrics of WSS are employed to determine the extent of endothelial damage caused by the needles and to ascertain how cannulation technique can reduce the risk of potential IH. A range of blood flow rates and needle positions are tested, including antegrade and retrograde placement of the AN. The influence of needle rotation is also examined.

6.2 Numerical Methods

6.2.1 Computational Domain

An idealised model of the outflow vein from a radial-cephalic AVF was created using SolidWorks 2012 (Dassault systems, Velizy-Villacoublay, France). To investigate the full range of cannulated needle positions, a 15 gauge needle was placed at three angles (10° , 20° and 30°), three depths (bottom, central and top) and three blood flow rates (200 ml/min, 300 ml/min, 400 ml/min). The venous needle was modelled in the antegrade orientation whilst the arterial needle was modelled in both an antegrade and retrograde orientation, conforming to current cannulation practice. The needles were also placed in the inserted position and rotated position as displayed in Figure 6.1.

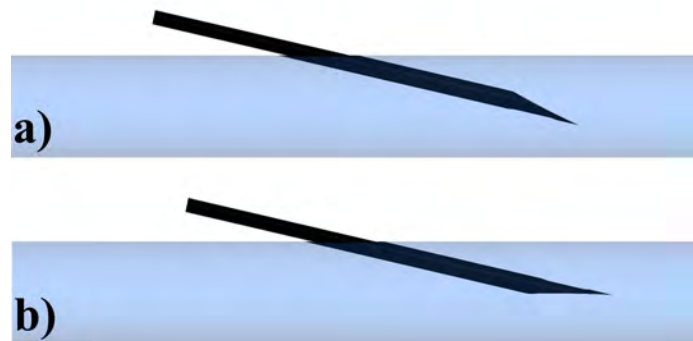


Figure 6.1: Schematic of the inserted and rotated needle position. a) Inserted
b) Rotated

The cephalic vein diameter is 10 mm (D) whilst the needle diameter is 1.35 mm (d) with a wall thickness of 0.18 mm. The needle was placed 100 mm ($10D$) upstream to ensure fully developed flow whilst a length of 200 mm ($40D$) was placed after the needle to allow sufficient development of the VNJ.

The true scale 15G needle with back eye is displayed in Figure 6.2 along with dimensions.

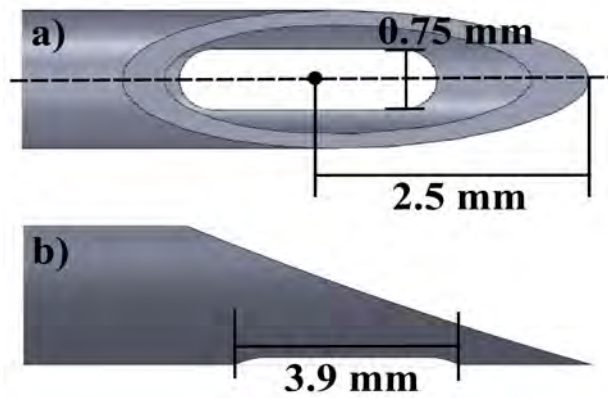


Figure 6.2: Back eye dimensions for a 15G needle

A fully structured hexahedral mesh was generated in ICEM CFD 14.5 (ANSYS Inc., Canonsburg, PA, USA). The boundary layer consisted of 40 layers with an initial size of 0.02 mm and a growth rate of 1.05 and a total of 8 million elements in the entire domain. Details of the mesh structure around the needle are displayed in Figure 6.3, where the boundary layer within and around the needle is evident.

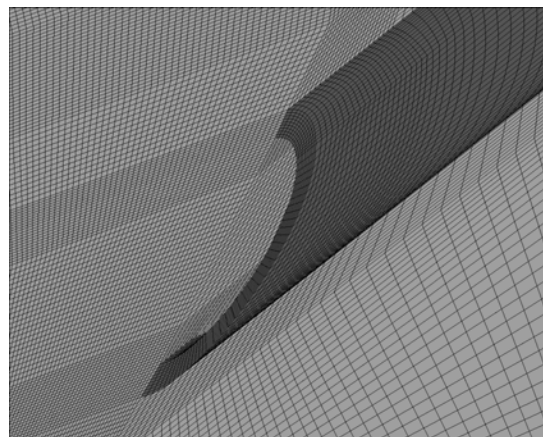


Figure 6.3: Detail of the hexahedral mesh around the needle tip

The Navier-Stokes equations describe fluid dynamics in terms of energy (not studied in this thesis), momentum and mass conservation. These governing equations were solved using the finite volume code in Fluent 14.5 (Fluent Inc., Lebanon, NH). For an isothermal, incompressible flow the conservation of mass and momentum are reduced to:

$$\nabla \cdot \vec{u} = 0 \quad (6.1)$$

$$\frac{\partial \vec{u}}{\partial t} + (\vec{u} \cdot \nabla) \vec{u} = \frac{1}{\rho} (-\nabla p + \nabla \cdot \vec{\tau}) \quad (6.2)$$

Where \vec{u} is the velocity vector, p is the pressure and $\vec{\tau}$ is the shear stress tensor. The shear stress tensor is the friction force imposed by the blood and is dependent on the velocity gradient and dynamic viscosity.

A laminar model was employed with a Pressure Implicit with Splitting of Operators (PISO) algorithm for the pressure-velocity coupling and spatial discretisation schemes set to bounded central differencing to stabilise the dissipation of the VNJ. The central difference was preferred over other schemes as it is inherently second order accurate and good at representing boundary layer flows which is necessary for precise measurement of the WSS. Furthermore, employing a laminar model over a turbulence model, coupled with a high density mesh and small time step (0.0001 seconds) provided a high resolution in both time and space.

Reynolds number, as previous defined in Chapter 4, was used to characterise the flows entering the domain. The Womersley number, which defines the pulsatile flow frequency in relation to viscous effects, was used to quantify the pulsatility of the venous waveform and AN waveform. The Womersley number is defined as:

$$\alpha = \frac{D_h}{2} \sqrt{\frac{\omega \rho}{\mu}} \quad (6.3)$$

Where D_h is the characteristic length of the blood vessel and ω is the angular velocity.

The simulations were run on the University of New South Wales high performance computing cluster (Leonardi), consisting of 48-cores running at 2.2 GHz. All simulations took approximately 40 days to resolve 10 cardiac cycles (50,000 iterations).

6.2.2 Boundary Conditions

The walls of the vein and needle were assumed to be rigid and smooth as the vein wall thickens from arterialisiation during the maturation process after the fistula is created. Furthermore, calculating wall displacements is computationally expensive and is of secondary importance compared to flow and geometric assumptions [148]. Blood was modelled as a Newtonian fluid with a density of 1045 kg/m^3 and a viscosity of $0.0035 \text{ Pa}\cdot\text{s}$ as the application of non-Newtonian blood models in turbulent flow is disputable [181].

The VN was modelled with a constant parabolic velocity inlet with Reynolds numbers of 924, 1,385 and 1,847 for blood flow rates of 200 ml/min, 300 ml/min and 400 ml/min, respectively. The AN was modelled with a pulsatile waveform incorporating the effects of the haemodialysis roller pump as described in Chapter 7. The AN waveform has a period of 0.64 seconds with equivalent average Reynolds numbers as previously mentioned. The waveform of the AN and VN is displayed in Figure 6.4. A zero pressure opening was imposed downstream to meet flow continuity.

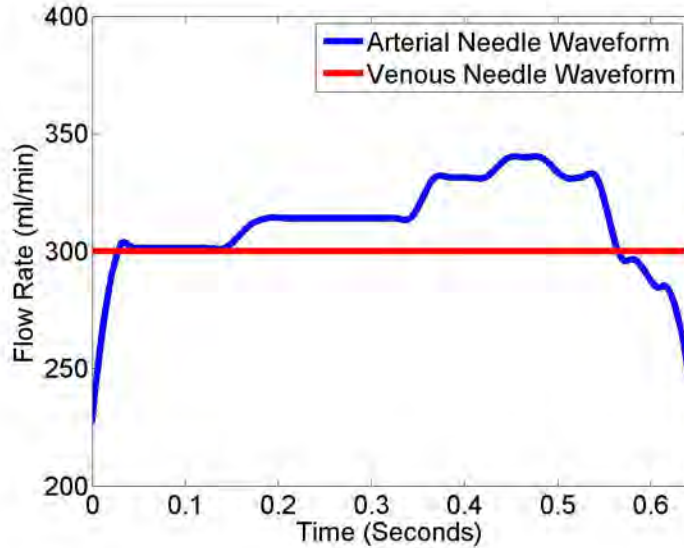


Figure 6.4: Needle waveform imposed on the arterial and venous needle for a blood flow rate of 300 ml/min. The arterial needle inlet was pulsatile due to the motion of the peristaltic pump. The waveform was captured using Duplex ultrasound as explained in Chapter 7. The venous needle flow remained constant due to the dampening effects of the air traps and dialyser.

A transient waveform with a period of one second as measured by Sivanesan et al. [98] was enforced at the cephalic vein inlet assuming an end to side fistula configuration with antegrade flow in the distal artery, and a resistive index (ratio of flow through the fistula to flow to the hand) of 0.75 as described by Ene-Iordache and Remuzzi [145]. The waveform imposed on the vein is displayed in Figure 6.5. The resultant Womersley number of the cephalic vein waveform was 2.8 and the maximum, minimum and mean Reynolds numbers are 930, 225 and 553, respectively.

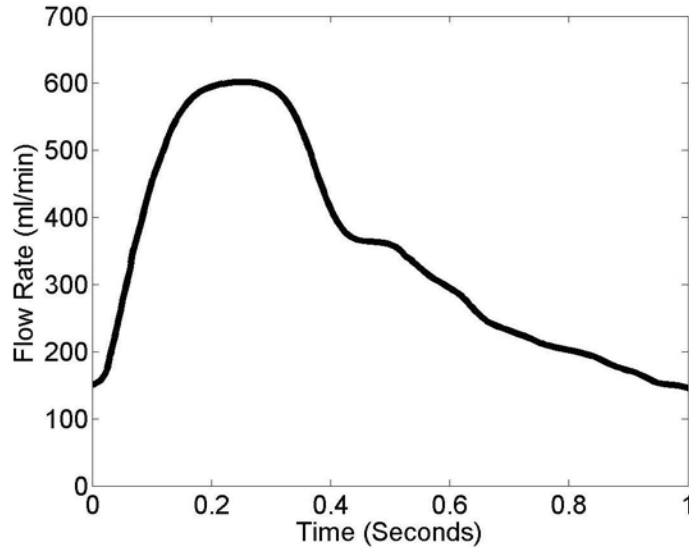


Figure 6.5: Transient waveform imposed on the cephalic vein as measured by Sivanesan et al [98]

The Reynolds numbers of the needles and venous waveform fall below the critical Reynolds number ($Re = 2300$) for turbulent flow in a pipe, confirming that the laminar model is sufficient to resolve the flow field.

The domain was initialised for 10 periods of the transient profile with a time step of 0.01 seconds to allow the flow fields produced by the vein and needle to stabilise. To reduce velocity fluctuations induced by inadequate time resolution the time step was then reduced to 0.0001 seconds ensuring the average Courant number remained below one. All residuals converged to 10^{-6} within five iterations. Furthermore, a time step of 0.0001 seconds concurs with the high resolution CFD recommendations of Steinman and colleagues [182–184], who concluded that at least 10,000 time steps per cardiac cycle are required in order to sufficiently resolve the complex haemodynamic flows. An overview of the computational setup and boundary conditions is displayed in Figure 6.6.

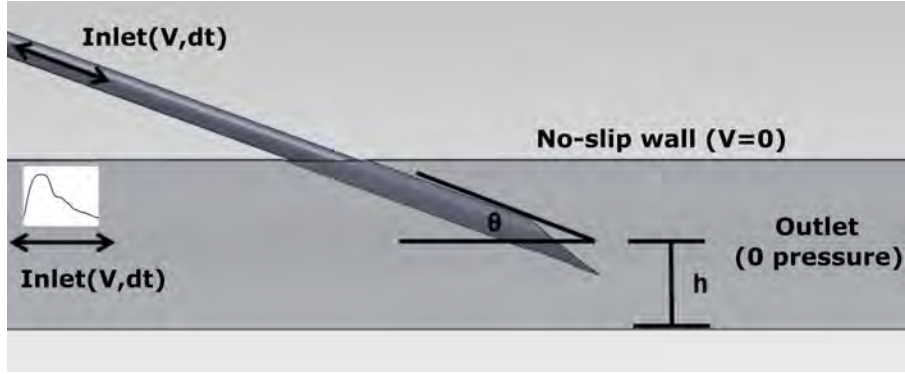


Figure 6.6: Summary of the computational setup

6.2.3 Metric Analysis

Two WSS metrics are employed in this study to analyse potential endothelial dysfunction; time averaged wall shear stress (TAWSS) and relative residence time (RRT). TAWSS is used to assess excessively high WSS produced by the VNJ which occurs over the cardiac cycle and was previously defined in section 2.1.2 as:

$$TAWSS = \frac{1}{T} \int_0^T |\tau_w| dt \quad (6.4)$$

RRT was proposed by Himburg et al. [45] and is sensitive to both the direction and magnitude of the WSS vector. RRT represents the relative time a particle near the wall will travel in one cardiac cycle and was previously defined in section 2.1.3 as:

$$RRT = [(1 - 2 \times OSI) |TAWSS|]^{-1} \quad (6.5)$$

This study utilises the RRT as a single metric for low and oscillating WSS, as previous studies have noted its robustness [38] and accuracy [44] in predicting intimal thickening. These metrics were calculated over 10 cardiac cycles to sufficiently represent the time averaged affects occurring over a dialysis session. This methodology has the same order of magnitude used by Lantz et al. [185] who required 50 cycles to produce statistically reliable data in a model of a patient specific human aorta. The area of high WSS and RRT was calculated using the average cell area and summing the total number of cells (j) above the maximum threshold, formulated as:

$$A_{>threshold} = \sum_{i=1}^j N_{>threshold} A_{average} \quad (6.6)$$

Where $A_{>threshold}$ is the vein area larger than the threshold value which can cause endothelial damage, $N_{>threshold}$ is the number of cells above the set threshold value and $A_{average}$ is the average cell area.

Visualisation of flow structures was conducted using isosurfaces of velocity magnitude to represent the jet flow characteristics of the VN. Velocity contours and pathlines on cross sectional planes are presented for the AN to show the three dimensional flow structures around the needle tip. The performance of the back eye in each needle position was also assessed by comparison of the mass flow passing through the central bore.

6.3 Numerical Uncertainty

Steady flow conditions were simulated in the grid convergence tests. Velocity fluctuations due to poor spatial resolution were minimised to within 1% when the mesh size exceeded 8 million elements. The boundary

layer was also assessed using the grid convergence index as outlined by Roache [186]. The maximum WSS within the vein produced by the impinging VNJ was measured on mesh sizes of 1, 2, 4, 8 and 16 million elements. A boundary layer consisting of 40 prismatic layers yielded a difference in the maximum WSS of 3.1%, confirming grid independence to a high accuracy. Velocity monitor points were used to examine a range of time steps, where a time step size of 0.0001 seconds was deemed most feasible based on numerical accuracy. Detailed information on the numerical uncertainty can be found in Appendix C.

6.4 Numerical Validation

Steady state computational models (scaled to the size of the experimental) were compared against the S-PIV measurements presented in Chapter 5 to validate the boundary conditions and mesh. It is difficult to measure WSS using PIV due to: reflections at the fluid-wall interface and high gradients near the boundary [139]. Therefore, the S-PIV measurements are used to validate the bulk flow features by comparing velocity profiles downstream of the needles. The computational models can subsequently be used to accurately determine the shear stresses on the vein wall. The results presented below represent the baseline case where the needle is placed at 20° in the middle of the vein with a blood flow rate of 300 ml/min.

Figure 6.7 presents velocity profiles (computational and experimental) for the AN in the antegrade orientation. The velocity profiles are measured at the needle tip and 5d, 10d and 15d downstream of the needle tip. The computational models identify the skewed velocity profiles produced by the needle and the M-shaped profile created by the flow entering the AN through the central bore and back eye, providing excellent agreement with the S-

PIV measurements. The computational model appears to overpredict the velocity in the vein slightly with a difference in maximum and average velocity of 5.98% and 13.26%, respectively. The greatest difference coincides with the presence of the needle tip; at the base of the M-profile. However, this difference arises from reflections of the metal needle and is attributed to experimental error.

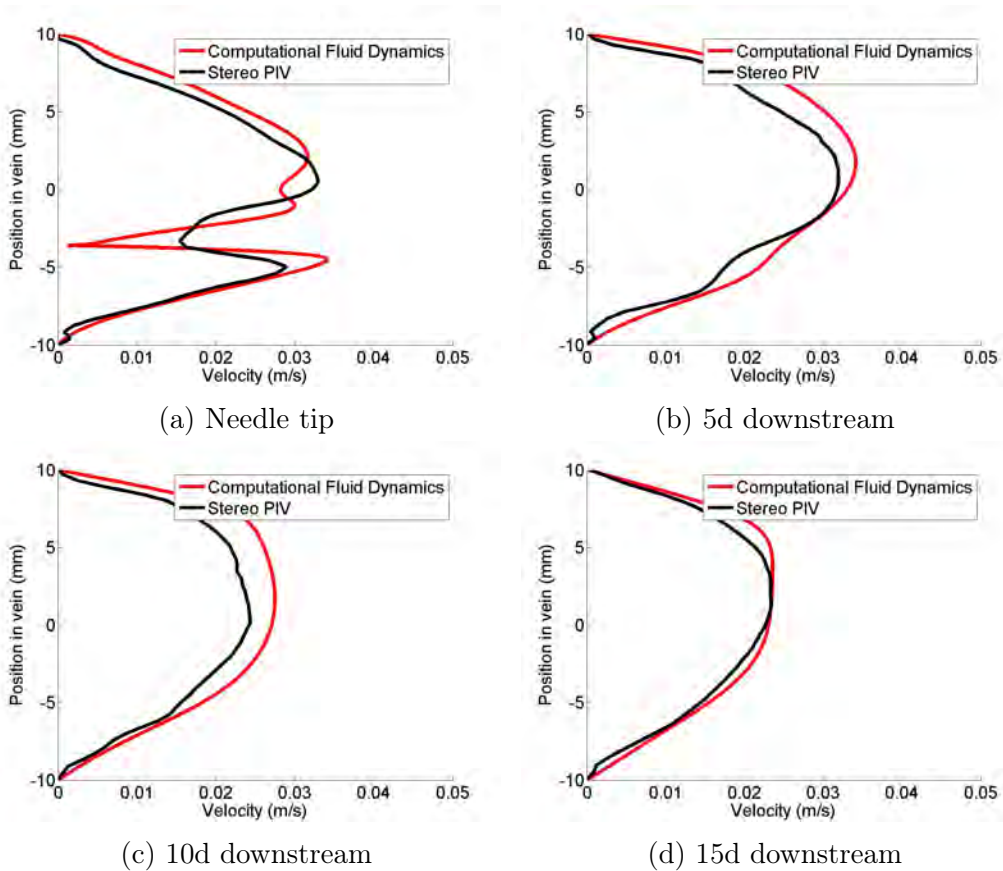


Figure 6.7: Comparison between experimental and computational velocity profiles from the arterial needle in the antegrade orientation at a blood flow rate of 300 ml/min. The needle tip is placed in the middle of the vein at an angle of 20° . a) Needle tip b) 5d downstream of the needle tip c) 10d downstream of the needle tip c) 15d downstream of the needle tip

As the mesh and boundary conditions change with each parameter, the velocity profiles were compared for every case. For brevity, only the baseline case is presented, with the other cases attached in Appendix D. Table 6.1 displays the average percentage difference in the maximum and mean velocity for each case and shows that the overall variation for the AN in the antegrade position was 8.28% and 15.23%, ensuring a reasonable level of validity against the experimental data.

Table 6.1: Summary of differences between computational and experimental results for the arterial needle in the antegrade orientation

Case	Percentage difference in maximum velocity	Percentage difference in mean velocity
200 ml/min	6.43%	8.42%
300 ml/min	5.98%	13.26%
400 ml/min	13.91%	19.32%
10°	15.46%	28.85%
30°	9.69%	4.54%
Needle at bottom of vein	4.12%	21.42%
Needle at top of vein	2.39%	10.82%
Average	8.28%	15.23%

Figure 6.8 compares velocity profiles (computational and experimental) for the AN in the retrograde orientation for the baseline case where the needle is placed at 20° in the middle of the vein with a blood flow rate of 300 ml/min. The velocity profiles are measured at the needle tip and 5d, and 10d downstream of the needle tip. The computational models show an even greater match with the experimental data than the antegrade orientation, particularly the M-shaped profile at the needle tip which identifies the flow entering the AN through the central bore and back eye. The only variation between the profiles is the added skew in the experimental data, which

occurred due to a slight variation in needle positions. Similarly, only the baseline case is presented with comparison for the other cases attached in Appendix D.

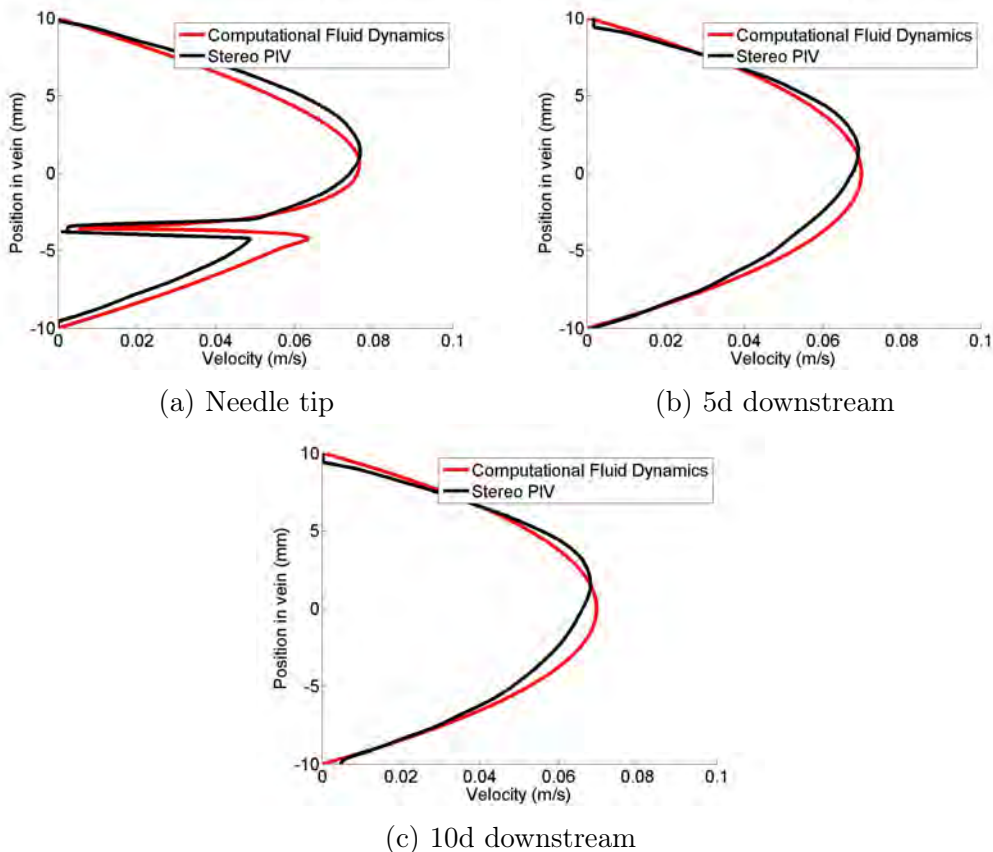


Figure 6.8: Comparison between experimental and computational velocity profiles from the arterial needle in the retrograde orientation at a blood flow rate of 300 ml/min. The needle tip is placed in the middle of the vein at an angle of 20° . a) Needle tip b) 5d downstream of the needle tip c) 10d downstream of the needle tip

Table 6.1 displays the percentage difference in the maximum and mean velocity for all cases where the AN is placed in the retrograde orientation. The table complements the results of the velocity profiles which showed

excellent agreement between the computation and experimental data. The average percentage difference in maximum and average velocity for the AN placed in retrograde is 5.68% and 4.48%, respectively.

Table 6.2: Summary of differences between computational and experimental results for the arterial needle in the retrograde orientation

Case	Percentage difference in maximum velocity	Percentage difference in mean velocity
200 ml/min	6.81%	5.84%
300 ml/min	1.19%	3.62%
400 ml/min	8.13%	8.16%
10°	10.62%	5.01%
30°	5.00%	3.91%
Needle at bottom of vein	6.12%	8.50%
Needle at top of vein	1.88%	3.33%
Average	5.68%	4.48%

Figure 6.9 displays velocity profiles (computational and experimental) for the VN placed at 20° in the middle of the vein with a blood flow rate of 300 ml/min. The velocity profiles are measured at the needle tip and 20d, 40d and 60d downstream of the needle tip. Only the baseline case is presented here, the comparison for the other cases can be found in Appendix D. The general shape of the VNJ and resultant wall jet is captured in the computational models, however the magnitude is overpredicted. Consequently, the S-PIV system was adjusted to capture the jet and core flow as accurately as possible, however PIV systems are limited in capturing a dynamic range of velocities.

Further downstream the variation becomes more apparent, where the remnants of the jet are not exhibited in the computational model. This is due to the laminar model imposed with the high resolution numerical methods which underestimate the dissipation of the jet.

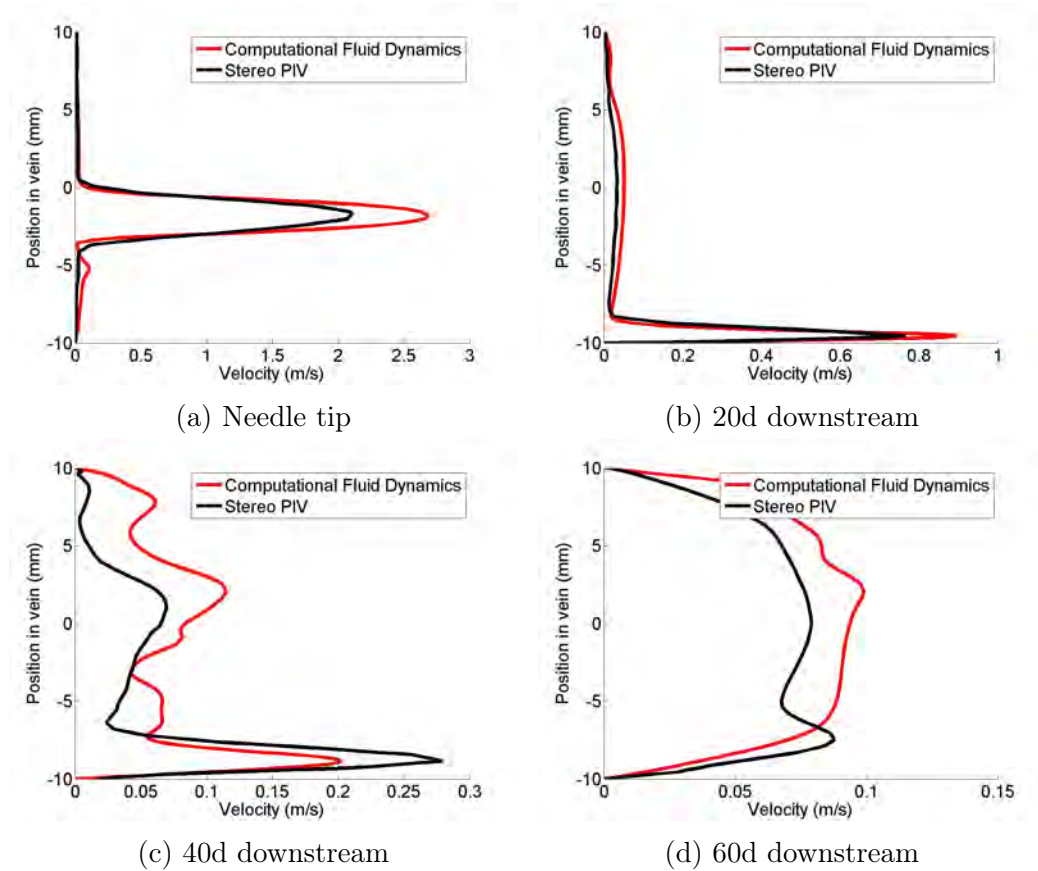


Figure 6.9: Comparison between experimental and computational velocity profiles from the venous needle at a blood flow rate of 300 ml/min. The needle tip is placed in the middle of the vein at an angle of 20° . a) Needle tip b) 20d downstream of the needle tip c) 40d downstream of the needle tip c) 60d downstream of the needle tip

Table 6.1 displays the percentage difference in the maximum and mean velocity for all cases of the VN. The average percentage difference in the maximum and mean velocity for all cases of the VN was 17.86% and 20.78%, respectively. Despite the mismatch in the jet dissipation further downstream, the computational results showed good agreement with the experimental data, particularly in capturing the VNJ, resultant wall jet and secondary flows which develop above the wall jet (position in the vein extending from -5 to 10 mm). The large differences (in specific regions) between the computational and numerical results are attributed to difficulties in measuring a dynamic flow field using S-PIV. Large gradients exist between the jet and secondary flow regions which can induce errors in the velocity calculation.

Table 6.3: Summary of differences between computational and experimental results for the venous needle

Case	Percentage difference in maximum velocity	Percentage difference in mean velocity
200 ml/min	17.98%	17.52%
300 ml/min	21.19%	25.89%
400 ml/min	27.26%	13.20%
10°	11.01%	18.86%
30°	23.01%	20.79%
Needle at bottom of vein	12.23%	24.81%
Needle at top of vein	12.34%	24.38%
Average	17.86%	20.78%

6.5 Results

6.5.1 Arterial Needle in Antegrade

Figure 6.10 displays velocity contours and streamlines on cross sectional planes for the AN placed in the antegrade orientation during diastole. In all cases, the blood being drawn through the needle is localised around the needle tip and a disturbed flow region exists directly above the central bore. The disturbed flow region consists of blood being extracted through the needle and its size remained consistent for all cases except when the needle tip was placed closer to the vein wall. In these positions the wall influenced the size of the disturbed flow region occurring above the needle tip, where a needle placed near the floor resulted in a larger disturbed flow region and a needle placed near the roof had a smaller disturbed flow region.

Disturbed flow downstream of the needle tip along the floor of the vein also formed at high blood flow rates, shallow needle angles and when the needle tip was placed towards the roof of the vein, although the disturbed flow that formed on the floor of the vein was not drawn into the AN.

The RRT on the surface of the vein is presented in Figure 6.11, with higher residence times coinciding with the location of the disturbed flows identified previously. The isometric view of the blood vessel highlights the three dimensional nature of the disturbed flows, as high residence times extend from the roof of the vein to the side walls. A higher blood flow rate increases the strength of the disturbed flows, whilst a variation of the needle angle and depth shifts the position of high residence times within the vein. Figure 6.10 shows that the needle disrupts the flow downstream, however these disturbed flows do not have high residence times except when the needle is placed near the roof of the vein.

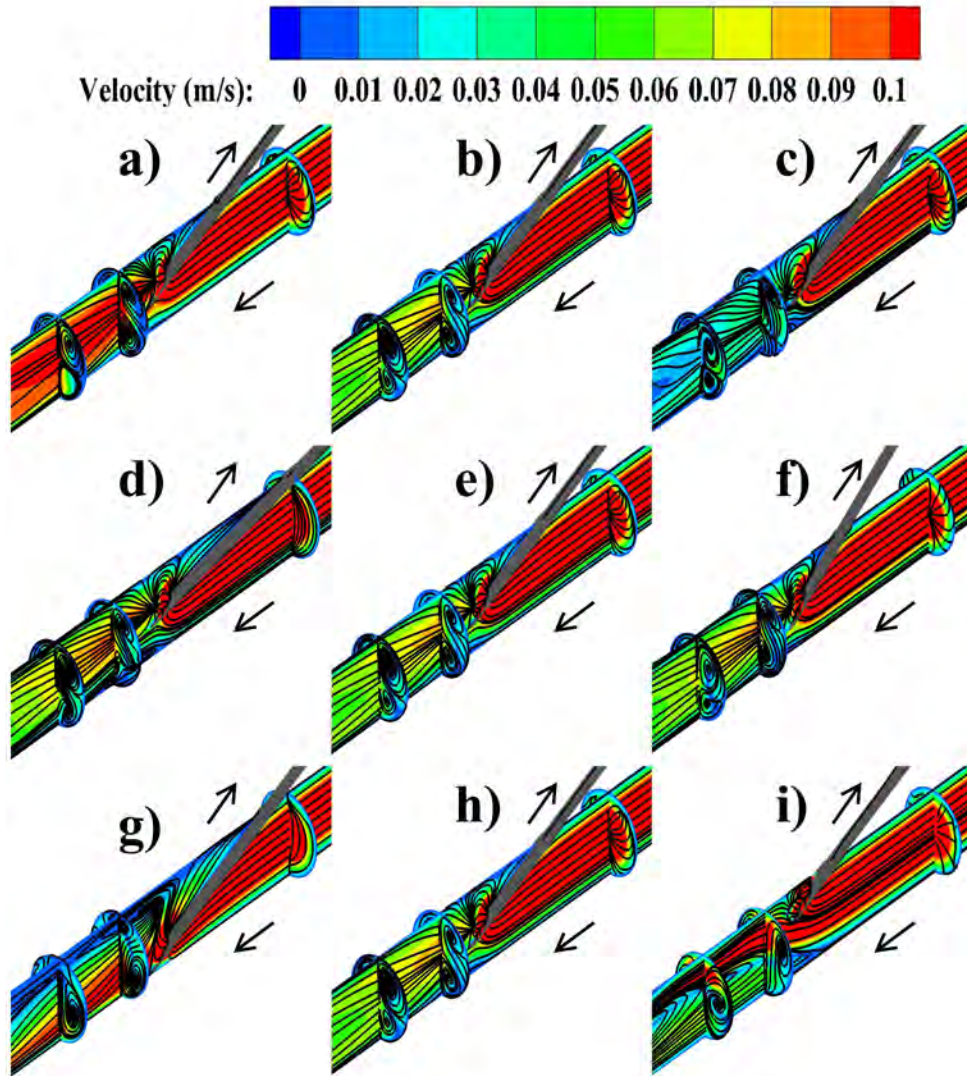


Figure 6.10: Pathlines and velocity contours on cross-sectional planes for the arterial needle in an antegrade orientation during diastole. Arrows indicate predominate direction of blood flow. a-c) Variation in blood flow rate (200 ml/min, 300 ml/min, 400 ml/min). Needle tip is placed in the middle of the vein at an angle of 20° . d-f) Variation in needle angle (10° , 20° , 30°). Needle tip is placed in the middle of the vein with an equivalent blood flow rate of 300 ml/min. g-i) Variation in needle position (bottom, middle, top). Needle is placed at an angle of 20° with an equivalent blood flow rate of 300 ml/min.

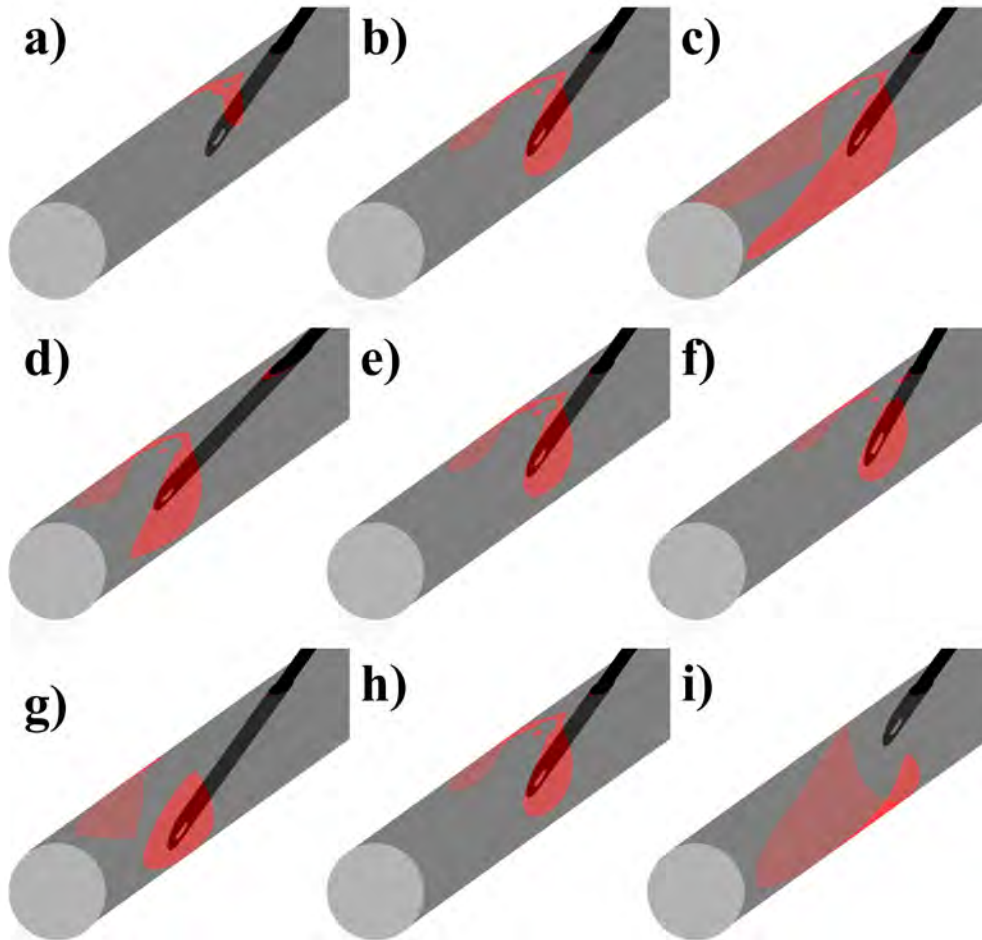


Figure 6.11: Relative residence time (time averaged over 10 cycles) on the wall of the vein normalised by the mean wall shear stress for the arterial needle in the antegrade orientation. Only high levels of RRT (>10) have been coloured in red to emphasise regions of strong secondary flows. a-c) Variation in blood flow rate (200 ml/min, 300 ml/min, 400 ml/min). Needle tip is placed in the middle of the vein at an angle of 20° . d-f) Variation in needle angle (10° , 20° , 30°). Needle tip is placed in the middle of the vein with an equivalent blood flow rate of 300 ml/min. g-i) Variation in needle position (bottom, middle, top). Needle is placed at an angle of 20° with an equivalent blood flow rate of 300 ml/min.

The area of high RRT and the amount of blood entering the back eye for the AN in antegrade is summarised in Table 6.4. Smaller regions were produced at lower blood flow rates, whilst the largest affected area occurred at blood flow rates of 400 ml/min. The severity of the affected area also increased with greater needle angles and a needle placed near the roof of the vein. The amount of flow entering the back eye remained fairly constant in all cases except when the needle position was varied. A needle placed towards the roof of the vein resulted in the highest amount of blood entering the needle.

Table 6.4: Summary of back eye flow and area of high RRT for all tested parameters of the arterial needle in the antegrade orientation

Parameter	Back Eye Flow (%)	Area of high RRT
200 ml/min	44%	3.98 cm ²
300 ml/min	42%	45.01 cm ²
400 ml/min	41%	122.51 cm ²
10°	41%	38.04 cm ²
20°	42%	45.01 cm ²
30°	43%	50.06 cm ²
Needle at bottom of vein	33%	43.67 cm ²
Needle in middle of vein	42%	45.01 cm ²
Needle at top of vein	48%	68.64 cm ²

6.5.2 Arterial Needle in Retrograde

Velocity contours and pathlines on cross sectional planes for the AN placed in the retrograde orientation during diastole are displayed in Figure 6.12. In this orientation the region of core flow being entrained by the needle is much smaller than the antegrade orientation. A disturbed flow region occurs above and below the needle tip, primarily around the needle insertion site. The needle position and blood flow rate has a strong influence on the size of the disturbed flow regions.

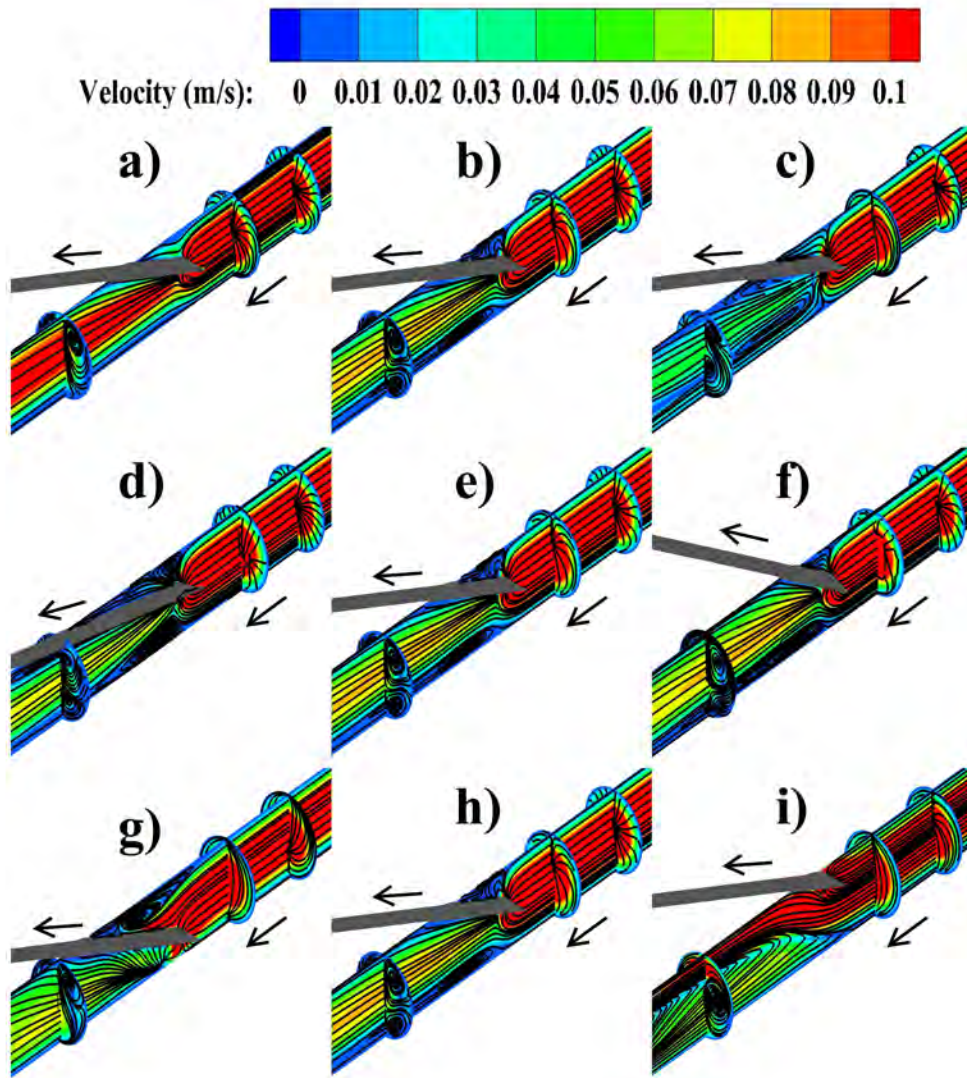


Figure 6.12: Pathlines and velocity contours on cross-sectional planes for the arterial needle in a retrograde orientation during diastole. Arrows indicate predominate direction of blood flow. a-c) Variation in blood flow rate (200 ml/min, 300 ml/min, 400 ml/min). Needle tip is placed in the middle of the vein at an angle of 20° . d-f) Variation in needle angle (10° , 20° , 30°). Needle tip is placed in the middle of the vein with an equivalent blood flow rate of 300 ml/min. g-i) Variation in needle position (bottom, middle, top). Needle is placed at an angle of 20° with an equivalent blood flow rate of 300 ml/min.

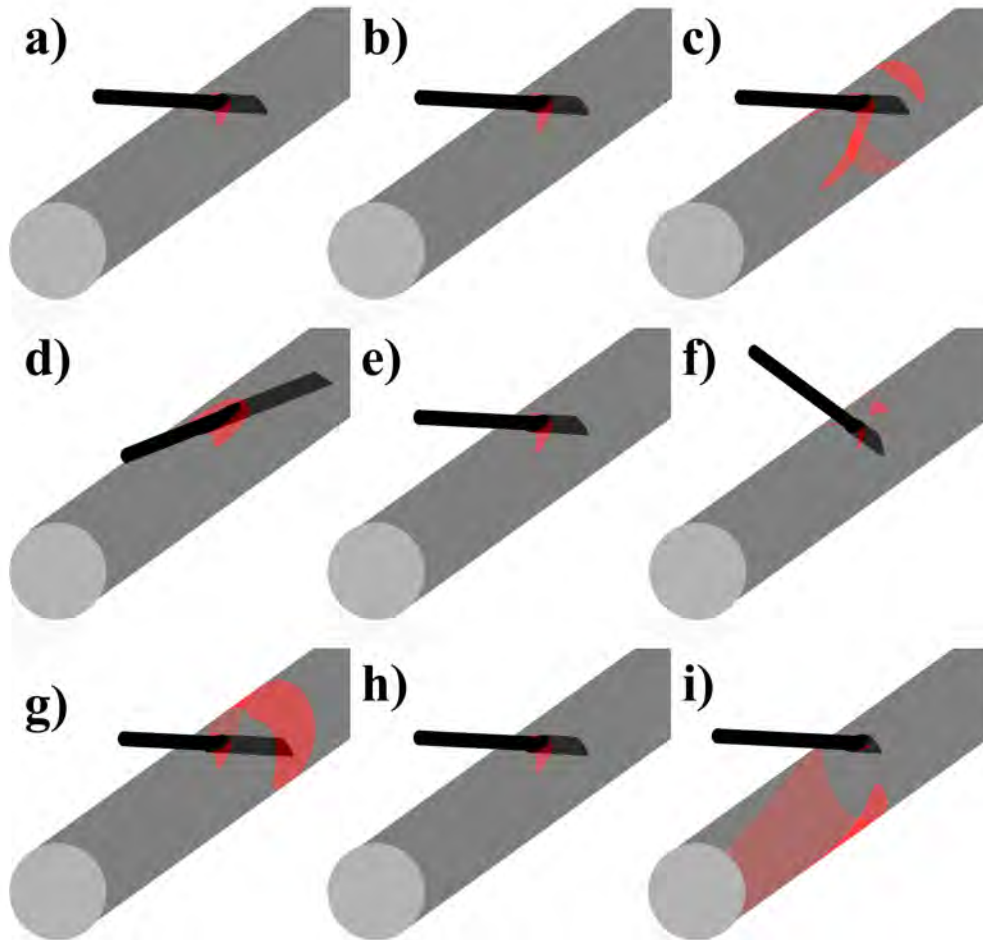


Figure 6.13: Relative residence time (time averaged over 10 cycles) on the wall of the vein normalised by the mean wall shear stress for the arterial needle in the retrograde orientation. Only high levels of RRT (>10) have been coloured in red to emphasise regions of strong secondary flows. a-c) Variation in blood flow rate (200 ml/min, 300 ml/min, 400 ml/min). Needle tip is placed in the middle of the vein at an angle of 20° . d-f) Variation in needle angle (10° , 20° , 30°). Needle tip is placed in the middle of the vein with an equivalent blood flow rate of 300 ml/min. g-i) Variation in needle position (bottom, middle, top). Needle is placed at an angle of 20° with an equivalent blood flow rate of 300 ml/min.

Figure 6.13 displays the RRT on the surface of the vein for the AN in the retrograde orientation. Regions of high residence time coincide with the locations of the disturbed flows displayed in Figure 6.12. High blood flow rates increased the area of high residence time; however the position of the needle tip with respect to the vein wall had the greatest influence.

Table 6.5 displays the area of high RRT and amount of blood entering the back eye for the AN in retrograde orientation. A retrograde orientation displayed smaller areas of high RRT compared to an antegrade orientation in all cases except for a needle placed near the bottom of the vein. Similar trends were exhibited where higher blood flow rates and greater needle angles increased residence times, although the effect of needle angle was minimal. A needle placed near the wall of the vein or with a blood flow rate of 400 ml/min yielded the largest areas. The amount of blood entering the back eye for a retrograde placed AN remained relatively similar for all blood flow rates and needle positions. The level of back eye flow was also lower in all cases compared to the antegrade orientation except for a needle placed near the floor of the vein.

Table 6.5: Summary of back eye flow and area of high RRT for all tested parameters of the arterial needle in the retrograde orientation

Parameter	Back Eye Flow (%)	Area of high RRT
200 ml/min	35%	1.82 cm ²
300 ml/min	37%	2.36 cm ²
400 ml/min	37%	12.90 cm ²
10°	37%	1.66 cm ²
20°	37%	2.36 cm ²
30°	36%	3.00 cm ²
Needle at bottom of vein	39%	55.40 cm ²
Needle in middle of vein	37%	2.36 cm ²
Needle at top of vein	37%	69.80 cm ²

6.5.3 Venous Needle

The structure of the VNJ and subsequent mixing is displayed in Figure 6.14. At blood flow rates of 200 ml/min and 300 ml/min the exiting jet structure is coherent and laminar. Upon impingement on the floor of the vein the jet begins to spread and secondary flows develop, followed by complex mixing. Secondary flows are exhibited in every case except at lower blood flow rates. At blood flow rates of 400 ml/min jet dissipation occurs directly after exiting the needle. The angle of the needle has little influence on the exiting jet structure and downstream mixing.

Table 6.6 shows that the flow exiting the VN back eye is minimal in every case, where the exiting jet structure is not influenced by the presence of the back eye in the VN. The percentage rises slightly when the needle is inserted at 30°.

Table 6.6: Summary of back eye flow and area of high RRT and high TAWSS for all tested parameters of the venous needle

Parameter	Back Eye Flow (%)	Area of high RRT	Area of high TAWSS (>40 Pa)
200 ml/min	0.43%	4.39 cm ²	7.02 cm ²
300 ml/min	0.29%	3.73 cm ²	9.92 cm ²
400 ml/min	0.25%	4.69 cm ²	14.65 cm ²
10°	0.07%	1.31 cm ²	0.00 cm ²
20°	0.29%	3.73 cm ²	9.92 cm ²
30°	1.99%	6.13 cm ²	15.06 cm ²
Needle at bottom of vein	0.44%	0.79 cm ²	28.21 cm ²
Needle in middle of vein	0.29%	3.73 cm ²	9.92 cm ²
Needle at top of vein	0.27%	8.97 cm ²	0.10 cm ²

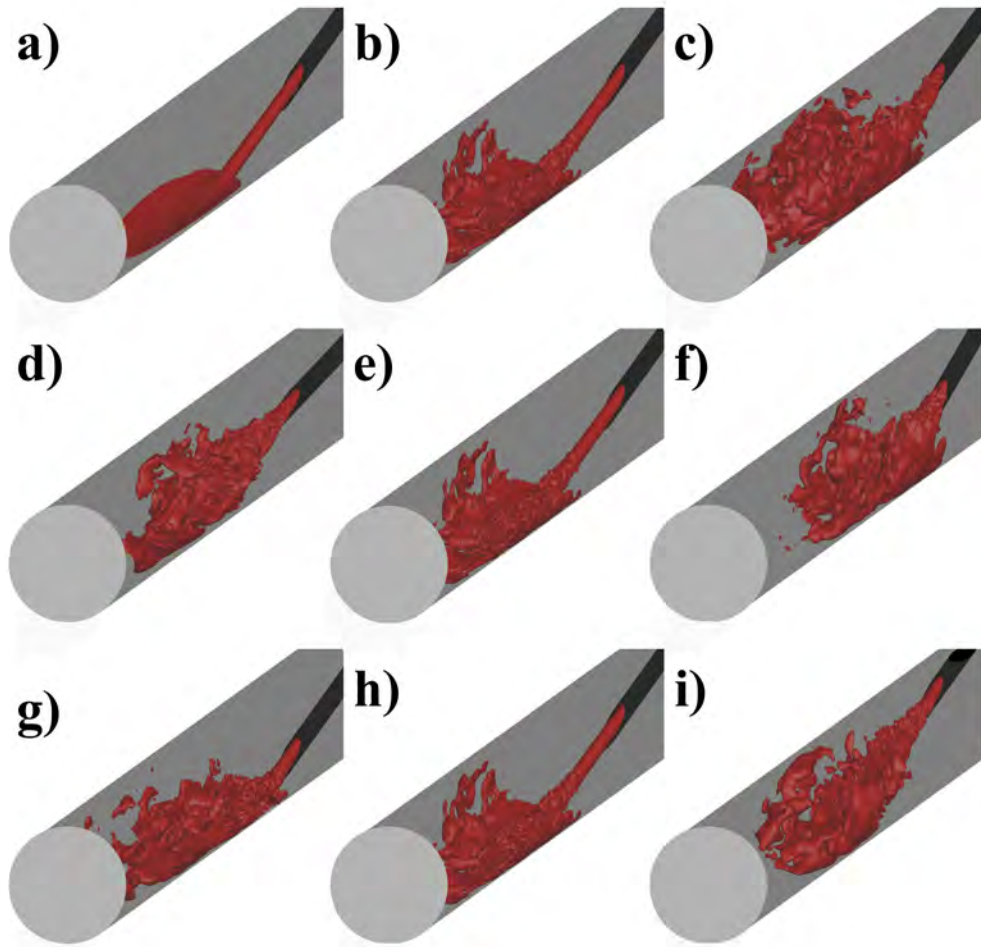


Figure 6.14: Velocity isosurfaces (1 m/s) visualising the venous needle jet during diastole. a-c) Variation in blood flow rate (200 ml/min, 300 ml/min, 400 ml/min). Needle tip is placed in the middle of the vein at an angle of 20° . d-f) Variation in needle angle (10° , 20° , 30°). Needle tip is placed in the middle of the vein with an equivalent blood flow rate of 300 ml/min. g-i) Variation in needle position (bottom, middle, top). Needle is placed at an angle of 20° with an equivalent blood flow rate of 300 ml/min.

The effects of excessively high TAWSS produced by the VN are displayed in Figure 6.15. In all cases except at shallow needle angles a large region of high TAWSS occurs at the point of jet impingement. The TAWSS exceeds the threshold (40 Pa) at which endothelial cells are damaged. The area of high TAWSS spreads out from the floor of the vein and represents the transition of the free stream jet to a wall jet. The TAWSS drops below 10 Pa downstream of the impingement zone as the effects of the jet begin to dissipate.

Table 6.6 also displays the area of TAWSS above 40 Pa. High blood flow rates and greater needle angles increase the area of excessively high TAWSS, however the greatest force is produced when the needle tip is placed closest to the floor of the vein. Conversely, a needle placed near the roof of the vein or at a shallow needle angle produced a negligible area of high TAWSS. The jet must travel a greater distance before impingement in these positions, resulting in a lower jet velocity as a greater level of jet dissipation occurs.

Figure 6.16 displays the RRT on the vein surface and indicates that pockets of the secondary flows contain low and oscillating WSS. Patches of high residence time appear on the roof of the vein above the needle tip and downstream, in the region where secondary flows are present after jet impingement.

The area of high RRT was presented previously in Table 6.6 and shows that high (400 ml/min) and low (200 ml/min) blood flow rates as well as sharp needle angles produce regions of higher residence times, whilst a needle placed near the roof of the vein produces the largest area.

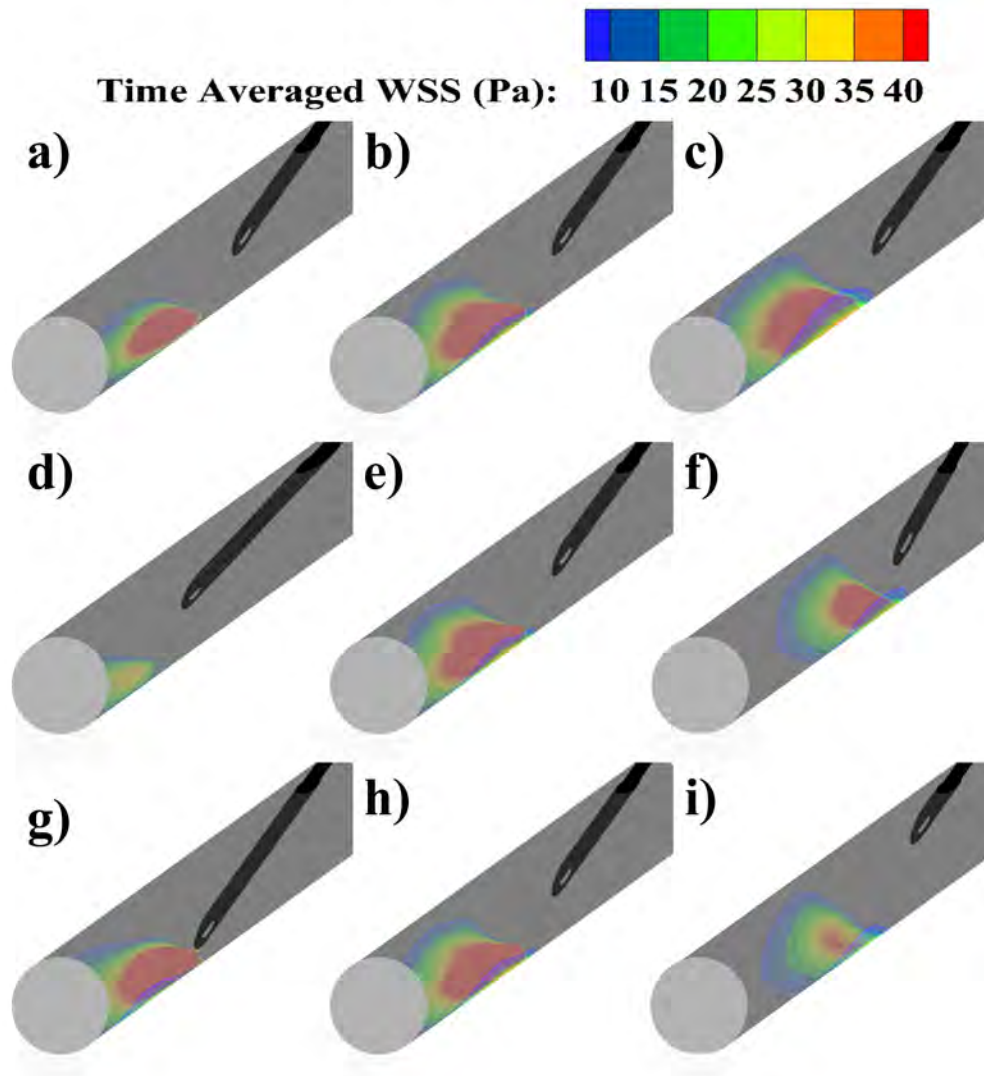


Figure 6.15: Time average wall shear stress (over 10 cycles) on the wall of the vein for the venous needle. Only regions above 10 Pa have been coloured to emphasise regions of excessively high stress. The scale has also been capped at the threshold reported to cause endothelial damage (40 Pa). a-c) Variation in blood flow rate (200 ml/min, 300 ml/min, 400 ml/min). Needle tip is placed in the middle of the vein at an angle of 20°. d-f) Variation in needle angle (10°, 20°, 30°). Needle tip is placed in the middle of the vein with an equivalent blood flow rate of 300 ml/min. g-i) Variation in needle position (bottom, middle, top). Needle is placed at an angle of 20° with an equivalent blood flow rate of 300 ml/min.

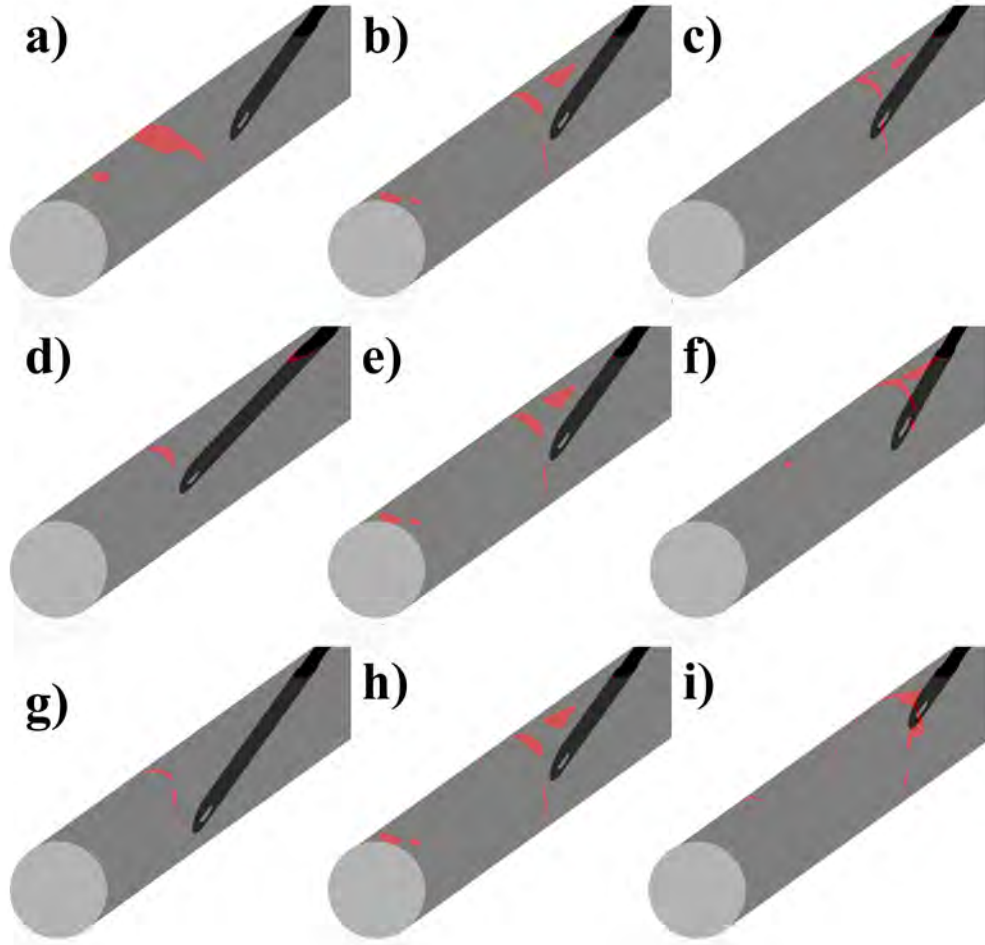


Figure 6.16: Relative residence time (time averaged over 10 cycles) on the wall of the vein normalised by the mean wall shear stress for the venous needle. Only high levels of RRT (>10) have been coloured in red to emphasise regions of strong secondary flows. a-c) Variation in blood flow rate (200 ml/min, 300 ml/min, 400 ml/min). Needle tip is placed in the middle of the vein at an angle of 20° . d-f) Variation in needle angle (10° , 20° , 30°). Needle tip is placed in the middle of the vein with an equivalent blood flow rate of 300 ml/min. g-i) Variation in needle position (bottom, middle, top). Needle is placed at an angle of 20° with an equivalent blood flow rate of 300 ml/min.

6.5.4 Needle Rotation

Pathlines and contours of velocity along the central plane of the vein for inserted and rotated AN positions during diastole are presented in Figure 6.17. The secondary flows are more focused around the needle tip with antegrade placement, whilst a large disturbed flow region forms on the floor of the vein for retrograde placement, similar to the results presented above. These secondary flows are similar in nature for both the inserted and rotated positions in either antegrade and retrograde placement.

Regions of high residence time on the surface of the vein for the AN in the inserted and rotated positions are displayed in Figure 6.18. The regions of high RRT are very similar in shape and size for both AN positions. These areas have been quantified in Table 6.7 and show that an AN in the inserted position for antegrade placement produces a slightly smaller region of high RRT whereas a rotated position produces a smaller region when placed in the retrograde orientation. However the difference in area between each position is small, indicating that AN rotation is negligible.

The TAWSS distribution along the floor of the vein produced by the VN in the inserted and rotated positions is displayed in Figure 6.19. The distribution is similar for both needles positions, with the WSS decreasing radially from the point of impingement, highlighting the localised nature of the flow exiting the VN. Both positions displayed regions of high TAWSS above the threshold reported to cause endothelial damage (40 Pa). Both positions also displayed similar areas of high TAWSS, with the inserted position displaying a slightly larger area as illustrated in Table 6.7.

The residence time on the surface of the vein produced by the VN in the inserted and rotated positions is displayed in Figure 6.20 whilst the area of high RRT for each position is shown in Table 6.7.

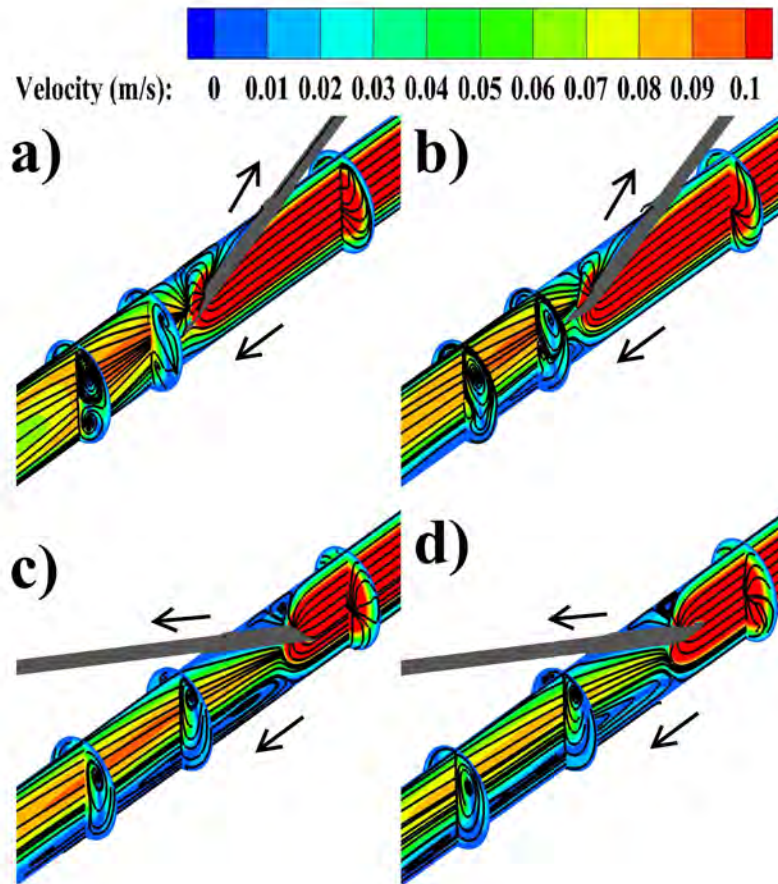


Figure 6.17: Pathlines and velocity contours on cross-sectional planes for the arterial needle in different positions during diastole. Arrows indicate predominate direction of blood flow. The needle tip is placed in the middle of the vein at an angle of 20° with an equivalent blood flow rate of 300 ml/min. a) Arterial needle in the inserted position (antegrade orientation) b) Arterial needle in the rotated position (antegrade orientation) c) Arterial needle in the inserted position (retrograde orientation) d) Arterial needle in the rotated position (retrograde orientation)

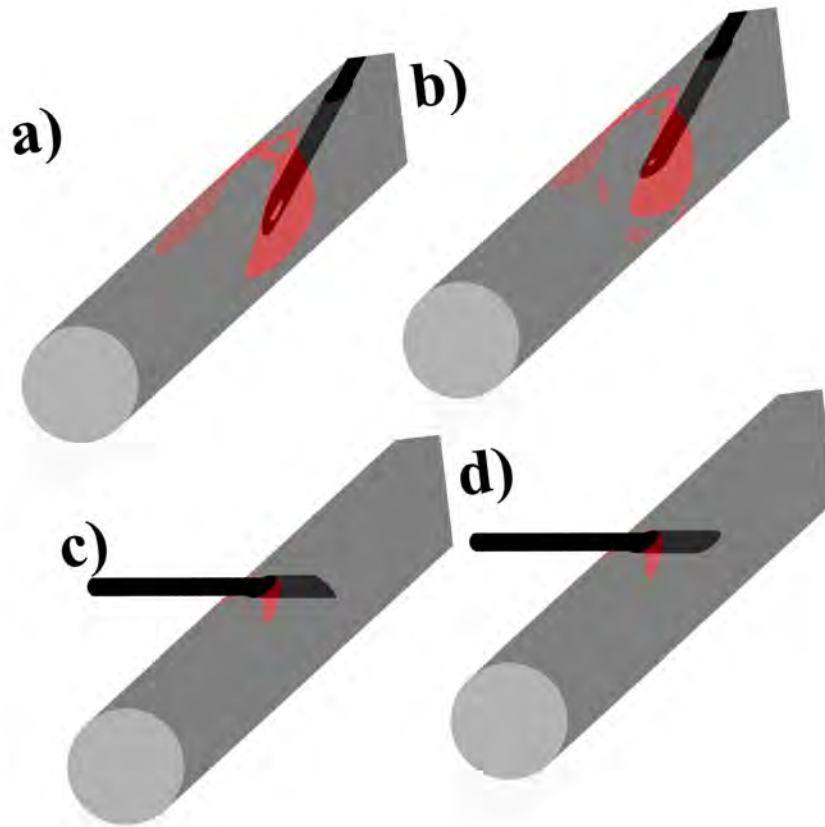


Figure 6.18: Relative residence time (time averaged over 10 cycles) on the wall of the vein normalised by the mean wall shear stress for the arterial needle in different positions. Only high levels of RRT (>10) have been coloured in red to emphasise regions of strong secondary flows. The needle tip is placed in the middle of the vein at an angle of 20° with an equivalent blood flow rate of 300 ml/min. a) Arterial needle in the inserted position (antegrade orientation) b) Arterial needle in the rotated position (antegrade orientation) c) Arterial needle in the inserted position (retrograde orientation) d) Arterial needle in the rotated position (retrograde orientation)

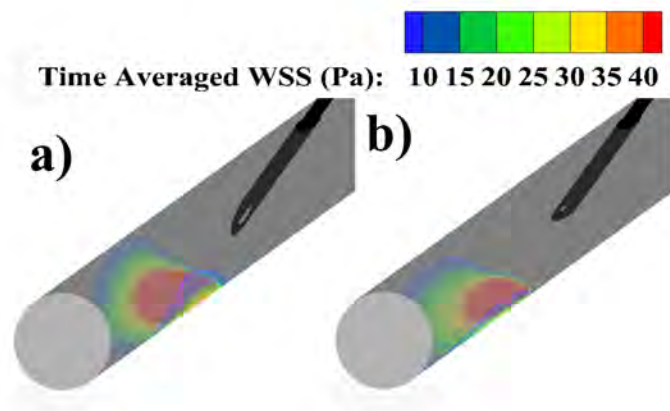


Figure 6.19: Time average wall shear stress (over 10 cycles) on the wall of the vein for the venous needle in the rotated and inserted position. Only regions above 10 Pa have been coloured to emphasise regions of excessively high stress. The scale has also been capped at the threshold reported to cause endothelial damage (40 Pa). The needle tip is placed in the middle of the vein at an angle of 20° with an equivalent blood flow rate of 300 ml/min. a) Venous needle in the inserted position b) Venous needle in the rotated position

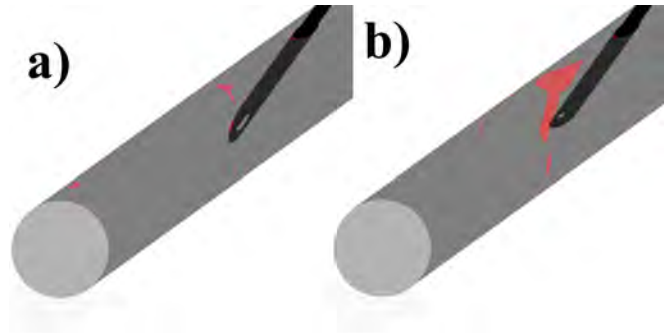


Figure 6.20: Relative residence time (time averaged over 10 cycles) on the wall of the vein normalised by the mean wall shear stress for the venous needle in different positions. Only high levels of RRT (>10) have been coloured in red to emphasise regions of strong secondary flows. The needle tip is placed in the middle of the vein at an angle of 20° with an equivalent blood flow rate of 300 ml/min. a) Venous needle in the inserted position b) Venous needle in the rotated position

The rotated position produced a much larger region of high residence time than the inserted position. The region of high RRT produced by a rotated needle was mainly located on the roof of the vein above the needle tip.

Table 6.7: Summary of the area of high RRT and high TAWSS for different needle positions

Needle	Orientation	Position	Area of high RRT	Area of high TAWSS (>40 Pa)
Arterial	Antegrade	Inserted	56.96 cm^2	-
		Rotated	58.58 cm^2	-
Arterial	Retrograde	Inserted	2.95 cm^2	-
		Rotated	2.05 cm^2	-
Venous	Antegrade	Inserted	1.86 cm^2	9.92 cm^2
		Rotated	9.55 cm^2	6.34 cm^2

Table 6.8 presents the amount of flow passing through the back eye for each needle in the inserted and rotated positions. For an AN placed in antegrade there is approximately 43% and 25% entering through the back eye in the inserted and rotated positions, respectively. A retrograde placement displayed similar results with approximately 37% entering through the back eye for the inserted position and 42% for the rotated position. The flow leaving the VN back eye in both positions is negligible, accounting for less than 1%. This indicates that VN needle position has no influence on the flow exiting the back eye.

Table 6.8: Summary of back eye flow for different needle positions

Needle	Orientation	Position	Back Eye Flow (%)
Arterial	Antegrade	Inserted	42%
		Rotated	25%
Arterial	Retrograde	Inserted	37%
		Rotated	42%
Venous	Antegrade	Inserted	<1%
		Rotated	<1%

6.6 Discussion

Stenosis due to IH develops as a response to endothelial injury and has a high correlation with blood flows; in particular low WSS [56], oscillatory WSS [4] or excessively high WSS [61, 62]. Dialysis needles may influence the formation of IH in the drainage vein of AVFs, which is a common problem in haemodialysis patients [27, 33, 98]. Stenotic lesions often lead to thrombosis, the primary reason of reduced patency in vascular access, due to reduced flow conditions or lesion rupture [1, 2].

6.6.1 Arterial Needle

Results for the AN in an antegrade and retrograde orientation demonstrated strong secondary flows localised around the needle tip, as the blood was withdrawn from the vein. In the antegrade orientation the flow must travel around the needle before being entrained through the central bore. The disturbed flow region is created from reduced flow produced by the entrainment of blood into the needle. Its size and strength is therefore highly dependent on the position of the needle within the vein. This was most clearly demonstrated when the needle was placed close to the vein floor, resulting in the strongest disturbed flows. Another disturbed flow region also formed along the floor of the vein at high blood flow rates and shallow needle angles and was most pronounced when the needle tip was placed towards the roof of the vein. The risk of access recirculation may be higher when the needle is in these positions as the secondary flows extended further downstream and may interact with the VN. Rothera et al. [119] examined the influence of needle separation distance on access recirculation and found that needles placed within 2.5 cm of each other do not result in access recirculation, which is similar to the results found in this study where secondary flows did not extend further than 2.5 cm. This indicates that a long cannulation segment in the drainage vein may not be required. Ultrasound guides can be used to optimise the needle position within the blood vessel to minimise potential access recirculation and the risk of intimal thickening, which is prone to developing in disturbed flows.

The region of core flow being entrained in the retrograde orientation is much smaller compared to the antegrade orientation. In this orientation the disturbed flow region was located around the needle tip and insertion site. A larger disturbed flow region also formed below the needle which may contribute to access recirculation if the secondary flows extend towards the

VN. However this only extended a few centimeters downstream indicating that the risk of access recirculation is not dependent on AN orientation. Ozmen et al. [123] also reported no statistical difference in access recirculation between antegrade and retrograde orientation. As the flow field around the AN remained localised around the needle tip, the needles can be placed in close proximity without increasing the risk of access recirculation. This may also increase the number of radiocephalic fistulae created as surgeons would not be required to create a long venous outflow for cannulation.

Endothelial cells are sensitive to flow reversal and oscillating flows as these flows change the structure of the endothelial layer from regular striated patterns to random orientations, which increases vascular permeability and endothelial cell turnover, leaving the blood vessel susceptible to the deposition of inflammatory mediators [41, 58]. The strong secondary flows around the AN coincided with regions of high residence time which may lead to IH. For the antegrade orientation they extend from the roof of the vein to the side walls whilst the retrograde orientation showed localised areas around the insertion site and floor of the vein. Aneurysms commonly form at the needle insertion sites due to a weakened blood vessel from repeated needle puncture [86]. The localisation of disturbed flows around the insertion site may be a contributing factor to this complication.

For both needle orientations the blood flow rate had the greatest influence on the area affected by high RRT, where higher flows coincided with a larger region of RRT. The position of the needle shifted the affected region, with the greatest reduction evident when the needle tip was located in the centre of the vein at a shallow angle, away from the walls of the blood vessel. For an AN in antegrade or retrograde orientation, the results of this study suggest that the optimum method to reduce the risk of IH is to use lower blood flow rates. However, it is noted that this can require longer dialysis

sessions to attain the required clearance which will conflict with the patient's lifestyle. Ensuring the needle tip is placed away from the walls of the blood vessel may also reduce the risk of intimal thickening. While this study found an association between antegrade orientation and larger RRT regions which would lead to IH, Parisotto et al. [124] reported an 18% increase in risk of access failure with the retrograde orientation. Access failure can occur from a range of factors such as infection or aneurysm blow out. The higher access failure of retrograde orientation has been attributed to the endothelial flap which is created with retrograde puncture, which can be held open through fistula flow forces after the needle is removed [124].

For the antegrade orientation the amount of blood entering the back eye remained consistent, between 41-44% for all needle angles and blood flow rates. Needle depth had the greatest influence on back eye flow due to the resistance imposed by the walls of the blood vessel. The amount of flow entering the back eye was lower in the retrograde orientation than antegrade orientation, remaining consistently between 35-39% for all needle positions and blood flow rates. The high level of back eye flow is similar to that reported in catheters and cannulas where the side holes can contribute between 30-50% of the total flow [115, 116, 118]. This result is explained through the position of the back eye, whose role is to reduce the resistance in the central bore. In the retrograde orientation the path of least resistance for the core flow is directly through the central bore due to the direction of needle placement. This study indicates that needle orientation influences the resistance of flow entering the AN, where an antegrade orientation may increase the negative pressure in the arterial line due to higher back eye efficiency.

6.6.2 Venous Needle

A high speed jet was shown to exit the VN. Upon impingement on the vein floor the jet begins to spread and creates complex secondary flows. These complex secondary flows were identified in every case except at blood flow rates of 200 ml/min because the jet is coherent and laminar at lower blood flow rates but becomes unstable at 400 ml/min. The potential core of all jets does not contain turbulent mixing and maintains a constant velocity [165], which explains the coherent structure seen in most cases. At higher blood flow rates the length of the potential core is reduced and the flow exiting the central bore becomes transitional as seen at blood flow rates of 400 ml/min. The increase in jet dissipation which occurs close to the impingement zone is due to a rise in static pressure near the wall caused by the decrease in momentum of the jet [187]. The effects of the wall are subsequently translated upstream through the jet, triggering early jet break down. The minimal flow through the back eye shows that this feature has very little influence on the exiting jet structure. The slight rise in back eye flow when the needle was placed at 30° can be attributed to the increased exposure to the core flow.

Elevated levels of TAWSS (above the threshold reported to denude the endothelium) were identified at the impingement zone. The region of high TAWSS is caused by the translation of momentum upon impingement. Higher blood flow rates, greater needle angles and a needle tip placed closer to the vein floor produced larger regions of elevated TAWSS. In these cases the velocity of the jet is higher or the effects of dissipation are constrained, as the jet travels a shorter distance resulting in a greater force upon impingement. High WSS has been shown by others at lower jet heights and higher jet Reynolds numbers on jet impingement on a flat plate at normal incidence [165]. Only a shallow needle angle prevented a region of high

TAWSS, as the jet travels a longer distance before impingement, providing greater dissipation which reduces the velocity of the jet. Therefore, lower blood flow rates, shallow needle angles and placement of the needle tip away from the floor of the vein can reduce the high TAWSS occurring at the point of jet impingement.

Endothelial cells which line the inner surface of blood vessels have the ability to detect blood flow. These endothelial cells are sensitive to flow direction and are commonly aligned in the predominant direction of axial flow under laminar flow conditions. Under multi-directional and oscillating flows, similar to that in the disturbed flow region, endothelial cells have been shown to change from a regular striated pattern to random orientations [59]. Blood vessel wall function is impaired when endothelial cells are randomly orientated as junctions between cells impede cellular communication and increased vascular permeability leaves the blood vessel susceptible to the deposition of inflammatory mediators [41, 42].

Regions of high RRT were found on the roof of the vein downstream of the needle tip, which coincided with the secondary flows produced by jet break down. This indicates that steady secondary flows occur in the disturbed flow regions which result in high residence times. High RRT can stimulate vascular smooth muscle cell migration and proliferation [56] and increases vascular permeability [41], potentially leading to IH [44]. Huynh et al. [48] examined the effects of the VNJ on endothelial cell function and identified a change in structure to the random orientation found by others. Nitric oxide, a chemical which mediates the anti-inflammatory response of the blood vessel, was also inhibited in the flow field produced by the VN. Therefore, the presence of the disturbed flow region produced by the VNJ may lead to endothelial dysfunction along the roof of the vein, suggesting that stenosis may form in the drainage vein due to the flows produced by the VN.

Similar regions of high RRT were found at blood flow rates of 200 ml/min and 400 ml/min, indicating that low blood flow rates produce steady secondary flows whilst high blood flow rates produce more pockets of complex secondary flows. This is linked to the transitional flow in the VN, where Reynolds numbers range between 924 and 1847 for the range of blood flow rates examined, indicating that an optimum blood flow rate exists which can minimise RRT. Ponce et al. [160] showed patients were at a significantly higher risk of AVF failure at blood flow rates below 310 ml/min and greater than 400 ml/min. Sharp needle angles and a needle tip placed near the roof of the vein also produced regions of higher residence time as these parameters influenced the production of secondary flows. Therefore, a blood flow rate around 300 ml/min, shallow needle angles and placement of the needle tip away from the roof of the vein may minimise the risk of IH.

6.6.3 Influence of the needles on vascular health

The influence of the needles can be examined in cases where cannulation is not conducted, such as animal models of fistulae and in patients who received a kidney transplant whose fistula was not tied off. Patard et al. [188] examined fistulae which remained open after kidney transplant and found that only 17.5% of AVFs thrombosed, over a mean time of 39 months representing a four year patency rate of 61%. Similar results have been reported in other studies over comparable time frames [189]. These figures compare favourably to the 48% four year patency rate found by Kazemzadeh et al. [21], indicating that the needles influence the development of vascular complications. However, Wang et al. [190] identified intimal thickening in the proximal vein of pig AVFs within 42 days of surgery, showing that other factors stimulate the development of IH.

Regions of high TAWSS and RRT were found downstream of the VN whilst disturbed flow regions with high RRT surround the AN, which may contribute to endothelial damage and IH. Glashan and Walker [191] examined vein samples in haemodialysis fistulae and found endothelial damage and loss in the vicinity of the needle tip. However, stenosis commonly forms at the anastomosis in AVFs [27, 98], despite the high potential of endothelial damage near the needles. This suggests that endothelial recovery plays an important role in vascular health. Reidy and Schwartz [192] used rats to study denudation and recovery by removing endothelial cells in the aorta. Reendothelialisation through migration and proliferation was complete after 2-4 days, highlighting the ability of the blood vessel to recover. Endothelial denudation has been shown to lead to intimal lesions if the period of denudation continues for several days [193]. The time frames of recovery are significant as haemodialysis sessions are usually conducted every 2-4 days, indicating that the blood vessel may recover from any damage caused by the needles, thus explaining why stenosis more frequently form at the anastomosis.

6.6.4 Needle Rotation

Disturbed flows were produced by the AN in both needle positions and orientations. These disturbed flows coincided with regions of high RRT on the roof of the vein which may cause endothelial damage potentially leading to IH. Rotation of the AN had minimal effect on the size of high residence time, proving that rotation of the AN does not reduce the harmful haemodynamics which can lead to IH. This is in agreement with Parisotto et al. [124], who reported that an antegrade orientation in the inserted position is associated with better access survival compared to the rotated position and retrograde orientation.

The VNJ resulted in high WSS values along the vein floor at the point of impingement for both needle positions, producing similar sized regions of high TAWSS above the range (40 Pa) cited for endothelial damage and erosion [61]. Break down of the VNJ produced disturbed flows within the vein which lead to regions of high RRT along the roof of the vein and potential sites of IH. The key difference in the VN position was that rotating the needle increased the area of high residence time on the roof of the vein. However, regions of high TAWSS and RRT are still present in the inserted position, indicating that needle rotation has minimal effect in mitigating the harmful shear stresses.

The technique of needle rotation is conducted to alleviate pressure in the arterial line as an increase in pressure indicates that the AN has become attached to the vein wall. The AN exhibited a large degree of flow through the back eye for both needle positions. The high level of back eye flow is similar to that reported in catheters and cannulas where the side holes can contribute between 30-50% of the total flow [115, 116, 118]. An AN in the inserted position which was placed antegrade produced the highest amount of flow through the back eye, accounting for 43%. Conversely, a rotated AN placed in the same orientation produced the smallest amount of flow through the back eye (25%). The inserted position represents a more effective use of this geometrical feature when the AN is placed in antegrade due to its exposure to the core flow, indicating that needle rotation may not be an ideal technique to alleviate pressure in the arterial line. Conversely, the opposite effect was observed for a retrograde orientation, however the increase in flow through the back eye was minor. As these two quantities are similar, needle rotation may not be an ideal technique to alleviate the pressure if the central bore becomes attached to the blood vessel wall when the AN is in the retrograde orientation.

From a clinical perspective, needle rotation carries a risk of coring the vein which can lead to infiltration [85]. As both positions produce potentially damaging levels of shear stress, it is concluded that needle rotation does not provide a significant haemodynamic benefit and should not be conducted as it increases the risk of infiltration. This opinion is in agreement with Parisotto et al. [124] who believe that needle rotation is unnecessary and the technique may cause additional trauma to the blood vessel. Furthermore, the amount of flow through the back eye was significant for all positions and orientations of the AN. Placement of the AN tip away from the vein wall should be sufficient to minimise the chance of the central bore becoming attached causing temporal blockage of the arterial line.

6.6.5 Limitations

A major limitation in this study was the use of an idealised geometry for the cephalic vein, which was produced to achieve a high quality hexahedral mesh. The use of hexahedral grids in vascular access studies has been shown to produce errors in WSS calculation as low as 2% [132, 141]. The geometry also excluded the secondary flows originating at the anastomosis. Broderick et al. [97] examined the influence of various factors of turbulence generation in an AVG and found that the production of transitional structures were highly influenced by vein diameter and flow split ratio, highlighting the case specificity of AVF flows. Bozzetto et al. [99] also showed that AVF flows arising from the anastomosis are case specific. In this study, the inclusion of case specific AVF flows would reduce the clarity of the parametric analysis, which is why a simplified geometry was selected. A future study may include the needles in real geometries to investigate how these results translate to patient specific cases. The model also did not account for the effects of vessel wall compliance. McGah et al. [148] compared rigid and compliant models of

an AVF and found that the rigid models over predicted WSS by up to 50%, however differences in the downstream vein were only 10%. Limitations of this approach also exist in the uncertainty of the elastic modulus and the non-homogeneity of the blood vessel wall. Shear stresses in rigid wall models are generally higher, thus the assumption in the simulations represent the worst case scenario. Future studies may address this limitation by employing fluid-structure interaction models, although these simulations come at a dramatic increase in computational cost [135]. The assumption of the Newtonian blood model is also acknowledged. This assumption was made under the premise that at shear rates greater than 100 s^{-1} blood acts as a Newtonian fluid with constant viscosity. The application of non-Newtonian models is questionable in applications with high flows such as those produced by dialysis needles. Decorato et al. [135] compared various blood rheology models and found the mean difference in WSS at the anastomosis and downstream vein of an AVF to be approximately 10% and 13%, respectively. A future study incorporating a patient specific fistula might also include a blood rheology model tailored to the patients' blood composition.

6.7 Conclusion

Maintaining the efficiency of haemodialysis treatment is crucial, with cannulation technique forming a key component in continuing patient health care. This chapter examined the haemodynamics produced by the AN and VN during haemodialysis and assessed the potential risk of endothelial damage from flow mediated effects which can lead to IH.

Regions of high residence time corresponding to areas of disturbed flow were examined on the vein wall for both needles. High TAWSS, above the threshold reported to cause endothelial damage, was also measured

downstream of the VN coinciding with the point of VNJ impingement. These regions of high residence time and high TAWSS indicate potential sites of endothelial dysfunction which may lead to IH. The use of shallow needle angles, a blood flow rate of approximately 300 ml/min and placement of the needle tip away from the walls of the vein mitigates this risk. The localised flow field around the AN also indicated that both needles can be placed in close proximity without increasing the risk of access recirculation. This may also increase the number of patients with radiocephalic fistulae, as other sites for vascular access creation are normally preferred to create a long venous outflow for cannulation.

The results for needle rotation indicate that the haemodynamic effects of needle rotation were negligible in improving factors that affect the patency of the vascular access. This technique is usually conducted to relieve the pressure in the arterial line when the AN becomes attached to the vein wall. An AN in the inserted position when placed in antegrade maintained 43% of the flow through the back eye, indicating that an inserted position is beneficial over a rotated position in terms of resistance produced by the needle. Furthermore, the change in the level of flow through the the back eye from rotating an AN in retrograde was insignificant. Placement of the AN tip away from the vein wall has the greatest influence in mitigating the risk of elevated pressures in the arterial line. In conclusion, needle rotation should only be applied to the AN, with care to avoid infiltration, if optimal placement of the needle tip is unachievable and the arterial pressure elevates.

Chapter 7

Analysis of Cavitation in Haemodialysis Needles

This chapter investigates the hypothesis that microbubbles can form near the tip of haemodialysis needles, under cavitation caused by turbulence and pressure changes. This hypothesis is examined in two parts. Firstly, a computational model with the same methodology as presented earlier in Chapter 6 is conducted. A high amplitude sinusoidal inlet condition is imposed on the needle to investigate the blood flow rates where the pressure is sufficient to cause cavitation. Secondly, clinical measurements are conducted using a Duplex ultrasound on the extracorporeal circuit to determine if the pulsatility generated by the roller pump produces the conditions (as identified in the computational model) where cavitation might occur.

7.1 Introduction

All haemodialysis circuits contain an air trap on the venous side to measure venous pressures and to prevent large air bubbles from entering the patient's circulation. An air trap is sometimes used on the arterial side for the same purpose. There have been several cases which report the presence of air emboli or microbubbles within the extracorporeal circuit [67–72].

Microbubbles have been shown to pass through the venous air trap and enter the blood stream without activating the alarm [68, 69, 72, 73]. In addition, computational simulations have shown the inefficiency of the venous air trap in trapping bubbles smaller than 200 μm [73]. It is important to identify the source of microbubble formation in haemodialysis as there are potential pathophysiological complications for the patient.

Tissue ischemia occurs when a bubble becomes lodged in the blood vessel, blocking the blood flow and preventing the nearby tissue from receiving nutrients and oxygen. The most severe cases of ischemia occur in the lungs or brain. Fairshter et al. [77] in a post mortem analysis reported that 95.7% of haemodialysis patients had acute lung disease whilst 80.4% had chronic lung disease, with reported incidents of haemorrhage and thromboembolism. Deterioration of neurological functions has also been correlated with the duration of dialysis treatment [78]. Cerebral atrophy [80] and neurocognitive dysfunctions [81] in chronic haemodialysis patients is a recognised problem.

Furthermore, it is unknown if the presence of microbubbles in the dialyser affects the efficiency of treatment. It is therefore imperative to determine the source, and implement methods to prevent their passage through the extracorporeal circuit and into the patient. Forsberg et al. [70] suggested a high blood level in the venous chamber and a wet stored dialyser as methods

of reducing the level of microbubbles passing into the circulation.

Several sources of microbubbles have been identified based on the location of detected microembolic signals using Doppler ultrasound. These sources have been identified as the following: air remaining in the extracorporeal circuit after priming [82], air entering through leaks on the arterial side from the high negative pressures [82, 83] or diffusion of air from oversaturated dialysate [82]. The needles have also been suggested as a potential location due to cavitation [67]. Supporting this theory is the correlation between pump speed and the amount of detected bubbles, indicating that cavitation may occur around the needles with high blood flows [68, 72].

Cavitation occurs when the static pressure falls below the vapour pressure of blood generating microbubbles and has been reported to occur in mechanical heart valves [194]. Previous studies have assumed that microbubbles consist of carbon dioxide due to its higher solubility and lower partial pressure within blood [194, 195]. As the majority of carbon dioxide is stored in plasma, the vapour pressure of plasma is similar to that of water; approximately -95000 Pa gauge pressure at 37°C [196].

The clinical relevance of this work is to determine if the needles contribute to the formation of microbubbles due to cavitation. The aim of this study was two fold; to determine the conditions in which cavitation may occur at the needles, and to evaluate the potential for cavitation to occur within the haemodialysis extracorporeal circuit based on the pulsatility of the roller pump. A full scale computational model of the needles is utilised with an extreme range of blood flow rates to examine the conditions in which the vapour pressure is reached. The velocity pulse produced by the roller pump was then measured in a clinical setting using a Sonosite S-series Ultrasound (FUJIFILM Sonosite Inc, Tokyo, Japan) at various locations throughout the extracorporeal circuit.

7.2 Methods

7.2.1 Computational Model

The computational model follows the settings described in Chapter 6, with slight variations imposed to simulate a worst case scenario to determine the conditions in which cavitation might occur. A 17G needle was placed at an angle of 30° to expose the back eye to the core flow and reduce the internal diameter, subsequently elevating the pressures within the needle. The AN was placed in both antegrade and retrograde orientations to cover all clinical setups. The VN was placed in the antegrade orientation according to normal convention.

The vein profile used in Chapter 6 was again enforced at the vein inlet, whilst elevated needle inlets were used. A sinusoidal waveform with a mean blood flow rate of 600 ml/min and an amplitude of 600 ml/min was imposed at the AN to simulate a large range of flows. The period of one cycle was approximated as 0.7 seconds to replicate clinical conditions. The VN was simulated with a constant blood flow rate of 600 ml/min as the literature suggests that cavitation may occur downstream of the VN in regions of turbulence [67]. Chapter 5 and Chapter 6 showed that complex secondary flow occurs downstream of the VN whilst the flow field around the AN remained localised. Based on these results, the pressure inside the AN and downstream of the VN was monitored, as these regions were mostly likely to produce a pressure drop sufficient for cavitation to occur. All cases were initialised for 7 cycles with a time step of 0.01 seconds, with 50 iterations per time step. The time step was then dropped to 0.0001 seconds, with data being collected over 2 cycles.

7.2.2 Clinical Analysis

7.2.2.1 Haemodialysis Setup

A patient was selected based on a normal functioning native arteriovenous fistula (fistula flow >600 ml/min) and dialysing under normal conditions. The velocity waveform was measured in 5 locations as displayed in Figure 7.1; between the AN and the roller pump, between the roller pump and the arterial air trap, between the arterial air trap and the dialyser, between the dialyser and venous air trap and between the venous air trap and VN. Ethical approval was provided by the Human Research Ethics Committee at the Prince of Wales Hospital (HREC Number: 13/313, SSA Number: 13/G/425). The patient gave informed written consent in accordance with the ethical standards prior to study participation.

Conventional haemodialysis procedure was conducted using an AK200S device (Gambro, Lund, Sweden), Gambro BL 208BD bloodlines and a high-flux Revaclear 400 dialyser (Gambro, Lund, Sweden). The extracorporeal circuit contained an arterial and venous air trap and a dual roller pump. Both needles were standard 15G fistula needles (Gambro, Lund, Sweden) and were inserted in a native radiocephalic fistula. The circuit was primed with 500 ml of saline and 3000 units of heparin sodium to prevent clotting. Anticoagulant therapy was maintained throughout the session in the form of hourly bolus injections of heparin sodium.

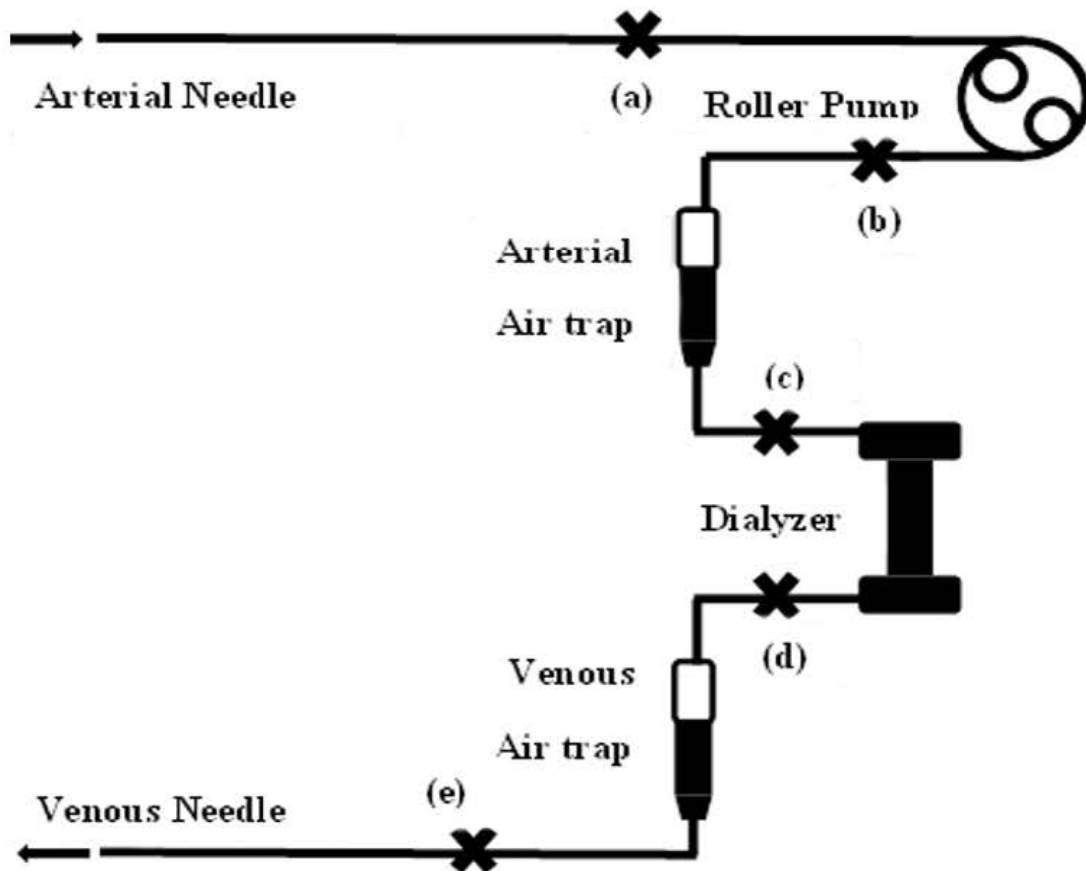


Figure 7.1: Locations (denoted by X) on the extracorporeal circuit where Doppler ultrasound measurements were conducted. a) between the arterial needle and the roller pump b) between the roller pump and arterial air trap c) between the arterial air trap and dialyser d) between the dialyser and venous air trap e) between the venous air trap and venous needle

The extracorporeal blood flow rate was 315 ml/min and the temperature of the dialysate remained constant at 36°C. The arterial pressure (measured at the arterial air trap) was -145 ± 5 mmHg whilst the venous pressure (measured at the venous air trap) was 126 ± 5 mmHg. The treatment conditions remained unaltered throughout the duration of the experiment.

7.2.2.2 Ultrasound Setup

The velocity waveform produced by the roller pump was measured ex-vivo using a Sonosite S-series Ultrasound (FUJIFILM Sonosite Inc, Tokyo, Japan). The velocity waveform was extracted using the Doppler mode and an L38xi 5 MHz transducer (FUJIFILM Sonosite Inc, Tokyo, Japan). Standard contrast gel was used as the coupling medium to efficiently transfer the signal from the transducer to the extracorporeal tubing. To ensure a clear signal was being returned to the transducer, the Color Doppler mode was used to image the tubing and blood flow, as displayed in Figure 7.2

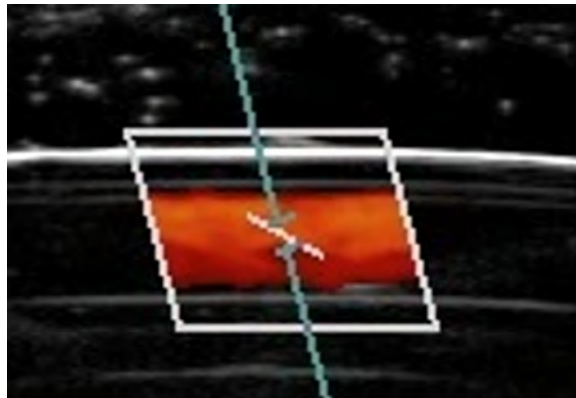


Figure 7.2: Colour Doppler imaging of the extracorporeal tubing and blood flow

The transducer was held parallel to the tubing, with a gel layer of approximately 2 cm in thickness on the surface to ensure a sufficient length was imaged and a clear signal received. The gate width was fixed at 1 mm to ensure a small sample volume was measured which minimised noise. The probe was set at 50° to align with the direction of blood flow (less than the recommended 60°, to minimise errors when measuring velocity). The repeatability of the haemodialysis machine was ensured by taking three measurements at each location.

7.2.2.3 Statistical analysis

The velocity and time points were extracted from the ultrasound images using graph digitising software (Silk Scientific Inc, Utah, USA). Repeatability of the pump performance was assessed by expressing the data as maximum instantaneous velocity +/- SD and minimum instantaneous velocity +/- SD, calculated over 10 pump cycles. The average tubing diameter was calculated based on the pump setting (315 ml/min) and the average velocity at each location over 10 pump cycles. The instantaneous velocities were subsequently converted to volumetric flow rates assuming an average tubing diameter of 3.89 mm. The computational simulations estimated the flow rates which would produce a sufficient pressure drop in the AN to cause cavitation. These flow rates are subsequently extrapolated to the clinical measurements based on the average tubing diameter. This enabled a comparative analysis between the clinical measurements and the computational results.

7.3 Results

7.3.1 Arterial Needle Computational Model

Figure 7.3 displays isosurfaces of vapour pressure (-95000 Pa) at various times in the sinusoidal inlet condition, for the AN placed in the antegrade orientation. At maximum flow (1200 ml/min) the pressure within the needle bore falls below -95000 Pa, indicating that cavitation may occur at extreme blood flow rates. The pressure drop occurs across the entire area of the needle entrance, extending from the trailing edge of the back eye to the top of the bevel. As the flow rate decreases, the pressure within the AN rises above the cavitation threshold pressure.

Isosurfaces of vapour pressure (-95000 Pa) at various times in the sinusoidal inlet condition for the AN placed in the retrograde orientation are displayed in Figure 7.4. Similarly, the pressure within the needle bore fell below the cavitation threshold at extreme blood flow rates. The pressure distribution at the needle entrance is similar for both antegrade and retrograde orientations, which indicates that blood flow rate is a primary factor which influences the pressure within the needle.

Figure 7.5 shows the relationship between the pressure drop at the AN entrance and the blood flow rate. The graph provides a clear indication that when the blood flow rate is above 600 ml/min in the pump cycle, the pressure at the needle entrance drops below -95000 Pa, providing the conditions for cavitation to occur. The pressure distribution is also identical over both pump cycles, indicating that microbubble formation may occur consistently throughout treatment under these conditions. Furthermore, needle orientation does not influence the pressure drop within the needle.

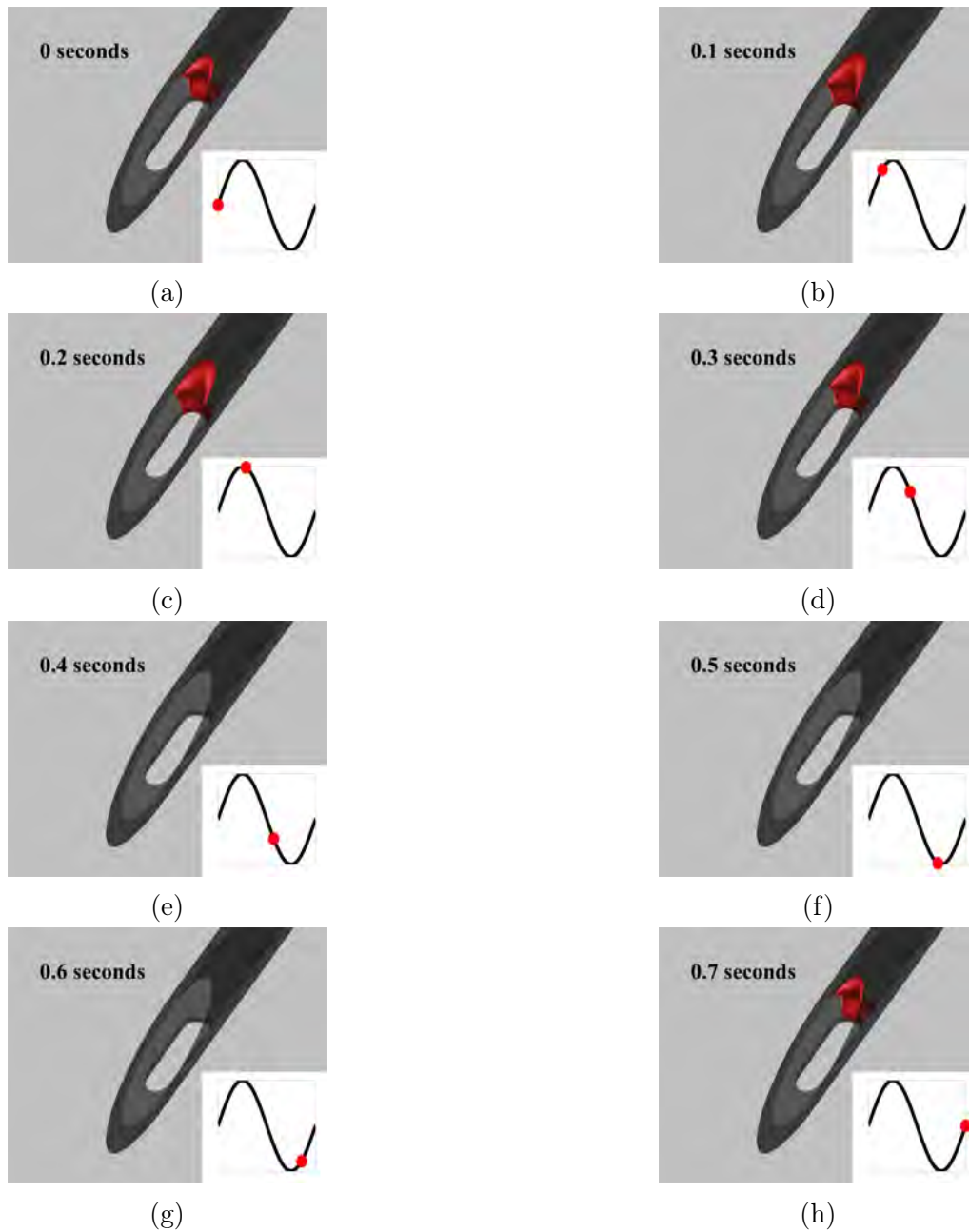


Figure 7.3: Isosurface of Vapour Pressure (-95000 Pa) in the arterial needle at different times in the sinusoidal inlet condition when the needle is placed in the antegrade orientation. a) 0 seconds b) 0.1 seconds c) 0.2 seconds d) 0.3 seconds e) 0.4 seconds f) 0.5 seconds g) 0.6 seconds h) 0.7 seconds

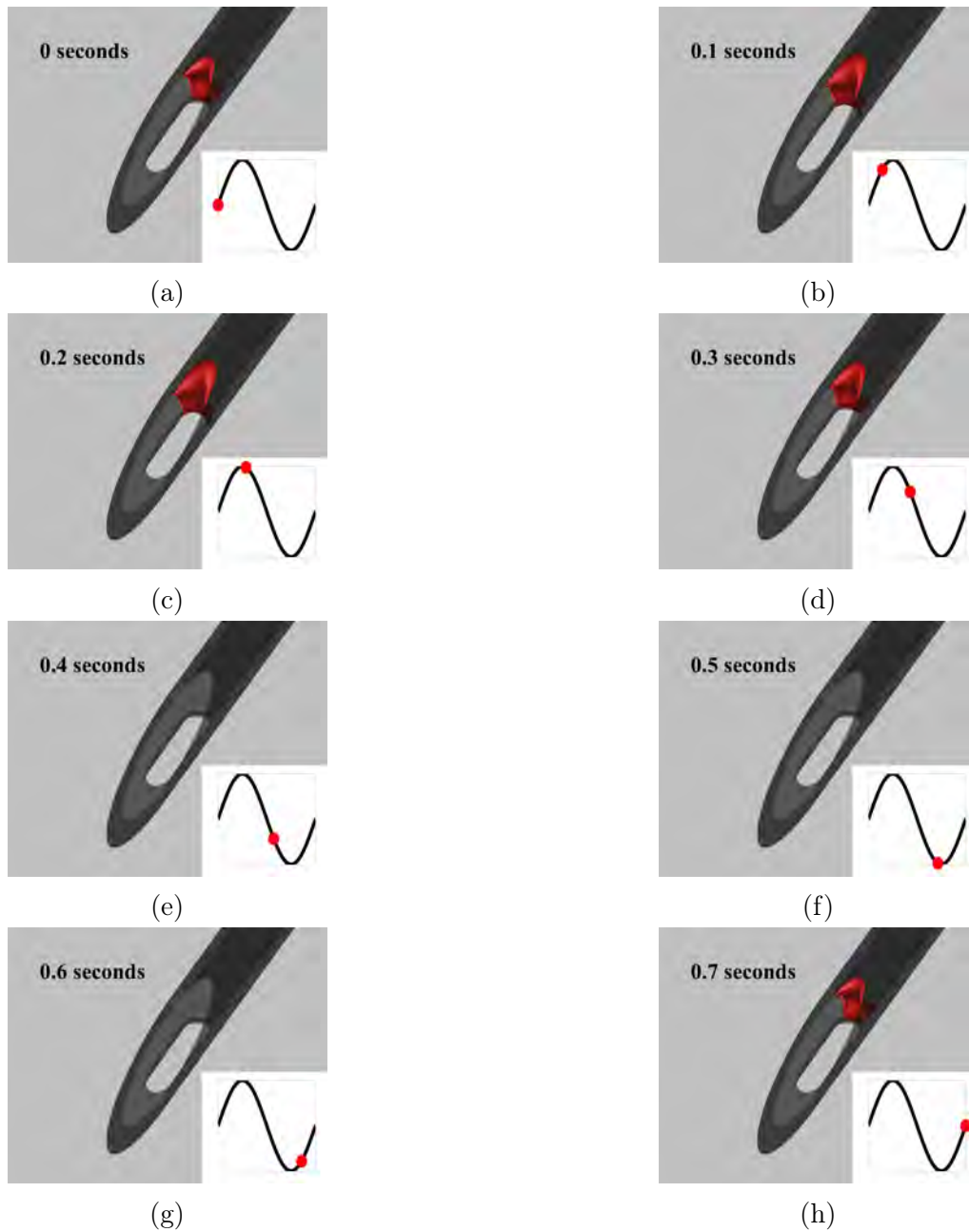


Figure 7.4: Isosurface of Vapour Pressure (-95000 Pa) in the arterial needle at different times in the sinusoidal inlet condition when the needle is placed in the retrograde orientation. a) 0 seconds b) 0.1 seconds c) 0.2 seconds d) 0.3 seconds e) 0.4 seconds f) 0.5 seconds g) 0.6 seconds h) 0.7 seconds

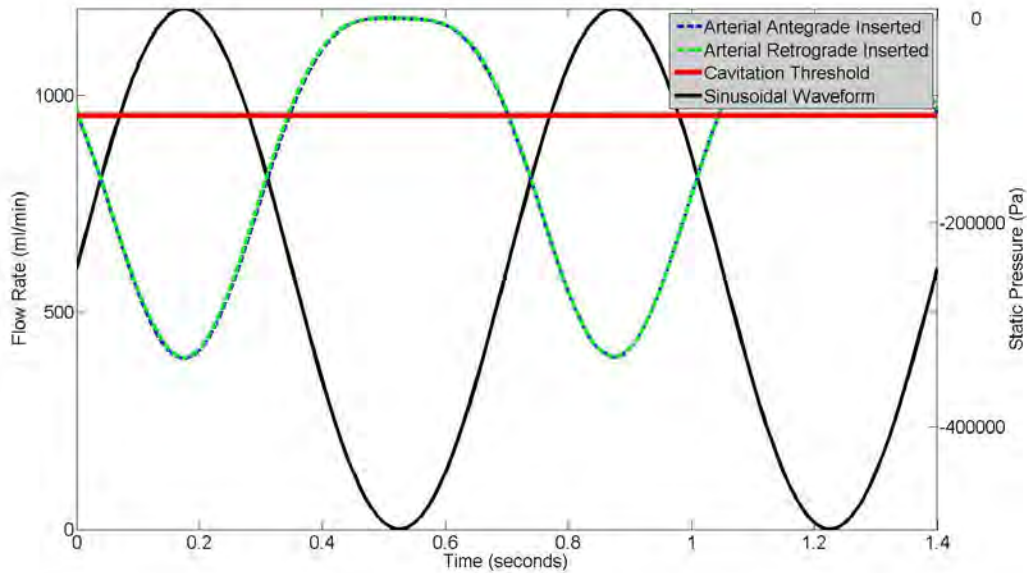


Figure 7.5: Range of pressures at the needle opening over two periods of the sinusoidal waveform. As the blood flow rate increases the pressure in both the antegrade and retrograde positions falls below the vapour pressure of blood; providing an environment for cavitation

7.3.2 Venous Needle Computational Model

No regions of pressure below the vapour pressure of blood (-95000 Pa) were found downstream of the VN. Isosurfaces and pressure plots have subsequently not been shown. These results indicate that the complex flows which form downstream of the VN do not produce the conditions in which microbubbles may form under cavitation.

7.3.3 Clinical Measurements

The velocity waveform as measured at each location in the extracorporeal circuit is displayed in Figure 7.6. It is evident that, although the pump is set at a constant flow rate, the extracorporeal system contains a highly pulsatile flow. This flow profile is generated by the rotary motion of the roller pump compressing the tubing during 360° of revolution. The waveform approaches a quasi-sinusoidal waveform when entering the extracorporeal circuit through the AN with an amplitude of approximately 20 cm/s (140 ml/min) indicating that the pulse extends in both directions across the roller pump. The largest pulse occurs directly after the roller pump and extends from approximately 58 cm/s (410 ml/min) to -72 cm/s (-513 ml/min) resulting in a brief period of flow reversal. The pulse created by the pump travels through the extracorporeal circuit. The dialyser has a dampening effect on this pulse as shown in Figure 7.6d. The waveform approaches a saw-tooth function with approximate amplitude of 15 cm/s (100 ml/min) after the dialyser. The component of flow reversal has been completely dampened after the venous air trap producing a quasi-constant flow exiting the VN.

The complete range of velocities and SD are displayed in Table 7.1. The pulse amplitude is largest after the roller pump (129.6 cm/s, 920 ml/min) and is gradually dampened by the arterial air trap (16.25 cm/s, 115 ml/min), dialyser (14.37 cm/s, 100 ml/min) and venous air trap (6.87 cm/s, 50 ml/min). The standard deviation remained relatively low (<6%) throughout the measured 10 cycles. Despite the pulse near the AN, the velocities are not sufficient to induce the pressure drop required for cavitation based on the results of the computational model. However, cavitation may be possible across the rollers of the pump as the largest pulse amplitude was measured at this location.

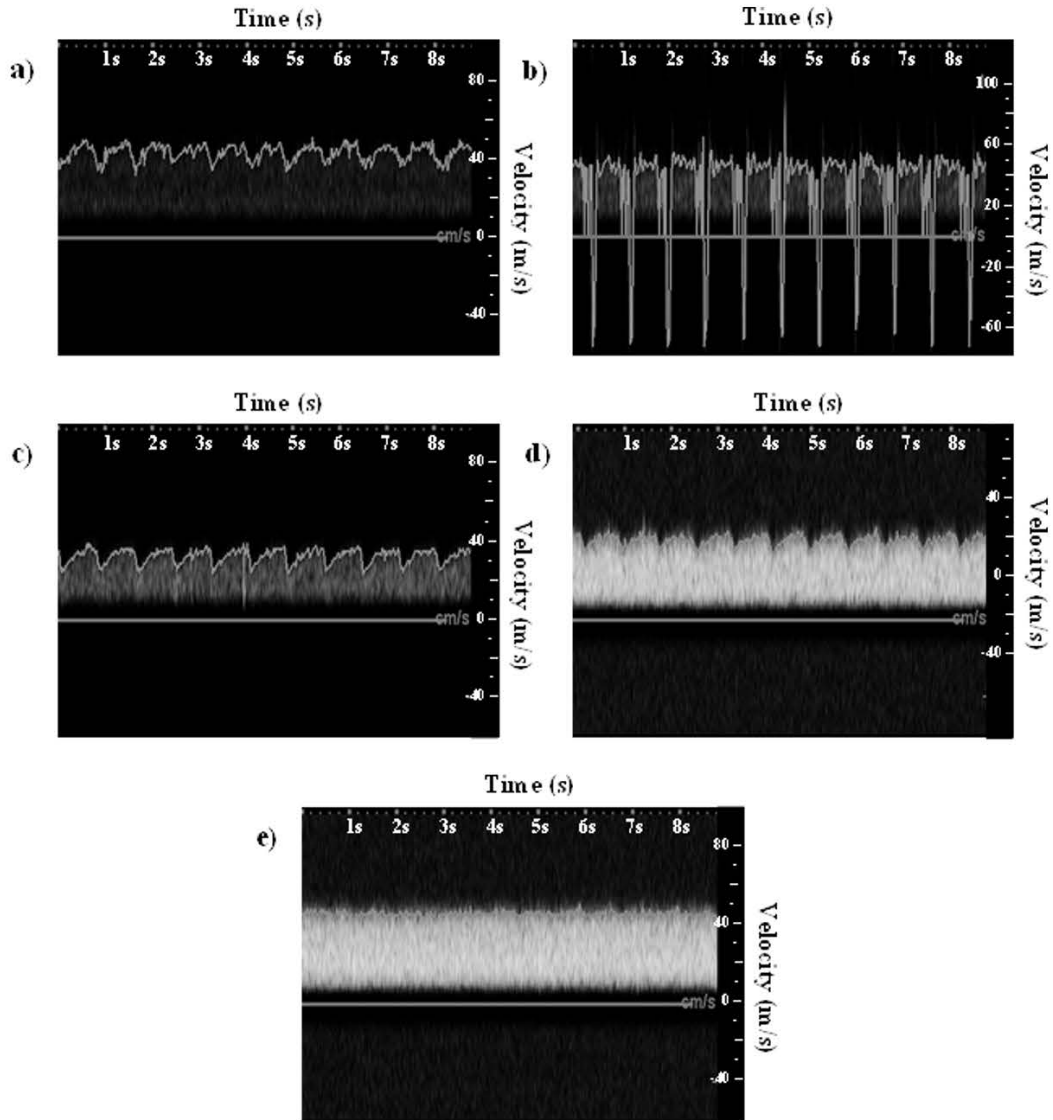


Figure 7.6: Velocity waveform as measured by Doppler ultrasound in the haemodialysis extracorporeal circuit. a) between the arterial needle and the roller pump b) between the roller pump and arterial air trap c) between the arterial air trap and dialyser d) between the dialyser and venous air trap e) between the venous air trap and venous needle

Table 7.1: Summary of maximum, minimum and the standard deviation over 10 cycles of the roller pump

Location	Maximum Velocity	Maximum Flow Rate	SD	Minimum Velocity	Maximum Flow Rate	SD
Arterial needle to Roller Pump	51.25 cm/s	365 ml/min	2.1%	31.73 cm/s	226 ml/min	5.8%
Roller Pump to Arterial Air Trap	57.60 cm/s	410 ml/min	3.0%	-72.00 cm/s	-513 ml/min	5.7%
Arterial Air Trap to Dialyser	39.38 cm/s	281 ml/min	2.5%	23.13 cm/s	165 ml/min	3.8%
Dialyser to Venous Air Trap	47.50 cm/s	339 ml/min	2.1%	33.13 cm/s	236 ml/min	3.0%
Venous Air Trap to Venous Needle	48.75 cm/s	348 ml/min	1.3%	41.88 cm/s	299 ml/min	3.1%

Figure 7.7 displays the pressures and velocity occurring near the peristaltic pump during rotation. Upon further observation of the motion of the pump it was evident that when the rollers are orientated at 0° and 180° , temporary occlusion occurs which results in a brief period of no flow (depicted by \blacktriangle in Figure 7.7). Directly after the instant of occlusion a high pressure exists in front of the roller resulting in the water hammer effect (surge of pressure when a fluid in motion is forced to stop or changes momentum) which produced a sudden reversal of flow (depicted by \bullet in Figure 7.7). For the majority of the cycle only one roller is compressing the tubing and is characterised by a high pressure in front of the roller and low pressure behind the roller. This results in a semi-constant net forward flow of blood (depicted by \blacksquare in Figure 7.7).

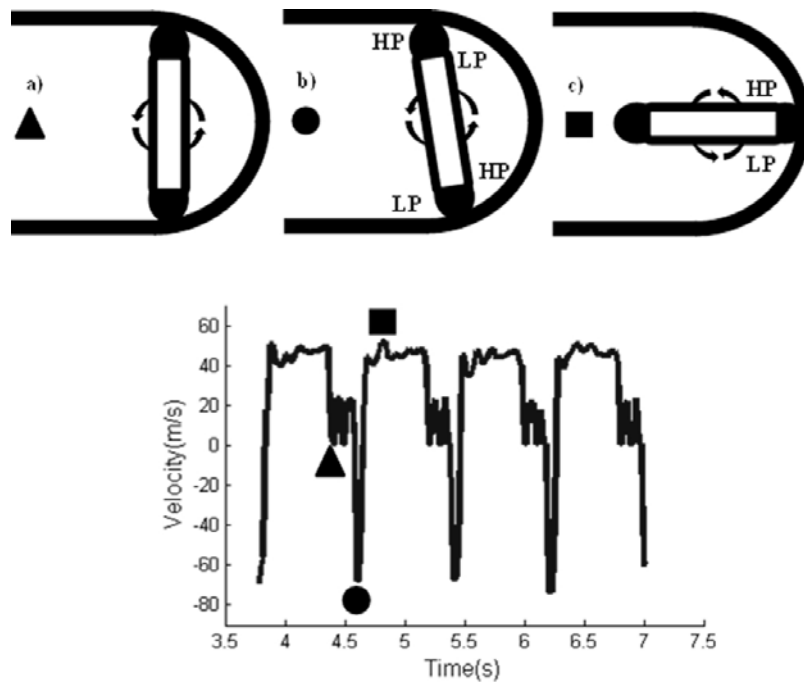


Figure 7.7: Instantaneous roller motion of the peristaltic pump (High Pressure - HP, Low Pressure - LP) a) Tubing is occluded b) Release of occluded tubing (water hammer effect) c) Smooth rotation producing maximum flow d) Velocity waveform measured after the roller pump

7.4 Discussion

Microbubbles generated in the extracorporeal circuit in haemodialysis patients have been shown to enter the blood stream without activating the alarm [68, 69, 72, 73] and can lead to tissue ischaemia. The long term effects from exposure to microbubbles is currently unknown. The source of microbubbles has not been verified, although several possibilities have been suggested including: air remaining in the extracorporeal circuit after priming [82], air entering through leaks on the arterial side from the high negative pressures [82, 83], diffusion of air from oversaturated dialysate [82] or cavitation at the needles [67]. Supporting the later theory is the correlation between pump speed and the amount of detected bubbles, indicating that cavitation may occur under high blood flows [68, 72]. Furthermore, it is unknown if the presence of microbubbles in the dialyser affects the efficiency of treatment. It is imperative to determine the source of microbubbles, and implement methods to prevent their passage through the extracorporeal circuit and into the patient.

The results of the computational model indicated that cavitation may occur at the AN at elevated blood flow rates. Large pressure drops were measured at the entrance to the AN, with the pressure falling below the vapour pressure at blood flow rates greater than 600 ml/min. Clinical measurements were conducted to supplement the computational models. The velocity pulse produced by the roller pump was measured using Duplex ultrasound, with the pump set to deliver a blood flow rate of 315 ml/min. The blood entered the AN with a pulse amplitude of 140 ml/min which produced a maximum instantaneous blood flow rate of 365 ml/min. This indicates that although cavitation can form at the AN at elevated blood flow rates, it is unlikely to do so within a clinical environment.

The computational models simulated a worst case scenario, where a 17G needle was placed at an angle of 30° to expose the back eye to the core flow and reduce the internal diameter to inflate the pressures within the needle. Clinically, smaller needles are used to reduce the trauma of blood vessel puncture, however they are unable to deliver the required blood flow rate for efficient dialysis. Most dialysis patients are cannulated with 15G and 16G needles, which would reduce the pressure within the needle. Furthermore, the orientation of the needle within the vein itself had no effect on the pressure drop occurring at the needle entrance. Therefore, it is unlikely that the instantaneous blood flow rate in the AN is sufficient to induce the pressure drop required for cavitation (>600 ml/min).

The computational models did not produce pressures below the vapour pressure near the VN, despite being simulated with a blood flow rate of 600 ml/min. The blood exiting the VN was found to be quasi-steady due to the dampening effect of the extracorporeal circuit. The amplitude of the pulse near the VN, as measured with Duplex ultrasound, was approximately 50 ml/min with a maximum instantaneous blood flow rate of 348 ml/min. This confirms that cavitation near the VN is unlikely, even at elevated blood flow rates. Furthermore, microbubbles have been detected consistently from the start of treatment at all locations in the extracorporeal tubing after the roller pump [67]. If microbubbles are generated at the VN, it would not explain the presence of microbubbles throughout the extracorporeal circuit. This provides further evidence that cavitation at the VN is unlikely to be the source of microbubbles in haemodialysis patients.

The rollers of the peristaltic pump are the key component affecting the pulsatility and pressure in the extracorporeal circuit. The largest pulse was measured between the roller pump and arterial air trap and was approximately 920 ml/min. During most of the rotation, one roller

compresses the tubing creating a forward travelling pressure wave. However, when the rollers are at 0° and 180° both rollers are compressing the tubing producing temporary occlusion. After this instant, the travelling pressure wave reverses direction due to a high post-pump pressure in a phenomenon known as the water hammer effect [197] which has previously been visualised in an FSI simulation [198]. It is this phenomenon that causes the extracorporeal tubing to pulse.

The computational results indicate that large pressure drops from sharp changes in geometry and elevated blood flow rates above 600 ml/min are necessary for blood to cavitate. Stegmayr et al. [68] compared various venous air traps based on the presence of air microbubbles, for blood flow rates ranging from 50-600 ml/min, and found that the amount of air microbubbles detected within the extracorporeal circuit increased with increasing pump speed. The ultrasound measurements in this chapter showed that the roller pump induces instantaneous flow reversal of approximately -513 ml/min directly after the roller leaves the occlusion position. After temporary occlusion, the blood flow rate jumps to an instantaneous value of 410 ml/min. Furthermore, when the rollers are in the occluded position sharp changes in the tubing diameter occur, which the computational model noted as a key factor for cavitation.

Large pressure drops may occur in the vicinity of the roller when in the occluded position as the instantaneous blood flow rate (-513 ml/min) was found to approach the critical value of 600 ml/min. The ultrasound measurements were conducted under normal haemodialysis conditions with a blood flow rate of 315 ml/min. The results suggests that cavitation may occur across the rollers when they are in the occluded position at elevated blood flow rates. Additionally, Rolle et al. [71] only detected microemboli after the roller pump at blood pump speeds higher than 450 ml/min, further supporting the conclusion that cavitation is unlikely to occur at the

AN but microbubbles may be generated through similar mechanisms at the roller pump under elevated pump speeds.

The venous air trap is an effective mechanism in the circuit to remove this pulse. The dialyser and distensibility of the tubing also provides a degree of dampening. Furthermore, it is apparent that the blood pressure within the vein counteracts the pulse traveling back towards the AN. This can be observed in Figure 7.6d through the repeatability of the waveform, as the periods of the heart and pump are inevitably asynchronous. The dampening effect of blood pressure further indicates that the necessary pressure drop at the AN to create microbubbles from cavitation would only occur at extreme blood flow rates.

The repeatability of the pump was also confirmed at each measured location across 10 pump cycles, with the standard deviation not exceeding 6% of the maximum and minimum velocities. This error arises from the variability in the pumping mechanism, transducer angle, signal deconstruction and movement of the tubing due to its flexibility. One proposed theory is that microbubbles form from air remaining in the extracorporeal circuit after priming [82]. However, the repeatability of the pump supports the theory that cavitation may occur at the roller pump, as microbubbles have been detected consistently throughout the duration of dialysis [68, 71].

A crucial factor in the computational results is the estimation of blood vapour pressure. As plasma has a high water content and a high solubility of carbon dioxide within it, the vapour pressure of blood is commonly estimated to be similar to that of water; a gauge pressure of approximately -95000 Pa [196]. The temperature of the blood is kept constant throughout the extracorporeal circuit as the dialysate solution is heated to 36°C. The haemodialysis machine also alarms if large changes in temperature occur.

This negates any subsequent variations in fluid properties due to large temperature changes. Therefore, the estimation of blood vapour pressure was appropriate for the computational study.

Another factor which influences cavitation is the presence of nuclei or weaknesses in the fluid. Chambers et al. [195] found that blood alone does not contain sufficiently large nuclei which can induce cavitation. However, the introduction of the needles and extracorporeal circuit provides locations for nucleation sites, such as gases caught in microscopic crevices or contaminant particles within the blood itself. The low pressures in the computational results were shown to occur at the entrance of the needle, in the vicinity of the back eye and bevel. The geometry in this region provides many sharp edges and cavities in which particles can become trapped, thereby providing nucleation sites. These locations also induce large pressure drops. However, the ultrasound measurements indicated that the pressure drops at the AN required for cavitation are unlikely to occur under normal haemodialysis conditions. Rolle et al. [71] measured the level of microemboli across the extracorporeal circuit using an ultrasound sensor and did not detect the presence of microemboli in the arterial line for blood flow rates between 200-450 ml/min, further supporting this conclusion.

Despite the venous air trap not being an effective mechanism at preventing the passage of small microbubbles, it was shown to significantly dampen the pulse produced by the pump. This is due to the free surface of blood and the pressure inside the air trap, which replicates the function of a windkessel. The level of blood remains relatively stable throughout treatment due to the constant pressure exerted on the free surface. The balance of forces between the blood volume and pressure both dampen the pulsatility of blood entering the venous air trap. Vortices are generated near the free surface from the incoming blood [73]. These vortices may also dampen the pulsed blood flow

entering the venous air trap. Furthermore, Forsberg et al. [70] suggested a high blood level in the venous chamber and a wet stored dialyser as methods of reducing the level of microbubbles passing into the circulation. It is advised that all haemodialysis circuits incorporate both an arterial and venous air trap to reduce the pulse produced by the pump and increase the potential of filtering microbubbles from the extracorporeal circuit.

In regards to the generation of microbubbles, this study showed that cavitation at the pump is a potential source of microbubble formation due to the large velocity drop across the two rollers which produced an instantaneous maximum and minimum blood flow rate of 410 ml/min and -513 ml/min, respectively. The instantaneous blood flow rates may approach the critical value of 600 ml/min identified in the computational study. If cavitation is occurring at the pump, the use of multiple rollers coupled with reduced compression of the tubing may prevent the total occlusion and subsequent flow reversal that was observed. A computational optimisation of a roller pump has shown that increasing the number of rollers can produce more uniform and steady flow conditions and reduces the instantaneous maximum velocity [198]. However, further investigation is required to determine if cavitation at the pump is the source of microbubble formation in the haemodialysis extracorporeal circuit.

7.5 Conclusion

Several sites in the extracorporeal circulation have been suggested as sources of microbubble formation. Computational simulations revealed that cavitation of blood is possible at elevated blood flow rates and in regions with sharp changes in geometry, which can produce large pressure drops sufficient to drop the static pressure below the vapour pressure of blood.

Doppler ultrasound measurements showed that the flow through the extracorporeal circuit is highly pulsatile due to the rotary motion of the peristaltic pump, with the greatest pulse occurring directly after the pump itself. Cavitation is unlikely to occur at the VN, may occur at the AN at elevated blood flow rates but most probably transpires at the roller pump at the instant where the two rollers are causing complete occlusion.

Chapter 8

Covidien Cannula: An alternative device for Vascular Access

This chapter examines the efficacy of the Argyle™ Safety Fistula Cannula with Anti-Reflux Valve to metal needles; in haemodialysis access. The same computational model used in the analysis of the needles is applied, with an emphasis on similar haemodynamic conditions. The VN is examined, as it was shown previously that the VN produces a larger flow field than the AN, with both high TAWSS and disturbed flows and thus has a greater impact on endothelial damage.

8.1 Introduction

Metal needles are the preferred device used to transfer blood to and from the dialysis circuit. Plastic cannulae have been used to extract blood in other areas of medicine with great success, such as ventricular assist devices [108–110], cardiopulmonary bypass [111–113] and central venous catheters

[114–116]. Developments in these fields have resulted in an optimised geometry of the tip and side holes, as well as improved placement in the respective blood vessel to reduce the risk of thrombus formation. In contrast the design of metal needles has remained relatively unchanged. Plastic cannulae are consequently the preferred product in these fields due to their higher performance and reduced risk of complications.

In terms of haemodynamic performance, the focus of research has been towards reducing shear rates and pressure drops within the cannula. However, the haemodynamics within the blood vessel are also important, as IH can develop as a result of vascular access [27, 33]. The haemodynamic conditions which have been correlated with endothelial damage were shown to occur around the needles in Chapter 6. Similar flow structures may also occur around the plastic cannula.

The plastic cannula requires a metal needle for cannulation, which the plastic cannula sheathes. Once the needle is positioned within the vein it is removed, leaving the cannula in-situ. The internal diameter of the cannula is subsequently larger than the metal needle, thereby reducing the velocity in the central bore. It is hypothesised that the incidence of IH may be reduced with plastic cannulae due to its unique design, in particular the larger diameter and symmetric arrangement of the side holes which may reduce the effects of the jet.

This chapter extends the work presented in Chapter 6 by investigating the haemodynamic conditions produced by a plastic cannula (Argyle™ Safety Fistula Cannula with Anti-Reflux Valve) when blood is returned to the cephalic vein using numerical models. The flow field produced by the plastic cannula is also compared against the metal needle to determine if this device offers any haemodynamic advantage.

8.2 Numerical Methods

The computational model follows the settings described in Chapter 6. A 15G Argyle™ Safety Fistula Cannula with Anti-Reflux Valve (Covidien Pty Ltd, Dublin, Ireland) was inserted in an idealised cephalic vein with a diameter of 10 mm. The cannula was fixed at an angle of 10°, a common position in clinical practice due to the cannula's unique insertion technique. The cannula consists of four circular side holes arranged in a staggered formation of two pairs as shown in Figure 8.1.

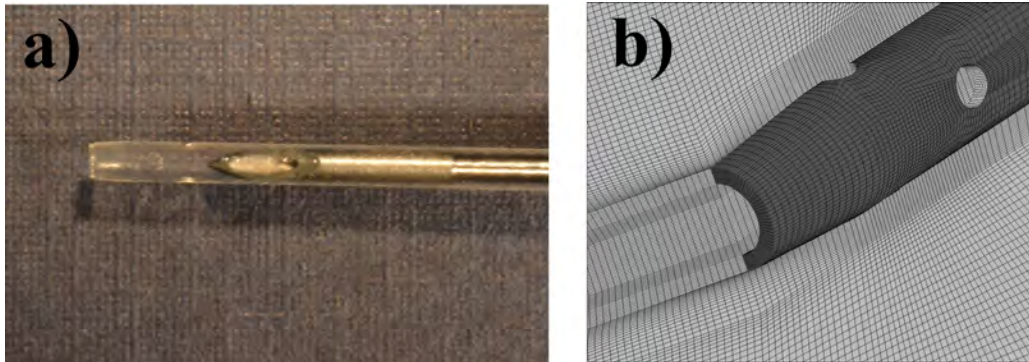


Figure 8.1: a) 15G Argyle™ Safety Fistula Cannula with Anti-Reflux Valve with insertion needle pulled back b) Cross-sectional cut depicting the cannula tip geometry and structured mesh

A fully structured hexahedral grid was created in ICEM 14.5 (ANSYS Inc., Canonsburg, PA, USA) using a similar blocking strategy to that in Chapter 6. The computational simulations were conducted in Fluent 14.5 (Fluent Inc., Lebanon, NH) under the assumption of non-compliant walls due to the arterialisation of the cephalic vein after AVF creation, and blood approximating a Newtonian fluid under the high shear forces within the cannula. The properties of blood were the same described in Chapter 6 where the density and viscosity were assumed to be 1045 kg/m^3 and 0.0035

Pa.s, respectively. The vein profile as measured by Sivanesan et al. [98] and used in Chapter 6 was enforced at the vein inlet, whilst the outlet was unconstrained by specifying it as an opening with zero pressure. The cannula inlet was constrained with a parabolic profile, with blood flow rates of 200 ml/min, 300 ml/min and 400 ml/min, with corresponding Reynolds numbers of 517, 776 and 1034. Three positions of the cannula tip were also examined; upper third, middle and lower third of the vein.

The simulation was initialised for 10 seconds at a time step size of 0.01 seconds to remove transient artefacts of the jet as it enters the cephalic vein. Time averaged data was then recorded over 10 cardiac cycles with 10,000 time steps per cycle. A central differencing solver was employed to achieve second order accuracy with a PISO algorithm (Pressure Implicit with Splitting of Operator) due to the transient nature of the simulation. The grid sizing and time step resolution are classified as high resolution as outlined in previous studies [182, 183] and are sufficient to capture flow instabilities.

Metrics of TAWSS, RRT and flow through the back eye, as presented previously, were used. The velocity field and instabilities are visualised using isosurfaces and monitors of velocity within the cannula jet as displayed in Figure 8.2.

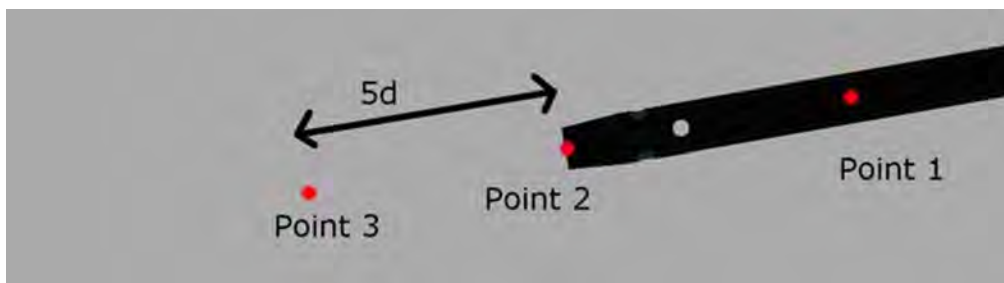


Figure 8.2: Monitor points of the velocity within the cannula

8.2.1 Validation and Verification

A similar blocking strategy to the needle was used. Therefore, the mesh density was based on the grid independence analysis as detailed in Appendix C. The mesh consisted of approximately 8 million cells, resulting in a maximum variation of peak WSS of 3.1%.

The numerical methods were validated against experimental data supplied by the manufacturer (Covidien Pty Ltd, Dublin, Ireland). The experiments compare the average pressure for a range of plastic cannulae under varying blood flow rates. Due to confidentiality, the pressure values on the y-axis are hidden. Figure 8.3 compares experimental results for a 15G cannula against the various computational models. The average difference in pressure for all simulated cases was 13.2%, insuring validity of the numerical method. The difference between the experimental data and simulations is attributed to the slight differences between the methods, namely the testing fluid, position of the cannula and variations in the flow conditions.

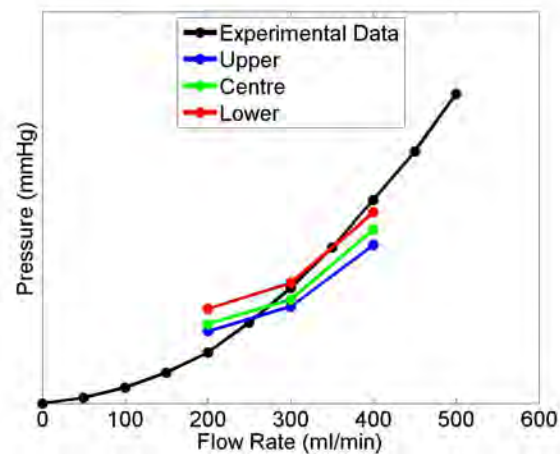


Figure 8.3: Comparison of cannula pressures calculated computationally compared to experimental data

8.3 Results

8.3.1 Analysis of the Cannula Flow Field

The blood exiting the cannula is visualised using isosurfaces of velocity and is displayed in Figure 8.4. At blood flow rates of 300 ml/min and 400 ml/min the jet immediately begins to dissipate after exiting the central bore and shows high levels of instability for all cannula positions. However at lower blood flow rates of 200 ml/min the jet does not begin to break up until closer to the impingement zone and maintains a laminar structure. Complex structures and mixing subsequently form after the jet impacts the floor of the blood vessel. In the cases of higher jet dissipation the mixing with the core flow is exacerbated. The amount of flow exiting the side holes was constant for all blood flow rates and needle positions, with 18% exiting the holes closest to the cannula tip and 9% exiting the other pair. The imbalance of side hole flow was due to the staggered formation and position of the holes relative to the cannula tip.

Monitors of velocity at the three locations within the cannula jet are displayed in Figure 8.5. The top row shows that the velocity within the cannula itself is constant and steady in all cases. The second row displays the velocity at the cannula exit, where the blood has passed the side holes and is entering the vein. Small fluctuations begin to manifest at the outlet of the cannula in some cases. These fluctuations are more pronounced with a lower needle position and higher blood flow rates. This indicates that the position of the cannula and blood flow rate is more influential on the exiting jet structure than the side holes. The blood flow rate inevitably controls the velocity within the cannula which influences the stability of the jet. The effect of cannula position highlights the influence of the vein wall.

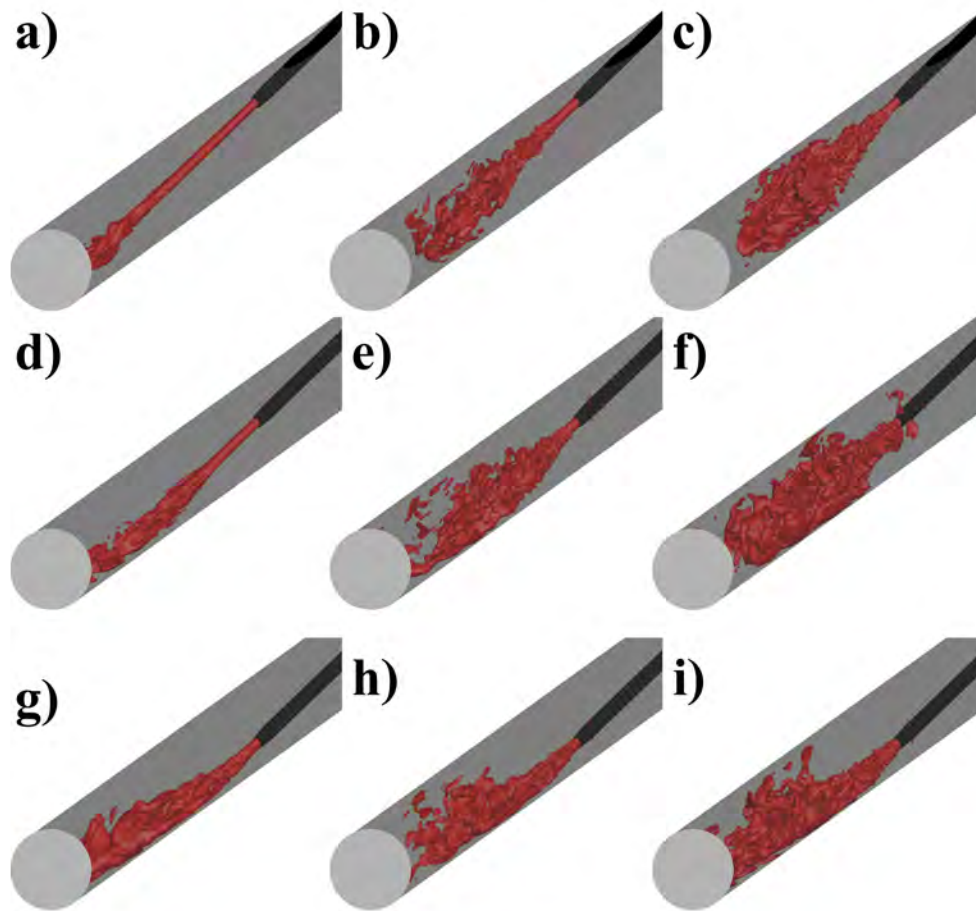


Figure 8.4: Velocity isosurface (1 m/s) depicting blood exiting the cannula through the central bore and side holes. First column: 200 ml/min. Second column: 300 ml/min. Third column: 400 ml/min. a-c) Upper d-f) Centre g-i) Lower

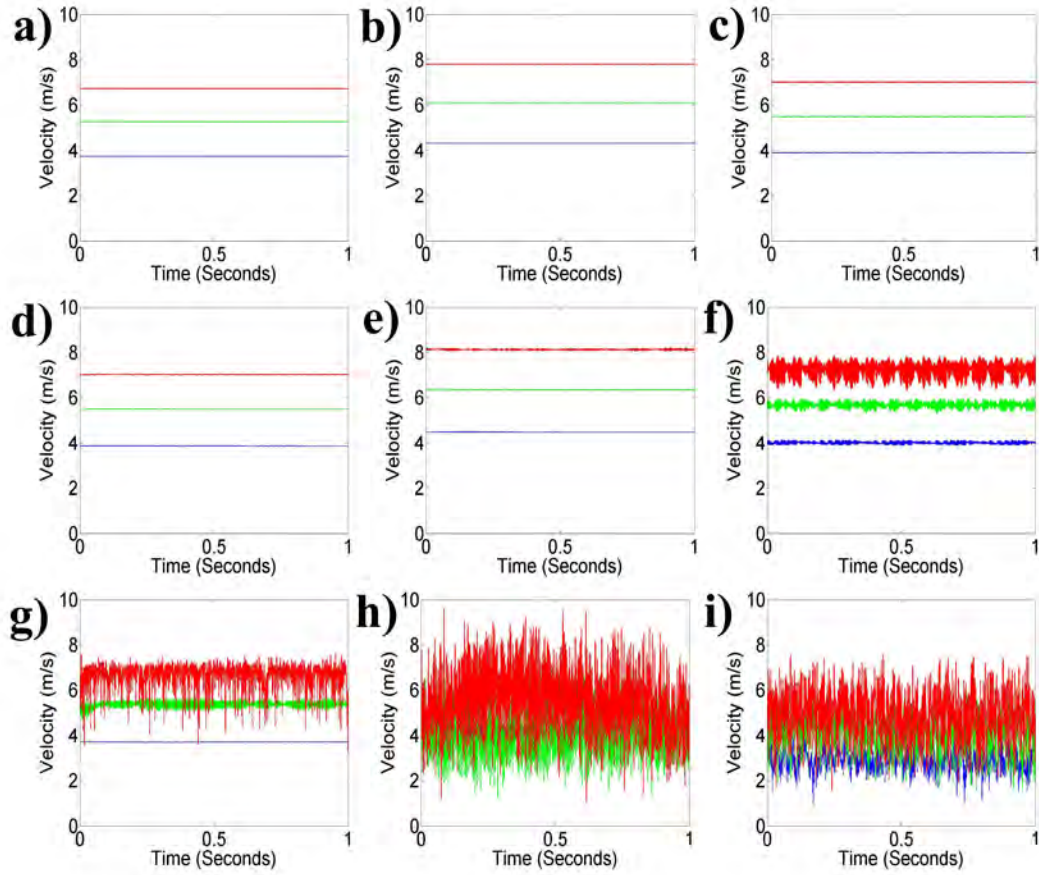


Figure 8.5: Monitor points of the velocity within the cannula. Blue line represents a blood flow rate of 200 ml/min. Green line represents a blood flow rate of 300 ml/min. Red line represents a blood flow rate of 400 ml/min. Left hand column: cannula position near the roof of the vein. Middle column: cannula position in the centre of the vein. Right hand column: cannula position near the floor of the vein. a-c) Monitor point inside cannula d-f) Monitor point at outlet of cannula g-i) Monitor point 5d downstream of cannula outlet

Velocity fluctuations are chaotic after the jet has exited the cannula in all cases except at a blood flow rate of 200 ml/min. At this blood flow rate the jet remained stable due to the lower Reynolds number (517). The large velocity fluctuations demonstrate a high degree of jet dissipation and break down within the vein. This was also evident in the velocity isosurface plots in Figure 8.4. The largest fluctuations occur when the cannula is placed in the centre of the vein, minimising the influence of the vein walls. Jet break down is reduced when the needle tip is placed further from the impingement zone, which indicates that the impact of the wall is translated upstream as the jet approaches the vein floor.

A time averaged approach over the cardiac cycle was used to examine regions of the blood vessel wall subject to high levels of TAWSS (>40 Pa) which can lead to endothelial damage. Figure 8.6 displays the TAWSS on the vein wall, where physiologically harmful TAWSS levels (>10 Pa) have been coloured and the maximum value is capped at 40 Pa in order to emphasise the regions subject to potentially damaging levels of TAWSS. Similar to the results presented in Chapter 6, the region of high TAWSS coincides with jet impingement on the vein floor. This region spreads out as the free stream jet transitions into a wall jet and spreads along the surface of the vein. High levels of TAWSS at the point of impingement are present when the cannula tip is closer to the vein floor, with the largest regions occurring at blood flow rates of 400 ml/min. This result shows that a large amount of energy is released upon jet impingement which produces jet dissipation and subsequent mixing, as shown previously.

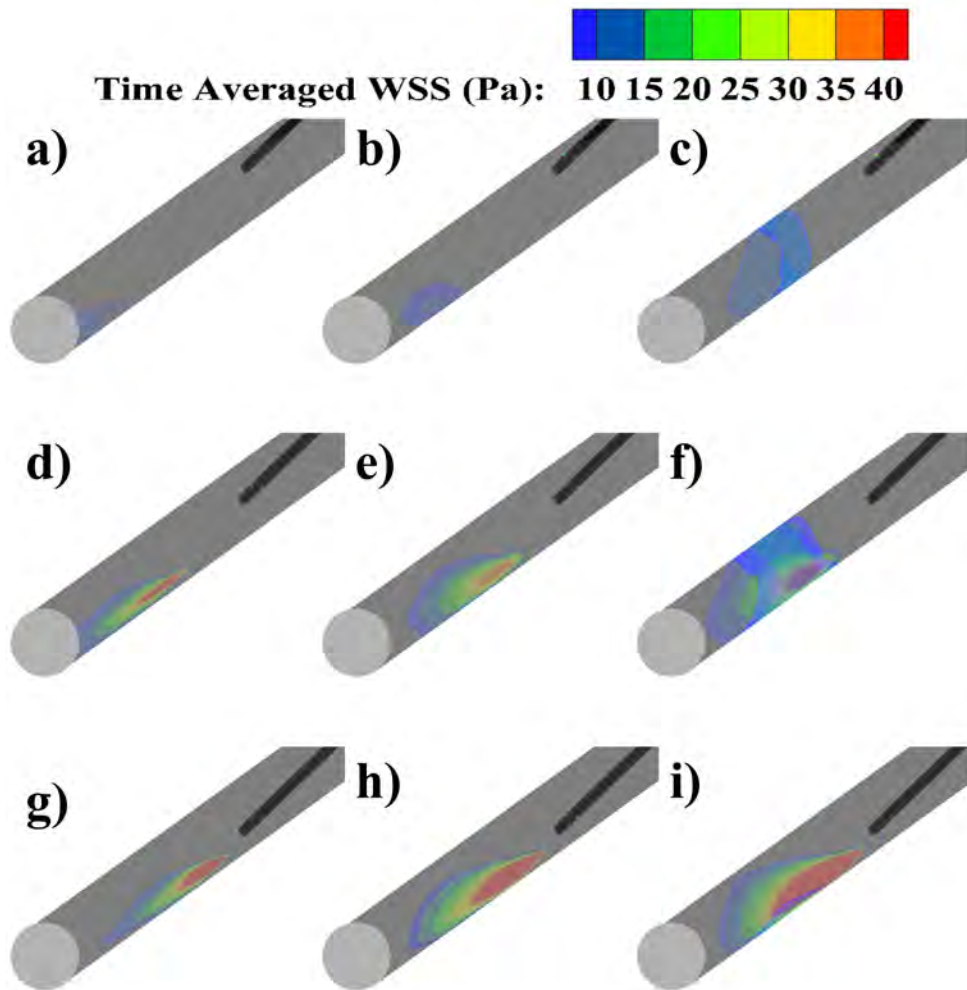


Figure 8.6: Time averaged wall shear stress (TAWSS) on the vein wall highlighting regions of high WSS. Only regions above 10 Pa have been coloured to emphasise regions of excessively high stress. The maximum WSS is cut at 40 Pa, which is the threshold in which endothelial denudation can occur. First column: 200 ml/min. Second column: 300 ml/min. Third column: 400 ml/min. a-c) Upper d-f) Centre g-i) Lower

Table 8.1 quantifies the area on the vein wall subject to high TAWSS above 40 Pa. The effects of the jet have mostly dissipated before impingement when the cannula is placed near the roof of the vein, as no regions of high TAWSS above 40 Pa were calculated. The area of high TAWSS increases as the cannula is placed closer to the vein floor, with the effects of the jet noticeable even when the cannula is placed in the middle of the vein. However, the most prominent increases occur when higher blood flow rates are forced through the cannula. A cannula placed near the vein floor with a blood flow rate of 400 ml/min produced the largest region of high TAWSS.

Table 8.1: Summary of the area of high TAWSS produced by the plastic cannula

Needle Position	Blood Flow Rate	Area of high TAWSS (>40 Pa)
Cannula at top of vein	200 ml/min	0.00 cm ²
Cannula at top of vein	300 ml/min	0.00 cm ²
Cannula at top of vein	400 ml/min	0.00 cm ²
Cannula in middle of vein	200 ml/min	0.59 cm ²
Cannula in middle of vein	300 ml/min	1.04 cm ²
Cannula in middle of vein	400 ml/min	1.73 cm ²
Cannula at bottom of vein	200 ml/min	1.88 cm ²
Cannula at bottom of vein	300 ml/min	3.96 cm ²
Cannula at bottom of vein	400 ml/min	6.24 cm ²

The RRT which represents regions of oscillatory and low WSS on the vein surface is displayed in Figure 8.7. Regions of high residence time are located around the cannula tip and downstream after impingement. These regions coincide with the secondary flows created by the blood exiting the side holes and the complex mixing generated after jet impingement and jet break down. Large regions of complex flows were examined in the velocity monitors and velocity isosurface plots, however it appears that these flows are not steady as evidenced by the low values of RRT. In fact, higher blood

flow rates produce a greater degree of mixing due to increased jet dissipation, which increases the unsteadiness of the secondary flows and minimises longer particle residence times. Subsequently, lower blood flow rates produce steady secondary flows which generate regions of oscillating WSS. The largest regions of high residence times were produced at blood flow rates of 200 ml/min.

Table 8.2 displays the area of high RRT on the vein surface. The position of the cannula influences the size of the oscillating WSS, where a cannula placed near the walls of the vein produces higher residence times. As higher blood flow rates increase the unsteadiness of the secondary flows, reducing the oscillatory nature of WSS on the vein wall, a cannula placed centrally with a high blood flow rate will produce the smallest region of high RRT and may minimise endothelial damage.

Table 8.2: Summary of the area of high RRT produced by the plastic cannula

Needle Position	Blood Flow Rate	Area of high RRT
Cannula at top of vein	200 ml/min	7.51 cm ²
Cannula at top of vein	300 ml/min	11.43 cm ²
Cannula at top of vein	400 ml/min	11.25 cm ²
Cannula in middle of vein	200 ml/min	9.49 cm ²
Cannula in middle of vein	300 ml/min	3.13 cm ²
Cannula in middle of vein	400 ml/min	1.94 cm ²
Cannula at bottom of vein	200 ml/min	12.74 cm ²
Cannula at bottom of vein	300 ml/min	13.01 cm ²
Cannula at bottom of vein	400 ml/min	1.84 cm ²

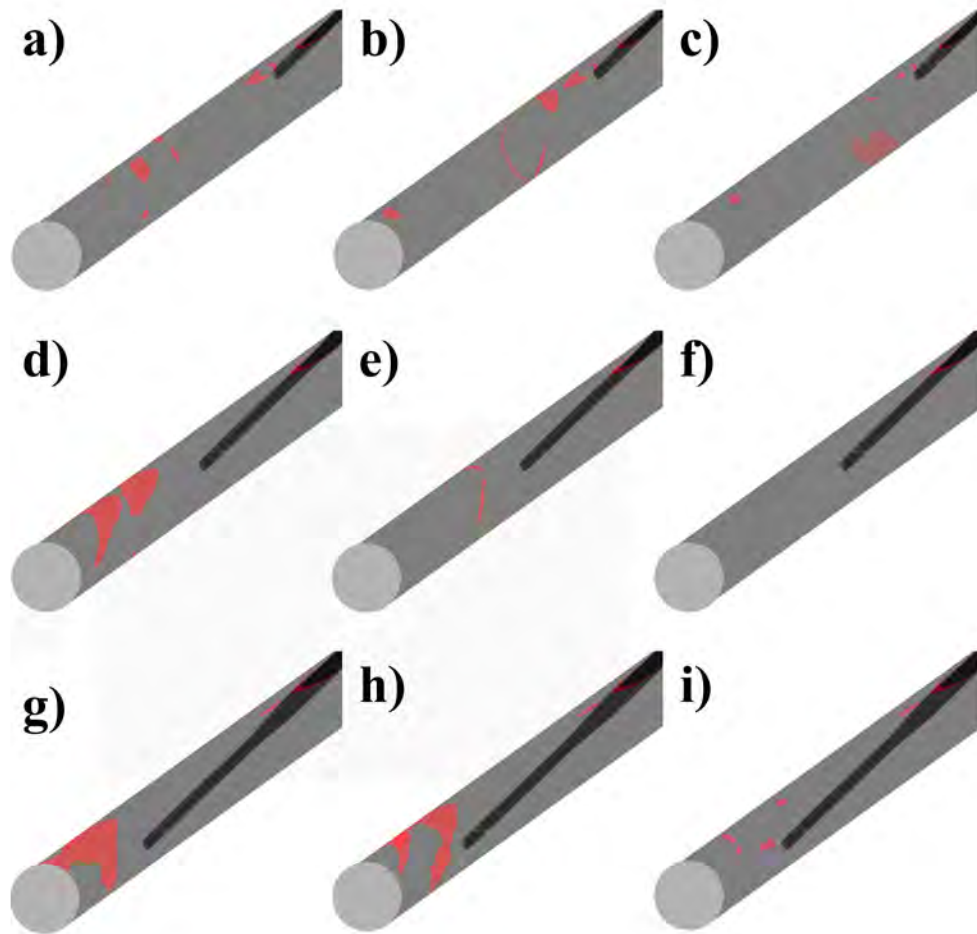


Figure 8.7: Relative residence time (RRT) on the vein wall highlighting regions at risk of developing IH. The scale has been normalised by the mean wall shear stress. Only high levels of RRT (>10) have been coloured in red to emphasise regions of strong secondary flows. First column: 200 ml/min. Second column: 300 ml/min. Third column: 400 ml/min. a-c) Upper d-f) Centre g-i) Lower

8.3.2 Comparison against the standard metal needle

Figure 8.8 compares velocity isosurfaces (1 m/s) of the jet exiting the needle and cannula at various blood flow rates. There is minimal jet dissipation for both devices at a blood flow rate of 200 ml/min, with the cannula displaying minor secondary structures after jet impingement. Heavy jet dissipation begins to occur a few diameters downstream of the central bore for both devices at blood flow rates greater than 300 ml/min. Jet break down continues until the point of impingement, in which large secondary flow structures are created as the jet begins to spread along the surface of the vein. The flow structures produced by the needle and cannula are very similar.

Figure 8.9 quantifies the break down of the jet exiting the needle and cannula by displaying the velocity at various time points. The velocity is measured within the device, at the exit and 5d downstream in the vein. Although the blood flow rate was matched for both devices in each respective setting, the internal diameter of the cannula is slightly larger than the needle due to the unique insertion method where the cannula is sheathed onto a needle. Subsequently, a standard metal needle has a slightly smaller internal diameter which results in a higher velocity within the needle, as displayed in all figures. The jet remains stable within each device for all blood flow rates as evident by the constant velocity. Jet break down begins to manifest at the exit of each device in some cases, specifically at blood flow rates of 400 ml/min where minor fluctuations begin to occur. These disturbances are slightly greater in the needle, indicating that they are created by the higher velocity within the needle and the asymmetry imposed by the position of the needle back eye.

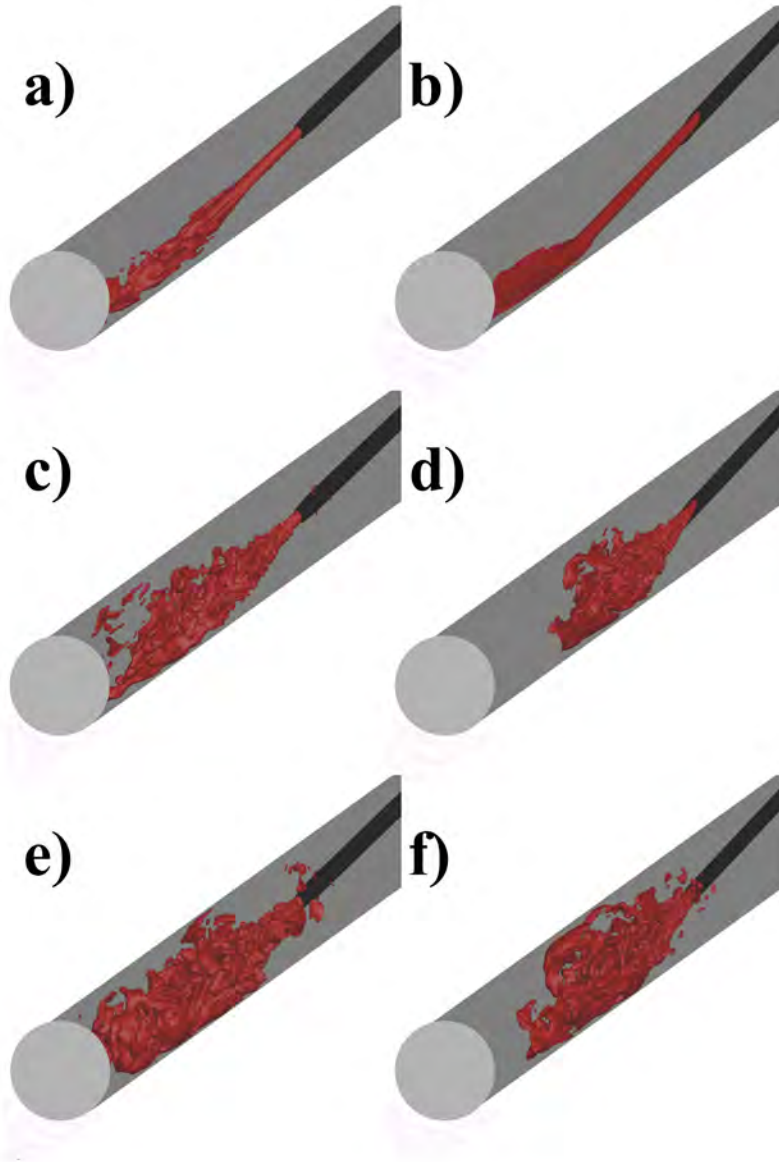


Figure 8.8: Velocity isosurfaces (1 m/s) visualising the jet exiting the cannula and needle. Left column displays the cannula. Right column displays the needle. a-b) Blood flow rate of 200 ml/min. c-d) Blood flow rate of 300 ml/min. e-f) Blood flow rate of 400 ml/min.

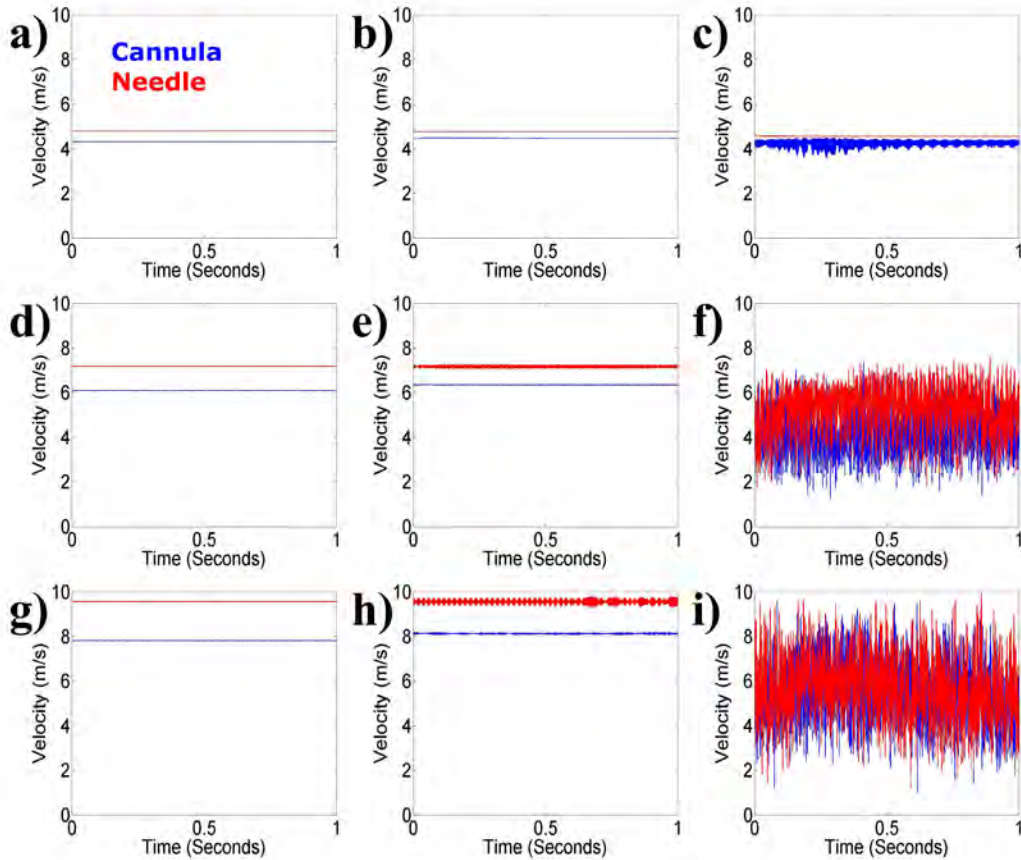


Figure 8.9: Monitor points of the velocity within the cannula. Blue line represents the cannula. Red line represents the needle. Left column displays the monitor point inside device. Middle column displays the monitor point at the outlet of the device. Right column displays the monitor point 5d downstream of the device outlet. a-c) Blood flow rate of 200 ml/min. d-f) Blood flow rate of 300 ml/min. g-i) Blood flow rate of 400 ml/min.

Upon entering the vein, a high level of jet dissipation occurs for both devices at blood flow rates higher than 300 ml/min. The jet dissipation produces secondary flow structures as presented in Figure 8.8. However, at blood flow rates of 200 ml/min the jet remains relatively steady for the needle, whilst the cannula displays minor fluctuations.

The TAWSS produced by the jet is shown in Figure 8.10, where the effects of excessively high WSS are highlighted. Both devices produce similar patterns of high TAWSS at the point of jet impingement for all blood flow rates, with evidence of jet spreading along the vein wall. The cannula produces a slightly higher value of WSS due to the greater dissipation which occurs within the needle.

Regions of high residence time and disturbed flows, as displayed by the RRT metric, produced by the plastic cannula and needle are presented in Figure 8.11. The flow structures exiting each device, as visualised in Figure 8.8 and Figure 8.9, were found to be similar. Subsequently, comparable regions of high RRT are evident on the vein wall around the insertion site and in the downstream portion, coinciding with the secondary flows produced by the impinging jet. The most notable effect is a decrease in regions of high residence time as the blood flow rate increases. This indicates that although larger secondary flow structures are created at higher blood flow rates, these structures are not steady and are continually washed out preventing the formation of stagnant flows.

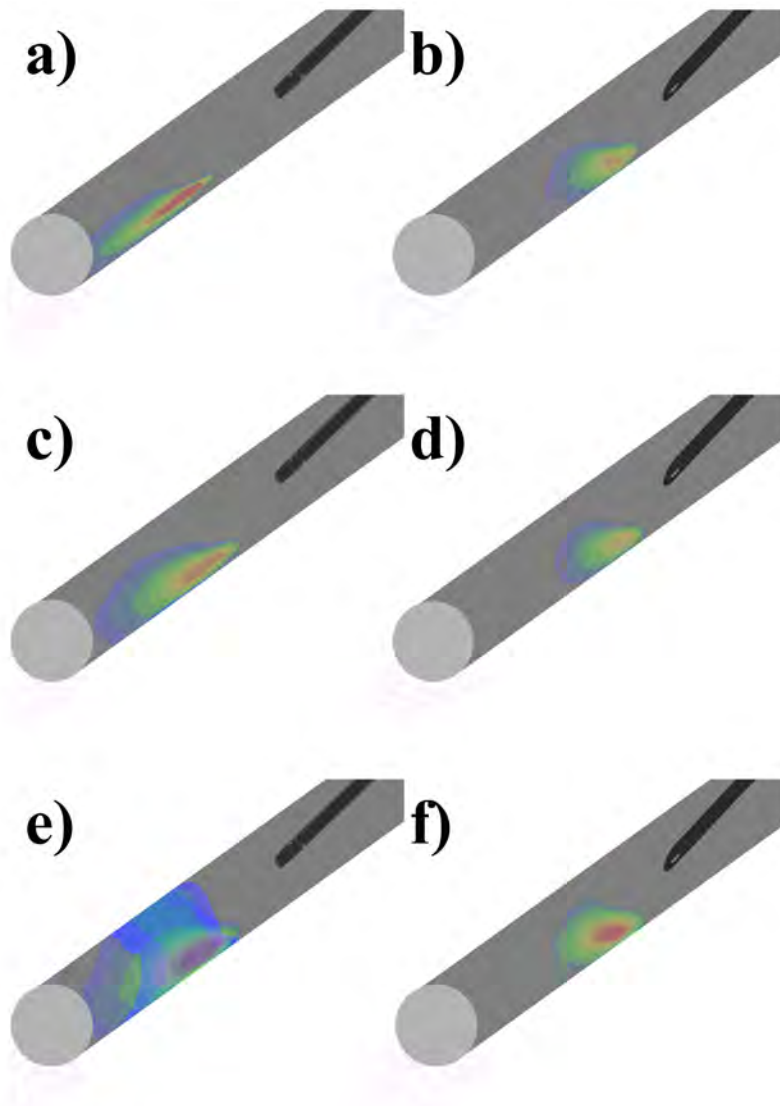


Figure 8.10: Time averaged wall shear stress (TAWSS) on the vein wall highlighting regions of high WSS. Only regions above 10 Pa have been coloured to emphasise regions of excessively high stress. The maximum WSS is capped at 40 Pa, which is the threshold at which endothelial denudation can occur. Left column displays the cannula. Right column displays the needle. a-b) Blood flow rate of 200 ml/min. c-d) Blood flow rate of 300 ml/min. e-f) Blood flow rate of 400 ml/min.

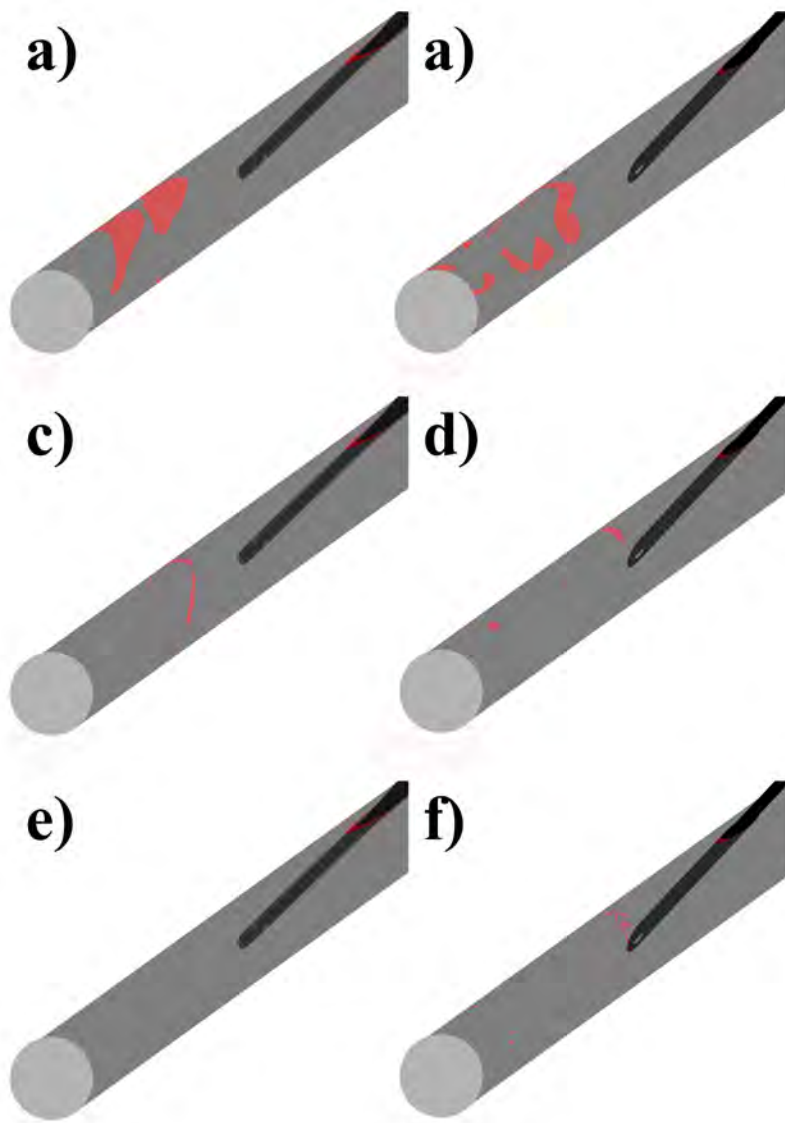


Figure 8.11: Relative residence time (RRT) on the vein wall highlighting regions at risk of developing IH. The scale has been normalised by the mean wall shear stress. Only high levels of RRT (>10) have been coloured in red to emphasise regions of strong secondary flows. Left column displays the cannula. Right column displays the needle. a-b) Blood flow rate of 200 ml/min. c-d) Blood flow rate of 300 ml/min. e-f) Blood flow rate of 400 ml/min.

Table 8.3 compares the areas of high TAWSS and RRT produced by the plastic cannula and needle. Despite the similar flow structures exiting each device, the cannula is found to produce a slightly larger area of high RRT and high TAWSS. The difference in RRT is greater at low blood flow rates but becomes negligible at blood flow rates of 400 ml/min. This indicates that potential endothelial damage from disturbed flows produced by the cannula can be minimised at higher blood flow rates. As displayed in Figure 8.10, the cannula produced slightly larger regions of high TAWSS, where higher blood flow rates affected a larger area. Evidently, an optimal blood flow rate around 300 ml/min can minimise larger regions of high residence time and high TAWSS in both devices.

Table 8.3: Comparison in the area of high RRT and high TAWSS produced by the plastic cannula and needle

Device	Blood Flow Rate	Area of high RRT	Area of high TAWSS (>40 Pa)
Cannula	200 ml/min	9.49 cm ²	0.59 cm ²
Needle	200 ml/min	4.62 cm ²	0.00 cm ²
Cannula	300 ml/min	3.13 cm ²	1.04 cm ²
Needle	300 ml/min	1.31 cm ²	0.00 cm ²
Cannula	400 ml/min	1.94 cm ²	1.73 cm ²
Needle	400 ml/min	1.19 cm ²	0.45 cm ²

8.4 Discussion

Plastic cannulae are commonly used to access blood efficiently, however they are not widely used in haemodialysis. Cannula design has received much attention resulting in an optimised geometry where more than 50% of blood flow enters through the side holes when extracting blood from the body, which contributes to increased jet break down [114–116, 118].

Conversely, the design of metal needles has remained relatively unchanged despite some studies suggesting methods to reduce the high WSS at impingement by improving flow distribution [106, 107, 187]. This chapter analysed the haemodynamic conditions created by the cannula jet, and compared the flow field to that produced by a standard clinical metal needle.

8.4.1 Flow Dynamics and Clinical Implications

The high speed jet exiting the VN has been cited as a potential source of IH in the cannulation segment and drainage vein of AVFs [7, 48]. Vascular damage leading to IH development may be initiated by high WSS following jet impingement [62] or secondary flows due to jet dissipation [7, 48]. Disturbed flows have previously been shown to affect endothelial alignment, increase cell turnover and decrease nitric oxide levels, a mediator of vascular homeostasis, resulting in a loss of vascular integrity [41, 42, 48]. Similar haemodynamic conditions produced by the VN, as examined in Chapter 6, were also identified downstream of the cannula.

A high level of jet dissipation occurred directly after the blood exited the cannula. Further downstream, after the jet impinges the floor of the vein, a high level of mixing and secondary flows develop. The high level of jet break down is a fluid dynamic feature that has previously been seen in catheters and is attributed to the presence of side holes which moves the location of maximum velocity from the catheter tip to inside the catheter itself, before the first side hole [115].

The jet was shown to be more stable when the cannula tip was placed further away from the impingement zone, indicating that the effects of the wall are translated upstream through the jet. Studies on impinging jets

have shown this effect through the increase in static pressure that accompanies the decrease in momentum as the jet approaches the wall.

This region is known as the stagnation point and the change in momentum and pressure invokes high WSS at the point of impingement [187]. Higher blood flow rates also increased the instability of the jet as it raised the Reynolds number (1034) closer to the transitional point in pipe flows (2300). The presence of the side holes adds small disturbances which will also lower the transitional point of cannula flow.

Approximately 27% of the blood passed through the side holes, with 18% exiting the pair near the front of the cannula and 9% exiting the other. This reduces the velocity of the jet exiting the central bore of the cannula, which helped minimise the high TAWSS produced on the floor of the vein. Weber et al. [115] showed similar results, where the presence of side holes in peripheral catheters reduced the maximum velocity at jet impingement.

The high level of flow exiting the side holes has also been visualised in-situ using B-Flow ultrasound, as displayed in Figure 8.12. The imbalance of flow between the side holes is attributed to their staggered positions and initiates small velocity fluctuations that were shown to manifest at the outlet of the cannula in some cases. The velocity fluctuations at the cannula tip were more pronounced with a lower needle position and higher blood flow rates. Although the staggered arrangement of the side holes influenced the stability of the jet, needle position and blood flow rate were shown to have a greater effect on jet dissipation.

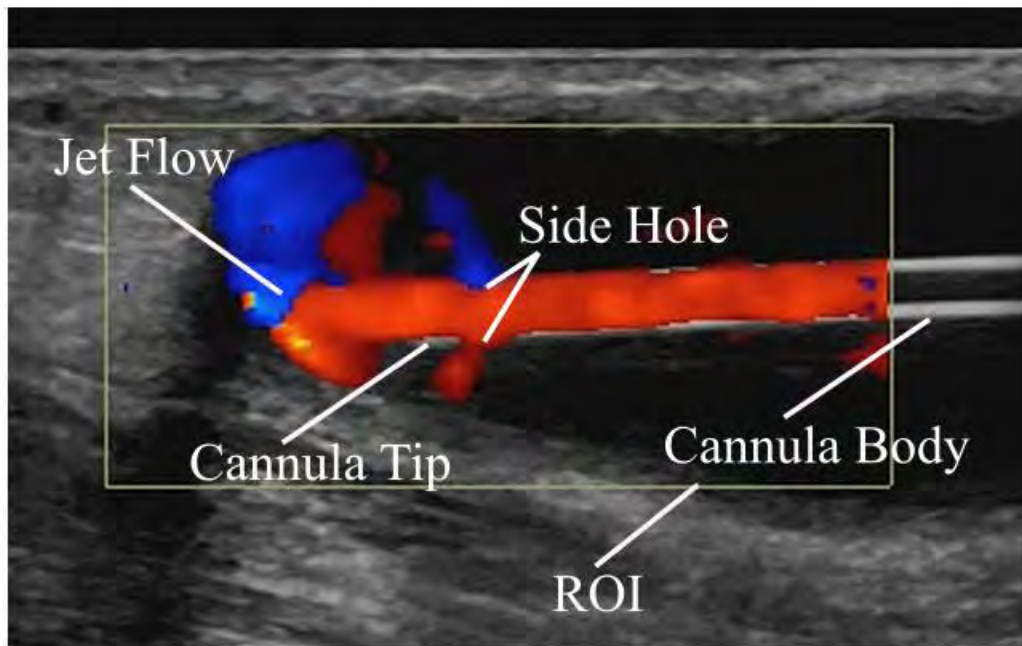


Figure 8.12: B-Flow images of the Argyle™ Safety Fistula Cannula in-situ (Image Courtesy of Dr Tim Spicer, Renal Medicine, Campbelltown Hospital, Sydney, Australia)

The residence time plots identified small areas at risk of endothelial dysfunction, with larger areas coinciding with lower blood flow rates and placement of the cannula near the vein walls. This indicates that the subsequent mixing between the cannula flow and core flow becomes steady at lower blood flow rates leading to higher particle residence times. The wall also has a large influence on the resultant secondary flows produced by jet break down. The use of higher blood flow rates, coupled with the elevated flows present in AVFs, may be sufficient to wash out the complex disturbed flows and prevent any large stagnation regions which can result in IH development secondary to endothelial damage.

Additionally, the computational model indicated a region of elevated TAWSS at the impingement site, which occurred despite the high level of jet dissipation, with levels of TAWSS above the threshold (>40 Pa) reported to denude the endothelium [61]. Phares et al. [165] measured the WSS produced by a normal impinging jet on a flat surface and found that lower jet heights and higher jet Reynolds numbers produced a greater increase in the WSS. A similar result was found in this study, where high levels of WSS were present at high blood flow rates or when the cannula tip was placed near the floor of the vein, where the largest regions occurred at blood flow rates of 400 ml/min. These results indicate that endothelial damage might occur at the impingement zone which may lead to intimal thickening, but can be reduced by placing the cannula away from the vein wall.

Results suggest that an optimal range of blood flow rates (between 300-400 ml/min) exist in which the potential risk of vascular damage can be minimised by reducing high residence times and regions of high TAWSS. This is in agreement with the results of Ponce et al. [160] who found that patients using metal needles were at a significantly higher risk of vascular access failure for blood flow rates below 310 ml/min and greater than 400 ml/min.

8.4.2 Benefit of using a plastic cannula over the standard metal needle

The jet structure and secondary flows produced by the cannula are similar to that created by the VN. Both devices produce a high speed jet which results in disturbed flows downstream of impingement. The haemodynamic differences between the plastic cannula and needle were minor, with the metal needle holding a slight advantage due to the slightly smaller regions of high

TAWSS and high residence time. This derives from small disturbances in the jet which were measured inside the needle near the exit and contribute to a slightly higher rate of jet break down. These disturbances are created by the higher velocity within the needle due to its smaller internal diameter and the asymmetric position of the back eye. This result shows that jet break down is a critical flow feature which can reduce the high levels of WSS that may damage the endothelium at the point of jet impingement on the floor of the vein.

Furthermore, it was previously shown that increased levels of jet unsteadiness, created by the staggered arrangement of the side holes, can minimise regions of high residence time by preventing the formation of steady oscillating flows. This indicates that higher blood flow rates may be used with plastic cannulae to capitalise on the geometrical benefit provided by the staggered arrangement of the four side holes, which increase the level of jet dissipation thereby reducing regions of high RRT. This will also increase the efficiency of dialysis and may minimise the potential of intimal thickening within the vein.

The cannula also had a significant portion of flow exiting through the side holes in comparison to the needle. Side holes and back eyes are primarily used to increase the efficiency of blood extraction and to prevent the needle from becoming attached to the vein wall in the arterial position. However, back eyes in the VN serve little purpose, as acknowledged in Chapter 6, where minimal blood flow exited the VN through this geometrical feature. The VN back eye has received attention in previous studies [106, 107], in order to increase its efficiency and reduce the effects of the VNJ. Zarate [106] states that needle technology has not kept up with advances in dialysis and proposed a new needle design which incorporates two back eyes and flow diverters within the main needle bore. This design minimises undesirable haemodynamics by creating three jets, which lowers the velocity of the main

needle jet and will aid in lowering the high WSS at impingement. The three jets also prevent the formation of secondary flows with high residence time. Van Tricht [107] also proposed multiple side eyes of various shapes, which increased the flow distribution in the AN, although the effect was minimal with the VN.

Despite the influence of the back eye, as acknowledged in the literature, dialysis needles have remained relatively unchanged. The high level of blood flow through the side holes highlights a major advantage in the cannula design compared to the metal needle, where the VN back eye was shown to be highly ineffective. The presence of four side holes in the cannula produced a reasonable flow distribution (27%) which aided in reducing the velocity in the main jet. This has also been shown in peripheral catheters [115]. Zarate [106] advocates the importance of reducing the velocity in the main jet as it may reduce the high TAWSS at the impingement zone and prevent the formation of secondary flows with high residence times. It also indicates that cannulae may have greater efficiency in extracting blood from the fistula compared to AN.

Additionally, metal needles pose a risk of infiltration, which occurs when the sharp tip of the needle punctures the blood vessel resulting in subcutaneous haematoma and potential thrombosis. Infiltration can also occur during the process of needle rotation. In a study on cannulation in haemodialysis, Lee et al. [87] found that 26% of metal needle infiltrations resulted in AVF thrombosis. The use of plastic cannulae in haemodialysis may reduce the risk of needle infiltration due to the blunt tip design. Furthermore, the technique of needle rotation, which is performed on metal needles to alleviate pressure, is unnecessary with cannula due to the symmetric design and large influence of the side holes. A patient using a plastic cannula is provided with a greater range of limb movement due to the absence of the sharp needle in-situ which will also improve the comfort of the dialysis session.

Plastic cannulae provide a viable alternative to the current standard metal needles used in haemodialysis, despite the slightly favourable haemodynamic conditions of needles, as cannulae offer additional benefits which may increase the efficiency and comfort of dialysis.

8.5 Conclusion

Computational models of blood flow exiting a plastic cannula (15G Argyle™ Safety Fistula Cannula) revealed a high level of jet dissipation which is influenced by the staggered positions of the side holes, position of the cannula within the vein and the imposed blood flow rate. Furthermore, approximately 27% of the flow exited through the cannula side holes, which contrasts previous studies on metal needles. Regions of high residence time indicating areas at risk of IH were identified in every case. Similarly, a large region of high TAWSS was identified at the site of jet impingement on the vein floor which may lead to endothelial damage and subsequent intimal thickening. The risk of IH may be minimised by using optimal blood flow rates between 300-400 ml/min and ensuring the cannula tip is placed away from the walls of the vein.

The haemodynamics produced by the plastic needle were found to be slightly less favourable to metal needle flows, although the difference was minor. Results indicate that cannulae can be run at higher blood flow rates without increasing the risk of endothelial damage from the jet as these conditions increase jet break down and prevent the formation of steady oscillating flows. This also increases the efficiency of blood filtration and can reduce the duration of dialysis. This chapter indicates that plastic cannulae are a viable alternative for haemodialysis cannulation as they hold several advantages in their unique design over metal needles.

Chapter 9

Conclusions

The main aim of this thesis was to investigate the flow field surrounding the AN and VN during haemodialysis and assess potential mechanisms to minimise damage to the vascular access. Computational models of haemodialysis cannulation provided high resolution information of the flow field around the needles as well as an accurate measure of the WSS. The computational models were validated against a dimensionally scaled experimental flow rig using S-PIV. These studies were supplemented with clinical data collected on haemodialysis patients. The significant findings from the results presented in this thesis will now be summarised. Additionally, any future work that is an extension from the presented work is outlined. The recommendations for future work are derived from assumptions in the modelling which were made for simplicity, time limitations or areas of research that are outside the scope of this thesis.

9.1 Key Findings

Maintaining vascular access patency is critical in haemodialysis treatment. In particular, cannulation technique forms a key component in effective patient health care. The central hypothesis of this thesis was that the flows produced by haemodialysis needles contribute to the high incidence of stenosis in the venous outflow of AVFs. Clinical data supported this hypothesis as stenosis in the venous outflow developed in 45% of patients, all of whom developed a healthy fistula and had begun treatment. In particular, the risk of developing stenosis was elevated in the first six months of fistula use, indicating that fistulae require an adjustment period to dialysis conditions when treatment first begins. It also highlights the importance of routine screening during this time.

The harmful effect of these flows was investigated through analysis of the WSS on the vein wall, which affects endothelial function. Damage to the endothelium or disruption of endothelial function initiates the intimal thickening process as a response to injury and can develop into clinical stenosis. It is difficult to measure the WSS vector in-vivo and using experimental flow rigs due to technological limitations in spatial and temporal accuracy. Computational models of cannulation were subsequently utilised to analyse the haemodynamic forces exerted on the vein wall. The models were also validated using S-PIV measurements conducted on a scaled bench top model.

The AN and VN were shown to produce very different flow fields, both of which may lead to stenosis formation via the pathway of intimal thickening. Both the experimental and numerical analysis revealed that the flow field surrounding the AN is highly localised around the needle tip in both antegrade and retrograde orientations. Disturbed flows develop as the

blood is extracted from the vein through the central bore and needle back eye. Regions of high residence time coincided with the disturbed flows around the AN tip and may lead to endothelial dysfunction, a precursor to IH.

The localised flow field around the AN indicates that the two needles can be placed in close proximity without increasing the risk of access recirculation. Placing the needles in close proximity to each other can increase the number of potential radiocephalic fistulae as the requirement to create a longer venous outflow is not needed. Additionally, comorbidities of diabetes and age (>65 years) were not statistically related to late fistula failure which indicates that these patients should not be disregarded for creation of a radiocephalic fistula as other variables may be more influential.

Conversely, the flow field produced by the VN extends far into the venous outflow due to the jet structure exiting the central bore. A wall jet forms upon impingement with the floor of the vein. Contra rotating vortices form as the wall jet spreads along the curvature of the vessel. Disturbed flows are produced by the interaction between the contra rotating vortices and wall jet. High TAWSS, above the threshold reported to cause endothelial damage, was measured at the point of VNJ impingement on the floor of the vein. Regions of high residence time were also examined on the roof of the vein which coincided with regions of disturbed flow, which may lead to further endothelial dysfunction.

The potential of microbubble formation from cavitation at the needles was also explored. Computational models revealed that cavitation may occur at the entrance of the AN under elevated blood flow rates, but is unlikely to occur at the VN. Elevated blood flow rates (>600 ml/min) and sharp changes in geometry were the conditions required to reduce the pressure below the vapour pressure of blood to facilitate cavitation. These conditions

were subsequently examined clinically by measuring the pulsatility produced by the roller pump using Doppler ultrasound. The largest pulse occurred directly after the roller pump and was subsequently dampened by the air traps and dialyser.

Although cavitation at the AN is possible, clinical measurements revealed that it is unlikely to occur at the range of blood flow rates used in treatment. However the large pulse which develops when the rollers in the pump are positioned at 0° and 180° may be sufficient to elevate the instantaneous blood flow rate to the critical value noted in the computational study. Furthermore, when the rollers are at the aforementioned positions, temporary occlusion occurs which produces sharp changes in the tubing diameter; another factor required for cavitation. The results from these studies indicate that microbubbles may form at the roller pump due to cavitation. Further observation is required to determine this possibility, however the use of multiple rollers and a lower blood flow rate may reduce the pulsatility, thereby minimising the number of microbubbles generated.

To improve the long term success of the vascular access it is pertinent to minimise potential endothelial damage caused by the needles. The most influential parameter on potential endothelial damage was the prescribed blood flow rate. Large regions of steady disturbed flows with high residence time developed under low blood flow rates (200 ml/min). Higher blood flow rates (400 ml/min) reduced the residence time in the disturbed flows but also generated high shear stresses at the point of jet impingement. Therefore an optimum blood flow rate around 300 ml/min minimises the potential endothelial damage caused by disturbed flows with high residence time and high shear stresses.

The proximity of the needle tip to the vein wall was also shown to have a large influence on the size of the disturbed flows. The high TAWSS at the point of VNJ impingement was also greatest when the needle was placed close to the floor of the vein. Placement of the needles away from the walls of the vein may reduce the haemodynamic forces which can lead to IH. The risk of infiltration is also reduced when the needle is placed within the centre of the vein. Ultrasound is an effective tool which can help facilitate an optimal needle placement so as to achieve safe and effective dialysis. Although less influential, a shallow needle angle ($<10^\circ$) may also minimise potential endothelial damage as the effects of the jet have mostly dissipated before impingement on the floor of the vein.

Alternatively, metal needles can be replaced with plastic cannulae, which have been used in other areas of medicine with great success. The Argyle™ Safety Fistula Cannula with Anti-Reflux Valve is relatively new in the field of haemodialysis and little research has been conducted on its use. Computational models identified similar flow structures to the VN, with a high level of jet dissipation which produced disturbed flows in the venous outflow. The cannula jet produced regions of high residence time coinciding with the disturbed flows on the roof of the vein, as well as high shear stresses at the point of jet impingement. These haemodynamic conditions were found to be slightly less favourable to metal needles, although the difference between the two devices was minimal. Results indicate that higher blood flow rates can be run with plastic cannulae without increasing the risk of endothelial damage. This can increase the efficiency of blood filtration and reduce the duration of treatment.

The main difference between the two products was the large amount of flow (27%) which exited the cannula side holes, which contrasts the small amount of flow ($<1\%$) exiting the VN back eye. Although the cannula placed in the arterial line was not examined in this thesis, these results

indicate that a plastic cannula may be beneficial in extracting blood to the dialyser over metal needles. Furthermore, the symmetry of the cannula and placement of four staggered side holes would negate the need to rotate or reposition the cannula after insertion. This technique is sometimes performed with metal needles to alleviate pressure in the arterial line when the AN becomes attached to the vein wall. However, this study found no haemodynamic advantage in rotating the needle. The back eyes also contributed less than 50% of the flow in the AN, indicating that a more suitable method to prevent high pressures in the arterial line is to place the AN away from the vein wall. The technique of needle rotation also carries a risk of infiltration. Plastic cannulae have several advantages over metal needles, namely a lower risk of infiltration due to the blunt tip design and plastic body. These results indicate that plastic cannulae are a viable alternative to standard metal needles, although further investigation is required.

An alternative approach in vascular access management is the development of a model to predict failure based on clinical variables of blood flow rate, arterial pressure, venous pressure or treatment frequency was found. No statistical relationship between late failure and the aforementioned clinical variables was discovered in this work. This may be due to the ability of the endothelium to recover from each treatment. Endothelial recovery was also reflected in the high incidence of stenosis at the anastomosis, as the haemodynamics in this region of the blood vessel exist even when the patient is not receiving treatment. The need to monitor the fistula frequently in the first year of dialysis is also recognised, as this period coincides with the greatest change in haemodynamics where the fistula adapts to treatment.

9.2 Future Direction

The results presented within this thesis identified the flow structures produced by dialysis needles and the haemodynamics likely to cause endothelial damage which may lead to intimal thickening. Several limitations such as rigid walls and Newtonian blood modelling were made to facilitate the analysis. Furthermore, an idealised cephalic vein was used to generate high resolution data computationally which was validated against the experimental results. Future work could utilise patient specific geometries incorporating a non-Newtonian blood model tailored to the patients' haematocrit, as well as distensible walls to gain a more comprehensive understanding of the flow features within the fistula during haemodialysis. These models could also be examined regularly to examine the evolution of the blood vessel over time. This would allow direct correlation between haemodynamics and the development of stenotic lesions in the fistula.

A further extension to accompany the patient specific models would be bench top models or animal studies of cannulation. The use of cell culture plates under controlled flow conditions have previously been used to correlate flows with endothelial function. However, these bench top experiments have been conducted under idealised flow conditions. A future study could examine cellular response under clinical flow conditions, such as flows produced by the needles incorporating the pulsatility of the cardiac cycle. Examination of blood vessels from cannulated animals would provide further data on the in-vivo response of endothelial cells to flows produced by the needles.

In regards to microbubble formation, this thesis found that cavitation may transpire at the AN under extreme blood flow rates, but is more likely to occur at the roller pump. Further examination of the flow and pressure produced by the roller pump is required to confirm this. An experiment conducted on a closed saline loop with elevated blood pump speeds could be used to examine the presence of microbubbles under a controlled setting. This thesis also suggested that increasing the number of rollers in the pump may reduce the pulsatility. Preventing the passage of microbubbles through the extracorporeal circuit and reducing the pulsatility produced by the roller pump should be a key focus of further research.

This thesis found plastic cannulae to be a viable alternative to metal needles. As this is a relatively new product there is very little clinical data on its efficacy. Future work should focus on a long term clinical study comparing the plastic cannula against the metal needle. Key areas of focus should include: the number of infiltrations, infection rates, incidence of stenosis and dialyser clearance. The computational models also identified a large amount of flow exiting the side holes. Whilst this is beneficial in terms of minimising the pressure within the cannula, it may contribute to increased rates of haemolysis. The level of haemolysis could be calculated using blood samples taken before and after treatment, using bench top flow rigs with animal blood or can be estimated through computational models.

The main limitations in the patient study was the low power due to the small cohort of patients. A long term study (>10 years), incorporating information from patients and nurses at every session will increase the power and the amount of available information on fistula failure. The negligible effect of age and diabetes on fistula survival indicated that fistula selection criteria may be more influential. The future study could also examine patients from their first consultation with the vascular access surgeon. The key findings should include: blood vessel diameter before and

after fistula creation, collected at regular intervals throughout the fistulae life, and should also include fistula flow data measured using a transonic. The inclusion of these variables may assist in determining factors that could improve long term AVF survival.

Appendix A

Experimental Uncertainty Analysis

The sections below follow the procedure used to calculate the experimental uncertainty shown above. Some variables propagate through the experiment via a data reduction equation. A nominal value is used to calculate the sensitivity coefficients when a variable propagates. The nominal value represents the average number these variables hold during the experimental procedure. The bias errors typically arose from manufacturing sources and specifications, calibration process and regression fitting. Precision errors were measured statistically through standard deviation over a range of experimental conditions. When the bias or precision error was difficult to measure accurately an estimation was made based on experience and engineering judgement.

A.1 Vein Diameter

Diameter measurements of the inlet and outlet were made using Vernier callipers for each acrylic test piece. As all blocks were made under the same procedure with the same equipment it is assumed that the uncertainty is the same in all acrylic test pieces. Manufacturing uncertainty was unquantifiable as the acrylic test pieces were made from different blocks at different times.

Nominal diameter (D): 20 mm

Bias errors:

Measurement bias (half scale of Vernier calliper): $B_m = 0.005$ mm

Precision errors:

Standard deviation from all measurements ($2S_r$): $P_{SD} = 0.1215$ mm

Total Uncertainty:

$$U_D^2 = B_m^2 + P_{SD}^2 \tag{A.1}$$

$$U_D^2 = 0.005^2 + 0.1215^2$$

$$U_D = \mathbf{0.122 \text{ mm (0.608 \%D)}}$$

A.2 Needle Diameter

The internal diameter of the needle was measured using Vernier callipers in a similar procedure to the vein diameter.

Nominal diameter (d): 2.692 mm

Bias errors:

Measurement bias (half scale of Vernier calliper): $B_m = 0.005$ mm

Precision errors:

Standard deviation from all measurements ($2S_r$): $P_{SD} = 0.048$ mm

Total Uncertainty:

$$U_d^2 = B_m^2 + P_{SD}^2 \quad (\text{A.2})$$

$$U_d^2 = 0.005^2 + 0.048^2$$

$$U_d = 0.048 \text{ mm (1.777 \%d)}$$

A.3 Solution Concentration

The mixing procedure to obtain the final 17L was limited by the size of the measuring instruments. The final batch was measured in four batches of 4L and one batch of 1L. The solution concentration was determined by measuring the mass of NaI, sodium thiosulfate, glycerol and distilled water. An optimum concentration of NaI to glycerol (76.5.%W/W) was required to

match the refractive index of the acrylic test pieces.

Nominal diameter (C): 76.5% (W/W)

Total mass of NaI (M_{NaI}): 15204.8 g

Total mass of H_2O (M_{H_2O}): 8646.2 g

Total mass of glycerol (M_g): 5021.715 g

Total mass of sodium thiosulfate (M_{ST}): 23.851 g

Data reduction equation:

$$C = 100 \times \frac{M_{NaI}}{M_{NaI} + M_g + M_{H_2O} + M_{ST}} \quad (A.3)$$

From the data reduction equation the sensitivity coefficients are:

$$\begin{aligned} \frac{\partial C}{\partial M_{NaI}} &= 100 \times \frac{M_g + M_{H_2O} + M_{ST}}{(M_{NaI} + M_g + M_{H_2O} + M_{ST})^2} \\ &= 1.64 \times 10^{-3} 1/g \end{aligned} \quad (A.4)$$

$$\begin{aligned} \frac{\partial C}{\partial M_{H_2O}} &= -100 \times \frac{M_{NaI}}{(M_{NaI} + M_g + M_{H_2O} + M_{ST})^2} \\ &= -1.82 \times 10^{-3} 1/g \end{aligned} \quad (A.5)$$

$$\begin{aligned} \frac{\partial C}{\partial M_g} &= -100 \times \frac{M_{NaI}}{(M_{NaI} + M_g + M_{H_2O} + M_{ST})^2} \\ &= -1.82 \times 10^{-3} 1/g \end{aligned} \quad (A.6)$$

$$\begin{aligned}\frac{\partial C}{\partial M_{ST}} &= -100 \times \frac{M_{NaI}}{(M_{NaI} + M_g + M_{H_2O} + M_{ST})^2} \\ &= -1.82 \times 10^{-3} 1/g\end{aligned}\tag{A.7}$$

For each batch the number of measurements made to fill the required amounts in the measuring instruments follows:

Table A.1: Summary of measurements during mixing of the blood analogue solution

Component	Number for 4L	Number for 1L	Total number of measurements
NaI	10	10	50
H_2O	3	2	14
Glycerol	10	3	43
Sodium Thiosulfate	1	1	5

Bias errors:

Measurement scale bias (maximum resolution): $B_{scale} = 0.01g$

Mass bias for NaI ($50^{1/2} \times B_{scale}$): $B_{s,NaI} = 0.071g$

Mass bias for H_2O ($14^{1/2} \times B_{scale}$): $B_{s,H_2O} = 0.037g$

Mass bias for glycerol ($43^{1/2} \times B_{scale}$): $B_{s,g} = 0.066g$

Mass bias for sodium thiosulfate ($5^{1/2} \times B_{scale}$): $B_{s,ST} = 0.022g$

NaI powder is hygroscopic (retains moisture) which results in a bias in mass over time. The increase in mass due to moisture absorption was measured for a sample over 30 minutes.

$$m_{initial} = 10.01g$$

$$m_{final} = 10.27g$$

The resultant sample increased its mass by 2.6%. Projecting this gain onto the average weight of NaI in each measurement:

$$B_{hyg,NaI} = 0.026 \times \sqrt{50} \times \frac{15204.8}{50}$$

Mass bias due to hygroscopic nature of NaI: $B_{hyg,NaI} = 55.91g$

NaI left in beaker (estimated): $B_{NaI,bk} = 0.5g$

H_2O left in beaker (estimated): $B_{H_2O,bk} = 0.1g$

Glycerol left in beaker (estimated): $B_{g,bk} = 0.1g$

Water mass lost due to evaporation (estimated): $B_{loss} = 5g$

The bias in NaI measurement is:

$$B_{m,NaI}^2 = B_{s,NaI}^2 + B_{hyg,NaI}^2 + B_{NaI,bk}^2 \quad (A.8)$$

$$B_{m,NaI}^2 = 0.071^2 + 55.91^2 + 0.5^2$$

$$B_{m,NaI} = 55.912g$$

The bias in H_2O measurement is:

$$B_{m,H_2O}^2 = B_{s,H_2O}^2 + B_{loss}^2 + B_{H_2O,bk}^2 \quad (A.9)$$

$$B_{m,H_2O}^2 = 0.037^2 + 5^2 + 0.1^2$$

$$B_{m,H_2O} = 5.001g$$

The bias in glycerol measurement is:

$$B_{m,g}^2 = B_{s,g}^2 + B_{g,bk}^2 \tag{A.10}$$

$$B_{m,g}^2 = 0.066^2 + 0.1^2$$

$$B_{m,g} = 0.120g$$

The bias in sodium thiosulfate measurement is:

$$B_{m,ST}^2 = B_{s,ST}^2 + B_{loss}^2 \tag{A.11}$$

$$B_{m,ST}^2 = 0.022^2 + 5^2$$

$$B_{m,ST} = 5.000g$$

The total bias is therefore:

$$\begin{aligned}
B_C^2 &= \left(\frac{\partial C}{\partial M_{NaI}}\right)^2 B_{m,NaI}^2 + \left(\frac{\partial C}{\partial M_{H_2O}}\right)^2 B_{m,H_2O}^2 + \left(\frac{\partial C}{\partial M_g}\right)^2 B_{m,g}^2 \\
&+ \left(\frac{\partial C}{\partial M_{ST}}\right)^2 B_{m,ST}^2 + 2\left(\frac{\partial C}{\partial M_{NaI}}\right)\left(\frac{\partial C}{\partial M_{H_2O}}\right)(B_{m,NaI})(B_{m,H_2O}) \\
&+ 2\left(\frac{\partial C}{\partial M_{NaI}}\right)\left(\frac{\partial C}{\partial M_g}\right)(B_{m,NaI})(B_{m,g}) + 2\left(\frac{\partial C}{\partial M_{NaI}}\right)\left(\frac{\partial C}{\partial M_{ST}}\right)(B_{m,NaI})(B_{m,ST}) \\
&+ 2\left(\frac{\partial C}{\partial M_{H_2O}}\right)\left(\frac{\partial C}{\partial M_g}\right)(B_{m,H_2O})(B_{m,g}) + 2\left(\frac{\partial C}{\partial M_{H_2O}}\right)\left(\frac{\partial C}{\partial M_{ST}}\right)(B_{m,H_2O})(B_{m,ST}) \\
&+ 2\left(\frac{\partial C}{\partial M_g}\right)\left(\frac{\partial C}{\partial M_{ST}}\right)(B_{m,g})(B_{m,ST})
\end{aligned} \tag{A.12}$$

$$\begin{aligned}
B_C^2 &= (1.64 \times 10^{-3})^2(55.912)^2 + (-1.82 \times 10^{-3})^2(5.001)^2 + (-1.82 \times \\
&10^{-3})^2(0.120)^2 + (-1.82 \times 10^{-3})^2(5.000)^2 + 2(1.64 \times 10^{-3})^2(-1.82 \times \\
&10^{-3})^2(55.912)(5.001) + 2(1.64 \times 10^{-3})^2(-1.82 \times 10^{-3})^2(55.912)(0.120) + \\
&2(1.64 \times 10^{-3})^2(-1.82 \times 10^{-3})^2(55.912)(5.000) + 2(-1.82 \times 10^{-3})^2(-1.82 \times \\
&10^{-3})^2(5.001)(0.120) + 2(-1.82 \times 10^{-3})^2(-1.82 \times 10^{-3})^2(5.001)(5.000) + \\
&2(-1.82 \times 10^{-3})^2(-1.82 \times 10^{-3})^2(0.120)(5.000)
\end{aligned}$$

$$B_C = 0.073g$$

Precision errors:

As the measurement for each batch was made once the precision error is estimated to be equal to the bias error: $P_C = 0.073$ g

Total Uncertainty:

$$U_d^2 = B_C^2 + P_C^2 \tag{A.13}$$

$$U_C^2 = 0.073^2 + 0.073^2$$

$$U_C = 0.104 \text{ g (0.135 \%C)}$$

A.4 Temperature

Temperatures ranging from 15°C-25°C (range of yearly room temperature) were measured with a thermometer. The temperature was controlled using a heat bath.

Nominal temperature (T): 20°C

Bias errors:

Measurement bias (half scale of thermometer): $B_m = 0.1^\circ\text{C}$

Regression bias from thermometer calibration (refer to Figure A.1) ($2S_r$):
(B_{reg}) = 0.393°C

The total bias is therefore:

$$B_T^2 = B_m^2 + B_{reg}^2 \tag{A.14}$$

$$B_T^2 = 0.1^2 + 0.393^2$$

$$B_T = 0.406^\circ\text{C}$$

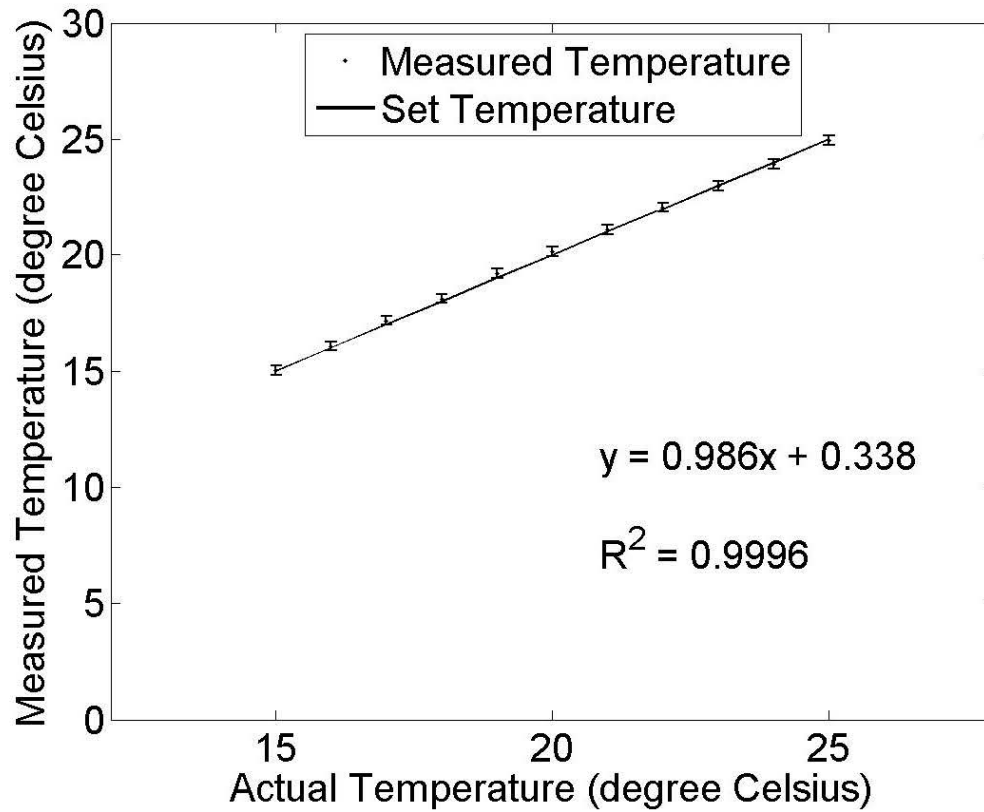


Figure A.1: Temperature Calibration

Precision errors:

Standard deviation from repeated measurements ($2S_r$): (P_{SD}) = 0.280°C

Total Uncertainty:

$$U_T^2 = B_T^2 + P_{SD}^2 \quad (\text{A.15})$$

$$U_T^2 = 0.406^2 + 0.280^2$$

$$U_C = 0.493^\circ\text{C} \text{ (2.463 \%T)}$$

A.5 Density

Density measurements were conducted on a 40ml sample of NaI.

Nominal density (ρ): $1651.65 \frac{\text{kg}}{\text{m}^3}$

Nominal mass (M): 0.066 kg

Nominal volume (V): 0.00004 m^3

Data reduction equation:

$$\rho = \frac{M}{V} \tag{A.16}$$

From the data reduction equation the sensitivity coefficients are:

$$\frac{\partial \rho}{\partial M} = \frac{1}{V} \tag{A.17}$$

$$\frac{\partial \rho}{\partial M} = 25000 \frac{1}{\text{m}^3}$$

$$\frac{\partial \rho}{\partial V} = \frac{-M}{V^2} \tag{A.18}$$

$$\frac{\partial \rho}{\partial V} = -4.129 \times 10^{-7} \frac{\text{kg}}{\text{m}^6}$$

Bias errors:

Measurement bias (half scale): $B_{m1} = 0.005 \times 10^{-3} \text{ kg}$

Scale error: $B_{m2} = 0.01 \times 10^{-3} \text{ kg}$

Pipette manufacturing error for Corning Pyrix 7065 10ml capacity:

$$B_{V1} = 6 \times 10^{-8} \text{ m}^3$$

Pipette scale (half scale): $B_{V2} = 5 \times 10^{-8} \text{ m}^3$

Regression bias from temperature variation (15°C-25°C) ($2S_r$):

$$B_{reg} = 13.791 \frac{\text{kg}}{\text{m}^3}$$

The bias in mass measurement is:

$$B_M^2 = B_{m1}^2 + B_{m2}^2 \quad (\text{A.19})$$

$$B_M^2 = (0.005 \times 10^{-3})^2 + (0.01 \times 10^{-3})^2$$

$$B_M = 1.118 \times 10^{-5} \text{ kg}$$

The bias in volume measurement is:

$$B_V^2 = B_{V1}^2 + B_{V2}^2 \quad (\text{A.20})$$

$$B_V^2 = (6 \times 10^{-8})^2 + (5 \times 10^{-8})^2$$

$$B_V = 7.810 \times 10^{-8} \text{ m}^3$$

The bias from the data reduction equation is:

$$B_{red}^2 = \left(\frac{\partial \rho}{\partial M} \right)^2 B_M^2 + \left(\frac{\partial \rho}{\partial V} \right)^2 B_V^2 \quad (\text{A.21})$$

$$B_{red}^2 = (25000)^2 (1.118 \times 10^{-5})^2 + (-4.129 \times 10^7)^2 (7.810 \times 10^{-8})^2$$

$$B_{red} = 3.237 \frac{kg}{m^3}$$

The total bias is therefore:

$$B_{\rho}^2 = B_{red}^2 + B_{reg}^2 \quad (A.22)$$

$$B_{\rho}^2 = 3.237^2 + 13.791^2$$

$$B_{\rho} = 14.166 \frac{kg}{m^3}$$

Precision errors:

Standard deviation from repeated measurements ($2S_r$): (P_{SD}) = 15.687 $\frac{kg}{m^3}$

Total Uncertainty:

$$U_{\rho}^2 = B_{\rho}^2 + P_{SD}^2 \quad (A.23)$$

$$U_{\rho}^2 = 14.166^2 + 15.687^2$$

$$U_{\rho} = \mathbf{21.137} \frac{kg}{m^3} \quad (\mathbf{1.280} \% \rho)$$

A.6 Viscosity

Viscosity measurements were measured using a Canon-Fenske viscometer and a heat bath for temperatures ranging from 15°C-25°C.

Nominal kinematic viscosity (ν): 4.277 cSt

Nominal concentration (C): 76.5%

Nominal temperature (T): 20°C

Data reduction equation:

$$\nu = 0.002738t \quad (\text{A.24})$$

The manufacturer's uncertainty for kinematic viscosity measurements between 0.6-3 cSt is 0.156%. The viscosity for each temperature was measured three times to ensure a higher confidence in the result. From the data reduction equation the sensitivity coefficients are:

$$\frac{\partial \nu}{\partial t} = 0.002738t \quad (\text{A.25})$$

The variation of viscosity due to temperature is displayed in Figure A.2.

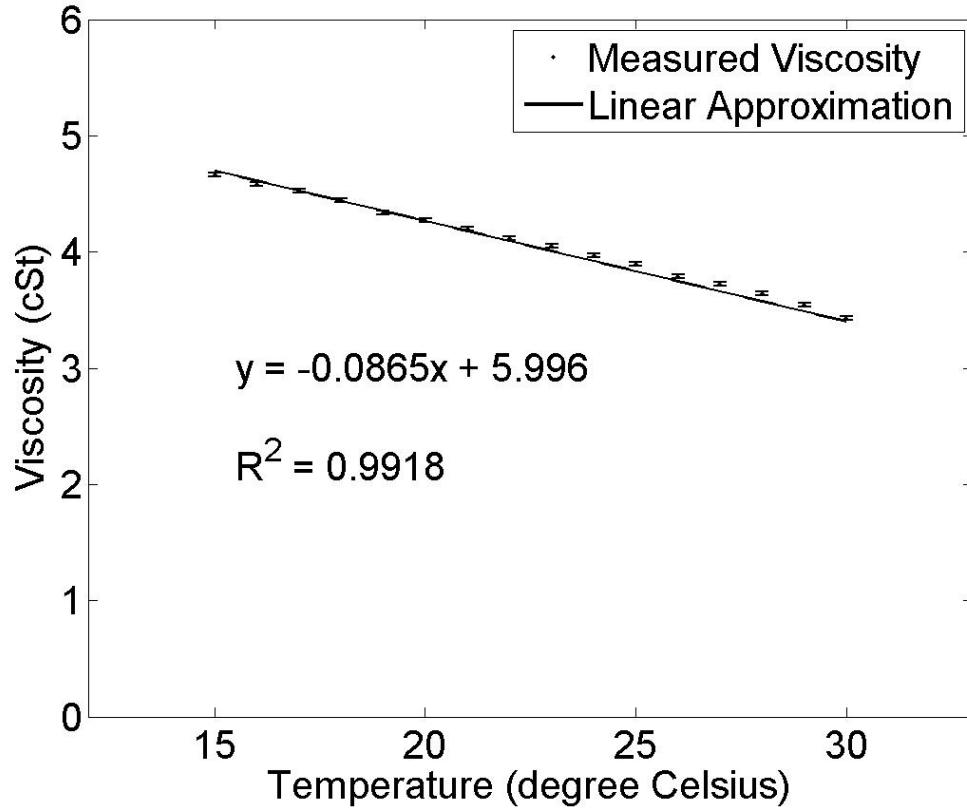


Figure A.2: Viscosity variation with temperature

The following regression equation was fitted to the data:

$$\nu = -0.0865T + 5.9957 \quad (\text{A.26})$$

The sensitivity coefficients to the regression equation are:

$$\frac{\partial \nu}{\partial T} = -0.0865 \frac{\text{cSt}}{^\circ\text{C}} \quad (\text{A.27})$$

Bias errors:

Bias in time (last significant figure): $B_t = 0.01$ seconds

Bias in viscometer (from manufacturer):

$$B_{man} = 0.00156 \times \text{Nominal Viscosity} = 0.007 \text{ cSt}$$

Regression bias due to temperature variation (15°C-25°C) ($2S_r$):

$$B_{reg} = 0.115 \text{ cSt}$$

The bias due to time is:

$$B_{\nu,t}^2 = \left(\frac{\partial \nu}{\partial t} \right)^2 B_t^2 \quad (\text{A.28})$$

$$B_{\nu,t}^2 = (0.002738)^2 (0.01)^2$$

$$B_{\nu,t} = 0.00002738 \text{ cSt}$$

The bias due to the relationship between temperature and viscosity is:

$$B_{\nu,eqn}^2 = \left(\frac{\partial \nu}{\partial T} \right)^2 U_T^2 \quad (\text{A.29})$$

$$B_{\nu,eqn}^2 = (-0.0865)^2 (0.436)^2$$

$$B_{\nu,eqn} = 0.038 \text{ cSt}$$

The total bias is therefore:

$$B_{\nu}^2 = B_{man}^2 + B_{reg}^2 + B_{\nu,t}^2 + B_{\nu,eqn}^2 \quad (\text{A.30})$$

$$B_\nu^2 = (0.007)^2 + (0.115)^2 + (0.0000278)^2 + (0.038)^2$$

$$B_\nu = 0.121 \text{ cSt}$$

Precision errors:

Regression error due to time ($2S_r$): $P_t = 41.934$ seconds

The total precision is therefore:

$$P_\nu^2 = \left(\frac{\partial \nu}{\partial t} \right)^2 P_t^2 \quad (\text{A.31})$$

$$B_\nu^2 = (0.002738)^2 (41.934)^2$$

$$B_\nu = 0.115 \text{ cSt}$$

Total Uncertainty:

$$U_\nu^2 = B_\nu^2 + P_{nu}^2 \quad (\text{A.32})$$

$$U_\nu^2 = 0.121^2 + 0.115^2$$

$$U_\nu = \mathbf{0.167 \text{ cSt (3.901}\% \nu)}$$

Converting this to dynamic viscosity:

$$U_\mu = \frac{\rho \nu}{10^6} \quad (\text{A.33})$$

Nominal dynamic viscosity (μ): 0.00706 Pa.s

Total Uncertainty:

$$U_{\mu} = 0.00028 \text{ Pa.s (3.901}\%_{\mu})$$

A.7 Piston Velocity (Fistula Pump)

The piston velocity was estimated by measuring the time taken to travel 0.1m from its start position. As the flow rate through the vein is constant the test was conducted at the constant flow rate of 11 ml/s.

Nominal flow rate (Q): 11 ml/s

Nominal velocity (V): 0.000858 m/s

Nominal time (t): 58.247 s

Data reduction equation:

$$V = \frac{x}{t} \tag{A.34}$$

From the data reduction equation the sensitivity coefficients are:

$$\frac{\partial V}{\partial x} = \frac{1}{t} \tag{A.35}$$

$$\frac{\partial V}{\partial x} = 0.017 \frac{1}{s}$$

$$\frac{\partial V}{\partial t} = \frac{-x}{t^2} \tag{A.36}$$

$$\frac{\partial V}{\partial t} = -1.5 \times 10^{-5} \frac{m}{s^2}$$

Bias errors:

Measurement bias (half scale): $B_x = 0.0005$ m

Bias in time (last significant figure): $B_t = 0.01$ seconds

Bias in pump (from manufacturer): $B_{man} = 0.03 \times \text{Nominal velocity} = 0.0000257$ m/s

Regression bias ($2S_r$): $B_{reg} = 0.0000111$ m/s

The bias from the data reduction equation follows:

$$B_{red}^2 = \left(\frac{\partial V}{\partial x}\right)^2 B_x^2 + \left(\frac{\partial V}{\partial t}\right)^2 B_t^2 \quad (\text{A.37})$$

$$B_{red}^2 = (0.017)^2(0.0005)^2 + (-0.000015)^2(0.01)^2$$

$$B_{red} = 0.00000859 \text{ m/s}$$

The total bias is therefore:

$$B_{V,Fistulapump}^2 = B_{man}^2 + B_{reg}^2 + B_{red}^2 \quad (\text{A.38})$$

$$B_{V,Fistulapump}^2 = (0.0000257)^2 + (0.0000111)^2 + (0.00000859)^2$$

$$B_{V,Fistulapump} = 0.0000293 \text{ m/s}$$

Precision errors:

Regression error due to time ($2S_r$): $B_t = 0.751$ seconds

The total precision is therefore:

$$P_{V,Fistulapump}^2 = \left(\frac{\partial V}{\partial t} \right)^2 P_t^2 \quad (\text{A.39})$$

$$P_{V,Fistulapump}^2 = (-0.000015)^2 (0.01)^2$$

$$P_{V,Fistulapump} = 0.0000111 \text{ m/s}$$

Total Uncertainty:

$$U_{V,Fistulapump}^2 = B_{V,Fistulapump}^2 + P_{V,Fistulapump}^2 \quad (\text{A.40})$$

$$U_{V,Fistulapump}^2 = 0.0000293^2 + 0.0000111^2$$

$$U_{V,Fistulapump} = \mathbf{0.0000313 \text{ m/s (3.652\%V)}}$$

A.8 Piston Velocity (Needle Pump)

The piston velocity was estimated by measuring the time taken to travel 0.1m from its start position. Although multiple needle flow rates are used, only the mean flow was conducted in this test.

Nominal flow rate (Q): 7.25 ml/s

Nominal velocity (V): 0.0023 m/s

Nominal time (t): 43.394 s

Data reduction equation:

$$V = \frac{x}{t} \quad (\text{A.41})$$

From the data reduction equation the sensitivity coefficients are:

$$\frac{\partial V}{\partial x} = \frac{1}{t} \quad (\text{A.42})$$

$$\frac{\partial V}{\partial x} = 0.023 \frac{1}{s}$$

$$\frac{\partial V}{\partial t} = \frac{-x}{t^2} \quad (\text{A.43})$$

$$\frac{\partial V}{\partial t} = -0.00005 \frac{m}{s^2}$$

Bias errors:

Measurement bias (half scale): $B_x = 0.0005 \text{ m}$

Bias in time (last significant figure): $B_t = 0.01 \text{ seconds}$

Bias in pump (from manufacturer): $B_{man} = 0.03 \times \text{Nominal velocity} = 0.000069 \text{ m/s}$

Regression bias ($2S_r$): $B_{reg} = 0.000029 \text{ m/s}$

The bias from the data reduction equation follows:

$$B_{red}^2 = \left(\frac{\partial V}{\partial x}\right)^2 B_x^2 + \left(\frac{\partial V}{\partial t}\right)^2 B_t^2 \quad (\text{A.44})$$

$$B_{red}^2 = (0.023)^2(0.0005)^2 + (0.00005)^2(0.01)^2$$

$$B_{red} = 0.000012 \text{ m/s}$$

The total bias is therefore:

$$B_{V,NeedlePump}^2 = B_{man}^2 + B_{reg}^2 + B_{red}^2 \quad (A.45)$$

$$B_{V,NeedlePump}^2 = (0.000069)^2 + (0.000029)^2 + (0.000012)^2$$

$$B_{V,NeedlePump} = 0.000076 \text{ m/s}$$

Precision errors:

Regression error due to time ($2S_r$): $B_t = 0.557$ seconds

The total precision is therefore:

$$P_{V,NeedlePump}^2 = \left(\frac{\partial V}{\partial t} \right)^2 P_t^2 \quad (A.46)$$

$$P_{V,NeedlePump}^2 = (0.00005)^2 (0.01)^2$$

$$P_{V,NeedlePump} = 0.00003 \text{ m/s}$$

Total Uncertainty:

$$U_{V,NeedlePump}^2 = B_{V,Needlepump}^2 + P_{V,Needlepump}^2 \quad (A.47)$$

$$U_{V,NeedlePump}^2 = 0.000076^2 + 0.00003^2$$

$$U_{V,NeedlePump} = \mathbf{0.000082 \text{ m/s (3.539\%V)}}$$

Appendix B

PIV Uncertainty Analysis

B.1 Image Distortion:

Image distortion arises due to the curvature of the lens. It manifests at the periphery of the image as the light passes through the lens onto the CCD array. Similar to the perspective error it forms a bias in particle displacements.

Based on the calibration images and the careful procedure used to focus the camera, the error from image distortion was deemed to be negligible.

$$\epsilon_{bias,imagedistortion} = 0 \text{ pixels}$$

B.2 Particle Image Diameter:

The particle image diameter must lie within a specific limit so that that Gaussian filter can register the light intensity difference between background

noise and that reflected by a particle. Referring to Figure B.1, the optimum particle image diameter is approximately 2 pixels. Using the optimum trigger rate will improve the particle image diameter as it reduces any streaks caused by the movement of the particle. The pre-conditioning filters which reduced the background noise also aided in optimising the particle image diameter. The particle image diameter in these experiments was between 1-3 pixels, yielding a random error of approximately 0.05 pixels.

$$\epsilon_{rms,particleimagediameter} = 0.05 \text{ pixels}$$

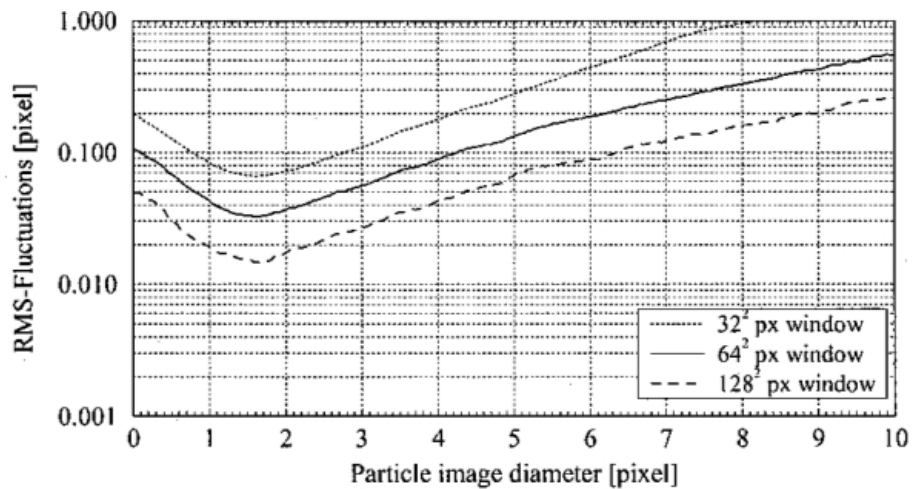


Fig. 5.23. Measurement uncertainty (RMS random error) in digital cross-correlation PIV evaluation with respect to varying particle image diameter: (a) single exposure/double frame PIV imaging, (b) double exposure/single frame PIV imaging. Simulation parameters: $QL = 8$ bits/pixel, no noise, optimum exposure, top-hat light sheet profile, $\mathcal{N} = 1/64 \text{ pixel}^{-1}$

Figure B.1: Random error for variations in particle image diameter [173]

B.3 Particle Image Displacement:

A bias and random error can arise from particle image displacements depending on the flow velocity and pulse distance. Figure B.2 shows that large uncertainty will always exist if the particle is displaced less than half a pixel. The adaptive PIV method used in this thesis offsets the interrogation window with respect to the mean displacement vector, thereby reducing the chance of small particle displacements. For the 32X32 interrogation window used, a random error of approximately 0.05 pixels exists.

$$\epsilon_{rms,particleimagedisplacement} = 0.05 \text{ pixels}$$

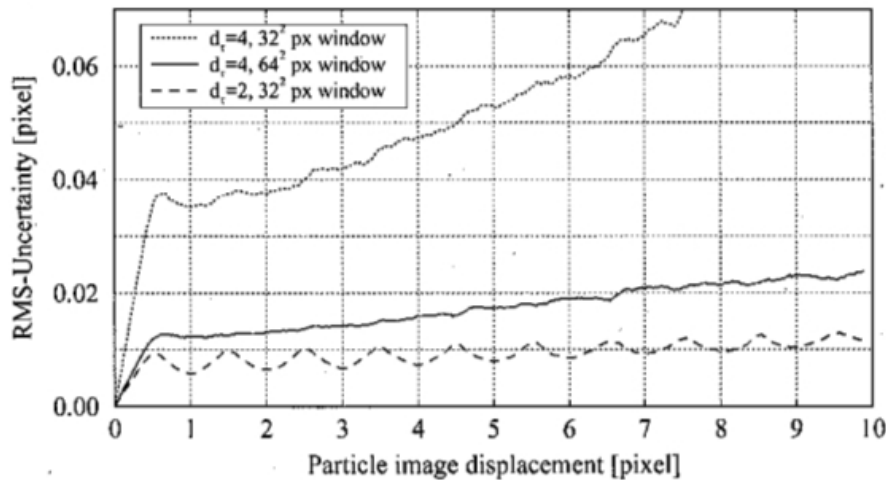


Fig. 5.26. Monte Carlo simulation results for the measurement uncertainty in digital cross-correlation PIV evaluation as a function of particle image displacement

Figure B.2: Random error from particle image displacements [173]

A bias error in particle image displacement will arise from the in-plane loss of pairs. From Figure B.3, using a 32X32 window the bias error is approximately -0.02 pixels.

$$\epsilon_{bias,particleimagedisplacement} = -0.02 \text{ pixels}$$

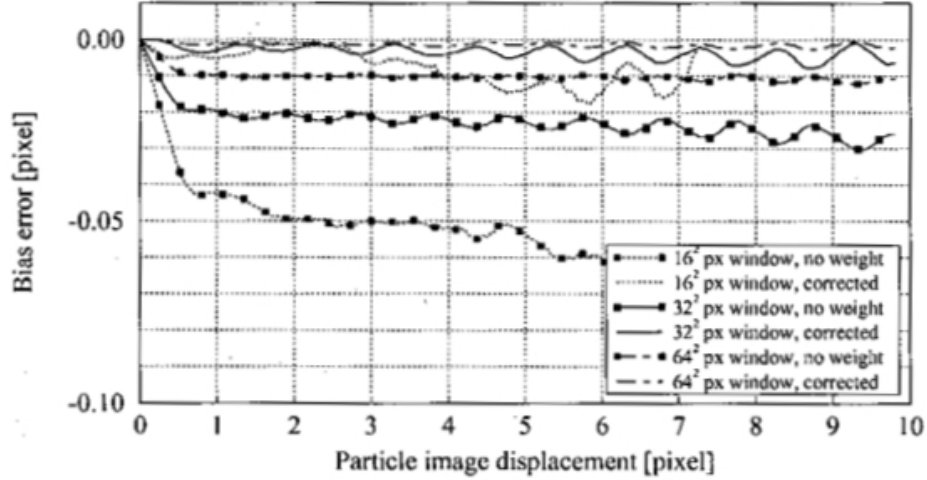


Fig. 5.27. Simulation results showing the difference between actual and measured displacement as a function of the particle image displacement. Bias correction removes the displacement bias (simulation parameters: $d_r = 2.0$, no noise, top-hat intensity profile, $\mathcal{N} = 1/64 \text{ pixel}^{-1}$)

Figure B.3: Bias error from particle image displacements [173]

B.4 Particle Image Density:

There is a greater probability of calculating a valid displacement if more particle pairs enter the correlation calculation. A random error will occur if the seeding density is either too low or high. Figure B.4 shows that when a 32X32 window is used with approximately 5-10 particles per window (N_i), the probability of a valid vector is greater than 90%. A criterion was used in the adaptive PIV process which controlled the interrogation window size based on a particle density of 10 particles per window to minimise this error source. The streamline direction of jet and core flow minimised out of plane loss of pairs (F_o) whilst a high laser power and use of the Gaussian filter

reduced the effect of in-plane loss of pairs (F_i).

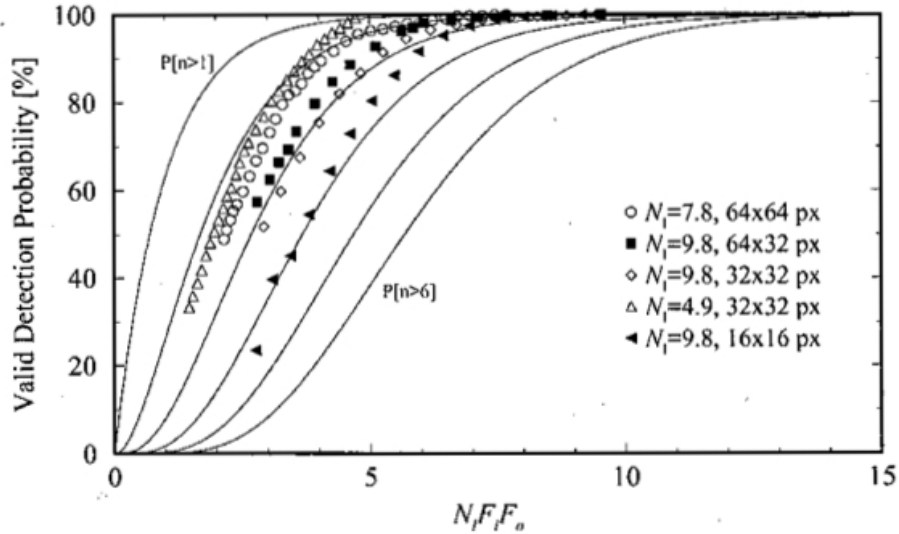


Fig. 5.28. Vector detection probability as a function of the product of image density N_i , in-plane loss of pairs F_i and out-of-plane loss of pairs F_o . The solid line represents the probability for having at least a given number of particle images in the interrogation spot (see also figure 4 in KEANE & ADRIAN [66])

Figure B.4: Probability of calculating the correct particle displacement as a function of particle image density [173]

Figure B.5 shows that the particle image density effects the random error substantially. However, if more than 10 particles per interrogation window are used (as controlled in this thesis); the random error is only 0.03 pixels.

$$\epsilon_{rms,particleimagedensity} = 0.03 \text{ pixels}$$

Using a high seeding density (>10) with a small interrogation window also provides a high validity, low measurement uncertainty and a high spatial resolution.

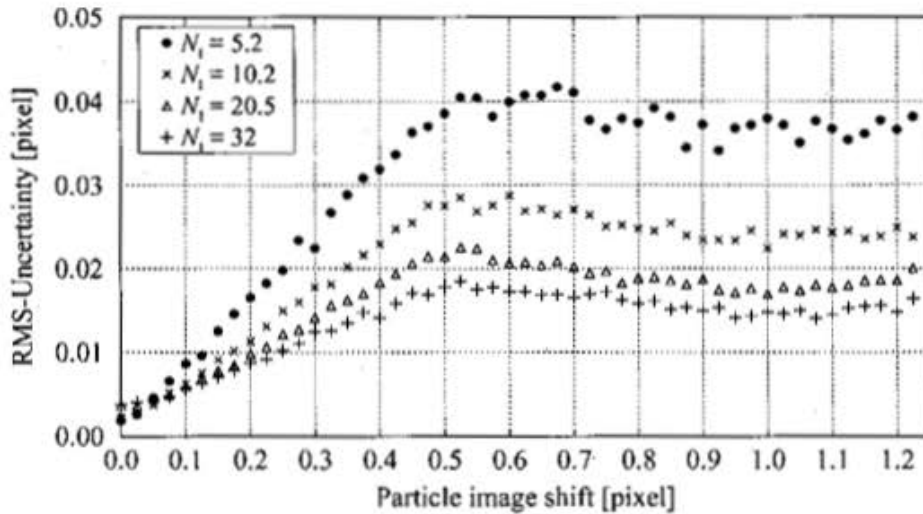


Fig. 5.29. Measurement uncertainty for single exposure/double frame PIV as a function of particle image shift for various particle image densities N_1 . (Simulation parameters: $d_r = 2.2$ pixel, $QL = 8$ bits/pixel, 32×32 pixel, no noise, optimum exposure, top-hat light sheet profile.)

Figure B.5: Random error due to particle image density [173]

B.5 Image Quantisation:

Random error can occur from the loss of information when the analogue input signal is converted to a digital signal and compressed. Referring to Figure B.6, for 8 bits/pixel and a particle image shift of 1.2 pixels, the random error is approximately 0.011 pixels.

$$\epsilon_{rms,imagequantisation} = 0.011 \text{ pixels}$$

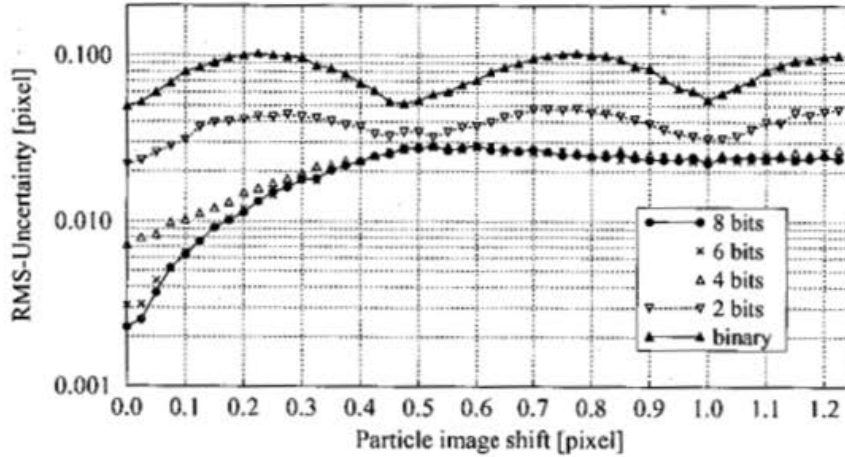


Fig. 5.30. Measurement uncertainty for single exposure/double frame PIV as a function of displacement and image quantization (simulation parameters: $d_r = 2.2$ pixel, $\mathcal{N}_I = 10.2$, 32×32 pixel, no noise, optimum exposure, top-hat light sheet profile)

Figure B.6: Random error from image quantisation [173]

B.6 Background Noise:

Background noise arises from reflections of the laser sheet which causes a variation in the reflected intensity of the seeding particles. The raw PIV images were filtered to remove reflections and normalise the background to a 0 light intensity. Background noise is minimised through masking in the PIV software, which eliminated any back scatter from the rig and allowed a higher intensity laser pulse to be used. All metallic parts were also anodised to a matte black finish to reduce reflections from the laser. Matching the refractive index of the sodium iodide and the perspex also reduced the reflected light on the boundary as it minimises refraction when the laser sheet passes through the different mediums. Referring to Figure B.7, for a particle shift more than 1.2 pixels and assuming 5% noise, the random error

from background noise is 0.012 pixels.

$$\epsilon_{rms,backgroundnoise} = 0.012 \text{ pixels}$$

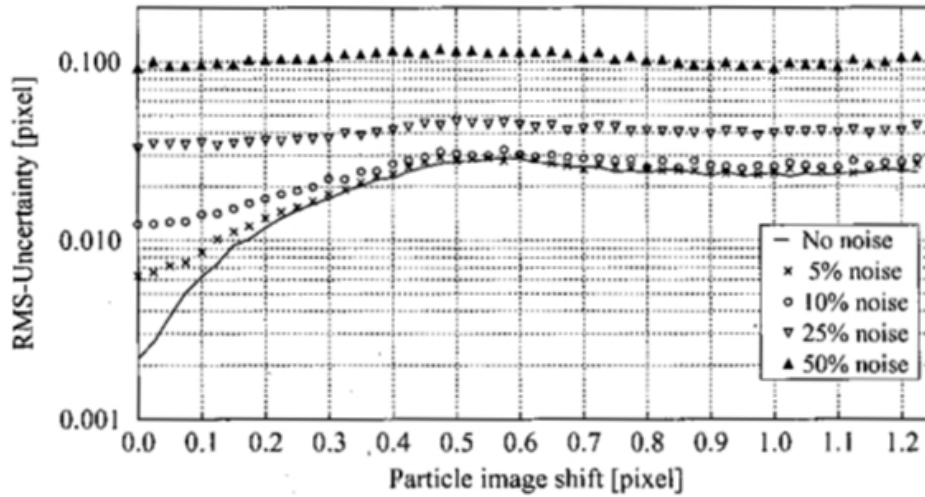


Fig. 5.32. Measurement uncertainty as a function of displacement and various amounts of white background noise (simulation parameters: $d_r = 2.2$ pixel, $\mathcal{N}_I = 10.2$, 32×32 pixel, optimum exposure, top-hat light sheet profile)

Figure B.7: Random error due to background noise [173]

B.7 Displacement Gradients:

As PIV measures the displacement of particles using statistical methods of correlation between two interrogation windows, a displacement gradient can result in an error. This bias arises from faster travelling particles leaving the window whilst slower particles will remain in it. Due to the existence of the venous and needle flows, it is assumed that high displacement gradients exist. For the worst case scenario, for a 32×32 window size with 20 particles per window and an average gradient of 0.07, Figure B.8 shows that a random error of 0.2 pixels will exist.

$$\epsilon_{rms,displacementgradient} = 0.5 \text{ pixels}$$

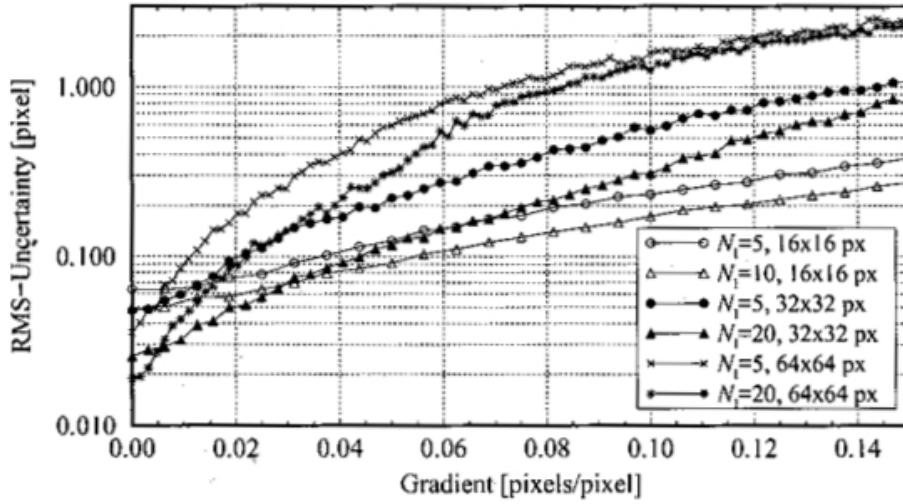


Fig. 5.33. Measurement uncertainty as a function of displacement gradient for various particle image densities and interrogation window sizes (simulation parameters: $d_r = 2.0$ pixel, $QL = 8$ bits/pixel, no noise, optimum exposure, top-hat light sheet profile)

Figure B.8: Random error due to displacement gradients [173]

Appendix C

Computational Sensitivity Analysis

C.1 Analysis of Mesh Size

A grid convergence study was undertaken to minimise the errors due to temporal discretisation. Roaches' theorem for grid convergence is utilised to quantify the numerical uncertainty between various mesh sizes [186]. The grid convergence index (GCI) is defined as:

$$GCI_{fine} = \frac{3\epsilon}{1 - r^p} \quad (\text{C.1})$$

Where ϵ is the solution obtained between two grids, r is the refinement factor and p is the formal order of accuracy. All computational simulations were run with a second order of accuracy.

The grid independence test was conducted using the midline settings where

the needle is placed at an angle of 20° with the tip placed centrally in the vein. Steady flow conditions were imposed on the vein and needle inlets with flow rates of 666 ml/min and 300 ml/min, respectively. The independence test was conducted on the venous needle as the downstream flow field is much more dynamic and larger than the arterial needle and is therefore more susceptible to grid size. Grid convergence is achieved with approximately two million hexahedral elements as displayed in Figure C.1.

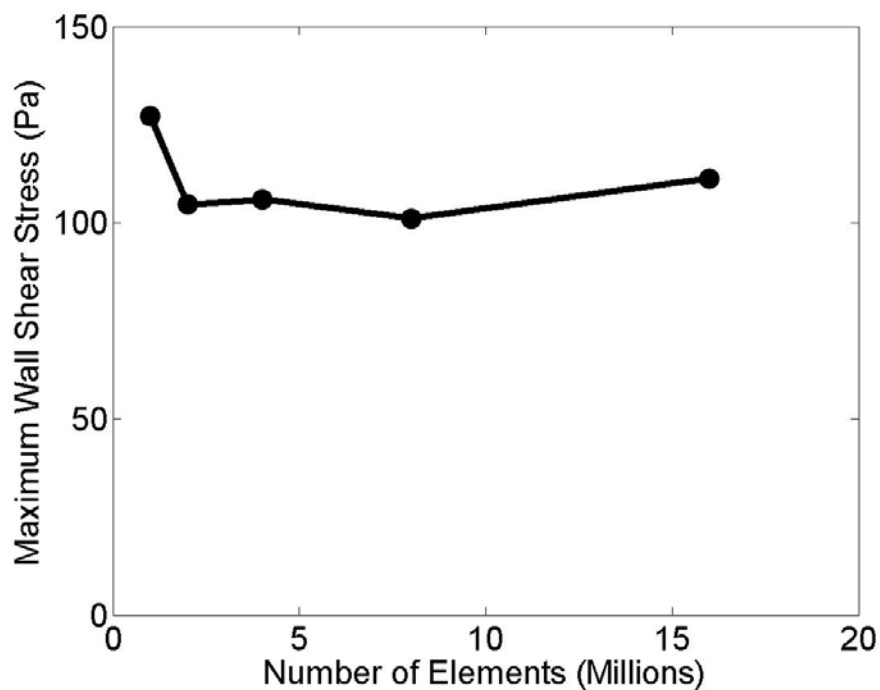


Figure C.1: Maximum WSS produced by the venous needle for different sizes

The GCI was also applied using the maximum WSS at the point of jet impingement and similarly showed grid convergence within 1% at two million elements as displayed in Table C.1.

Table C.1: Grid Convergence Index on maximum WSS produced by the venous needle

No. of Elements (millions)	Maximum WSS (Pa)	GCI_{fine} (%)
1	127.2	7.1
2	104.6	0.4
4	105.9	1.6
8	101.0	3.1
16	111.0	0.4

Monitor points were also imposed to analyse the grid size downstream of the needle where the venous needle jet mixes with the core flow. Quasi-steady velocities are expected as steady inlet conditions were imposed. Figure C.2 displays the velocity at the outlet of the model for difference mesh sizes. Velocity fluctuations are present with a grid size of 1 million elements but begin to stabilise as the grid is refined beyond 2 million elements, which is in agreement with the GCI and WSS convergence test. Upon closer examination, small fluctuations persist due to poor resolution of the mixing regime when a courser mesh is used. However, these fluctuations disappear when the grid size is increased beyond 8 million elements. Figure C.3 displays the velocity 20 diameters downstream of the needle tip, where the core flow and venous needle jet heavily mix. Similar to the above trend, large fluctuations are minimised in mesh sizes larger than 8 million elements.

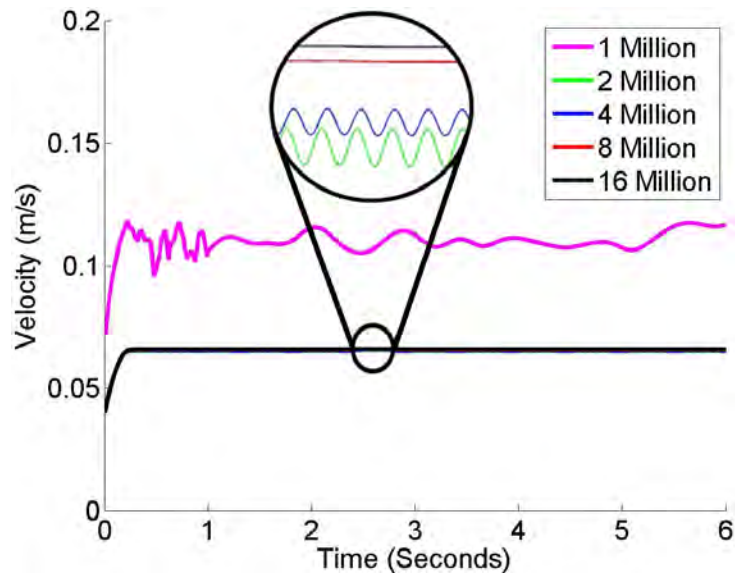


Figure C.2: Velocity at the outlet for different mesh sizes

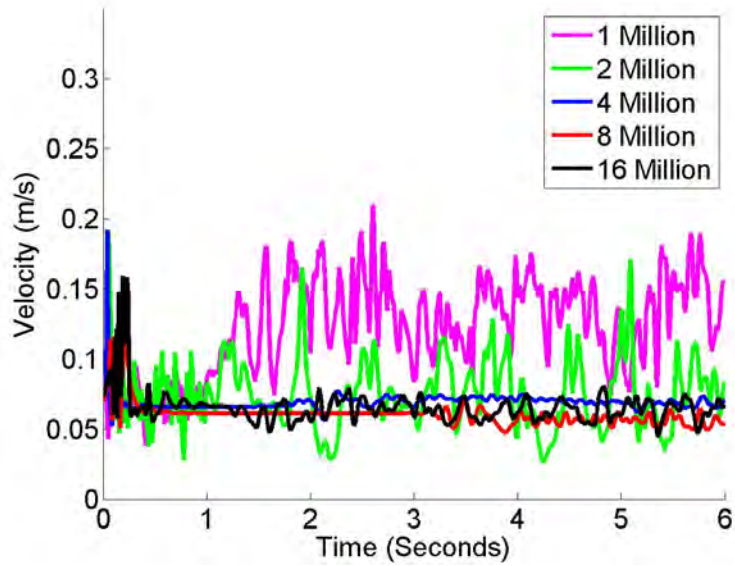


Figure C.3: Velocity downstream of the venous needle (20d) where the jet and core flow mix for different mesh sizes

Therefore, to ensure grid convergence on WSS at the point of jet impingement and adequate resolution of secondary flows in the mixing zone, all geometries were discretised with a mesh size of approximately 8 million elements.

C.2 Analysis of Time Step Size

For a time-independent solution it is essential to discretise in time to accurately resolve any transient features. However, a decreased time step will result in an increase in computational cost which can result in impractical simulation times. Thus, all transient simulations were initialised for 10 seconds to allow the flow fields produced by the vein and needle to stabilise. This ensured that the model simulated conditions which accurately represented the middle of a dialysis session. It was found that data recorded over 10 cycles was sufficient to represent the time averaged wall shear stresses. This methodology has the same order of magnitude used by Lantz et al. [185] who required 50 cycles to produce statistically reliable data in a model of a patient specific human aorta.

Time step size for transient analysis was analysed based on the Courant-Friedrichs-Lewy (CFL) condition to obtain stability, which is defined as:

$$CFL = \frac{u\Delta t}{\Delta x} \quad (C.2)$$

Where u is velocity magnitude, Δt is the time step size and Δx is the length of a single cell. Ideally, the CFL should be less than one, indicating that the flow does not travel further than one cell per time step, hereby increasing the resolution of the solution. However, as previously mentioned,

a smaller time step can significantly increase computational costs. Table C.2 outlines the maximum and average Courant number, residual level reached and the required solver time for the midline case with a mesh density of 8 million.

Table C.2: Summary of Time Step Analysis

Time Step	Maximum Courant Number	Average Courant Number	Residual Level	Solution Time (days)
0.01	778.269	1.385	10^{-5}	3
0.001	77.817	0.138	10^{-5}	12
0.0001	7.782	0.088	10^{-6}	42
0.00005	0.778	0.002	10^{-9}	>100

Further analysis was conducted by placing a velocity monitor 20 diameters downstream from the needle, in the region where the venous needle jet and core flow mix. As steady inlet conditions were imposed the solution should display a quasi-constant velocity after the initial transients have settled. Figure C.3 identifies velocity fluctuations when a course time step is used, however these are minimised when a time step of 0.0001 seconds or smaller is utilised.

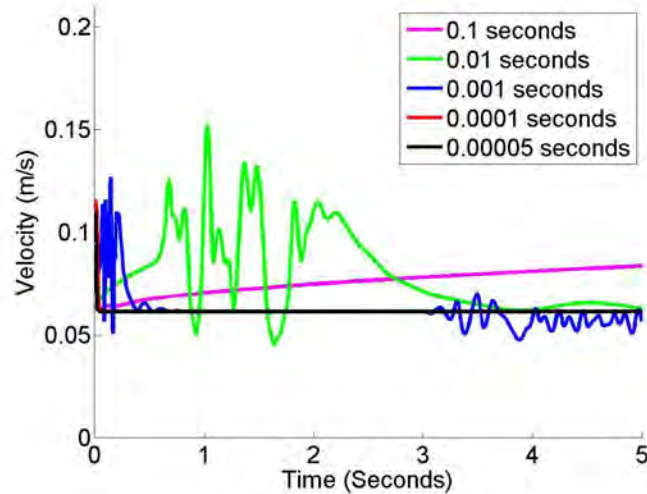


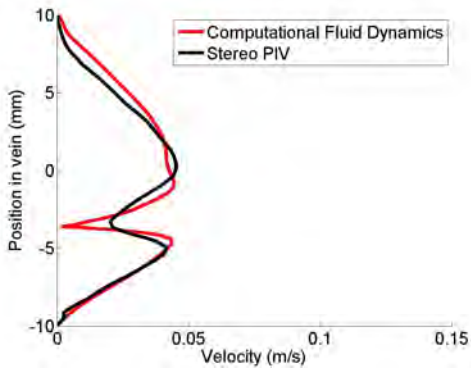
Figure C.4: Velocity downstream of the venous needle (20d) where the jet and core flow mix for different time step sizes

Furthermore, Steinman and colleagues [182–184] have conducted an extensive investigation on the effect of high resolution CFD in intracranial aneurysms by increasing the grid size and number of time steps per cardiac cycle. They concluded that at least 10,000 time steps per cardiac cycle are required in order to sufficiently resolve the complex haemodynamic flows which have been cited to affect fistula patency.

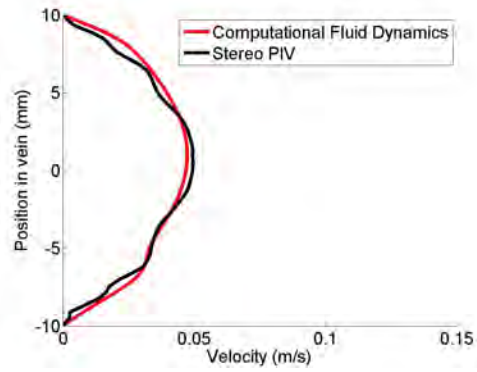
Therefore, a time step of 0.0001 seconds was deemed most feasible based on the study criteria (numerical accuracy and computational cost). This adheres to the recommendations by Steinman and colleagues [182–184] to conduct high resolution simulations of blood vessels. It is noted that the maximum Courant number is greater than one in this case. However, this occurs at the point of maximum velocity where the jet exits the needle. As this study focuses on the WSS in the blood vessel and the flow field downstream of the needles, the location where the maximum Courant number occurs is not critical.

Appendix D

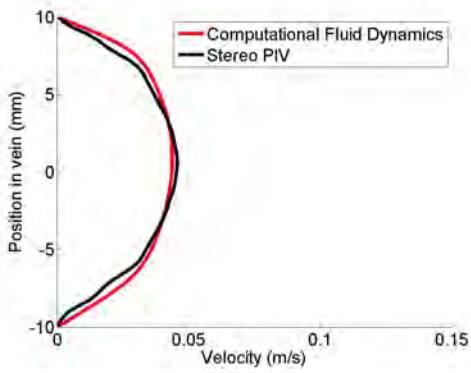
Numerical Validation



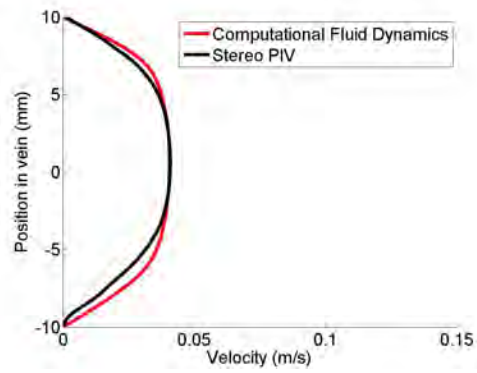
(a)



(b)



(c)



(d)

Figure D.1: Comparison between experimental and computational velocity profiles from the arterial needle in the antegrade orientation at a blood flow rate of 200 ml/min. a) Needle tip b) 5d downstream of the needle tip c) 10d downstream of the needle tip d) 15d downstream of the needle tip

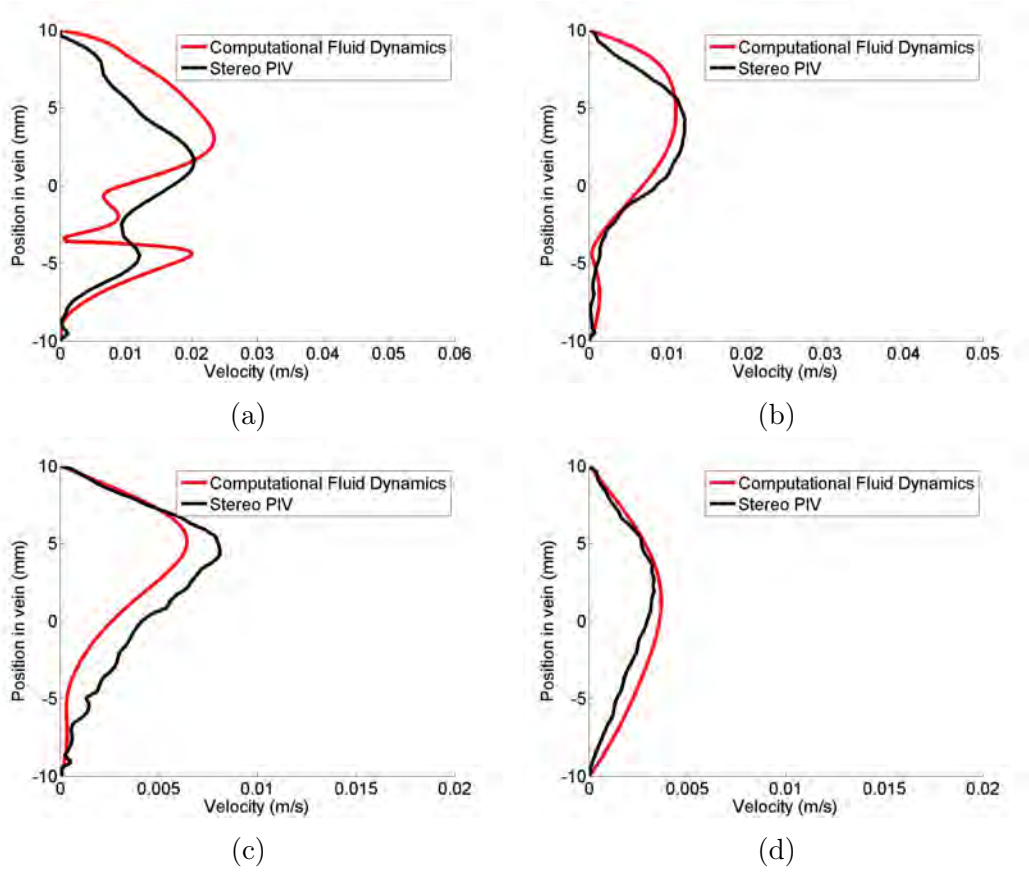
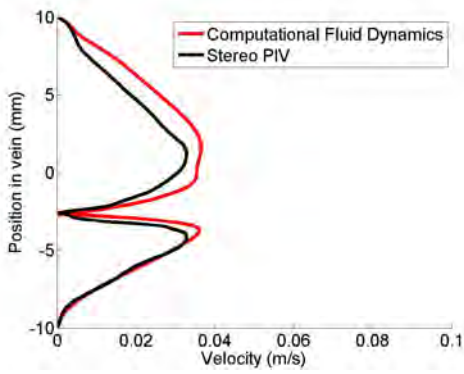
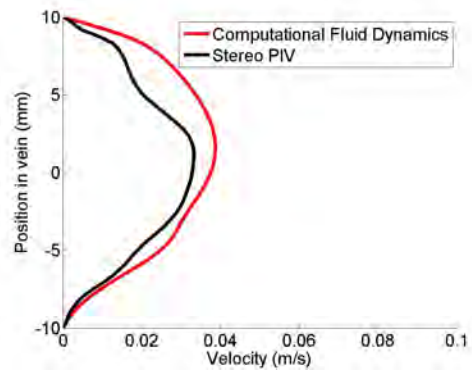


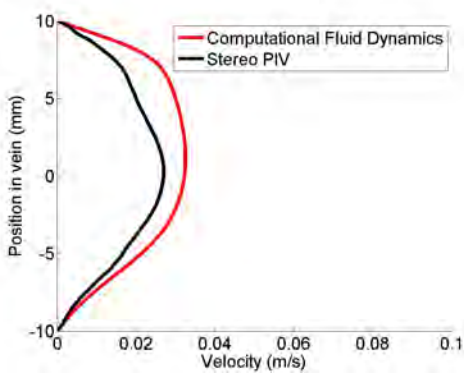
Figure D.2: Comparison between experimental and computational velocity profiles from the arterial needle in the antegrade orientation at a blood flow rate of 400 ml/min. a) Needle tip b) 5d downstream of the needle tip c) 10d downstream of the needle tip d) 15d downstream of the needle tip



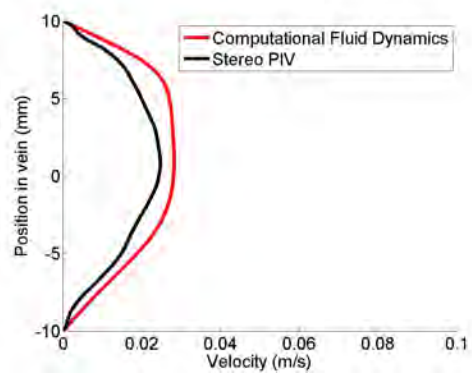
(a)



(b)



(c)



(d)

Figure D.3: Comparison between experimental and computational velocity profiles from the arterial needle in the antegrade orientation at a needle angle of 10° . a) Needle tip b) 5d downstream of the needle tip c) 10d downstream of the needle tip c) 15d downstream of the needle tip

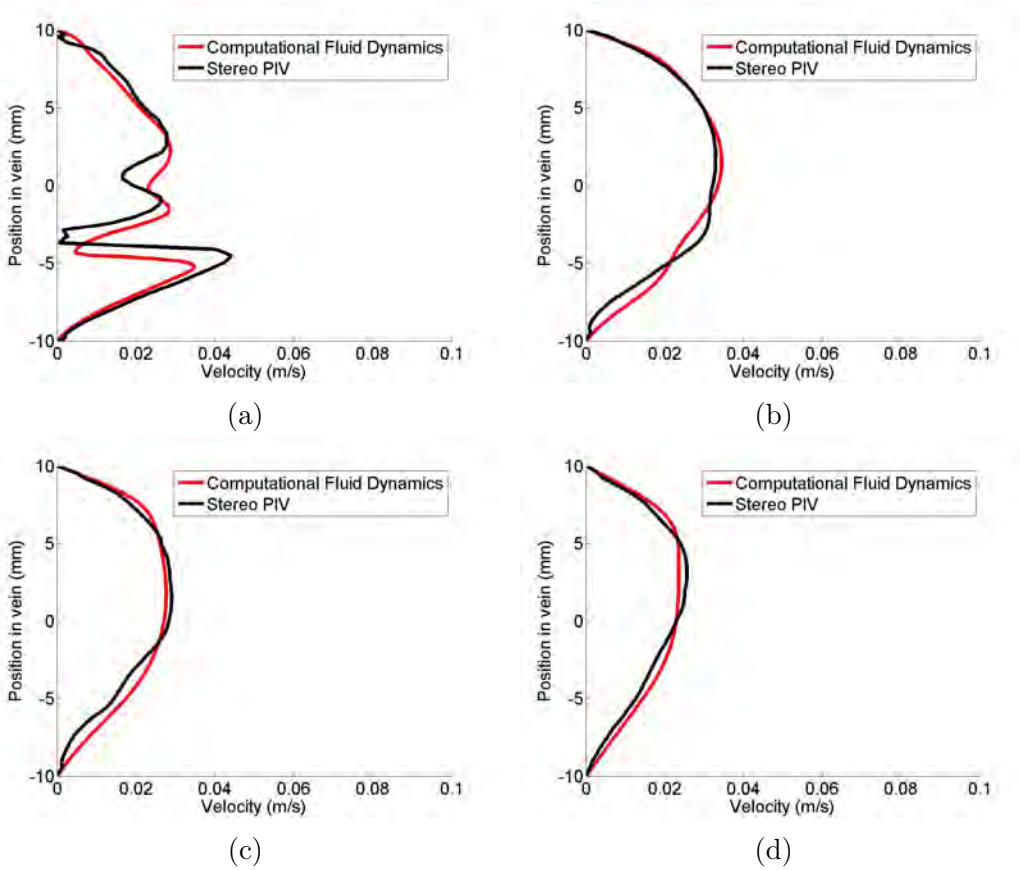


Figure D.4: Comparison between experimental and computational velocity profiles from the arterial needle in the antegrade orientation at a needle angle of 30° . a) Needle tip b) 5d downstream of the needle tip c) 10d downstream of the needle tip d) 15d downstream of the needle tip

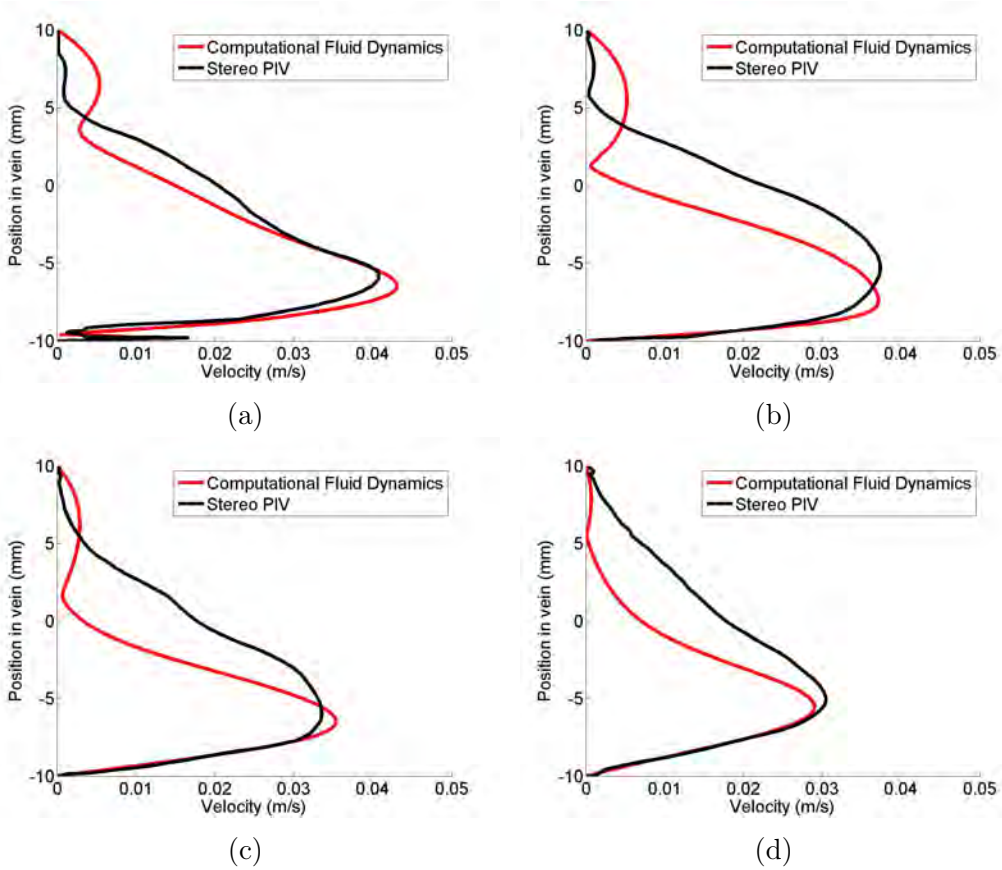
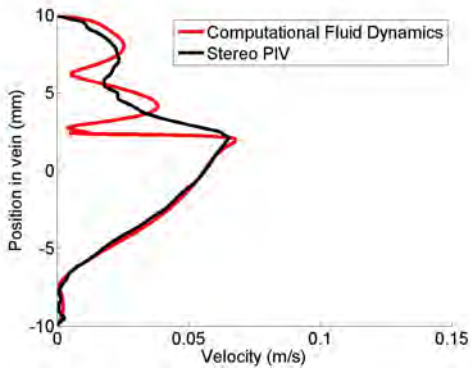
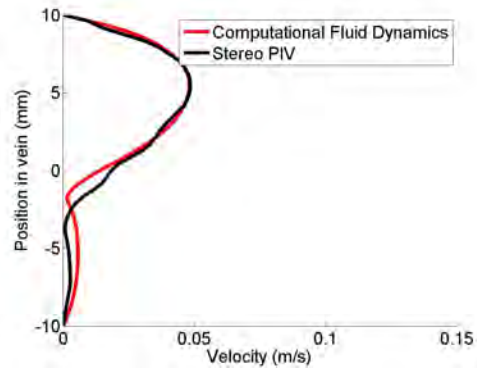


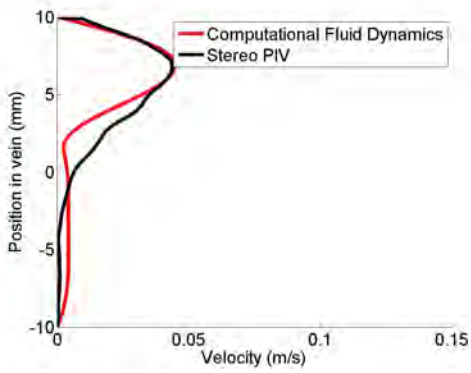
Figure D.5: Comparison between experimental and computational velocity profiles from the arterial needle in the antegrade orientation at the bottom of the vein. a) Needle tip b) 5d downstream of the needle tip c) 10d downstream of the needle tip d) 15d downstream of the needle tip



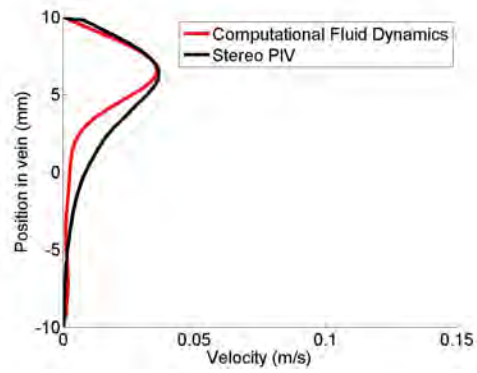
(a)



(b)



(c)



(d)

Figure D.6: Comparison between experimental and computational velocity profiles from the arterial needle in the antegrade orientation at the top of the vein. a) Needle tip b) 5d downstream of the needle tip c) 10d downstream of the needle tip d) 15d downstream of the needle tip

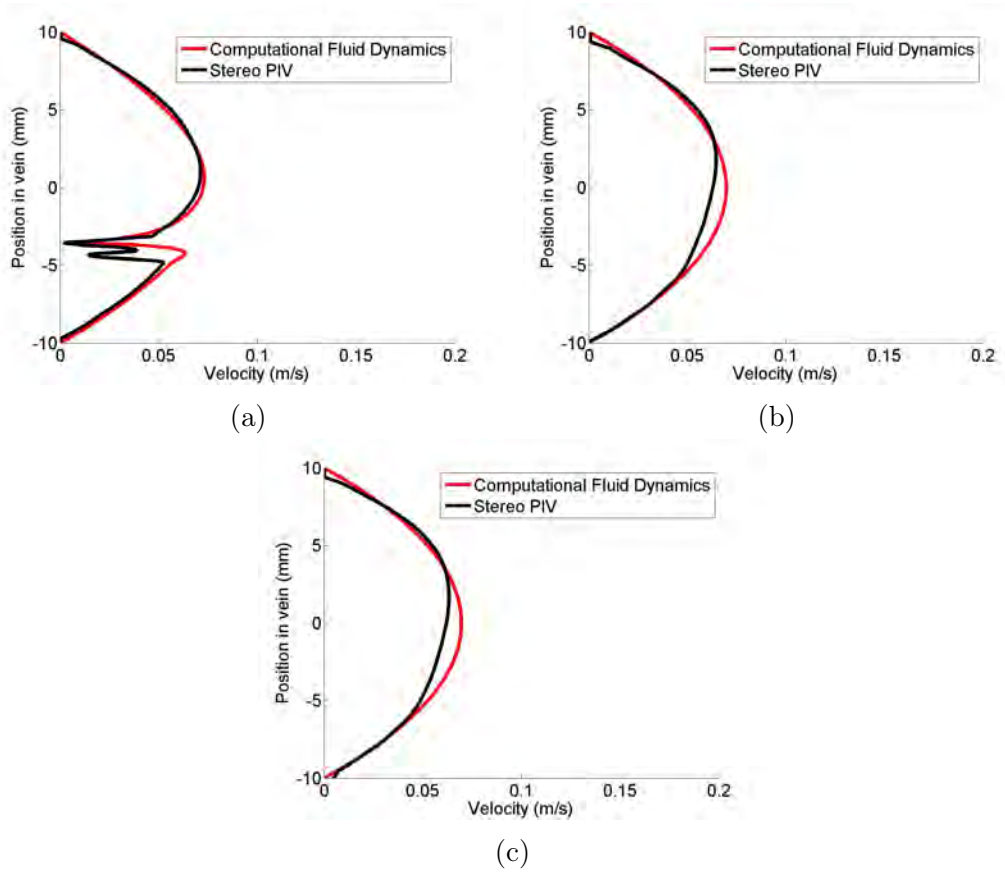


Figure D.7: Comparison between experimental and computational velocity profiles from the arterial needle in the retrograde orientation at a blood flow rate of 200 ml/min. a) Needle tip b) 5d downstream of the needle tip c) 10d downstream of the needle tip

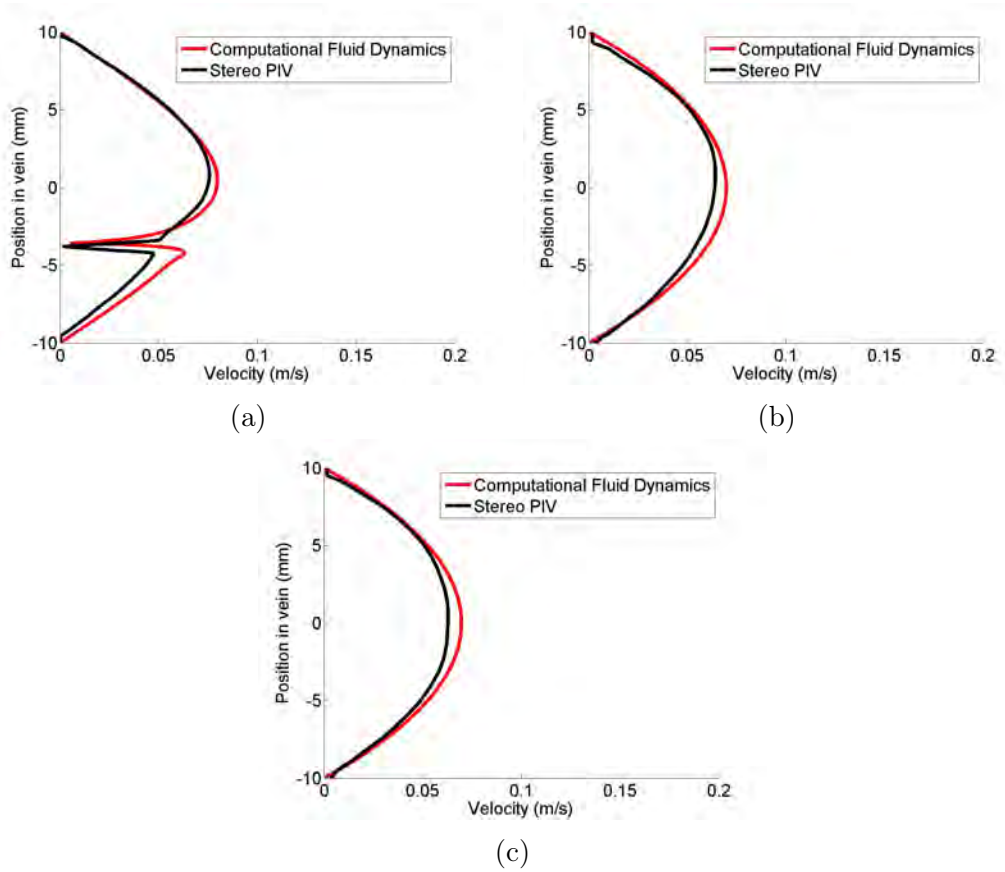


Figure D.8: Comparison between experimental and computational velocity profiles from the arterial needle in the retrograde orientation at a blood flow rate of 400 ml/min. a) Needle tip b) 5d downstream of the needle tip c) 10d downstream of the needle tip

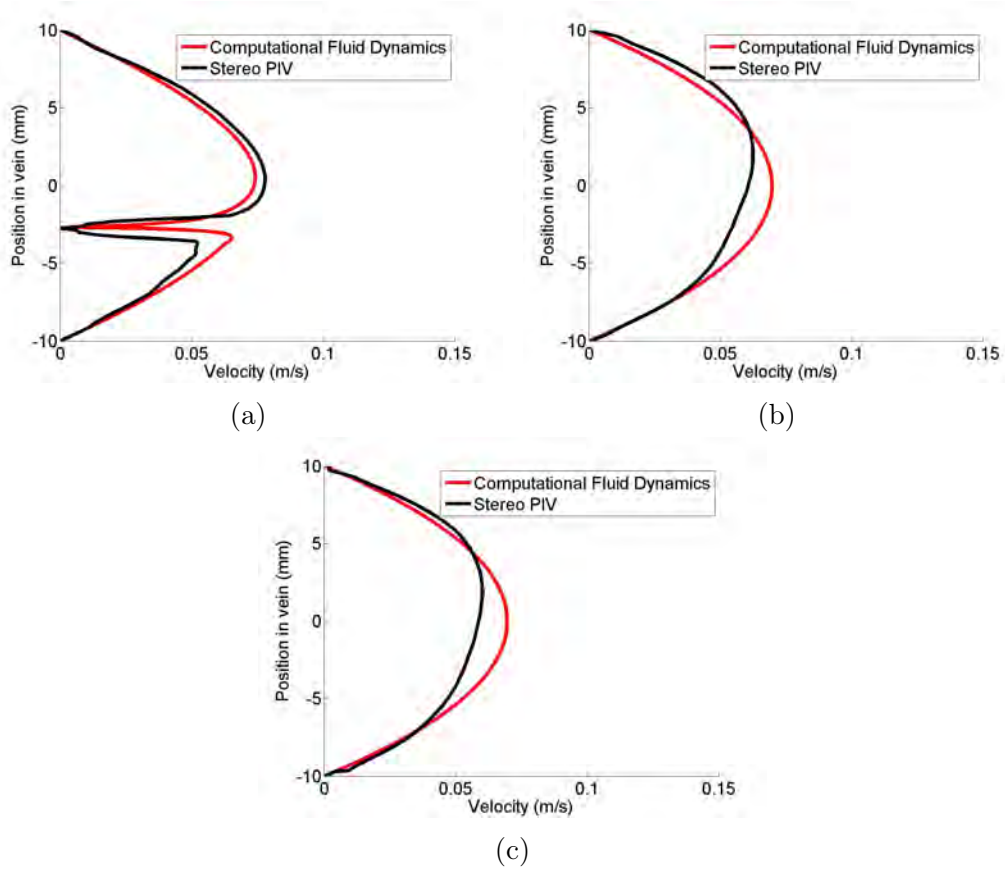


Figure D.9: Comparison between experimental and computational velocity profiles from the arterial needle in the retrograde orientation at a needle angle of 10° . a) Needle tip b) 5d downstream of the needle tip c) 10d downstream of the needle tip

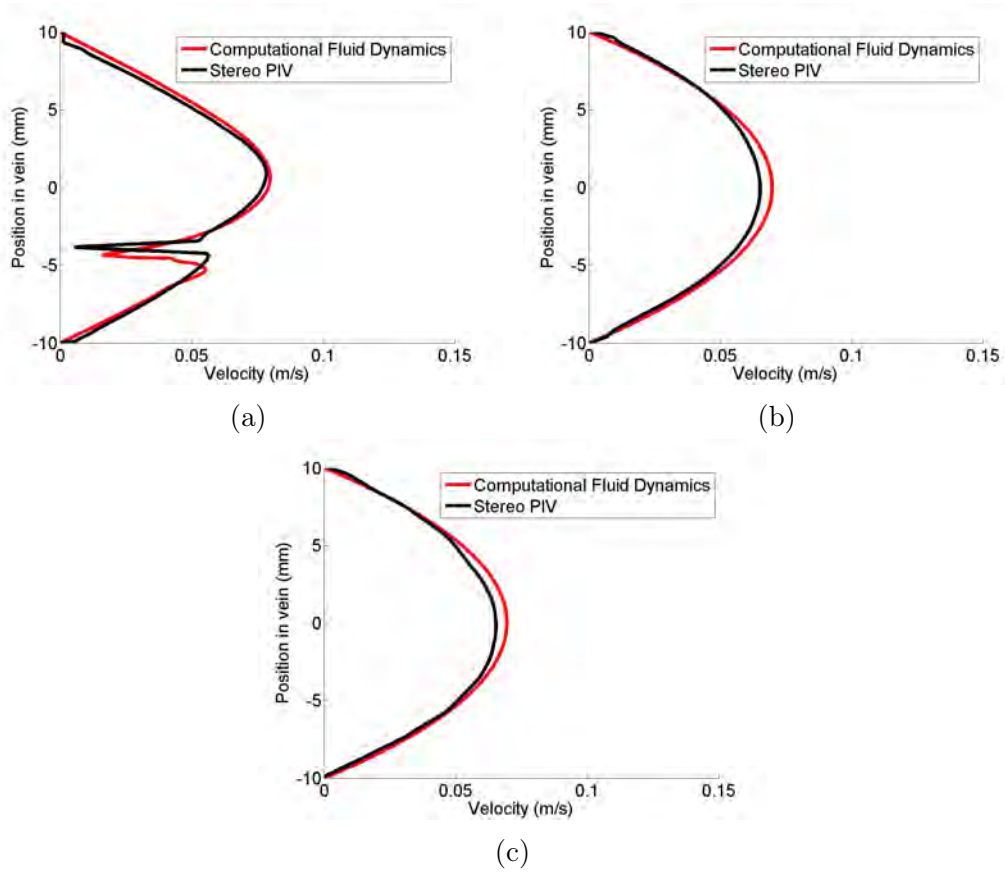


Figure D.10: Comparison between experimental and computational velocity profiles from the arterial needle in the retrograde orientation at a needle angle of 30° . a) Needle tip b) 5d downstream of the needle tip c) 10d downstream of the needle tip

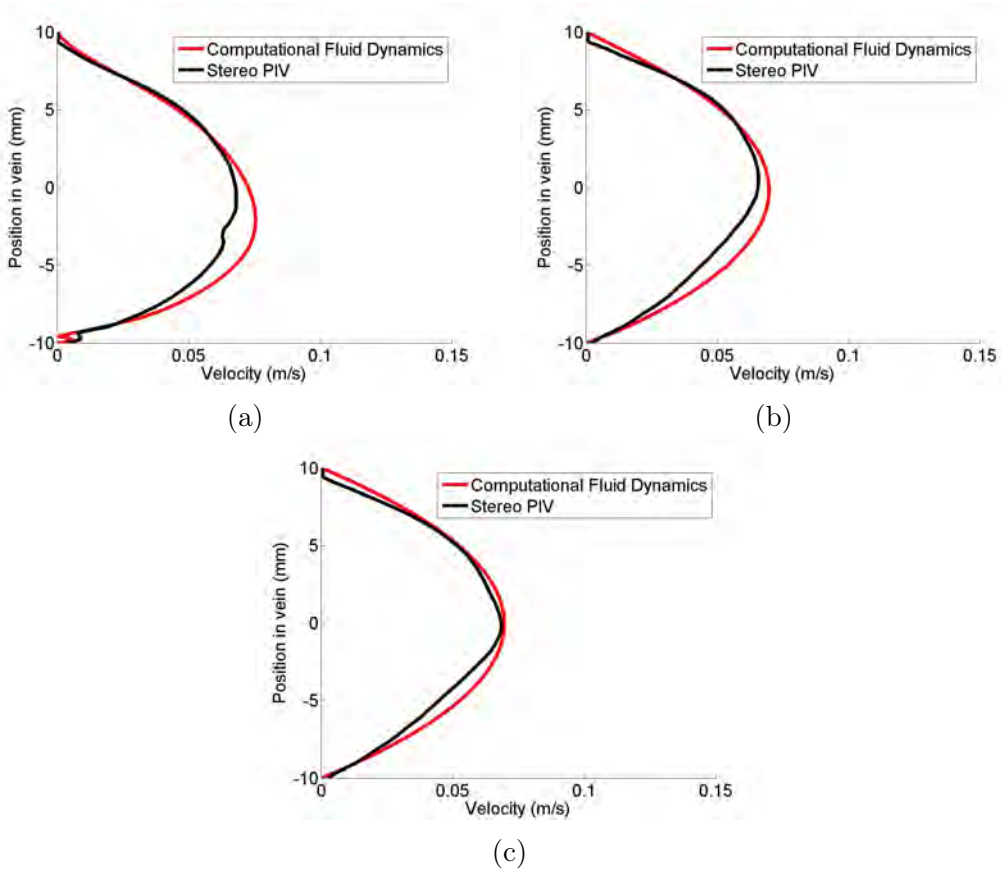


Figure D.11: Comparison between experimental and computational velocity profiles from the arterial needle in the retrograde orientation at the bottom of the vein. a) Needle tip b) 5d downstream of the needle tip c) 10d downstream of the needle tip

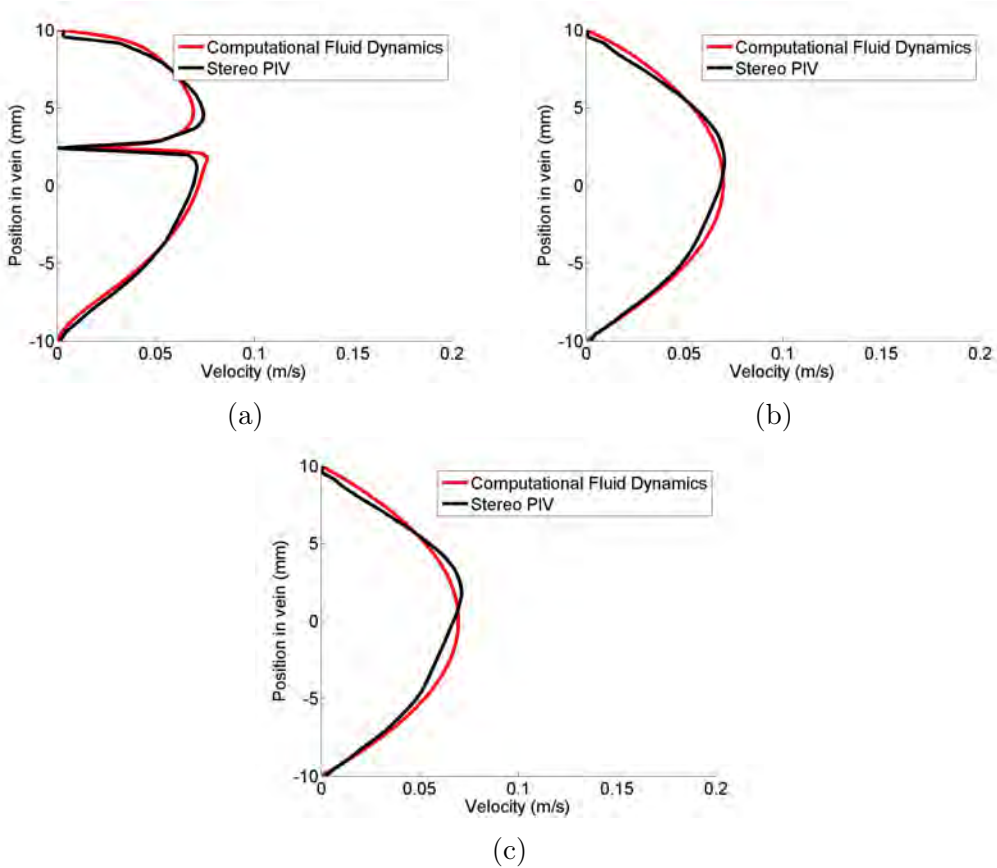


Figure D.12: Comparison between experimental and computational velocity profiles from the arterial needle in the retrograde orientation at the top of the vein. a) Needle tip b) 5d downstream of the needle tip c) 10d downstream of the needle tip

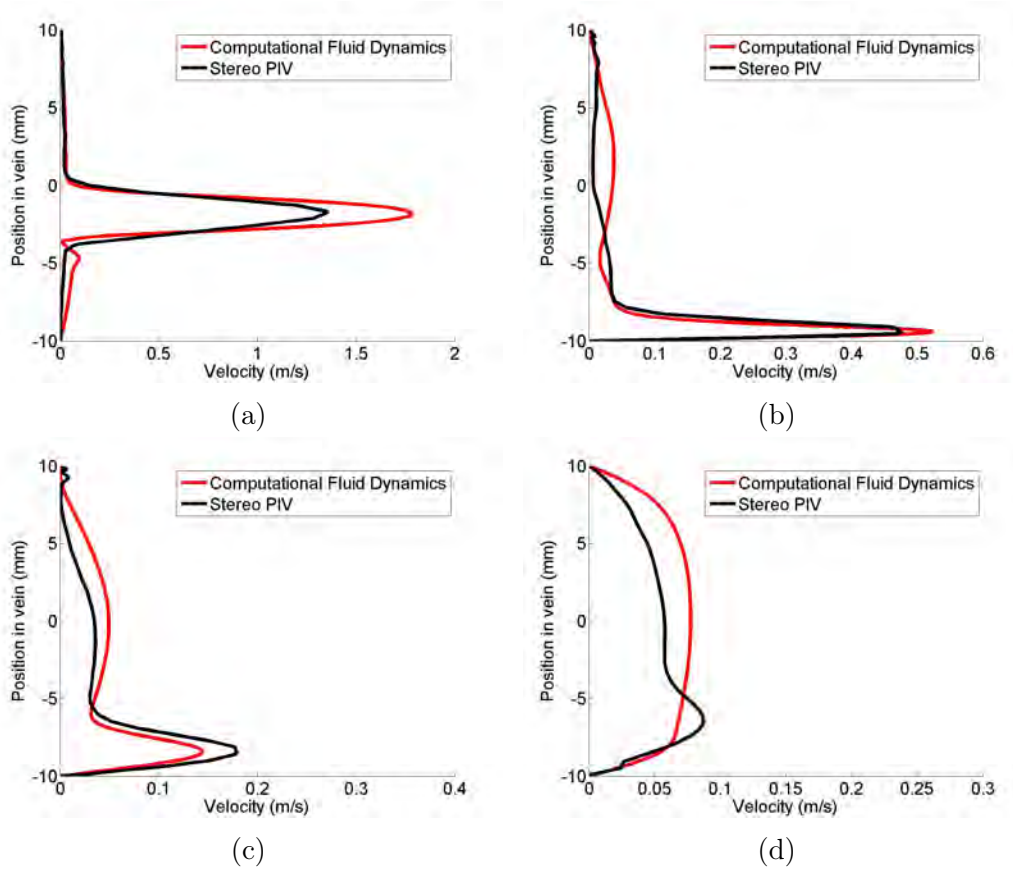


Figure D.13: Comparison between experimental and computational velocity profiles from the venous needle at a blood flow rate of 200 ml/min. a) Needle tip b) 20d downstream of the needle tip c) 40d downstream of the needle tip d) 60d downstream of the needle tip

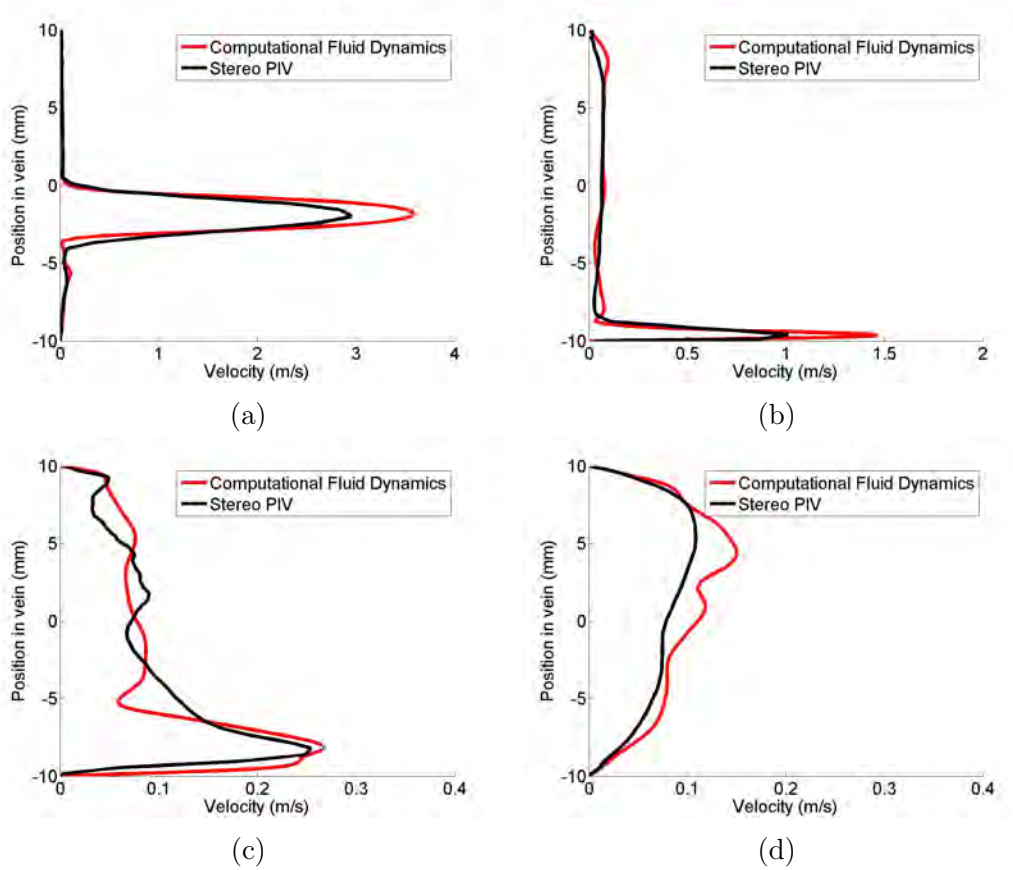


Figure D.14: Comparison between experimental and computational velocity profiles from the venous needle at a blood flow rate of 400 ml/min. a) Needle tip b) 20d downstream of the needle tip c) 40d downstream of the needle tip d) 60d downstream of the needle tip

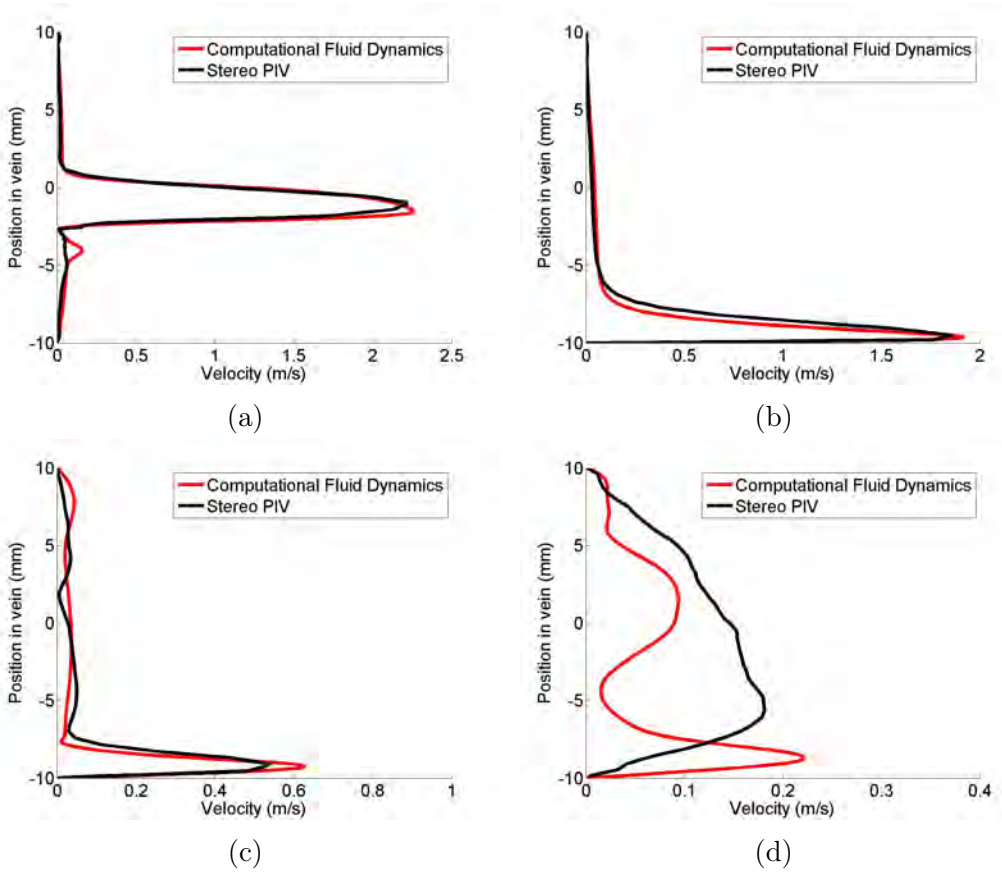
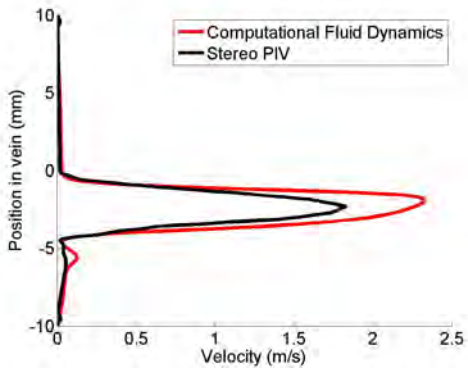
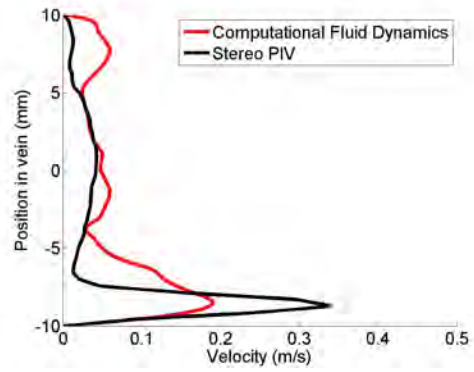


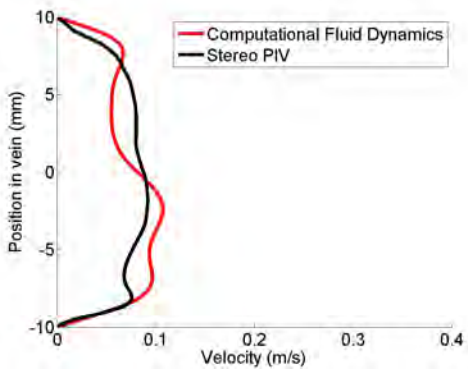
Figure D.15: Comparison between experimental and computational velocity profiles from the venous needle at a needle angle of 10° . a) Needle tip b) 20d downstream of the needle tip c) 40d downstream of the needle tip c) 60d downstream of the needle tip



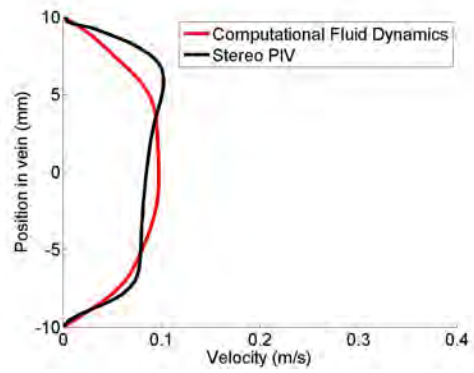
(a)



(b)

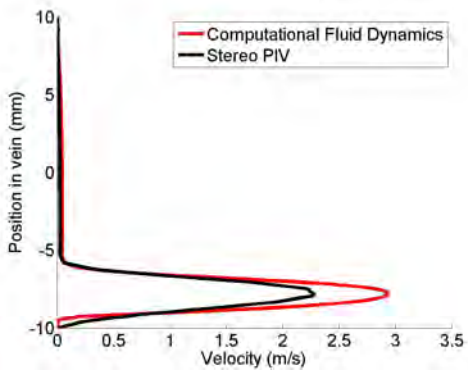


(c)

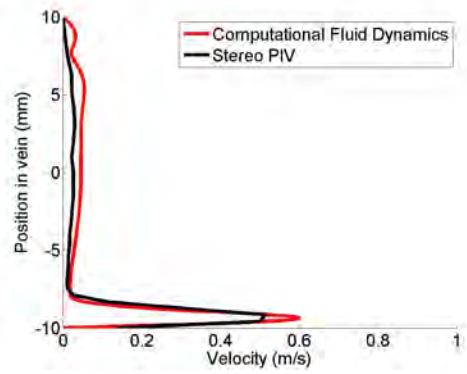


(d)

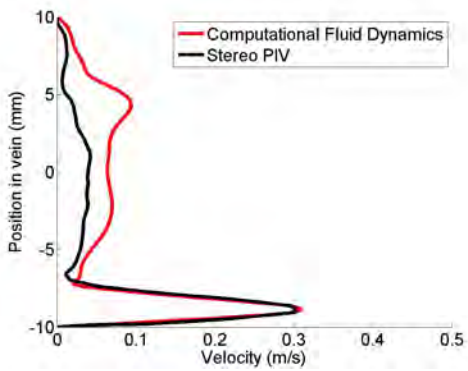
Figure D.16: Comparison between experimental and computational velocity profiles from the venous needle at a needle angle of 30° . a) Needle tip b) 20d downstream of the needle tip c) 40d downstream of the needle tip c) 60d downstream of the needle tip



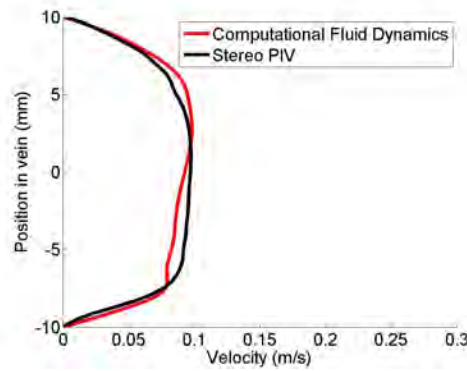
(a)



(b)



(c)



(d)

Figure D.17: Comparison between experimental and computational velocity profiles from the venous needle placed at the bottom of the vein. a) Needle tip b) 20d downstream of the needle tip c) 30d downstream of the needle tip c) 60d downstream of the needle tip

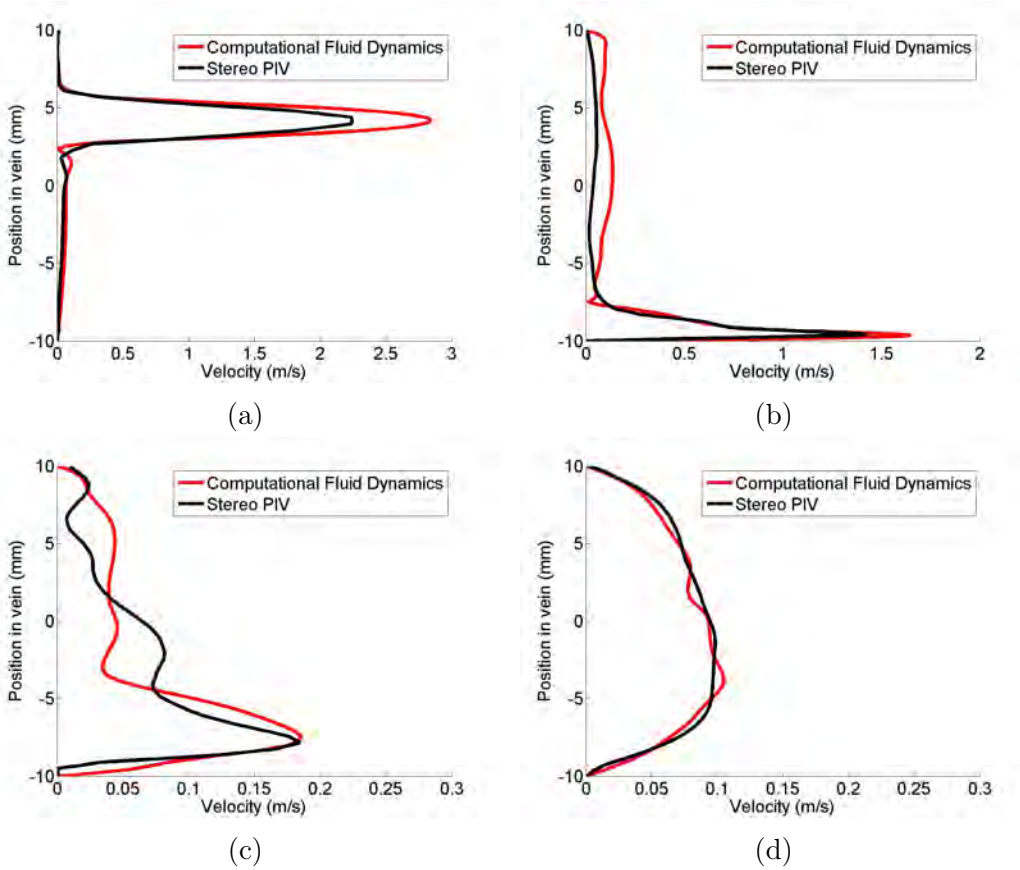


Figure D.18: Comparison between experimental and computational velocity profiles from the venous needle placed at the top of the vein. a) Needle tip b) 20d downstream of the needle tip c) 40d downstream of the needle tip d) 60d downstream of the needle tip

Bibliography

- [1] Illse Van Tricht, Dirk De Wachter, Jan H. M. Tordoir, and Pascal Verdonck. Hemodynamics and complications encountered with arteriovenous fistulas and grafts as vascular access for hemodialysis: a review. *Annals of Biomedical Engineering*, 33(9):1142–57, 2005.
- [2] Khushboo Kaushal and Samuel E. Wilson. *Thrombophilia as a Cause of Recurrent Vascular Access Thrombosis in Hemodialysis Patients*, book section 6, pages 44–47. Lippincott Williams and Wilkins, Philadelphia, USA, 5 edition, 2010.
- [3] Timmy Lee, Yang Wang, Lois Arend, Virgilius Cornea, Begona Campos, Rino Munda, and Prabir Roy Chaudhury. Comparative analysis of cellular phenotypes within the neointima from vein segments collected prior to vascular access surgery and stenotic arteriovenous dialysis accesses. *Seminars in Dialysis*, 27(3):303–309, 2014.
- [4] Robert S. Keynton, Mary M. Evancho, Rick L. Sims, Nancy V. Rodway, Andrea Gobin, and Stanley E. Rittgers. Intimal hyperplasia and wall shear in arterial bypass graft distal anastomoses: An in vivo model study. *Journal of Biomechanical Engineering*, 123(5):464–473, 2001.
- [5] Mary Hammes and Umberto Benedetto. Hemodynamic and biologic determinates of arteriovenous fistula outcomes in renal failure patients. *BioMed Research International*, 2015, 2015.

- [6] Tonia. C. Rothuizen, ChunYu Wong, Paul H. A. Quax, Anton J. van Zonneveld, Ton J. Rabelink, and Joris I. Rotmans. Arteriovenous access failure: more than just intimal hyperplasia? *Nephrology Dialysis Transplantation*, 2013.
- [7] Sunil Unnikrishnan, Thanh N. Huynh, Brigitta C. Brott, Yasumasa Ito, Chi-Hung Cheng, Alan M. Shih, Michael Allon, and Andreas S. Anayiotos. Turbulent flow evaluation of the venous needle during hemodialysis. *Journal of Biomechanical Engineering*, 127(7):1141–1146, 2005.
- [8] Cindy L. Stanfield and William J Germann. *Principles of Human Physiology*. Pearson Benjamin Cummings, San Fransisco, USA, 3rd edition, 2009.
- [9] Nosratola D. Vaziri, Cyril H. Barton, and Ashish Kalthia. *Epidemiology and Pathophysiology of Chronic Renal Failure and Guidelines for Initiation of Hemodialysis*, book section 10, pages 81–85. Lippincott Williams and Wilkins, Philadelphia, USA, 5 edition, 2010.
- [10] Andrew S. Levey, Josef Coresh, Ethan Balk, Annamaria T. Kausz, Adeera Levin, Michael W. Steffes, Ronald J. Hogg, Ronald D. Perrone, Joseph Lau, and Garabed Eknoyan. National kidney foundation practice guidelines for chronic kidney disease: Evaluation, classification, and stratification. *Annals of Internal Medicine*, 139(2):137–147, 2003.
- [11] Martin Gallagher, Denise Campbell, Michelle Irving, Allison Tong, Pamela Lopez-Vargas, Martin Howell, and Venersha Naidoo. Caring for australasians with renal impairment @ONLINE, Jan 2012.
- [12] Icahn School of Medicine at Mount Sinai. Kidney disease and dialysis access @ONLINE, Sept 2016.

- [13] Anton N. Sidawy, Lawrence M. Spergel, Anatole Besarab, Michael Allon, William C. Jennings, Frank T. Padberg Jr, M. Hassan Murad, Victor M. Montori, Ann M. O'Hare, Keith D. Calligaro, Robyn A. Macsata, Alan B. Lumsden, and Enrico Ascher. The society for vascular surgery: Clinical practice guidelines for the surgical placement and maintenance of arteriovenous hemodialysis access. *Journal of Vascular Surgery*, 48(5, Supplement):S2–S25, 2008.
- [14] Matthew D. Danielson, Larry-Stuart Deutsch, and Geoffrey H. White. *Central Venous Cannulation for Hemodialysis Access*, book section 16, pages 120–138. Lippincott Williams and Wilkins, Philadelphia, USA, 5 edition, 2010.
- [15] Radojica Stolic. Most important chronic complications of arteriovenous fistulas for hemodialysis. *Medical Principles and Practice*, 22(3):220–228, 2013.
- [16] Samuel E. Wilson. *Interposition Arteriovenous Grafts (Bridge Fistulas) for Hemodialysis*, book section 14, pages 104–113. Lippincott Williams and Wilkins, Philadelphia, USA, 5 edition, 2010.
- [17] Brian Mailey, Khushboo Kaushal, and Samuel E. Wilson. *New Synthetic Grafts ad Early Access*, book section 15, pages 114–119. Lippincott Williams and Wilkins, Philadelphia, USA, 5 edition, 2010.
- [18] Klaus Konner. A primer on the av fistula—achilles' heel, but also cinderella of haemodialysis. *Nephrology Dialysis Transplantation*, 14(9):2094–2098, 1999.
- [19] Geoffrey H. White and Michael S. Hayashi. *Autogenous Vein for Fistulas and Interposition Grafts*, book section 12, pages 92–98. Lippincott Williams and Wilkins, Philadelphia, USA, 5 edition, 2010.

- [20] Geoffrey H. White and Samuel E. Wilson. *Patient Assessment and Planning for Vascular Access Surgery*, book section 2, pages 7–12. Lippincott Williams and Wilkins, Philadelphia, USA, 5 edition, 2010.
- [21] Gholam Hosein Kazemzadeh, Mohammad-Hadi Saeed Modaghegh, Hassan Ravari, Mohammad Reza Daliri, Leila Hoseini, and Mohammad Reza Nateghi. Primary patency rate of native av fistula: long term follow up. *International Journal of Clinical Experimental Medicine*, 5(2):173–178, 2012.
- [22] United States Renal Data System. 2014 usrds annual data report: Epidemiology of kidney disease in the united states. Report, National Institutes of Health, 2014 2014.
- [23] Heshmatollah Salahi, Afsoon Fazelzadeh, Alireza Mehdizadeh, Ali Razmkon, and Seyed Ali Malek-Hosseini. Complications of arteriovenous fistula in dialysis patients. *Transplantation Proceedings*, 38(5):1261–1264, 2006.
- [24] Zarin Gundevia, Heather Whalley, Martin Ferring, Martin Claridge, Stephen Smith, and Teun Wilmink. Effect of operating surgeon on outcome of arteriovenous fistula formation. *Journal of Vascular Surgery*, 47(5):1122, 2008.
- [25] Peter F. Davies. Haemodynamic influences on vascular remodelling. *Transplant Immunology*, 5(4):243–5, 1997.
- [26] Anatole Besarab, Ravi P. K. Parasurman, and Stanley Frinak. *Vascular Access for Haemodialysis*, volume 2, pages E1–E1. Nature Publishing Group, 2006.
- [27] Luc Turmel Rodrigues, Josette Pengloan, Serge Baudin, Didier Testou, Mohamed Abaza, Georges Dahdah, Albert Mouton, and Didier Blanchard. Treatment of stenosis and thrombosis in haemodialysis

- fistulas and grafts by interventional radiology. *Nephrology Dialysis Transplantation*, 15(12):2029–2036, 2000.
- [28] Sharmila Sivanesan, Tien V. How, and Ali Bakran. Sites of stenosis in av fistulae for haemodialysis access. *Nephrology Dialysis Transplantation*, 14(1):118–120, 1999.
- [29] Luc Turmel Rodrigues, Josette Pengloan, Dominique Blanchier, Mohamed Abaza, Béatrice Birmele, Olivier Haillet, and Didier Blanchard. Insufficient dialysis shunts: improved long-term patency rates with close hemodynamic monitoring, repeated percutaneous balloon angioplasty, and stent placement. *Radiology*, 187(1):273–278, 1993.
- [30] Sidney Glanz, David H. Gordon, Khalid M. Butt, Joon Hong, Roland J. Adamson, and Salvatore J. Sclafani. Dialysis access fistulas: treatment of stenoses by transluminal angioplasty. *Radiology*, 152(3):637–642, 1984.
- [31] Sidney Glanz, David H. Gordon, Khalid M. Butt, Joon Hong, and George S. Lipkowitz. The role of percutaneous angioplasty in the management of chronic hemodialysis fistulas. *Annals of Surgery*, 206(6):777, 1987.
- [32] Gerald A. Beathard. Percutaneous transvenous angioplasty in the treatment of vascular access stenosis. *Kidney International*, 42(6):1390–1397, 1992.
- [33] Mukadder Ayse Bilgic, Hakki Yilmaz, Alper Bozkurt, Huseyin Tugrul Celik, Ismail Celal Bilgic, Ozgul Malcok Gurel, Ismail Kirbas, Nuket Bavbek, and Ali Akcay. Relationship of late arteriovenous fistula stenosis with soluble e-selectin and soluble epcr in chronic hemodialysis patients with arteriovenous fistula. *Clinical and Experimental Nephrology*, 19(1):133–139, 2015.

- [34] Mineo Motomiya and Takeshi Karino. Flow patterns in the human carotid artery bifurcation. *Stroke*, 15(1):50–56, 1984.
- [35] Hani N. Sabbah, Frederick J. Walburn, Paul D. Stein, Dieter Liepsch, A Poll, Jack Strigberger, Hani N. Sabbah, and Paul D. Stein. Patterns of flow in the left coronary artery. *Journal of Biomechanical Engineering*, 106(3):272–279, 1984.
- [36] Toshihisa Asakura and Takeshi Karino. Flow patterns and spatial distribution of atherosclerotic lesions in human coronary arteries. *Circulation Research*, 66(4):1045–1066, 1990.
- [37] Jocelyn Bale-Glickman, K Selby, Omer Savas, and David Saloner. Experimental flow studies in exact-replica phantoms of atherosclerotic carotid bifurcations under steady input conditions. *Journal of Biomechanical Engineering*, 125(1):38–48, 2003.
- [38] Sang-Wook Lee, Luca Antiga, and David A. Steinman. Correlations among indicators of disturbed flow at the normal carotid bifurcation. *Journal of Biomechanical Engineering*, 131(6):061013–1–061013–7, 2009.
- [39] David N. Ku, Don P. Giddens, Christopher K. Zarins, and Seymour Glagov. Pulsatile flow and atherosclerosis in the human carotid bifurcation. positive correlation between plaque location and low oscillating shear stress. *Arteriosclerosis, Thrombosis, and Vascular Biology*, 5(3):293–302, 1985.
- [40] Xiaoyi He and David N. Ku. Pulsatile flow in the human left coronary artery bifurcation: Average conditions. *Journal of Biomechanical Engineering*, 118(1):74–82, 1996.
- [41] Shu Chien. Effects of disturbed flow on endothelial cells. *Annals of Biomedical Engineering*, 36(4):554–562, 2008.

- [42] Peter F. Davies, Andrea Remuzzi, Ethel J. Gordon, Forbes C. Dewey, and Michael A. Gimbrone. Turbulent fluid shear stress induces vascular endothelial cell turnover in vitro. *Proceedings of the National Academy of Sciences of the United States of America*, 83(7):2114–2117, 1986.
- [43] Yumnah Mohamied, Ethan M. Rowland, Emma L. Bailey, Spencer J. Sherwin, Martin A. Schwartz, and Peter D. Weinberg. Change of direction in the biomechanics of atherosclerosis. *Annals of Biomedical Engineering*, 43(1):16–25, 2014.
- [44] Joseph Knight, Ufuk Olgac, Stefan C. Saur, Dimos Poulikakos, William Marshall, Philippe C. Cattin, Hatem Alkadhi, and Vartan Kurtcuoglu. Choosing the optimal wall shear parameter for the prediction of plaque location—a patient-specific computational study in human right coronary arteries. *Atherosclerosis*, 211(2):445–450, 2010.
- [45] Heather A. Himburg, Deborah M. Grzybowski, Andrew L. Hazel, Jeffrey A. LaMack, Xue-Mei Li, and Morton H. Friedman. Spatial comparison between wall shear stress measures and porcine arterial endothelial permeability. *American Journal of Physiology Heart Circulatory Physiology*, 286(5):H1916–22, 2004.
- [46] Seiji Ohira, Tadamasa Kon, and Takashi Imura. Evaluation of primary failure in native av fistulae (early fistula failure). *Hemodialysis International*, 10(2):173–179, 2006.
- [47] V. Wong, Richard A. Ward, Jack D. Taylor, Sadasivam Selvakumar, Tien V. How, and Ali Bakran. Factors associated with early failure of arteriovenous fistulae for haemodialysis access. *European Journal of Vascular and Endovascular Surgery*, 12(2):207–213, 1996.
- [48] Thanh N. Huynh, Balu K. Chacko, Xinjun Teng, Brigitta C. Brott, Michael Allon, Stacey S. Kelpke, John A. Thompson, Rakesh P.

- Patel, and Andreas S. Anayiotos. Effects of venous needle turbulence during ex vivo hemodialysis on endothelial morphology and nitric oxide formation. *Journal of Biomechanics*, 40(10):2158–2166, 2007.
- [49] Prabir Roy Chaudhury, Lawrence M. Spergel, Anatole Besarab, Arif Asif, and Pietro Ravani. Biology of arteriovenous fistula failure. *Journal of Nephrology*, 20(2):150–63, 2007.
- [50] Prabir Roy Chaudhury, Vikas P. Sukhatme, and Alfred K. Cheung. Hemodialysis vascular access dysfunction: A cellular and molecular viewpoint. *Journal of the American Society of Nephrology*, 17(4):1112–1127, 2006.
- [51] Sarah L. Waters, Jordi Alastruey, Daniel A. Beard, Peter H. M. Bovendeerd, Peter F. Davies, Girija Jayaraman, Oliver E. Jensen, Jack Lee, Kim H. Parker, Aleksander S. Popel, Timothy W. Secomb, Maria Siebes, Spencer J. Sherwin, Rebecca J. Shipley, Nicolas P. Smith, and Frans N. van de Vosse. Theoretical models for coronary vascular biomechanics: progress and challenges. *Progress Biophysics Molecular Biology*, 104(1-3):49–76, 2011.
- [52] Peter F. Davies. Flow-mediated endothelial mechanotransduction. *Physiology Review*, 75(3):519–60, 1995.
- [53] Marina Noris, Marina Morigi, Roberta Donadelli, Sistiana Aiello, Marco Foppolo, Marta Todeschini, Silvia Orisio, Giuseppe Remuzzi, and Andrea Remuzzi. Nitric oxide synthesis by cultured endothelial cells is modulated by flow conditions. *Circulation Research*, 76(4):536–543, 1995.
- [54] Francis Loth, Paul F. Fischer, Nurullah Arslan, Christopher D. Bertram, Seung E. Lee, Thomas J. Royston, Wael E. Shaalan, and Hisham S. Bassiouny. Transitional flow at the venous anastomosis

of an arteriovenous graft: Potential activation of the erk1/2 mechanotransduction pathway. *Journal of Biomechanical Engineering*, 125(1):49–61, 2003.

- [55] Francis Loth, Steven A. Jones, Christopher K. Zarins, Don P. Giddens, Raja F. Nassar, Seymour Glagov, and Hisham S. Bassiouny. Relative contribution of wall shear stress and injury in experimental intimal thickening at ptfе end-to-side arterial anastomoses. *Journal of Biomechanical Engineering*, 124(1):44–51, 2002.
- [56] Shari L. Meyerson, Christopher L. Skelly, Michael A. Curi, Umar M. Shakur, James E. Vosicky, Seymour Glagov, and Lewis B. Schwartz. The effects of extremely low shear stress on cellular proliferation and neointimal thickening in the failing bypass graft. *Journal of Vascular Surgery*, 34(1):90–97, 2001.
- [57] Stanley E. Rittgers, Panayotis E. Karayannacos, Julia F. Guy, Robert M. Nerem, George M. Shaw, Jephtha R. Hostetler, and John S. Vasko. Velocity distribution and intimal proliferation in autologous vein grafts in dogs. *Circulation Research*, 42(6):792–801, 1978.
- [58] Hisham S. Bassiouny, Scott White, Seymour Glagov, Eric Choi, Don P. Giddens, and Christopher K. Zarins. Anastomotic intimal hyperplasia: mechanical injury or flow induced. *Journal of Vascular Surgery*, 15(4):708–717, 1992.
- [59] Chong Wang, Brendon M. Baker, Christopher S. Chen, and Martin Alexander Schwartz. Endothelial cell sensing of flow direction. *Arteriosclerosis, Thrombosis, and Vascular Biology*, 33(9):2130–2136, 2013.
- [60] Jennifer M. Dolan, John Kolega, and Hui Meng. High wall shear stress and spatial gradients in vascular pathology: A review. *Annals of Biomedical Engineering*, 41(7):1411–1427, 2013.

- [61] Donald L Fry. Acute vascular endothelial changes associated with increased blood velocity gradients. *Circulation Research*, 22(2):165–197, 1968.
- [62] Ramesh N. Vaishnav, Dali J. Patel, Bulent H. Atabek, Madan D. Deshpande, Fred Plowman, and Jafar Vossoughi. Determination of the local erosion stress of the canine endothelium using a jet impingement method. *Journal of Biomechanical Engineering*, 105(1):77–83, 1983.
- [63] Zsolt Kulcsar, Adam Ugron, Miklos Marosfoi, Zsolt Berentei, Gyorgy Paal, and Istvan Szikora. Hemodynamics of cerebral aneurysm initiation: the role of wall shear stress and spatial wall shear stress gradient. *American Journal of Neuroradiology*, 32(3):587–94, 2011.
- [64] Samuel E. Wilson. *Autologous Arteriovenous Fistulas: Direct Radiocephalic Anastomosis for Hemodialysis*, book section 11, pages 86–91. Lippincott Williams and Wilkins, Philadelphia, USA, 5 edition, 2010.
- [65] Jean-Philippe Lafrance, Elham Rahme, Jacques Lelorier, and Sameena Iqbal. Vascular access-related infections: Definitions, incidence rates, and risk factors. *American Journal of Kidney Diseases*, 52(5):982–993, 2008.
- [66] Andrew R. Ready, Al Hassanein, John A. C. Buckels, and Samuel E. Wilson. *Infection in Vascular Access Procedures*, book section 24, pages 187–195. Lippincott Williams and Wilkins, Philadelphia, USA, 5 edition, 2010.
- [67] David Woltmann, Richard A. Fatica, Jonathan M. Rubin, and William Weitzel. Ultrasound detection of microembolic signals in hemodialysis accesses. *American Journal of Kidney Diseases*, 35(3):526–8, 2000.

- [68] Christofer J. Stegmayr, Per Jonsson, Ulf Forsberg, and Bernd G. Stegmayr. Development of air micro bubbles in the venous outlet line: An in vitro analysis of various air traps used for hemodialysis. *Artificial Organs*, 31(6):483–488, 2007.
- [69] Per Jonsson, Lars Karlsson, Ulf Forsberg, Margareta Gref, Christofer J. Stegmayr, and Bernd G. Stegmayr. Air bubbles pass the security system of the dialysis device without alarming. *Artificial Organs*, 31(2):132–139, 2007.
- [70] Ulf Forsberg, Per Jonsson, Christofer J. Stegmayr, and Bernd G. Stegmayr. A high blood level in the air trap reduces microemboli during hemodialysis. *Artificial Organs*, 36(6):525–529, 2012.
- [71] Florence Rollé, Josette Pengloan, Mohamed Abazza, Jean Michel Halimi, Michel Laskar, Léandre Pourcelot, and François Tranquart. Identification of microemboli during haemodialysis using doppler ultrasound. *Nephrology Dialysis Transplantation*, 15(9):1420–1424, 2000.
- [72] Bernd G. Stegmayr, Ulf Forsberg, Per Jonsson, and Christofer J. Stegmayr. The sensor in the venous chamber does not prevent passage of air bubbles during hemodialysis. *Artificial Organs*, 31(2):162–6, 2007.
- [73] Gholamreza Keshavarzi, Tracie Barber, Guan Yeoh, Anne Simmons, and John A. Reizes. Two dimensional computational analysis of microbubbles in hemodialysis. *Artificial Organs*, 37(8):E139–E144, 2013.
- [74] Ulf Forsberg, Per Jonsson, Christofer J. Stegmayr, and Bernd G. Stegmayr. Microemboli, developed during haemodialysis, pass the lung barrier and may cause ischaemic lesions in organs such as the brain. *Nephrology Dialysis Transplantation*, 25(8):2691–2695, 2010.

- [75] Dirk W. Droste, Karsten Kühne, Roland M. Schaefer, and Bernd E. Ringelstein. Detection of microemboli in the subclavian vein of patients undergoing haemodialysis and haemodiafiltration using pulsed doppler ultrasound. *Nephrology Dialysis Transplantation*, 17(3):462–466, 2002.
- [76] Bernd G. Stegmayr, Thomas Brännström, Ulf Forsberg, Per Jonson, Christofer J. Stegmayr, and Johan Hultdin. Microbubbles of air may occur in the organs of hemodialysis patients. *ASAIO Journal*, 58(2):177–179, 2012.
- [77] Ronald D. Fairshter, Dabir N. Vaziri, and Michael K. Mirahmadi. Lung pathology in chronic hemodialysis patients. *International Journal of Artificial Organs*, 5(2):97–100, 1982.
- [78] Michal Barak and Yeshayahu Katz. Microbubbles*: Pathophysiology and clinical implications. *Chest*, 128(4):2918–32, 2005.
- [79] Sudhakar George, Stephen Holt, and David Hildick-Smith. Patent foramen ovale, dialysis and microembolization. *Nephrology (Carlton)*, 17(6):569–74, 2012.
- [80] Giorgio M. Savazzi, Ferdinando Cusmano, Sergio Vinci, and Luigi Allegri. Progression of cerebral atrophy in patients on regular hemodialysis treatment: long-term follow-up with cerebral computed tomography. *Nephron*, 69(1):29–33, 1995.
- [81] Neil H. Pliskin, Helene M. Yurk, Tammy L. Ho, and Jason G. Umans. Neurocognitive function in chronic hemodialysis patients. *Kidney International*, 49(5):1435–1440, 1996.
- [82] Hans-Dietrich Polaschegg. Hemodialysis machine air detectors need not detect microbubbles. *Artificial Organs*, 31(12):911–912, 2007.
- [83] Glenda D. Graves. Arterial and venous pressure monitoring during haemodialysis. *Nephrology Nursing Journal*, 28(1):23–30, 2001.

- [84] Samuel E. Wilson. *Complications of Vascular Access: Thrombosis, Venous Hypertension, Congestive Heart Failure, Neuropathy and Aneurysm*, book section 21, pages 168–177. Lippincott Williams and Wilkins, Philadelphia, USA, 5 edition, 2010.
- [85] Lesley C. Dinwiddie, Lynda Ball, Deborah Brouwer, Sheila Doss-McQuitty, and Janet Holland. What nephrologists need to know about vascular access cannulation. *Seminars in Dialysis*, 26(3):315–322, 2013.
- [86] Magda M. van Loon, Tony Goovaerts, Alfons G. H. Kessels, Frank M. van der Sande, and Jan H. M. Tordoir. Buttonhole needling of haemodialysis arteriovenous fistulae results in less complications and interventions compared to the rope-ladder technique. *Nephrology Dialysis Transplantation*, 25(1):225–230, 2010.
- [87] Timmy Lee, Jill Barker, and Michael Allon. Needle infiltration of arteriovenous fistulae in hemodialysis: Risk factors and consequences. *American Journal of Kidney Diseases*, 47(6):1020–1026, 2006.
- [88] Michael A. Gimbrone Jr, Keith R. Anderson, and James N. Topper. The critical role of mechanical forces in blood vessel development, physiology and pathology. *Journal of Vascular Surgery*, 29(6):1104–1151, 1999.
- [89] Theodoros G. Papaioannou and Christodoulos Stefanadis. Vascular wall shear stress: basic principles and methods. *Hellenic Journal of Cardiology*, 46(1):9–15, 2005.
- [90] Peter F. Davies. Hemodynamic shear stress and the endothelium in cardiovascular pathophysiology. *Nature Clinical Practice Cardiovascular Medicine*, 6(1):16–26, 2009.
- [91] Donald A. McDonald. *Blood flow in arteries*. The Williams and Wilkins Co, Baltimore, 1974.

- [92] Byron L. Leverett, David J. Hellums, Clarence P. Alfrey, and Edward C. Lynch. Red blood cell damage by shear stress. *Biophysical journal*, 12(3):257–273, 1972.
- [93] Worth P. Longest and Clement Kleinstreuer. Numerical simulation of wall shear stress conditions and platelet localization in realistic end-to-side arterial anastomoses. *Journal of Biomechanical Engineering*, 125(5):671–681, 2003.
- [94] Yunus A. Cengel and John M. Cimbala. *Fluid Mechanics: Fundamentals and Applications*. McGraw Hill, New York, 2nd edition, 2010.
- [95] Sarah Kefayati, David W. Holdsworth, and Tamie L. Poepping. Turbulence intensity measurements using particle image velocimetry in diseased carotid artery models: Effect of stenosis severity, plaque eccentricity, and ulceration. *Journal of Biomechanics*, 47(1):253–263, 2014.
- [96] Tamie L. Poepping, Richard N. Rankin, and David W. Holdsworth. Flow patterns in carotid bifurcation models using pulsed doppler ultrasound: effect of concentric vs. eccentric stenosis on turbulence and recirculation. *Ultrasound in Medicine and Biology*, 36(7):1125–1134, 2010.
- [97] Stephen P. Broderick, Graeme J. Houston, and Michael T. Walsh. The influence of the instabilities in modelling arteriovenous junction haemodynamics. *Journal of Biomechanics*, 48(13):3591–3598, 2015.
- [98] Sharmila Sivanesan, Tien V. How, Ryan A. Black, and Ali Bakran. Flow patterns in the radiocephalic arteriovenous fistula: an in vitro study. *Journal of Biomechanics*, 32(9):915–925, 1999.

- [99] Michela Bozzetto, Bogdan Ene-Iordache, and Andrea Remuzzi. Transitional flow in the venous side of patient-specific arteriovenous fistulae for hemodialysis. *Annals of Biomedical Engineering*, pages 1–14, 2015.
- [100] Véronique Peiffer, Spencer J. Sherwin, and Peter D. Weinberg. Computation in the rabbit aorta of a new metric—the transverse wall shear stress—to quantify the multidirectional character of disturbed blood flow. *Journal of Biomechanics*, 46(15):2651–2658, 2013.
- [101] Yuchen Qiu and John M. Tarbell. Interaction between wall shear stress and circumferential strain affects endothelial cell biochemical production. *Journal of Vascular Research*, 37(3):147–57, 2000.
- [102] Janice Ward, Kate Shaw, and Andrew Davenport. Patients’ perspectives of constant-site (buttonhole) cannulation for haemodialysis access. *Nephron Clinical Practice*, 116(2):c123–7, 2010.
- [103] Hugh C. Rayner, Ronald L. Pisoni, Brenda W. Gillespie, David A. Goodkin, Takashi Akiba, Tadao Akizawa, Akira Saito, Eric W. Young, and Friedrich K. Port. Creation, cannulation and survival of arteriovenous fistulae: Data from the dialysis outcomes and practice patterns study. *Kidney International*, 63(1):323–330, 2003.
- [104] David Shemesh, Ilya Goldin, Daniel Berelowitz, Ibrahim Zaghal, Charles Zigelman, and Oded Olsha. Blood flow volume changes in the maturing arteriovenous access for hemodialysis. *Ultrasound in Medicine and Biology*, 33(5):727–733, 2007.
- [105] Yancheng Wang, Roland K. Chen, Bruce L. Tai, Patrick W. McLaughlin, and Albert J. Shih. Optimal needle design for minimal insertion force and bevel length. *Medical Engineering and Physics*, 36(9):1093–1100, 2014.

- [106] Alfredo R. Zarate. New needle for two needle hemodialysis. *ASAIO Journal*, 44(5):549–554, 1998.
- [107] Illse Van Tricht. *Hemodynamics of vascular access for hemodialysis*. Thesis, 2005.
- [108] Kai Chun Wong, Martin Büsen, Carrie Benzinger, René Gäng, Mirko Bezema, Nicholas Greatrex, Thomas Schmitz Rode, and Ulrich Steinseifer. Effect of inflow cannula tip design on potential parameters of blood compatibility and thrombosis. *Artificial Organs*, 38(9):810–817, 2014.
- [109] Mauro Grigioni, Carla Daniele, Umberto Morbiducci, Giuseppe D’Avenio, Giacomo Di Benedetto, Costantino Del Gaudio, and Vincenzo Barbaro. Computational model of the fluid dynamics of a cannula inserted in a vessel: incidence of the presence of side holes in blood flow. *Journal of Biomechanics*, 35(12):1599–1612, 2002.
- [110] Jun Y. Park, Chan Young Park, and Byoung Goo Min. A numerical study on the effect of side hole number and arrangement in venous cannulae. *Journal of Biomechanics*, 40(5):1153–1157, 2007.
- [111] Michael Neidlin, Sebastian Jansen, Anton Moritz, Ulrich Steinseifer, and Tim A. S. Kaufmann. Design modifications and computational fluid dynamic analysis of an outflow cannula for cardiopulmonary bypass. *Annals of Biomedical Engineering*, 42(10):2048–2057, 2014.
- [112] Idit Avrahami, Benny Dilmoney, Aliza Azuri, Moshe Brand, Oved Cohen, Liran Shani, Rony Reuven Nir, and Gil Bolotin. Investigation of risks for cerebral embolism associated with the hemodynamics of cardiopulmonary bypass cannula: a numerical model. *Artificial Organs*, 37(10):857–865, 2013.

- [113] Prahlad G Menon, James F Antaki, Akif Undar, and Kerem Pekkan. Aortic outflow cannula tip design and orientation impacts cerebral perfusion during pediatric cardiopulmonary bypass procedures. *Annals of Biomedical Engineering*, 41(12):2588–2602, 2013.
- [114] Guy Mareels, Radoslav Kaminsky, Sunny Eloot, and Pascal Verdonck. Particle image velocimetry-validated, computational fluid dynamics-based design to reduce shear stress and residence time in central venous hemodialysis catheters. *ASAIO Journal*, 53(4):438–446, 2007.
- [115] Paul W. Weber, Courtney A. Coursey, Laurens E. Howle, Rendon C. Nelson, Eli B. Nichols, and Sebastian T. Schindera. Modifying peripheral iv catheters with side holes and side slits results in favorable changes in fluid dynamic properties during the injection of iodinated contrast material. *American Journal of Roentgenology*, 193(4):970–977, 2009.
- [116] Guy Mareels, Dirk S. De Wachter, and Pascal Verdonck. Computational fluid dynamics-analysis of the niagara hemodialysis catheter in a right heart model. *Artificial Organs*, 28(7):639–648, 2004.
- [117] José Luis Teruel, Milagros Fernandez Lucas, Roberto Marcen, Jose R. Rodriguez, J. Lopez Sanchez, Teresa M. Rivera, Fernando Liano, and Joaquín Ortuno. Differences between blood flow as indicated by the hemodialysis blood roller pump and blood flow measured by an ultrasonic sensor. *Nephron*, 85(2):142–7, 2000.
- [118] Carmine De Bartolo, Alessandra Nigro, Gionata Fragomeni, Francesco M. Colacino, Dongfang Wang, Cameron C. Jones, and Joseph Zwischenberger. Numerical and experimental flow analysis of the wang-zwische double-lumen cannula. *ASAIO Journal*, 57(4):318–327, 2011.

- [119] Christina Rothera, Charlotte McCallum, Susan Huang, Paul Heidenheim, and Robert Lindsay. The influence of between-needle cannulation distance on the efficacy of hemodialysis treatments. *Haemodialysis International*, 15(4):546–552, 2011.
- [120] William F. Weitzel. Analysis of novel geometry-independent method for dialysis access pressure-flow monitoring. *Theoretical Biology and Medical Modelling*, 5(1):22, 2008.
- [121] Deborah J. Brouwer. Cannulation camp: Basic needle cannulation training for dialysis staff. *Dialysis and Transplantation*, 24(11):606–612, 1995.
- [122] Monica Schoch, Scott Wilson, and John W. M. Agar. Variations in vascular access flows in haemodialysis can depend on needle orientation. *Renal Society of Australasia Journal*, 4(2):13–18, 2008.
- [123] Sehmus Ozmen, Ali Kemal Kadiroglu, Cihan Akgul Ozmen, Ramazan Danis, Dede Sit, Davut Akin, and Mehmet Emin Yilmaz. Does the direction of arterial needle in av fistula cannulation affect dialysis adequacy? *Clinical Nephrology*, 70(3):229–232, 2008.
- [124] Maria Teresa Parisotto, Volker U. Schoder, Cristina Miriunis, Aileen H. Grassmann, Laura P. Scatizzi, Peter Kaufmann, Andrea Stopper, and Daniele Marcelli. Cannulation technique influences arteriovenous fistula and graft survival. *Kidney International*, 86(4):790–797, 2014.
- [125] Vikrom S. Sottiurai, James Yao, Robert Batson, Shirley Sue, Randy Jones, and Yukihiro Nakamura. Distal anastomotic intimal hyperplasia: Histopathologic character and biogenesis. *Annals of Vascular Surgery*, 3(1):26–33, 1989.
- [126] Prabir Roy Chaudhury, Burnett S. Kelly, Mary Ann Miller, Anita Reaves, Janice Armstrong, Nuwan Nanayakkara, and Sue C.

- Heffelfinger. Venous neointimal hyperplasia in polytetrafluoroethylene dialysis grafts. *Kidney International*, 59(6):2325–2334, 2001.
- [127] Zane S. Jackson, Hiroyuki Ishibashi, Avrum I. Gotlieb, and Lowell B. Langille. Effects of anastomotic angle on vascular tissue responses at end-to-side arterial grafts. *Journal of Vascular Surgery*, 34(2):300–307, 2001.
- [128] Remuzzi Andrea, Ene-Iordache Bogdan, Mosconi Lidia, Bruno Simona, Anghileri Abramo, Antiga Luca, and Remuzzi Giuseppe. Radial artery wall shear stress evaluation in patients with arteriovenous fistula for hemodialysis access. *Biorheology*, 40(1):423–430, 2003.
- [129] Ted R. Kohler, Thomas R. Kirkman, Larry W. Kraiss, Brenda K. Zierler, and Alexander W. Clowes. Increased blood flow inhibits neointimal hyperplasia in endothelialized vascular grafts. *Circulation Research*, 69(6):1557–1565, 1991.
- [130] Robert S. Keynton, Mark C. S. Shu, and Stanley E. Rittgers. The effect of angle and flow rate upon hemodynamics in distal vascular graft anastomoses: an in vitro model study. *Journal of Biomechanical Engineering*, 113(4):458–463, 1991.
- [131] Francis Loth, Steven A. Jones, Don P. Giddens, Hisham S. Bassiouny, Seymour Glagov, and Christopher K. Zarins. Measurements of velocity and wall shear stress inside a ptfе vascular graft model under steady flow conditions. *Journal of Biomechanical Engineering*, 119(2):187–194, 1997.
- [132] Ming Lei, Don P. Giddens, Steven A. Jones, Francis Loth, and Hisham S. Bassiouny. Pulsatile flow in an end-to-side vascular graft model: Comparison of computations with experimental data. *Journal of Biomechanical Engineering*, 123(1):80–87, 2001.

- [133] Michael Heise, Sven Schmidt, Ulf Krüger, Robert Pfitzman, Hans Scholz, Peter Neuhaus, and Utz Settmacher. Local haemodynamics and shear stress in cuffed and straight ptfе-venous anastomoses: an in-vitro comparison using particle image velocimetry. *European Journal of Vascular and Endovascular Surgery*, 26(4):367–73, 2003.
- [134] Zaher Kharboutly, Valerie Deplano, Eric Bertrand, and Cecile Legallais. Numerical and experimental study of blood flow through a patient-specific arteriovenous fistula used for hemodialysis. *Medical Engineering and Physics*, 32(2):111–118, 2010.
- [135] Iolanda Decorato, Zaher Kharboutly, Tommaso Vassallo, Justin Penrose, Cecile Legallais, and Anne Virginie Salsac. Numerical simulation of the fluid structure interactions in a compliant patient specific arteriovenous fistula. *International Journal for Numerical Methods in Biomedical Engineering*, 30(2):143–159, 2014.
- [136] Michael Heise, Ulf Krüger, Ralph Rückert, Robert Pfitzman, Peter Neuhaus, and Utz Settmacher. Correlation of intimal hyperplasia development and shear stress distribution at the distal end-side-anastomosis, in vitro study using particle image velocimetry. *European Journal of Vascular and Endovascular Surgery*, 26(4):357–366, 2003.
- [137] Michael Heise, Sven Schmidt, Ulf Krüger, Ralph Rückert, Stefan Rösler, Peter Neuhaus, and Utz Settmacher. Flow pattern and shear stress distribution of distal end-to-side anastomoses. a comparison of the instantaneous velocity fields obtained by particle image velocimetry. *Journal of Biomechanics*, 37(7):1043–1051, 2004.
- [138] Patrick H. Geoghegan, Nicolas A. Buchmann, Callum J. T. Spence, Steve Moore, and Mark Jermy. Fabrication of rigid and flexible refractive-index-matched flow phantoms for flow visualisation and

- optical flow measurements. *Experiments in Fluids*, 52(5):1331–1347, 2012.
- [139] Furanz Durst, Hiroshige Kikura, I Lekakis, Jovan Jovanović, and Q Ye. Wall shear stress determination from near-wall mean velocity data in turbulent pipe and channel flows. *Experiments in Fluids*, 20(6):417–428, 1996.
- [140] Eleyas Shaik, Klaus A. Hoffmann, and Jean-Francois Dietiker. Numerical simulations of pulsatile non-newtonian flow in an end-to-side anastomosis model. *Simulation Modelling Practice and Theory*, 16(9):1123–1135, 2008.
- [141] Koen Van Canneyt, Umberto Morbiducci, Sunny Eloot, Gianluca De Santis, Patrick Segers, and Pascal Verdonck. A computational exploration of helical arterio-venous graft designs. *Journal of Biomechanics*, 46(2):345–353, 2013.
- [142] Stephanie M. Kute and David A. Vorp. The effect of proximal artery flow on the hemodynamics at the distal anastomosis of a vascular bypass graft: Computational study. *Journal of Biomechanical Engineering*, 123(3):277–283, 2001.
- [143] Seung E. Lee, David S. Smith, Francis Loth, Paul F. Fischer, and Hisham S. Bassiouny. Importance of flow division on transition to turbulence within an arteriovenous graft. *Journal of Biomechanics*, 40(5):981–992, 2007.
- [144] Bogdan Ene-Iordache, Lidia Mosconi, Giuseppe Remuzzi, and Andrea Remuzzi. Computational fluid dynamics of a vascular access case for hemodialysis. *Journal of Biomechanical Engineering*, 123(3):284–292, 2001.

- [145] Bogdan Ene-Iordache and Andrea Remuzzi. Disturbed flow in radial-cephalic arteriovenous fistulae for haemodialysis: low and oscillating shear stress locates the sites of stenosis. *Nephrology Dialysis Transplantation*, 27(1):358–368, 2012.
- [146] Gráinne T. Carroll, Tim M. McGloughlin, P. E. Burke, Mike Egan, F. Wallis, and Michael T. Walsh. Wall shear stresses remain elevated in mature arteriovenous fistulas: A case study. *Journal of Biomechanical Engineering*, 133(2):021003, 2011.
- [147] Patrick M. McGah, Daniel F. Leotta, Kirk W. Beach, Eugene R . Zierler, and Alberto Aliseda. Incomplete restoration of homeostatic shear stress within arteriovenous fistulae. *Journal of Biomechanical Engineering*, 135(1):011005, 2013.
- [148] Patrick M. McGah, Daniel F. Leotta, Kirk W. Beach, and Alberto Aliseda. Effects of wall distensibility in hemodynamic simulations of an arteriovenous fistula. *Biomechanics and Modeling in Mechanobiology*, 13(3):679–695, 2014.
- [149] Siobhan O’Callaghan, Michael Walsh, and Timothy McGloughlin. Numerical modelling of newtonian and non-newtonian representation of blood in a distal end-to-side vascular bypass graft anastomosis. *Medical Engineering and Physics*, 28(1):70–74, 2006.
- [150] U.S. Renal Data System. Usrds 2012 annual data report: Chapter 1 incidence, prevalence, patient characteristics, and modalities. Report, National Institutes of Health, 2012.
- [151] Juan Carlos Jimenez and Robert S. Bennion. *Socioeconomic Implications of Vascular Access Surgery*, book section 29, pages 226–231. Lippincott Williams and Wilkins, Philadelphia, USA, 5 edition, 2010.

- [152] Michelle L. Robbin, Nathan E. Chamberlain, Mark E. Lockhart, Michael H. Gallichio, Carlton J. Young, Mark H. Deierhoi, and Michael Allon. Hemodialysis arteriovenous fistula maturity: Us evaluation 1. *Radiology*, 225(1):59–64, 2002.
- [153] Steven B. Palder, Robert L. Kirkman, Anthony D. Whittimore, Raymond M. Hakim, Michael J. Lazarus, and Nicholas L. Tilney. Vascular access for hemodialysis. patency rates and results of revision. *Annals of surgery*, 202(2):235, 1985.
- [154] Klaus Konner. Primary vascular access in diabetic patients: an audit. *Nephrology Dialysis Transplantation*, 15(9):1317–1325, 2000.
- [155] Luigi Vernaglione, Giuseppe Mele, Claudio Cristofano, Cosimo Distratis, Franco Perrone, Marcello Frascina, Fabio Pennacchiotti, and Stefano Chimienti. Comorbid conditions and gender impact the primary survival of distal radio-cephalic arteriovenous fistula in patients on long-term hemodialysis. *Journal of Nephrology*, 18(3):276, 2005.
- [156] Miltos K. Lazarides, George S. Georgiadis, George A. Antoniou, and Dimitrios N. Staramos. A meta-analysis of dialysis access outcome in elderly patients. *Journal of Vascular Surgery*, 45(2):420–426. e2, 2007.
- [157] Dilek Gibyeli Genek, Canan Tuncer Altay, Tarkan Unek, Aykut Sifil, Mustafa Seçil, and Taner Camsari. Can primary failure of arteriovenous fistulas be anticipated? *Hemodialysis International*, 19(2):296–305, 2015.
- [158] Weronika Oleskowska Florek, Alicja Polubinska, Ewa Baum, Monika Matecka, Malgorzata Pyda, Krzysztof Pawlaczyk, and Andrzej Breborowicz. Hemodialysis induced changes in the blood composition affect function of the endothelium. *Hemodialysis International*, 18(3):650–656, 2014.

- [159] Eriko Shibata, Kojiro Nagai, Risa Takeuchi, Yasuhiro Noda, Tomomi Makino, Yusuke Chikata, Michael Hann, Sakiya Yoshimoto, Hiroyuki Ono, and Sayo Ueda. Reevaluation of prepump arterial pressure to avoid inadequate dialysis and hemolysis: Importance of prepump arterial pressure monitoring in hemodialysis patients. *Artificial Organs*, 39(7):627–634, 2015.
- [160] Pedro Ponce, Daniele Marcelli, Caecilia Scholz, Wolfgang Wehmeyer, Pedro Gonçalves, Aileen Grassmann, Katharina Brand, and Bernard Canaud. Does the extracorporeal blood flow affect survival of the arteriovenous vascular access? *Hemodialysis International*, 12(2):314–322, 2014.
- [161] Mouhammad El Hassan, HassanHassan Assoum, Vaclav Sobolik, Jérôme Vétel, Kamel Abed-Meraim, André Garon, and Anas Sakout. Experimental investigation of the wall shear stress and the vortex dynamics in a circular impinging jet. *Experiments in Fluids*, 52(6):1475–1489, 2012.
- [162] Amina Meslem, Mouhammad El Hassan, and Ilinca Nastase. Analysis of jet entrainment mechanism in the transitional regime by time-resolved piv. *Journal of Visualization*, 14(1):41–52, 2011.
- [163] Trung B. Le, Daniel R. Troolin, Devesh Amatya, Ellen K. Longmire, and Fotis Sotiropoulos. Vortex phenomena in sidewall aneurysm hemodynamics: experiment and numerical simulation. *Annals of Biomedical Engineering*, 41(10):2157–2170, 2013.
- [164] John Charonko, Satyaprakash Karri, Jaime Schmieg, Santosh Prabhu, and Pavlos Vlachos. In vitro comparison of the effect of stent configuration on wall shear stress using time-resolved particle image velocimetry. *Annals of Biomedical Engineering*, 38(3):889–902, 2010.

- [165] Denis J. Phares, Gregory T. Smedley, and Richard C. Flagan. The wall shear stress produced by the normal impingement of a jet on a flat surface. *Journal of Fluid Mechanics*, 418(1):351–375, 2000.
- [166] Norbert Didden and Chih-Ming Ho. Unsteady separation in a boundary layer produced by an impinging jet. *Journal of Fluid Mechanics*, 160:235–256, 1985.
- [167] Joseph W. Hall and Daniel Ewing. On the dynamics of the large-scale structures in round impinging jets. *Journal of Fluid Mechanics*, 555:439–458, 2006.
- [168] Christopher C. Landreth and Ronald J. Adrian. Impingement of a low reynolds number turbulent circular jet onto a flat plate at normal incidence. *Experiments in Fluids*, 9(1-2):74–84, 1990.
- [169] Nallamuthu Rajaratnam, David Z. Zhu, and S. P. Rai. Turbulence measurements in the impinging region of a circular jet. *Canadian Journal of Civil Engineering*, 37(5):782–786, 2010.
- [170] Adrian Melling. Tracer particles and seeding for particle image velocimetry. *Measurement Science and Technology*, 8(12):1406, 1997.
- [171] Hui Hu. Stereo particle imaging velocimetry techniques: Technical basis, system setup, and application. *Handbook of 3D Machine Vision: Optical Metrology and Imaging*, 1:71–100, 2013.
- [172] Nicholas J. Lawson and Jie Wu. Three-dimensional particle image velocimetry: experimental error analysis of a digital angular stereoscopic system. *Measurement Science and Technology*, 8(12):1455, 1997.
- [173] Markus Raffel, Christian E. Willert, and Jürgen Compenhans. *Particle Image Velocimetry: A Practical Guide*. Springer-Verlag, Germany, 1st edition, 1998.

- [174] Hugh W. Coleman and Glenn W. Steele. Engineering application of experimental uncertainty analysis. *AIAA journal*, 33(10):1888–1896, 1995.
- [175] Cameron Stanley. *Experimental investigation of cavitation in a cylindrical orifice*. Thesis, 2012.
- [176] Richard A. Bajura and MR Catalano. Transition in a two-dimensional plane wall jet. *Journal of Fluid Mechanics*, 70(04):773–799, 1975.
- [177] Sandeep Gogineni and Chiang Shih. Experimental investigation of the unsteady structure of a transitional plane wall jet. *Experiments in Fluids*, 23(2):121–129, 1997.
- [178] Fei-Bin Hsiao and Shyh-Shiun Sheu. Double row vortical structures in the near field region of a plane wall jet. *Experiments in Fluids*, 17(5):291–301, 1994.
- [179] Jun Ding, Zengsheng Chen, Shuqiong Niu, Jiafeng Zhang, Nandan K. Mondal, Bartley P. Griffith, and Zhongjun J. Wu. Quantification of shear induced platelet activation: High shear stresses for short exposure time. *Artificial Organs*, 2015.
- [180] George M. Nassar, Edward Rhee, Abdul Jabbar Khan, Binh Nguyen, Katafan Achkar, and Gerald Beathard. Percutaneous thrombectomy of avf: Immediate success and long term patency rates. *Seminars in Dialysis*, 28(2):15–22, 2015.
- [181] Luca Antiga and David A. Steinman. Rethinking turbulence in blood. *Biorheology*, 46(2):77–81, 2008.
- [182] Malek O. Khan, Kristian Valen-Sendstad, and David A. Steinman. Narrowing the expertise gap for predicting intracranial aneurysm hemodynamics: Impact of solver numerics versus mesh and time-step resolution. *American Journal of Neuroradiology*, 2015.

- [183] Kristian Valen-Sendstad, Marina Piccinelli, and David A. Steinman. High-resolution computational fluid dynamics detects flow instabilities in the carotid siphon: Implications for aneurysm initiation and rupture? *Journal of Biomechanics*, 47(12):3210–3216, 2014.
- [184] Kristian Valen-Sendstad and David A. Steinman. Mind the gap: impact of computational fluid dynamics solution strategy on prediction of intracranial aneurysm hemodynamics and rupture status indicators. *American Journal of Neuroradiology*, 35(3):536–543, 2014.
- [185] Jonas Lantz, Roland Gårdhagen, and Matts Karlsson. Quantifying turbulent wall shear stress in a subject specific human aorta using large eddy simulation. *Medical Engineering and Physics*, 34(8):1139–1148, 2012.
- [186] Patrick J. Roache. Quantification of uncertainty in computational fluid dynamics. *Annual Review of Fluid Mechanics*, 29(1):123–160, 1997.
- [187] Juliana B. R. Loureiro and Atila P. Silva Freire. Wall shear stress measurements and parametric analysis of impinging wall jets. *International Journal of Heat and Mass Transfer*, 55(23–24):6400–6409, 2012.
- [188] Jean-Jacques Patard, Karim Bensalah, Antoine Lucas, Alejandro Rodriguez, Andrea Manunta, Joseph Rivalan, Patrick Le Pogamp, Bernard Lobel, and François Guillé. Management of vascular access for hemodialysis after successful kidney transplantation. *Scandinavian Journal of Urology and Nephrology*, 36(5):373–376, 2002.
- [189] Barbara Vajdic, Rafael Ponikvar, Aljosa Kandus, and Jadranka Buturovic Ponikvar. Hemodialysis arteriovenous fistula related complications and surgery in kidney graft recipients. *Therapeutic Apheresis and Dialysis*, 17(4):444–447, 2013.

- [190] Yang Wang, Mahesh Krishnamoorthy, Rupak Banerjee, Jianhua Zhang, Steven Rudich, Christy Holland, Lois Arend, and Prabir Roy Chaudhury. Venous stenosis in a pig arteriovenous fistula model—anatomy, mechanisms and cellular phenotypes. *Nephrology Dialysis Transplantation*, 23(2):525–533, 2008.
- [191] Robin W. Glashan and Frank Walker. A histological examination of veins used in artificial arteriovenous (‘quinton/scribner’) shunts. *British Journal of Surgery*, 55(3):189–193, 1968.
- [192] Michael A. Reidy and Stephen M. Schwartz. Endothelial regeneration. iii. time course of intimal changes after small defined injury to rat aortic endothelium. *Laboratory investigation; a journal of technical methods and pathology*, 44(4):301–308, 1981.
- [193] Jurgen Fingerle, Tina Y. P. Au, Alexander W. Clowes, and Michael A. Reidy. Intimal lesion formation in rat carotid arteries after endothelial denudation in absence of medial injury. *Arteriosclerosis, Thrombosis, and Vascular Biology*, 10(6):1082–1087, 1990.
- [194] Hsin-Yi Lin, Brian A. Biancucci, Steven Deutsch, Arnold A. Fontaine, and John M. Tarbell. Observation and quantification of gas bubble formation on a mechanical heart valve. *Journal of Biomechanical Engineering*, 122(4):304–309, 2000.
- [195] Sean D. Chambers, Robert H. Bartlett, and Steven L. Ceccio. Determination of the in vivo cavitation nuclei characteristics of blood. *ASAIO Journal*, 45(6):541–549, 1999.
- [196] Arthur Grollman. The vapour pressure of dog’s blood at body temperature. *J Gen Physiol*, 11(5):495–506, 1928.
- [197] Thomas A. Depner, Syed Rizwan, and Terri A. Stasi. Pressure effects

on roller pump blood flow during hemodialysis. *ASAIO Journal*, 36(3):M456–458, 1990.

- [198] Xiaoming Zhou, Xin M. Liang, Gang Zhao, Youchao Su, and Yang Wang. A new computational fluid dynamics method for in depth investigation of flow dynamics in roller pump systems. *Artificial Organs*, 38(7):106–117, 2014.